Syenite-hosted gold mineralization and hydrothermal alteration at the Young-Davidson deposit, Matachewan, Ontario

by

Ryan D. Martin

A thesis

presented to the University of Waterloo

in fulfillment of the

thesis requirement for the degree of

Master of Science

in

Earth Sciences

Waterloo, Ontario, Canada, 2012

AUTHOR'S DECLARATION

I hereby declare that I am the sole author of this thesis. This is a true copy of the thesis, including any required final revisions, as accepted by my examiners.

_____, Ryan D. Martin

I understand that my thesis may be made electronically available to the public.

_____, Ryan D. Martin

Abstract

The syenite-hosted Young-Davidson (YD) gold deposit is located at the western extension of the Cadillac-Larder-Lake deformation zone (CLLDZ), southwest of Kirkland Lake, in the southern Abitibi greenstone belt, Canada. Gold is predominantly hosted by syenite, and to a lesser extent by Timiskaming sedimentary rocks and mafic volcanic rocks in veins and/or small pervasively altered shear zones related to the CLLDZ. Historical gold production was mainly from quartz veins and disseminated pyrite hosted in altered syenite. Recent drilling by AuRico Gold Corporation (formerly Northgate Minerals Co.) has expanded the underground resource to 14.6 million tonnes (measured and indicated) at an average grade of 2.03 g/t Au and an underground reserve of 39.1 million tonnes (proven and probable) at an average grade of 2.79 g/t Au, where most of the gold is hosted in the syenite.

Three generations of veins have been identified based on crosscutting relationships mapped at an underground ore crosscut: V_1 boudinaged iron-carbonate veins, V_2 folded quartz-pyrite veinlets and V_3 planar quartz-carbonate veins. Structural characterization of the vein sets indicates that V_2 and V_3 extensional vein arrays developed during the D_2 deformation, which generated the steeply dipping east-west striking penetrative S_2 foliation that is found elsewhere along the CLLDZ. Petrographic analysis of mineralized syenite shows that native gold grains are most abundant in zones of intense potassic-hematite-pyrite alteration as inclusions and along cracks in vein-related and disseminated pyrite. Volcanic-hosted gold is mainly located in quartz-iron-carbonate veins hosted in narrow sheared and pervasively albite-iron-carbonate-pyrite altered volcanic rocks. Whole rock lithogeochemical analyses and mass balance calculations show that mineralized syenite is characterized by enrichments in K, S, Na, Ba and W whereas mineralized volcanic rocks are characterized by strong enrichments in Na, Al, Si, K, Fe, S, Ba and W. Geochemical contouring of 279 analyses of drill core along two N-S sections through the YD syenite show broad cross section scale correlation of gold mineralization with K_2O, S and Ba. Sulfur is the most strongly correlated with gold mineralization; however, the most intense sulfidation is generally coincident with zones containing coarse altered feldspars and a fine-grained groundmass of iron-carbonate, Na- and K-feldspar and minor quartz.

Bulk sulfur isotopic analyses of syenite-hosted pyrite grains indicate that the dominant source of sulfur is magmatic but there is also a component that has interacted with the reduced Archean atmosphere. Pyrite grains in syenite and volcanic rocks contain up to 15,000 ppm Co, 4,000 ppm Ni and 4,200 ppm As. Chemical mapping of Co, Ni and As from different vein associated pyrite grains show: 1) Arsenic in pyrite is low, <1,000 ppm; 2) Pyrite shows Co-Ni zoning and gold in V_1 vein pyrite is associated with Co-Ni rich pyrite overgrowths of earlier corroded pyrite grains; 3) gold along fractures in V_2 vein pyrite is also associated with Co-Ni enrichment; and 4) gold in V_3 veins crosscuts Co-Ni patterns in pyrite, which suggests that the V_3 style of mineralization has precipitated by different mechanisms. Pyrite mapping combined with alteration assemblages, mineralization characteristics and mineral chemistry suggests that the syenite-hosted mineralization has formed from interaction between multiple fluids with distinct physicochemical conditions. The proposed formational model for the Young-Davidson deposit is of fluid mixing between magmatic and metamorphic fluids during the deformation events that generated the extensive veining systems at Young-Davidson.

Acknowledgements

AuRico Gold Corporation provided logistical and financial support throughout this study. This study has also been funded by the NSERC grant of Robert Linnen. The support from AuRico Gold Corporation during many field seasons was vital to the completion of this thesis.

This work would not have been possible if not for my supervisor, Dr. Robert L. Linnen. Through many technical discussions in the field, laboratory discussions, discussions about data, comments and suggestions about methods and analytical processes, and general discussions over coffee, my fundamental understanding of the data collected in all parts of this study has greatly improved, and I am very thankful. Special thanks to Jian Zhang, at the University of Hong Kong, for teaching me structural 'thinking' and for extensive guidance during multiple field mapping seasons. Through many discussions on important outcrops, my understanding of how local structures tie into regional frameworks has greatly improved. Thank you both for your guidance and patience during field work, laboratory work and data analysis. Thanks to the geologists at AuRico Gold Corporation, J. Janzen, C. Edmunds and C. Rockingham, for assistance, discussions and suggestions while at the study site. Special thanks to Y. Liu, N. Heinig, C. Henderson, L. Hayden and A. Rittau for technical support and advice during data collection. Thanks to Dr. M. Coniglio for guidance and comments regarding laboratory testing, and to Dr. S. Lin for many insightful comments and suggestions during field mapping. I would also like to thank Dr. R. Linnen, Dr. M. Coniglio and Dr. S. Lin for being a part of my thesis committee, and for the comments and suggestions that have added to the quality of this thesis.

I would like to thank my friends for supporting me over the course of this study; Ryan, Katrina, Jess, Jon, Kaitlin, Ben, Nathan, Joel, Jen, Niloufar and many others. Your comments, suggestions and general outlook on life have improved mine, and I am very thankful.

Finally, my loving family, Mom, Dad, Craig, Jane, Tara, Kyle, Alan and girlfriend, Lisa, have supported me throughout the course of my thesis and I am forever grateful.

Table of Contents

List of Figures

List of Tables

Chapter 1
General Introduction

1.1 General Introduction

Gold mineralization in the Superior Province of the Canadian Shield is an important source of gold for the Canadian economy. The Superior Province contains abundant mineral wealth compared to the other provinces of the Canadian Shield; 80 VMS deposits, 100+ lode gold deposits, magmatic nickel sulfide deposits, iron-oxide deposits and several vein-associated copper deposits (Poulsen et al., 1992). Quartz-carbonate vein deposits in the Abitibi account for 48.1% of the total Canadian gold production from all deposit types. The Abitibi greenstone belt accounts for 72.4% of all Canadian gold production from greenstone-hosted quartz-carbonate vein type deposits and is home to 6 of the 12 'world-class' giant deposits, those containing > 250 tonnes of gold (Dubé and Gosselin, 2007). Lode gold deposits in the Abitibi are associated with first order crustal-scale structures and second order splay and fault structures (e.g., Hodgson, 1989). They also show strong correlation with felsic intrusive rocks and, to a lesser extent, Timiskaming meta-sedimentary rocks (e.g., Robert, 2001). Gold-bearing veins in the Abitibi can be hosted by any lithology, but the majority of the mineralization is hosted in iron-rich tholeiitic volcanic rocks, iron-rich gabbroic sills and felsic intrusions (Dubé and Gosselin, 2007). Two major crustal-scale structures are present in the southern Abitibi: the Porcupine-Destor deformation zone (PDDZ) and the Cadillac-Larder-Lake deformation zone (CLLDZ), shown in Figure 1.1.The Young-Davidson gold mine is a syenite-hosted deposit that lies along the western extension of the CLLDZ, a few kilometers west of the town of Matachewan, approximately 70 km west-southwest of Kirkland Lake. Known gold mineralization along the CLLDZ extends from Young-Davidson, east through Kirkland Lake, to the Val d'Or mining camp in Quebec. Similarly, to the north, the world-class Timmins mining camp occurs along the east-west striking PDDZ.

Archean-aged gold deposits in the Abitibi can be grouped into 4 key genetic types as outlined by Poulsen et al. (2000): greenstone-hosted quartz-carbonate vein deposits; intrusion-associated deposits; turbidite-associated deposits; and gold-rich VMS deposits. Individual gold deposits generally contain distinct features that permit grouping into one of the genetic types. These characteristics generally include: tectonic setting, geologic association, alteration styles, fluid association, metal associations and general mineralizing characteristics. Some individual deposits contain characteristics that are representative of more than one genetic model, which leads to difficulties describing the controls on mineralization. This in turn affects the exploration model as exploration strategies for each type of deposit differ. To complicate matters further, even though each type of deposit forms at different

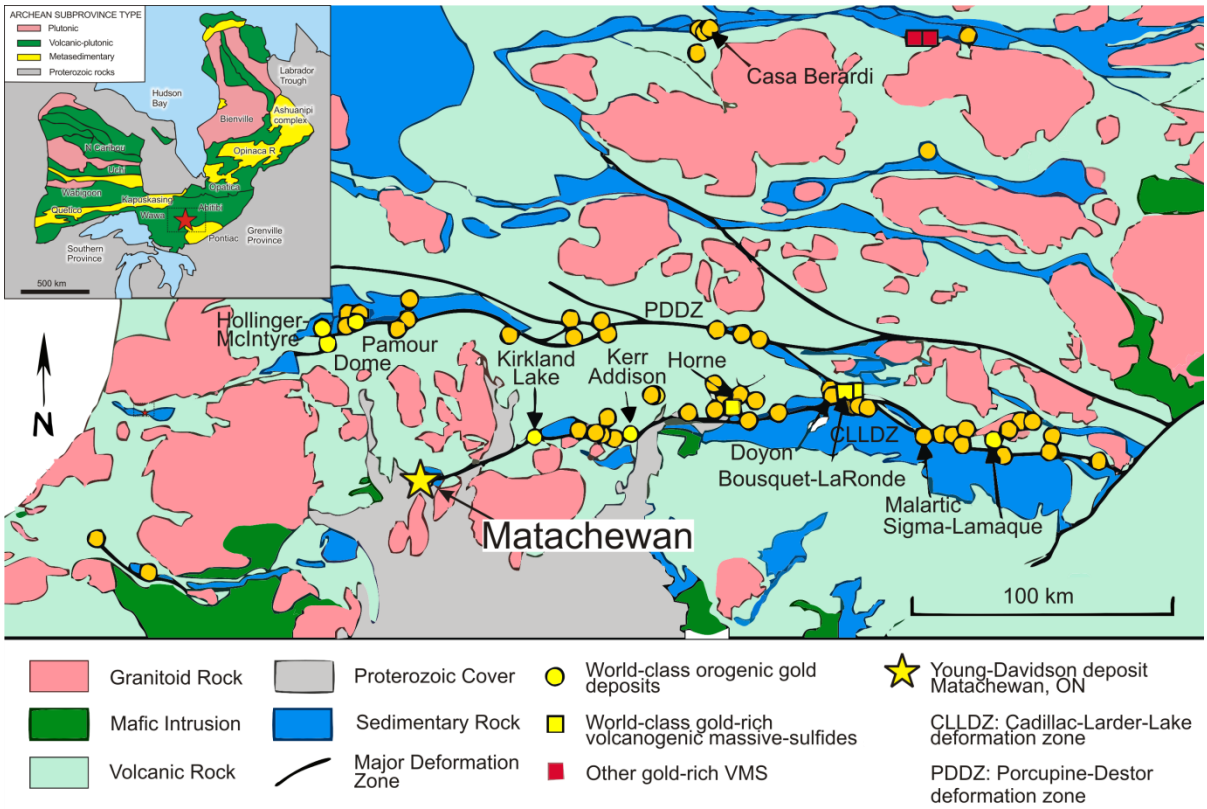

Figure 1.1: General geologic map of the southern Abitibi greenstone belt showing location of major crustal scale deformation zones the Porcupine-Destor deformation zone (PDDZ) and the Cadillac-Larder-Lake deformation zone (CLLDZ). All types of gold deposits in the southern Abitibi show correlation with these major crustal scale structures and their splays. Study area shown in red on inset map (Modified from Dubé and Gosselin, 2007 and Dinel et al., 2008)

crustal levels, from different fluids in distinct tectonic settings (e.g., VMS vs. intrusion-associated; Figure 1.2), compressional deformation and development of regional fault zones has often superimposed later vein related alteration/mineralization styles on earlier mineralization styles. Since many gold deposits in the Abitibi lie along major crustal-scale deformation zones or related secondary structures and are associated with intrusions near thick volcanic sequences, often the mineralizing characteristics do not clearly support a single formational model. It is important to be able to determine the most important factors controlling mineralization at each deposit so exploration criteria can be developed to find further mineralization. For example, does mineralization occur along a specific lithology/chemically favorable horizon? Is it constrained to a certain correlatable vein set or common structure? Determining such controls requires understanding the relationship between mineralization and volcanic construction, intrusion events, regional deformation, veins and alteration.

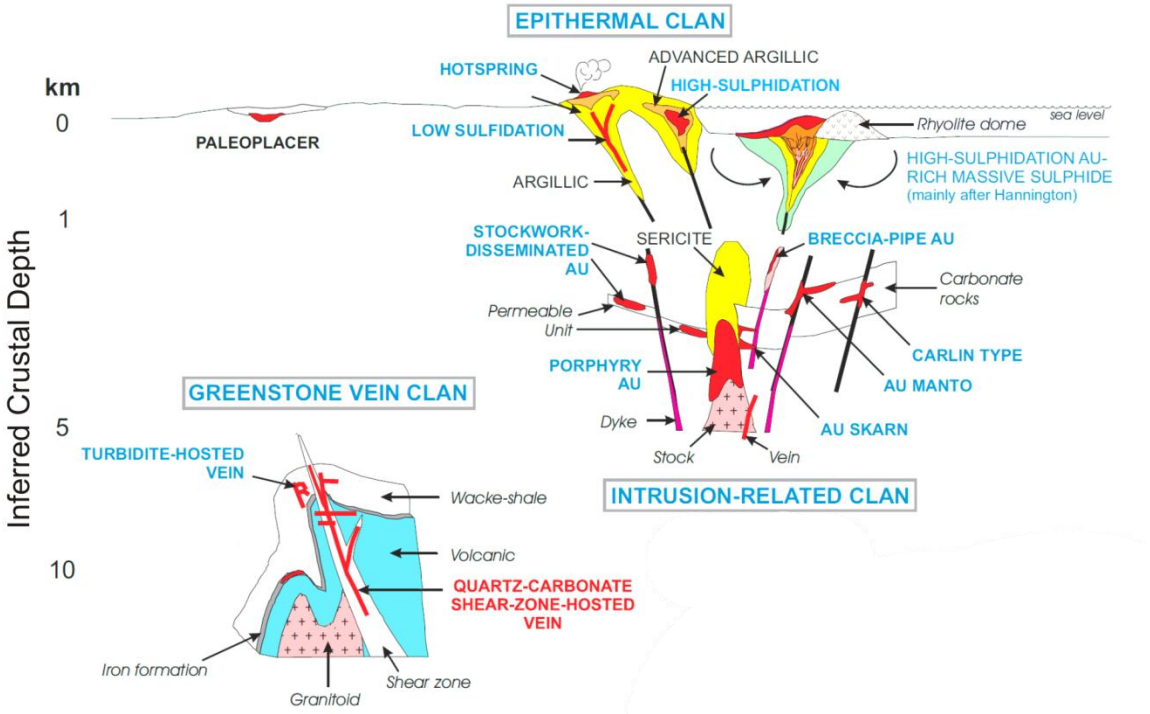

Figure 1.2: Formational models for different classes of gold deposits found in the southern Abitibi greenstone belt (Modified from Dubé and Gosselin, 2007).

Gold deposits in the southern Abitibi can be subdivided based on geologic setting, age, host rocks and formational models. Recognized deposit models in the southern Abitibi include: gold-rich VMS deposits (e.g., LaRonde Penna), greenstone-hosted quartz-carbonate vein deposits (e.g., Kerr Addison), turbidite-hosted Au mineralization (e.g., Pamour) and intrusion-related gold deposits (e.g., Canadian Malarctic, Upper Beaver) (Dubé and Gosselin, 2007; Dubé et al., 2007). Gold-rich VMS deposits are thought to have formed during volcanic-construction of the Abitibi in a shallow water to subaerial volcanic setting (Dubé et al., 2007). By contrast, intrusion-associated gold deposits are thought to form during regional compression and orogenesis at greater depths (Robert, 2001). During regional-scale deformation, shear-related quartz-carbonate vein deposits formed along major structures and may have locally overprinted, upgraded or remobilized earlier intrusion-related or Au-rich VMS styles of mineralization located along those deformation zones (Dubé and Gosselin, 2007). Therefore at a single deposit, gold mineralization may be controlled by two temporally distinct events that are spatially associated. Alternatively, for intrusion-associated deposits, Robert (2001) showed that the characteristics of mineralization (veining styles, pyritization styles, alteration styles, isotopic signatures) are distinctly different from the mineralizing-characteristics at quartz-carbonate vein

deposits hosted by other lithologies. Robert (2001) further classified syenite-hosted deposits as a distinct deposit type based on the strong spatial association with syenite to monzonite stocks, contrasting vein types, alteration characteristics and a lack of structural controls.

1.2 Thesis Objectives

Orogenic lode gold deposits are well characterized in the southern Abitibi and in addition to the strong spatial association with crustal-scale deformation zones, also show spatial correlation with Timiskaming sedimentary rocks and felsic intrusions. This study is the geochemical component of a combined structural-geochemical study on the syenite-hosted mineralization at the Young-Davidson gold deposit. Since the Young-Davidson syenite is the dominant host of mineralization but is also in close proximity to the CLLDZ, a geochemical investigation requires a structural context to correlate mineralization features with regional structural events. A combined structural-geochemical approach will help address the controversy of the role of felsic intrusions in gold mineralization at this deposit. A structural study of the deposit by Zhang et al. (2012) has outlined the relative timing of veining within the syenite, and related veining to local structural events that correlate to regional events from elsewhere in the Abitibi. In order to propose a genetic model for the syenite-hosted gold mineralization at Young-Davidson, this geochemical study will:

1. Assess the relationship between mineralization, alteration and veining and correlate findings with the structural framework developed by Zhang et al. (2012)
2. Characterize the geochemical enrichments associated with gold mineralization in the syenite and volcanic rocks at Young-Davidson
3. Determine the deposit-scale lithogeochemical trends along two north-south cross sections through the Young-Davidson syenite
4. Calculate the mass changes in mineralized rocks at Young-Davidson
5. Characterize the textures of the ore-related minerals: rutile, pyrite and gold
6. Determine the chemistry of rutile, pyrite and gold grains, from different locations in the Young-Davidson syenite, grouped by vein types and relative textures, to obtain information about the ore-controlling fluids
7. Obtain chemical maps and bulk sulfur isotopic analyses of pyrite grains from distinct vein sets and textural styles of pyrite mineralization

1.3 Thesis Organization

This thesis is organized into 4 chapters. The current chapter is intended to highlight a number of key background criteria and methodology that does not fit in the paper style format of Chapters 2 and 3. This first chapter includes an introduction to the problem that is to be addressed in this thesis, a historical summary of the Young-Davidson deposit, general background information on the formation of the lithological units in the Abitibi and a summary of the methods used in this thesis. In addition Chapter 1 also provides a short discussion of the quality of the data and some problems encountered during data collection. Chapter 2 and 3 are written as standalone papers; there is repetition in the introduction, background and method sections for both papers. In general, Chapter 2 highlights the geology, petrography, alteration and geochemical characteristics of the mineralization at the Young-Davidson deposit whereas Chapter 3 addresses the chemical and stable isotopic characteristics of ore-related minerals at the Young-Davidson deposit. The final chapter summarizes the results from Chapters 2 and 3 and provides unifying discussion and conclusions, tying the results of Chapters 1, 2 and 3 into a complete thesis.

1.4 Background

1.4.1 Local Setting

The Young-Davidson syenite is a coarse trachytic to porphyritic syenite that has intruded roughly along the contact between Timiskaming sedimentary rocks to the north and Tisdale mafic and ultramafic volcanic rocks to the south (Figure 1.3 and Figure 1.4). The Young-Davidson syenite is part of an overturned sequence dipping approximately 75-80 degrees to the south. Since all of the Archean rocks in the Matachewan area are metamorphosed to greenschist facies (locally up to amphibolite facies; Lovell, 1967), the prefix meta- is implied for all Archean units (e.g., meta-volcanic) and will be omitted in the following sections. A minor component of late brittle movement is developed along the N-S trending Mistinigon Lake and the Montreal River faults west and east of Young-Davidson, respectively (Figure 1.4). The mine-scale geology of Young-Davidson is shown in Figure 2.3 and discussed further in Section 2.4.

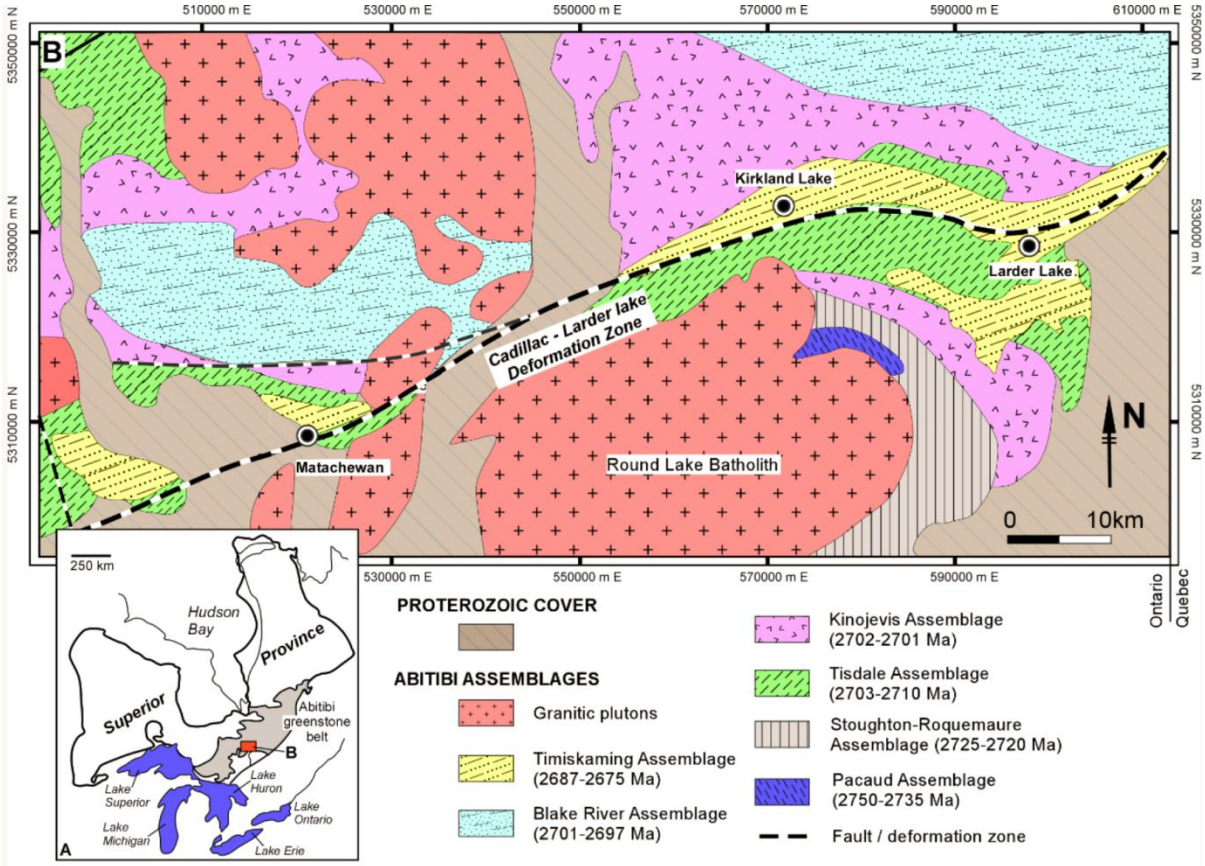

Figure 1.3: Southern Abitibi greenstone belt showing the location of the Cadillac-Larder-Lake deformation zone, Matachewan, Kirkland Lake, Larder Lake and various available age dates from the area (Modified from Zhang et al., 2012).

1.4.2 History of Young-Davidson

The Young-Davidson gold deposit was discovered by Jake Davidson in 1916. The discovery of gold mineralization led to a staking rush that established the Matachewan Consolidated Mine. Native gold in a quartz vein crosscutting carbonate-altered volcanic rocks was part of the initial discovery and is still found on the mine site today. In 1917, gold was found in reddish brown syenite and grey volcanic rocks in the adjoining Matachewan Consolidated property. Between 1934 and the mid to late 1950's, approximately 964,000 oz of Au were produced from the two mines, operating at either end of the current deposit, at an average grade of 0.094 oz/ton Au from the Young-Davidson mine and 0.107 oz/ton Au from the Matachewan Consolidated Mine (Evans, 2007). In 2003, Northgate Minerals Corporation gained ownership of the property and in 2005 initiated an extensive surface and

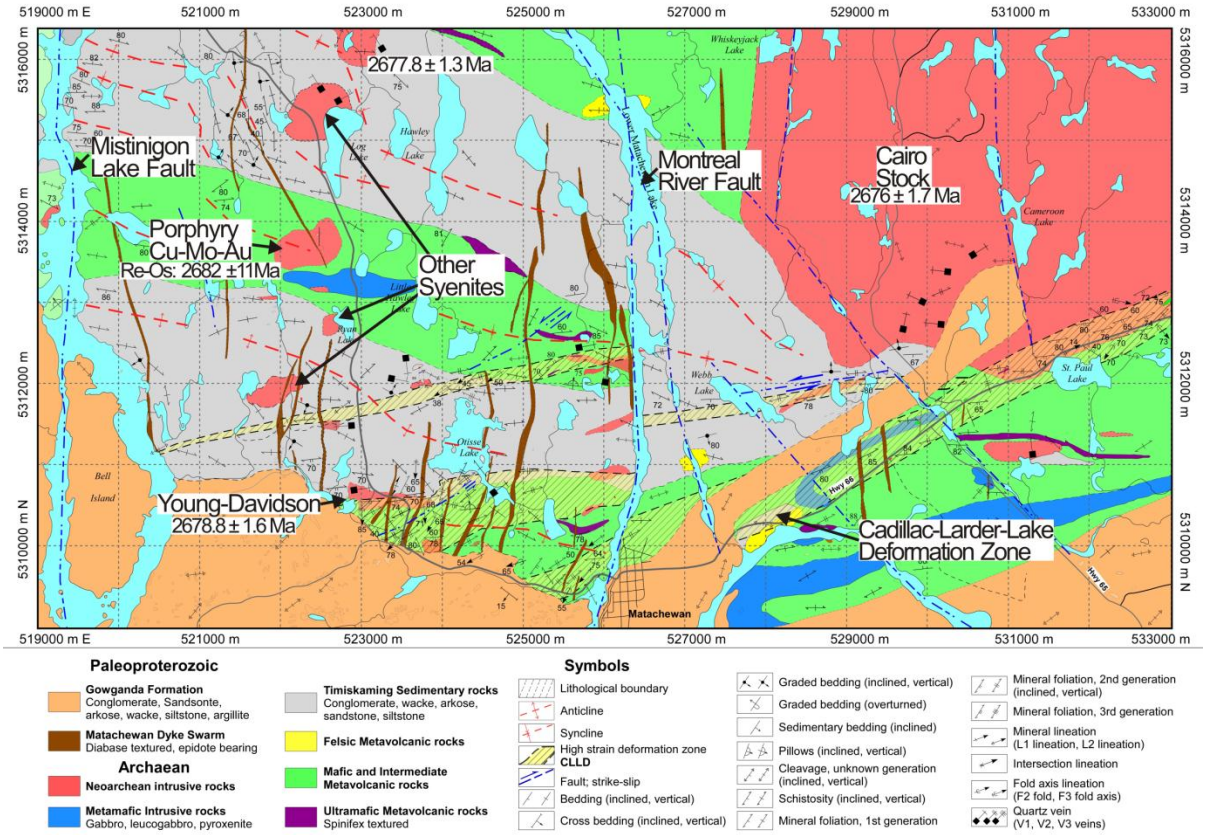

Figure 1.4: Local geology of the Matachewan area showing location of Young-Davidson, Cadillac-Larder-Lake deformation zone, Montreal River Fault, Mistinigon Lake Fault and other felsic intrusions in the area (Modified from Zhang et al., 2012).

underground drilling program that has added considerably to the resource. The newly delineated zones are mostly hosted in coarse-grained syenite that is crosscut by abundant quartz veins and is intensely pyrite and potassic-hematite altered. The drilling program has extended the deposit from surface to a depth of approximately 1.3 km, and over a lateral extent of up to 1 km. Surface drilling has also uncovered quartz-carbonate vein hosted and replacement styles of volcanic-hosted mineralization in deformed and albitized volcanic rocks east of the syenite along strike with the CLLDZ. An additional resource is also being drilled to the west of the current reserves in a similar coarse-grained syenite that is crosscut by veining, hematite-potassic alteration and host to abundant pyrite. In 2011, the property was acquired by AuRico Gold Incorporated.

1.4.3 Formation of the southern Abitibi greenstone belt

The Superior Province of the Canadian Shield consists of alternating east-west trending volcano-plutonic and sedimentary subprovinces; the southernmost volcano-plutonic belt is the Abitibi Subprovince (Poulsen et al., 1992). The majority of the gold mineralization in the Superior Province is found within the Abitibi greenstone belt, and more specifically is hosted by quartz-carbonate vein deposits that occur along crustal-scale deformation zones (Dubé and Gosselin, 2007). Within the Abitibi there are 9 supracrustal assemblages that are thought to represent volcanic construction and subsequent deformation and sedimentation (Ayer et al., 2002). The 7 earliest volcanic assemblages (Pacaud, Deloro, Stoughton-Roquemaure, Kidd-Munro, Tisdale, Kinojevis and Blake River) range in age from 2750 to 2697 Ma and consist of variable amounts of ultramafic, mafic and felsic volcanic rocks, with calc-alkaline, tholeiitic and MORB-like affinities (Ayer et al., 2002). The 2 youngest sedimentary assemblages (Porcupine and Timiskaming) were unconformably deposited over older assemblages and consist of wacke, siltstone and mudstone in the Porcupine assemblage and clastic polymictic conglomerate, sandstone and fluvial fan-type deposits in the younger Timiskaming assemblage (Ayer et al., 2002; Bateman and Bierlein, 2007). Deposition of the two sedimentary assemblages was roughly coeval with emplacement of syntectonic granitoid intrusions, regional folding and reactivation of earlier accretionary faults (Ayer et al., 2002).

The construction and evolution of the Abitibi Subprovince is thought to involve mamgas from different mantle sources in a periodic rifting-convergent plate tectonic setting (Ayer et al., 2002). During volcanic construction, from 2750 to 2697 Ma, the general tectonic setting in the Abitibi varied from extensional, to back-arc settings, to plume-related volcanic (with uplift) to a faulting and subsidence dominated setting related to rifting (Ayer et al., 2002). After 2696 Ma, the tectonic regime changed from volcanic construction in rifting and plume-related environments to a compressional orogenic environment with associated deformation, metamorphism, sedimentation and emplacement of granitoid intrusions (Ayer et al., 2002). The first orogenic phase lasted from 2696 Ma to 2690 Ma and resulted in the deposition of the wackes, siltstones and mudstones of the Porcupine assemblage, the formation of the oldest folding structures and the first syn-tectonic intrusions recognized in the Abitibi (Ayer et al., 2002 and ref. therein). The second deformation and metamorphism event lasted from 2687 Ma to 2675 Ma and resulted in deposition of the conglomerate, sandstone and localized volcanic rocks of the Timiskaming assemblage and emplacement of alkalic plutons (Ayer et al., 2002). The final deformation phase in the Abitibi post-dated Timiskaming sedimentation and resulted

in folding and emplacement of Algoman granites and S-type granites from 2660 to 2640 Ma (Ayer et al., 2002).

Gold-rich mineral deposits are associated with each tectonic phase of the development of the Abitibi. Compressive regional deformation superimposed different mineralization styles upon one another where the end result was overprinting of the existing mineralization or generation of new styles of mineralization (Dubé and Gosselin, 2007). The most important mineral deposits in the Abitibi are gold deposits, of which there are 3 main types: greenstone-hosted quartz-carbonate vein deposits, intrusion-related gold deposits and Au-rich VMS deposits. Au-rich VMS deposits will not be considered further because of the significant temporal and genetic differences of those deposits compared to intrusion-related deposits.

1.4.4 Greenstone-hosted quartz-carbonate vein mineralization

Greenstone-hosted quartz-carbonate gold deposits are most abundant type of gold-deposit in the southern Abitibi greenstone belt. Mineralization is characterized by moderately- to steeply-dipping structurally-controlled networks of laminated gold-bearing, quartz-carbonate, fault-fill veins set within altered wall rock (Dubé and Gosselin, 2007). Although gold-bearing veins can be found in any lithology present at the mine scale, they are preferentially hosted by mafic to ultramafic volcanic rocks, competent iron-rich tholeiitic gabbroic sills and granitoid intrusions of Archean age (Dubé and Gosselin, 2007). These deposits generally possess weak carbonate-chlorite alteration related to regional greenschist-grade metamorphism. Alteration styles that are observed at specific gold deposits include Fe-carbonatization (ankerite alteration), albitization, tourmalinization, K-feldspathization, sericitization, silicification and chloritization peripheral to mineralization. Greenstone hosted quartz-carbonate vein deposits, in general, have a number of common features, regardless of the host rock type (from Dubé and Gosselin, 2007): 1) fault and shear zone related extensional veins hosted in carbonate altered and pyrite- or arsenopyrite-bearing host rocks; 2) deposits are typically hosted within first order regional-scale structures or related second-order structures; and 3) deposits have significant vertical extent with restricted metallic zonation. The alteration styles at each deposit depend on the type of host rock, but in general, iron-carbonate alteration is ubiquitous.

1.4.5 Intrusion-associated mineralization

Intrusion-associated gold deposits in the Abitibi are similar to quartz-carbonate vein deposits with respect to location and some alteration and mineralization characteristics. Robert (2001) proposed a distinct classification of intrusion-associated deposits because of mineralizing and alteration differences between intrusion-associated deposits and typical quartz-carbonate vein deposits. Intrusion-associated mineralization is characterized by zones of disseminated pyrite with quartz stockwork veins hosted in larger zones of carbonate, albite and K-feldspar alteration in the intrusions (Robert, 2001). Robert (2001) interpreted that gold is genetically related to intrusions and is deposited from the magmatic-hydrothermal system rather than fluids associated with regional scale fault zones. The intrusion-associated characteristics considered unique from quartz-carbonate vein deposits include: 1) the lack of through-going quartz-carbonate veins; 2) oxidized mineralizing conditions indicated by hematite-magnetite ± anhydrite; and 3) negative to magmatic $\delta^{34}S$ values in pyrite (Robert, 2001).

1.4.6 Structures in the Abitibi

Gold mineralization in the Abitibi Subprovince shows strong spatial correlation with regional-scale structures, namely the Porcupine-Destor deformation zone in the north and the Cadillac-Larder-Lake deformation zone in the south (Figure 1.1). Gold mineralization locally correlates with structural traps along these regional deformation zones, including: dilational fault systems; rheological contrasts; and lithologies with specific chemistry and intersection of different structures (McCuaig and Kerrich, 1998). The distribution of gold at quartz-carbonate vein deposits is controlled by veins developed within shear zones hosted within the larger scale deformation corridors (Hodgson, 1989). The overall structural development at most deposits is well constrained by regional mapping, geochronological work and mine-scale vein and crosscutting relationships.

1.5 Sample and Data Collection Methodology

Characterization of the mineralization at the Young-Davidson deposit is accomplished through a combination of hand specimen observation, rock slab staining, transmitted and reflected light petrographic analysis, scanning electron microscope (SEM) analysis, wavelength-dispersive electron-microprobe (EMP) analysis and major and trace element geochemistry analyzed by a variety of

methods detailed in the sections below. A total of 464 samples were collected: 280 samples of drill core from holes drilled by Northgate Minerals Corporation between 2006 and 2010; 132 samples from an underground ore crosscut that was mapped in the summer of 2008; and 52 surface samples from around the Matachewan area collected during field mapping in 2009. Two-hundred seventy-nine major and trace element lithogeochemical analyses were obtained from two commercial laboratories (details below); 221 samples of drill core, 33 from the ore crosscut, and 25 from select surface exposures. A total of 238 polished thin sections: 148 from drill core, 47 from the ore crosscut and 43 from surface exposures were examined in the course of this thesis.

1.5.1 Samples

The strategy for sampling drill core for major and trace element geochemistry was to collect samples that contained the least amount of vein material. Samples were chosen based on a number of criteria: alteration type; alteration intensity; the relative location to the ore zone; lithology; and intrusive textures. Geochemical samples were collected at a spacing of approximately 25 m (or less) down hole, depending on the relative changes in the above criteria. In general, if the sampling criteria varied substantially over the 25 m interval, additional samples were collected to represent the variation for that interval. The end goal of geochemical sampling was to construct two N-S cross sections through all zones of the mineralized syenite and to present the deposit-wide geochemistry of the syenite on vertical N-S sections through the deposit. Two cross sections were created and are discussed further in Chapter 2; Section 2.3 and Section 2.6.

At the ore crosscut, representative wall rock samples were collected at a 2 m spacing along the 80 m N-S crosscut (discussed in Section 2.5.2). Samples were collected in conjunction with the structural study of the ore crosscut by Zhang et al. (2012) to determine the geochemical and petrographic characteristics of each vein set in a structural context. Large veins were removed from each sample prior to analysis.

Surface samples were collected to obtain least-altered syenite samples far from the mineralized Young-Davidson syenite. Samples were chosen based on weathering intensity and the relative distance from the mine site and the CLLDZ. Since fresh syenite is generally absent from drill core sampling, one goal of surface sampling was to see if a true unaltered sample of syenite could be found

north of the mine site away from the deformation zone. Prior to geochemical analysis, veins and the weathered crust were removed from surface samples.

Samples were collected for petrography during all stages of sampling. Interesting vein and alteration related features were collected for petrographic analysis to determine the relative mineral paragenesis for different alteration styles and intensities of alteration. The focus of petrographic study was to determine the ore-related minerals associated with each stage of mineralization outlined at the ore crosscut. Therefore, veins and disseminated sulfides in syenite represent a majority of the collected petrographic samples. A small number of volcanic and sediment samples were also collected for analysis.

A full list of drill core samples with hand specimen descriptions and sample photos can be found in Appendix A.

1.5.2 Staining

Select samples from the ore crosscut were stained for K-feldspar to determine if there were variations in the abundance of K-feldspar in the syenite and to determine any trends that could be related to mineralization. Thin section blocks and larger slab samples were cut, and sent to Vancouver Petrographics for K-feldspar staining. Samples were etched with concentrated HF solution for 3 minutes, dipped in water, dipped in a barium chloride solution and then immersed in a solution containing sodium cobaltinitrite for 1 minute, thereby staining K-feldspars yellow (as outlined by Bailey and Stevens, 1960). A full photo collection of K-feldspar-stained samples can be found in Appendix H.

A number of samples were stained for iron-carbonate at the University of Waterloo in an effort to better characterize the carbonate minerals in the fine-grained altered groundmass and in the different vein generations. Thin section blocks were first submersed in a deionized water bath, then placed in a mixture of deionized water, HCl, alizarin red ($C_{14}H_8O_4$), and K-ferricyanide for 4 minutes with constant agitation (Conliglio pers. comm., 2011). A full photo collection of iron-carbonate stained samples can be found in Appendix I.

1.5.3 Geochemical analyses

Samples were analyzed at Geoscience Laboratories (GeoLabs) in Sudbury, Ontario and Activation Laboratories (ActLabs) in Ancaster, Ontario.

GeoLabs analyzed major elements by XRF (with LOI from weighing), trace elements by fused pellet ICP-MS, S by infrared absorption and Fe^{2+} by titration. Samples were first processed with a small jaw-crusher, riffle-split and then pulverized in a 99.8% pure Al_2O_3 planetary ball mill to 170 mesh (80 μm); a minor amount of Al is expected to be added to the sample during this preparation method. Major elements were determined by X-ray fluorescence (XRF); samples were first run for LOI and then fused with a borate flux to produce a glass bead. Trace elements were determined by ICP-MS; the sample was dissolved in a closed vessel multi-acid (hydrofluoric, hydrochloric, nitric and perchloric) digestion chamber that is designed to promote total dissolution prior to analysis. Total S was analyzed by infrared absorption where sulfur was oxidized by combustion and measured by infrared absorption. Ferrous iron was analyzed by titration where samples were dissolved in an aggressive non-oxidizing acid mix, and titrated with standardized permanganate. Precision for major elements analyzed by XRF, tested with sampling duplicates, is better than 5%. Precision for trace elements analyzed by ICP-MS, tested with sampling duplicates, is better than 10% except for Ba (precision 100%), Be (40%), Bi (60%), Cd (50%), Dy (20%), Gd (15%), In (15%), Sr (80%) and Tm (30%). The low precision for Ba and Sr is because of extremely high contents of each in the samples (> 2000 ppm for each, analyzed by pressed pellet XRF; Naderi, unpubl. data). For Cd, the low precision is due to values near detection limits. LOI and total S analyses are precise to 10%, tested by sampling duplicates. Due to redox complications arising from Fe^{2+}, Fe^{3+}, S^{2-} and S^{6+} being present in the samples, Fe^{2+} analyses are precise to 80%, and thus were omitted from the results presented in this thesis (Geoscience Laboratories, 2011).

ActLabs analyzed major and trace elements by fused pellet ICP-MS; total S was determined by infrared absorption and As, Au, Br, Cr, Ir, Sc and Se were analyzed by INAA. At ActLabs, samples are first crushed to 1.7 mm, riffle-split and then approximately 100 g of sample is pulverized to 150 mesh (105 μm) in a mild steel mill that does not introduce Cr or Ni. Major and trace elements are determined by fused pellet ICP-MS where samples are fused with a lithium metaborate/tetraborate flux to produce a glass bead that is dissolved and analyzed by ICP-MS. Since major elements at GeoLabs were analyzed by XRF, a subset of samples was also analyzed for major elements by XRF at ActLabs to compare with the ICP-MS data. Precision between XRF and ICP-MS analyses at

ActLabs is better than 5% and major element ICP-MS analyses are considered comparable with results produced by XRF. Precision for all major and trace element data at ActLabs is better than 10% tested by sampling duplicates, except for Zn (50%), As (50%), Sb (80%), W (15%), Tl (20%), Pb (20%) and Bi (30%) (Actlabs Group of Companies, 2011).

Since the data used in this study was obtained by two labs, a subset of samples analyzed at GeoLabs was reanalyzed at ActLabs for comparison. From these duplicate analyses it was determined that major elements are precise to 25% and trace elements are precise to 80%. Lab standards were utilized during geochemical testing to ensure accuracy and to check and correct for instrument drift. Comparing data from analyses obtained from two laboratories utilizing different methods is not ideal. Conclusions from figures using data from both labs as a complete dataset are thus considered to be semi-quantitative, whereas conclusions from calculations using data from a single lab are quantitative. Therefore only data obtained from ActLabs will be used in the mass balance calculations presented in Chapter 2; Section 2.7.

A full database of the geochemical data obtained from both labs is provided in Appendix D.

1.5.4 Mineral-chemical analyses

The chemical composition of ore-related minerals (rutile, pyrite and gold) was analyzed with a wavelength-dispersive electron microprobe at the University of Toronto, Ontario, and the University of Michigan, Michigan, USA. Rutile and gold grains were analyzed on the Cameca SX50 electron microprobe at the University of Toronto, which is equipped with 3 tunable wavelength dispersive spectrometers. Rutile compositions were determined with the following operating conditions: 20 kV, 50 nA, 1 μm beam size and element counting times detailed in Section 3.3. Gold compositions were determined with the following operating conditions: 20 kV, 20 nA, 1 μm beam size and element counting times detailed in Section 3.3. Pyrite grains were analyzed on the Cameca SX100 electron microprobe at the University of Michigan, which is equipped with 5 tunable wavelength dispersive spectrometers. Pyrite compositions were determined with the following operating conditions: 20 kV, 100 nA, 1 μm beam size and element counting times detailed in Section 3.3. A detailed summary of the rutile, gold and pyrite analytical conditions is provided in Section 3.3.

Chapter 2

Geology, alteration and geochemistry of the syenite-hosted Young-Davidson gold deposit, Matachewan, Ontario

2.1 Introduction

The syenite-hosted Young-Davidson gold deposit is located in the southern Abitibi greenstone belt of the Canadian Shield, Ontario, Canada. The southern Abitibi is renowned for orogenic gold deposits hosted within a variety of lithologies and spatially related to Timiskaming sedimentary rocks, felsic intrusions and regional scale deformation zones such as the Porcupine-Destor deformation zone (PDDZ) and the Cadillac-Larder-Lake deformation zone (CLLDZ) seen in Figure 2.1 (Dubé and Gosselin, 2007). Evidence at some deposits suggests that gold mineralization is genetically related to emplacement of the felsic intrusion; these deposits have been termed intrusion-associated gold-deposits (Robert, 2001). Many orogenic deposits are spatially associated with felsic intrusions, and the role of the intrusion at some orogenic deposits is still controversial. At some deposits gold is spatially related to intrusions but is dominantly hosted in veins within other rock types (e.g., Hollinger-McIntyre and Ross) whereas mineralization at other deposits is hosted mostly within the intrusions (e.g., Upper-Beaver, Beattie and Young-Davidson; Robert, 2001). The role of intrusions is generally interpreted in two ways: 1) mineralization is localized in the intrusion because of favorable rheological and geochemical contrasts; or 2) gold is related to the magmatic-hydrothermal system that was associated with emplacement of the intrusion and has subsequently been overprinted by regional deformation (Robert, 2001). Studies of select syenite-hosted gold deposits has outlined unique mineralization and alteration styles that support the genetic model and contrast with characteristics from typical orogenic gold deposits (Robert and Poulsen, 1997; Robert, 2001). By contrast, other studies on other intrusion-related gold deposits in the Abitibi Subprovince have shown that the association is due to rheological contrasts and geochemically favorable host lithologies (Kerrich and Watson, 1984; Ispolatov et al., 2008). Evidence for a direct relationship between gold mineralization and the intrusive hosts include: disseminated mineralization that is nearly completely hosted within intrusive stocks, a lack of through-going quartz-carbonate veins (that are typical of orogenic deposits), evidence for fluids with relatively high fO_2 (i.e., abundant sulfate and oxide minerals relative to sulfides), sulfur isotopic compositions for pyrite and temporal relationships that suggest mineralization has been overprinted by regional structures (Robert, 2001).

The Young-Davidson gold deposit is hosted dominantly in coarse-grained porphyritic to trachytic syenite that intruded roughly along the contact between Timiskaming sedimentary rocks and Tisdale volcanic rocks (Figure 2.2 and Figure 2.3). The Young-Davidson syenite and neighboring rocks are interpreted to lie along the western extension of the regional-scale CLLDZ that is found affecting

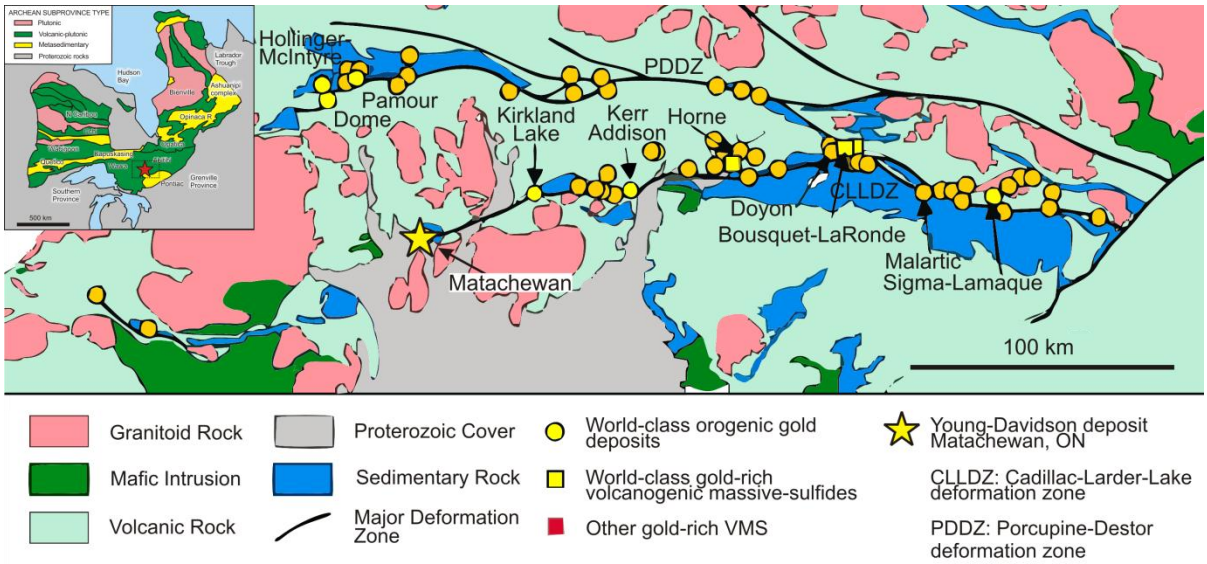

Figure 2.1: Gold deposits in the southern Abitibi greenstone belt, Canada. (Modified from Dubé and Gosselin, 2007)

similar rocks in the Kirkland Lake area (Ispolatov et al., 2008). Gold mineralization at Young-Davidson is characterized by intense potassic-hematite-pyrite altered syenite that is crosscut by abundant quartz and quartz-carbonate veins. The majority of the defined resource at Young-Davidson is hosted by syenite; however, gold can also be concentrated in altered volcanic and sedimentary rocks that host quartz and quartz-carbonate veins and have been deformed. Robert (2001) considered that the characteristics of the Young-Davidson intrusion are consistent with intrusion-related gold mineralization. The localization of gold dominantly in syenite combined with oxidized mineral assemblages and a magmatic S isotope signature has been used as evidence for a genetic relationship between the intrusion and gold at Young-Davidson (Sinclair, 1982; Cameron and Hattori, 1987; Robert and Poulsen, 1997). A recent study by Zhang et al. (2012) has shown that at Young-Davidson, gold-bearing vein sets hosted in the syenite can be related to regional movements along the CLLDZ. Therefore the mineralization at Young-Davidson can be interpreted to have characteristics of both typical-orogenic and intrusion-associated styles of mineralization. The aim of this study is to characterize the vein, alteration, mineralization and geochemical characteristics of the syenite-hosted mineralization in a structural context outlined by Zhang et al. (2012). By performing alteration, mineralization and geochemical studies on samples within a structural context the goal is to develop a genetic model for the gold mineralization at the Young-Davidson deposit.

2.2 General geology

The general geology of the Matachewan area is shown in Figure 2.2. The main lithological units consist of roughly east-west trending southward-dipping units of lower greenschist-grade meta-sedimentary and meta-volcanic rocks (Berger, 2006). Volcanic and sedimentary rocks have been intruded by syenite, crosscut by north-south trending diabase dikes of the Matachewan swarm and overlain by relatively horizontal Proterozoic sediments of the Cobalt Group. Since all of the Archean rocks in the Matachewan area are metamorphosed to greenschist facies (locally up to amphibolite facies; Lovell, 1967), the prefix meta- is implied for all Archean units (e.g., meta-volcanic) and will be omitted in the following sections. The main structural feature in the Matachewan area is the east-west striking regional-scale CLLDZ. Intense deformation and alteration is generally restricted to areas affected by the CLLDZ, however, in the northern part of the map area small gold-bearing shear zones are interpreted as splays off of the CLLDZ (Zhang et al., 2012). A minor component of late brittle movement developed along the N-S trending Mistinigon Lake and the Montreal River faults west and east of Young-Davidson, respectively (Figure 2.2). These late faults have variable amounts of left-lateral offset (Lovell, 1967; Ayer et al., 2002) and are likely related to the emplacement of the N-S trending Matachewan swarm diabase dikes. There are a number of felsic porphyritic intrusions in the Matachewan area, north of and including the Young-Davidson intrusion. The Cairo stock is the largest pluton in the area and is relatively fresh compared to the Young-Davidson syenite. The relationship between the Cairo stock and the Young-Davidson intrusion has been interpreted as a distal dike system by Lovel (1967). The U-Pb zircon age of the Young-Davidson intrusion (Zhang et al., 2012) is consistent with age of the Cairo stock (U-Pb zircon age; Berger, 2006) and supports the interpretation of Young-Davidson as a distal dike to the Cairo stock. Southern portions of the Cairo stock contain deformation and alteration characteristics that are interpreted to represent influence from the CLLDZ (Berger, 2006). Small syenite intrusions north of Young-Davidson between the Montreal River and Mistinigon Lake faults are relatively undeformed and are generally barren (with exception of the Cu-Mo-Au bearing Ryan Lake intrusion; Sinclair 1979) with only minor carbonate ± barite ± quartz ± fluorite veins.

The mine scale geology of Young-Davidson is shown in Figure 2.3. Based on field relationships, Zhang et al. (2012) determined that the Young-Davidson syenite is closely associated with the CLLDZ. This deformation zone is > 600 m wide in the Matachewan area and is outlined in both Figure 2.2 and Figure 2.3 (Zhang et al., 2012). West-southwest of Young-Davidson Archean rocks

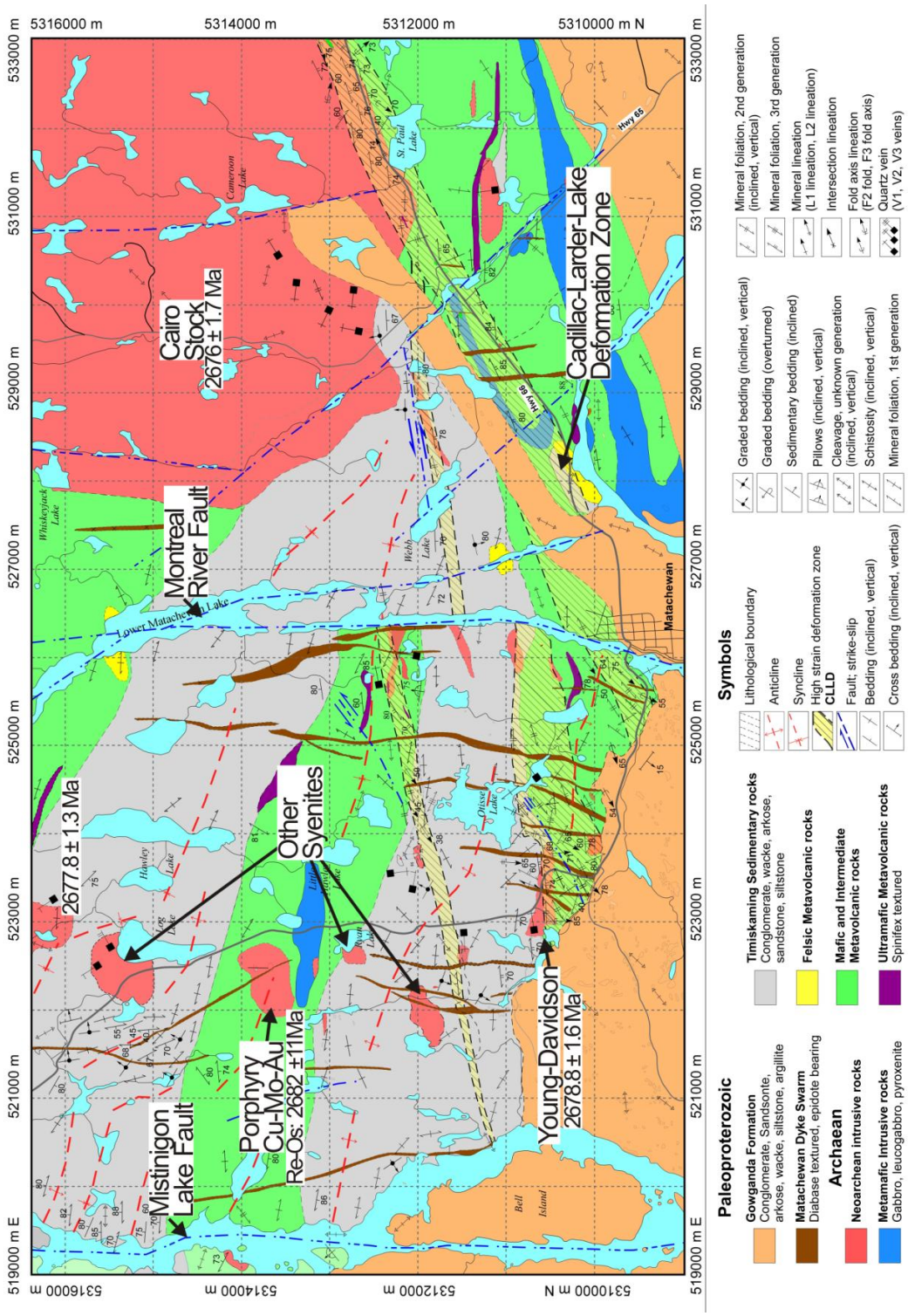

Figure 2.2: General geology of the Matachewan area (modified from Zhang et al., 2012). Cairo U-Pb age from Berger (2006), Young-Davidson and north intrusion U-Pb ages from Zhang et al. (2012), and Ryan Lake (porphyry Cu-Mo-Au) Re-Os molybdenite age from R.L. Linnen (unpubl. data).

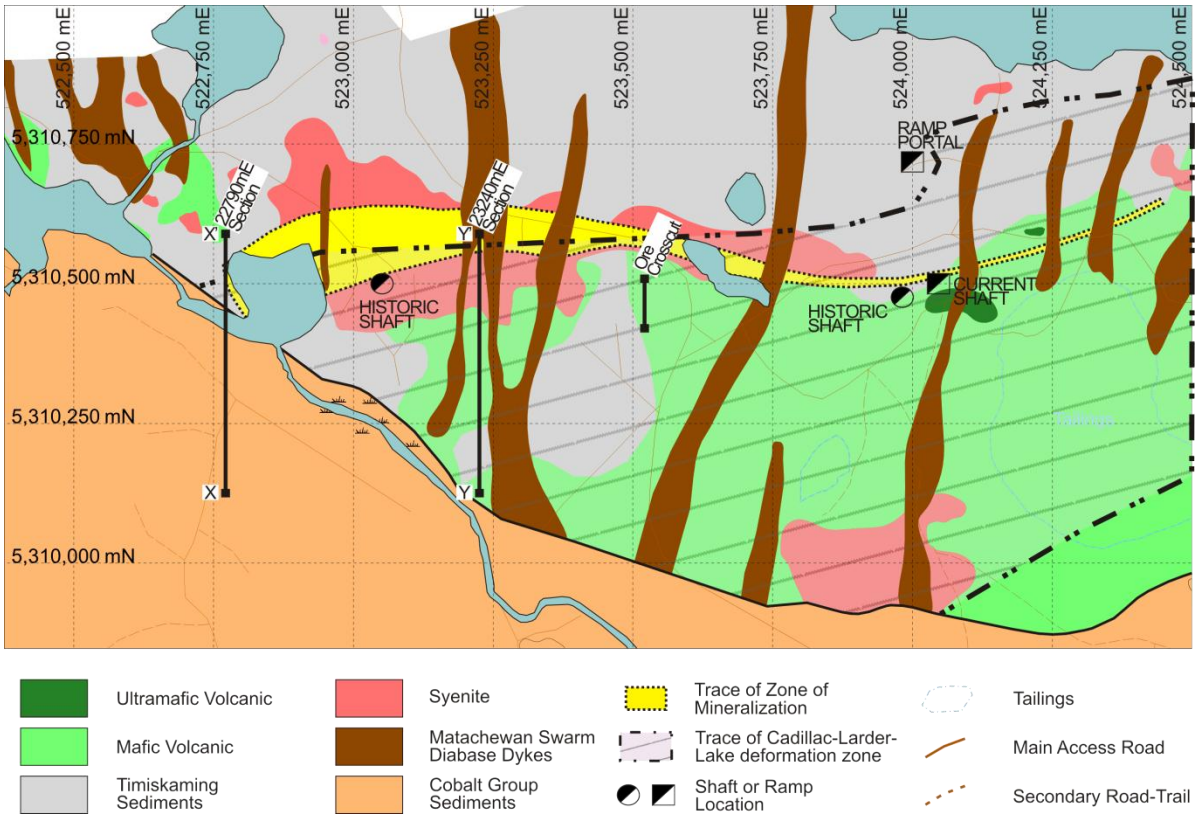

Figure 2.3: Mine-scale geologic map of Young-Davidson showing the distribution of major Archean rock types and the location of the CLLDZ (Zhang et al., 2012). Historic and current shaft/ramp locations are shown and labeled. Mineralization is highlighted in yellow and the location of the two N-S vertical cross sections X-X' and Y-Y' from Figure 2.5 are shown. The location of the ore crosscut is projected to surface. Grid is in meters, i.e., 50 m x 50 m. (Modified after Lucas, 2008 and Zhang et al., 2012)

are overlain by undeformed Proterozoic cover; therefore the location and extent of the CLLDZ is poorly constrained.

2.3 History of Young-Davidson

Gold mineralization at Young-Davidson is hosted dominantly by syenite. Two former mines, Young-Davidson and Matachewan Consolidated collectively mined the west and east end of the Young-Davidson syenite, respectively (Sinclair, 1982). Historic production at Young-Davidson consisted of quartz-carbonate vein-associated gold mostly from intrusive rocks, but also from volcanic and sedimentary rocks. The distribution of Archean rocks and surface projection of the mineralized zone at the Young-Davidson mine site is shown by the plan view map in Figure 2.3. Since acquisition of Young-Davidson by Northgate Minerals Corporation in late 2005, drilling has expanded the

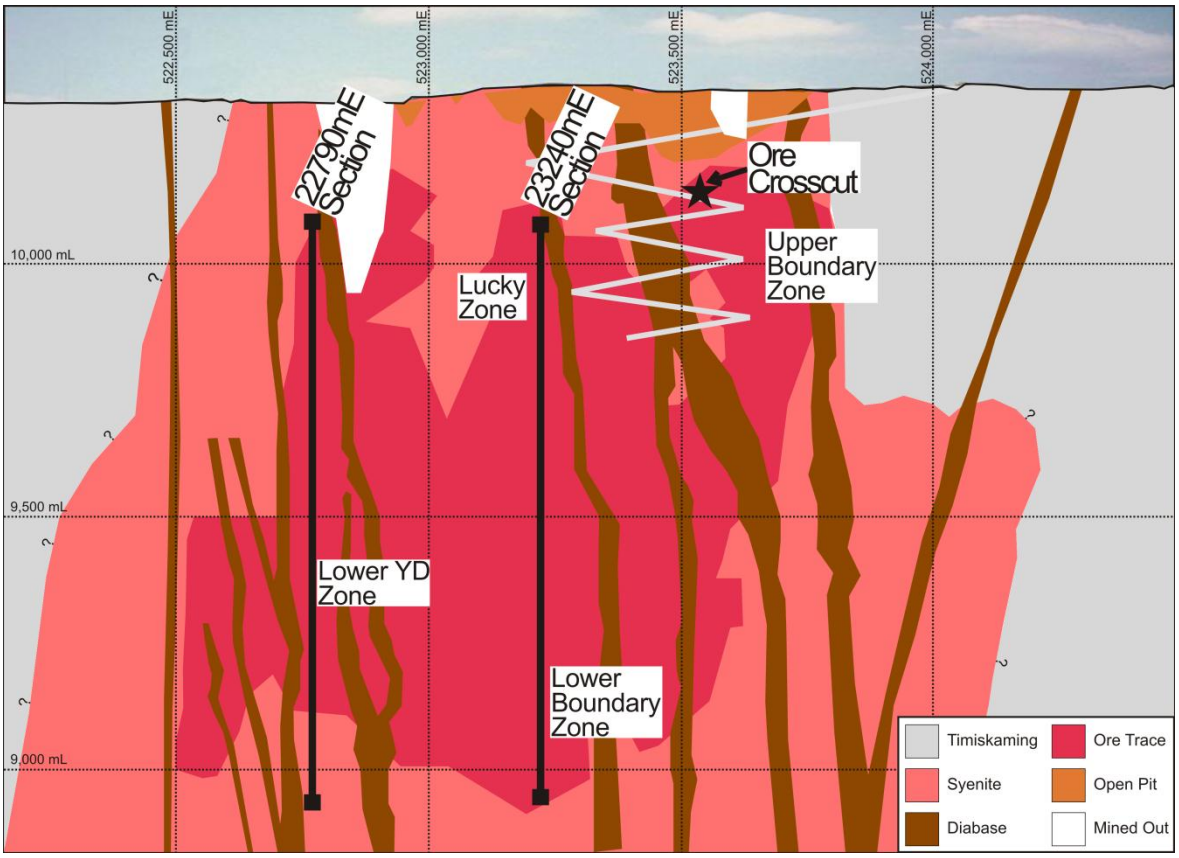

Figure 2.4: Schematic long section through the Young-Davidson deposit (looking north) showing location of the Upper Boundary Zone (UBZ), Lower Boundary Zone (LBZ), Lucky Zone (LZ) and Lower YD Zone (LYDZ). The location of the studied ore crosscut is indicated with the black star. The location of the two N-S geological cross sections at 22790 mE and 23240 mE from Figure 2.5 are indicated with vertical black lines. (Based on unpublished data from: Edmunds, 2012)

underground resource (as of 2011) to 14.6 million tonnes (measured and indicated) at an average grade of 2.03 g/t Au and an underground reserve of 39.1 million tonnes (proven and probable) at an average grade of 2.79 g/t Au (AuRico, 2011). In 2011, Northgate Minerals Corporation was acquired by the current owner-operator AuRico Gold Corporation. Gold mineralization at Young-Davidson is subdivided into 4 main zones: Upper Boundary Zone (UBZ), Lower Boundary Zone (LBZ), Lucky Zone (LZ) and the Lower YD Zone (LYDZ); shown in Figure 2.4. As part of this study, an 80 m long N-S oriented ore crosscut (back star; Figure 2.4) was chosen for detailed structural mapping, ore petrography and lithogeochemistry in order to characterize the mineralization with respect to alteration and different vein generations at this locality. The framework developed during this initial study was then applied to the deposit wide study of the mineralization at Young-Davidson. Drill holes from two N-S vertical cross sections were re-logged and sampled. These sections cut through the

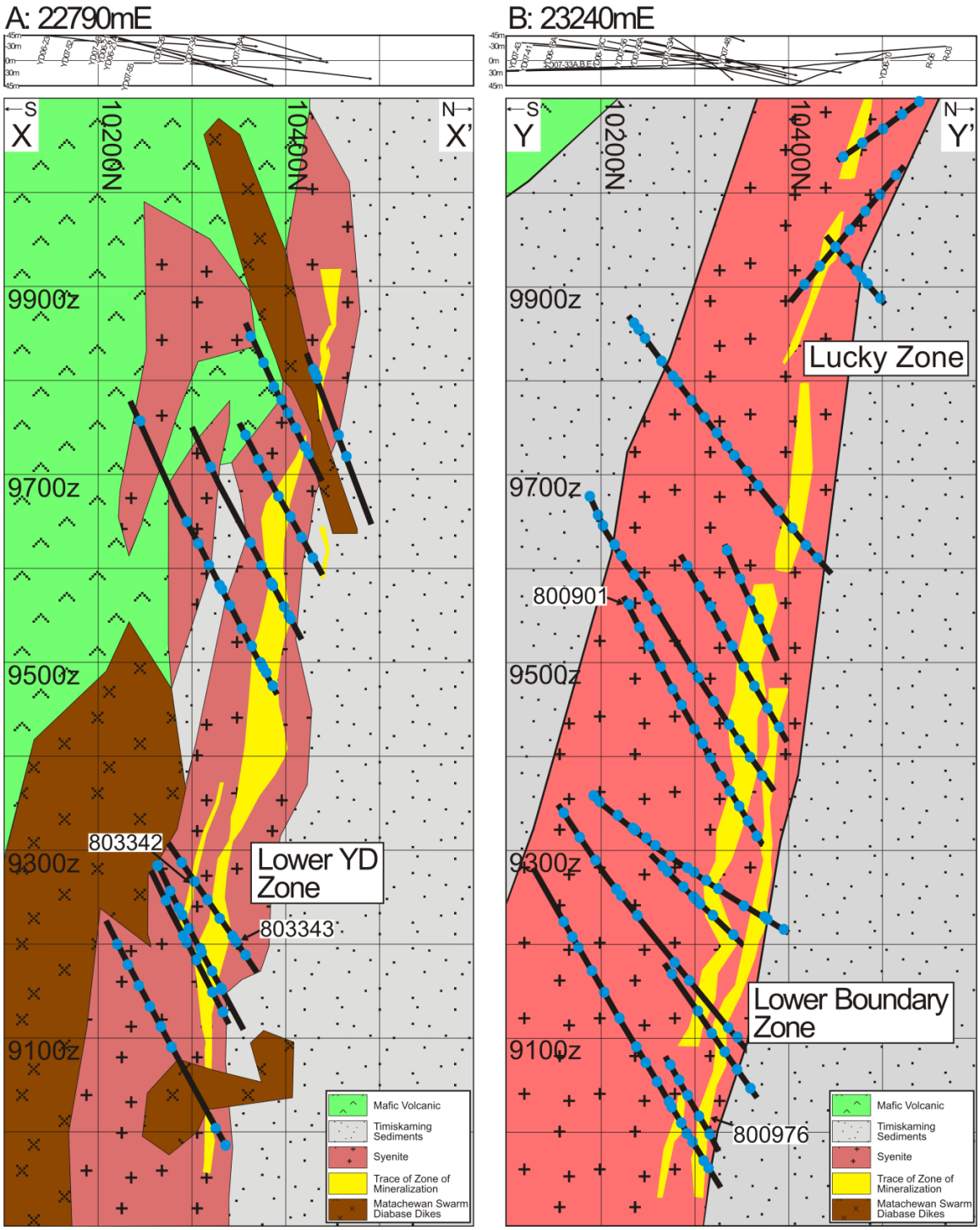

Figure 2.5: Geology of N-S vertical cross sections at (A) 22790 mE and (B) 23240 mE looking west. Drill holes on these cross sections intersect mineralization in the Lower YD Zone, Lucky Zone and the Lower Boundary Zone, as labeled. Drill hole surface traces (plan view) are shown above each cross section with the distances east and west of each section indicated by the negative and positive distances, respectively. The trace of mineralization is shown in yellow and defined by 3D modeling by Young-Davidson geologists during resource modeling. Core logging by AuRico geologists. Grid spacing is 100 m. Ground surface is at approximately 10300z; these cross sections do not intersect the surface.

center and western portion of the deposit, at 23240 mE and 22790 mE (mine scale) respectively. The N-S horizontal extent of each section is shown by the labeled black lines in Figure 2.3 and the vertical extent of each section is shown by the labeled black lines in Figure 2.4. Lithology, drill hole traces and sample locations from each cross section are shown in Figure 2.5. Cross sections were constructed using a 45 m window on either side (90 m total slice width) to allow for sampling of drill core above and below the mineralized zone.

2.4 Local geology

2.4.1 Structure

There are 3 recognizable post-Timiskaming deformation events in the Archean rocks of the Matachewan area (Zhang et al., 2012). The details of that study are only summarized here, but an important observation is that structures from the regional pre-Timiskaming D_1 deformation are absent from the present study area; thus the Matachewan D_1 deformation correlates to the regional D_2 (Matachewan D_2 = Regional D_3; Zhang et al., 2012) and in the text below all abbreviations (D for deformation and S for foliation) refer to Matachewan observations.

Syenite emplacement and Timiskaming sedimentation were coeval, and pre-dated the D_1 deformation. D_1 consists of northeast to southwest compression with a series of top-to-the-north-northeast thrust faults, and is recorded as a weak to penetrative S_1 foliation that overprints bedding in volcanic and Timiskaming sedimentary rocks at small angles (Zhang et al., 2012). This foliation is generally observed north of the Young-Davidson syenite, distal to the CLLDZ. Close to the mine site and CLLDZ, intense shearing during D_2 has nearly completely overprinted earlier structures. The S_2 foliation can be identified in isolated shear zones north of Young-Davidson that are interpreted as splays off of the CLLDZ; however, S_2 is dominantly restricted to areas directly affected by the CLLDZ in the southern portion of the map area (Zhang et al., 2012). The dominant fabric in the Matachewan area developed during the D_2 deformation and is spatially and temporally related to development of the CLLDZ. The D_2 deformation occurred under northwest to southeast compression and was characterized by top to the northwest oblique thrusting and strike-slip shearing (Zhang et al., 2012). Rocks within and adjacent to the CLLDZ show steeply south-dipping east-trending S_2 foliation that ranges from open folding, isoclinal folding, crenulation cleavage and eventual transposition to the penetrative S_2 fabric (Zhang et al., 2012). A similar post-Timiskaming D_2 deformation that generated east-striking, steeply dipping penetrative foliation along the CLLDZ is observed in the Kirkland Lake

area (Ispolatov et al., 2008). At Matachewan, tight isoclinal F_2 folds of early quartz-carbonate veins are observed in Tisdale mafic and ultramafic volcanic rocks and Timiskaming sedimentary rocks. In drill core, the penetrative S_2 foliation is the dominant structure. Boudinaged veins and stretched pebbles are associated with S_2 and locally S_2 is masked by intense veining. The major east-west trending penetrative foliation has been overprinted by late brittle-ductile D_3 deformation which generated F_3 open folds and subvertical S_3 cleavage (Zhang et al., 2012).

The east-west trending CLLDZ is the most important structure in the Matachewan area and developed during the D_2-D_3 deformation. Based on local detailed structural mapping, Zhang et al. (2012) determined that the CLLDZ nearly completely envelops the Young-Davidson syenite and the surrounding sedimentary and volcanic rocks (Figure 2.3).This deformation zone is known to extend east from Matachewan, through Kirkland Lake and as far west as Val d'Or in Quebec (e.g., Robert, 1989). The Young-Davidson syenite hosts several vein generations that can be related to regional structural events (Zhang et al., 2012). Similarly, volcanic-hosted quartz-carbonate veins have been historically mined at Young-Davidson (Edmunds, 2009); these veins possess alteration and mineralization characteristics similar to volcanic-hosted quartz-carbonate vein deposits elsewhere in the Abitibi (e.g., McCuaig and Kerrich, 1998).

2.4.2 Tisdale Ultramafic and Mafic Volcanic Rocks

Ultramafic and mafic volcanic rocks are the oldest rocks in the Matachewan area and form east-west trending south-dipping folded bands of volcanic rock, as seen in Figure 2.2**.** The volcanic rocks in Matachewan were formerly known as the Larder-Lake but are now part of the Tisdale assemblage, deposited at 2710 to 2703 Ma (U-Pb, zircon; Ayer et al., 2002). Regionally, the Tisdale assemblage consists of komatiites, tholeiitic basalts, rhyolites and intermediate to felsic calc-alkaline volcanic rocks (Ayer et al., 2002). At Young-Davidson, this group is dominantly basalt with lesser amounts of ultramafic and felsic volcanic rocks (Lovell, 1967, Zhang et al., 2012). Undeformed ultramafic and mafic flows north of the CLLDZ show well preserved primary structures: spinifex and pillow structures, respectively. Ultramafic volcanic rocks are also encountered in drill core close to the Young-Davidson syenite, however proximal to the CLLDZ ultramafic rocks are strongly foliated and intensely altered. Since primary structures from deformed ultramafic rocks are absent, they are identified based on the presence of fuchsite, talc, chlorite and iron-carbonate alteration. Mafic

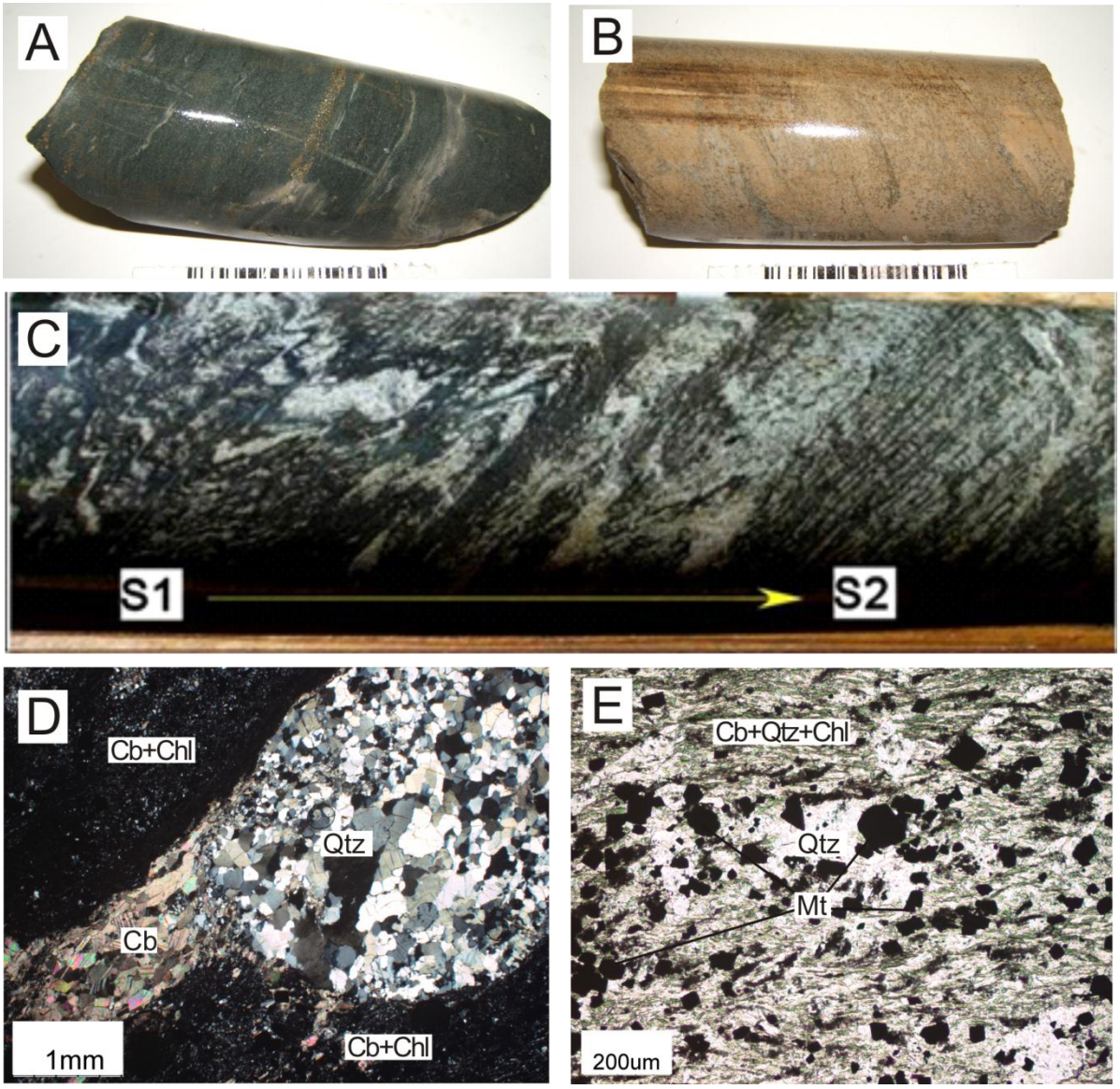

Figure 2.6: Features of mafic volcanic rocks in drill core at Young-Davidson. A) Relatively fresh weakly foliated chlorite-carbonate-albite altered volcanic rock with minor albite alteration along foliation. B) Gold-bearing intensely albite-iron-carbonate-pyrite altered volcanic rock. Abundant pyrite, weakly magnetic, foliation defined by wisps of pyrite. C) Transposition of S_1 defined by early iron-carbonate stringers to the dominant S_2 foliation (unpublished photo by J. Zhang). D) Photomicrograph of boudinaged quartz-carbonate veinlet in relatively fresh fine-grained chlorite-carbonate-bearing mafic-volcanic rock. Cross polarized light. E). Fresh volcanic rock with fine-grained chlorite defining foliation, coarser carbonate grains associated with fine-grained euhedral black magnetite. Plane polarized light.

volcanic rocks close to the mine site and CLLDZ tend to be weakly to strongly foliated with variable alteration styles, veining and evidence of transposition where primary structures have been overprinted by penetrative foliation (Figure 2.6A, B and C).

Least-altered equivalent mafic volcanic rocks at Young-Davidson are typically very fine-grained (< 200 μm), dark green to green-grey in color, and are composed primarily of chlorite, iron-carbonate, calcite, magnetite and hematite with accessory rutile, pyrite, quartz and feldspar (Figure 2.6D and E). The rocks are commonly foliated and are variably crosscut by carbonate ± quartz stringers that are associated with fine to medium-grained cubic pyrite (Figure 2.6A). In thin section, foliated volcanic rocks typically contain alternating coarse quartz ± carbonate layers and fine-grained chlorite ± carbonate layers. Coarse quartz and carbonate grains occur in boudinaged lenses that also commonly contain barren, cubic pyrite. These boudinaged quartz-carbonate lenses represent pre-D_2 quartz-carbonate veins that were deformed during regional deformation. Pyrite in fresh volcanic rocks is euhedral compared to that hosted in altered volcanic rocks, and with pyrite found in the syenite. Chalcopyrite is commonly as anhedral grains along the outer boundaries of this phase of pyrite, and less commonly within the boudinaged veins away from the pyrite grains. Chlorite defines the local foliation within volcanic rocks, and in fresh rocks early carbonate ± quartz ± pyrite veins are deformed and do not crosscut the local foliation.

2.4.3 Timiskaming Sedimentary Rocks

Regionally the Timiskaming sediments have been dated by Ayer et al. (2002) at 2687 to 2675 Ma (U-Pb, youngest detrital zircon). In the Matachewan area these sediments are made up of conglomerate, sandstone, fine sandstone and siltstone that are generally grey, to grey-green, but are reddish-brown in color proximal to the CLLDZ and the Young-Davidson syenite. Sedimentary rocks within a few 10's of meters of altered syenite intrusions commonly have acquired similar alteration styles and intensities as the neighboring intrusive rocks. These similarities lead to difficulty differentiating sediments from syenite where both are fine grained, in contact and lack characteristic sedimentary or intrusive features. The Timiskaming sediments, in general, contain < 1% to 15% subangular to subrounded sedimentary or volcanic clasts that are < 5 mm to 10 cm across. During core logging, AuRico geologists subdivide Timiskaming rocks into conglomerates (> 15% clasts) and clast-bearing sandstones or siltstones (< 5% or fewer clasts). Close to the CLLDZ, sedimentary clasts are ellipsoidal and are elongated parallel to the major penetrative S_2 foliation along the CLLDZ. North of CLLDZ, clast elongation in sediments is rarer but occurs locally in small shear zones. Younging indicators found in the northern band of sediments (Figure 2.7A) indicate younging to the northeast and indicators in the southern band closer to the mine site indicate younging to the south.

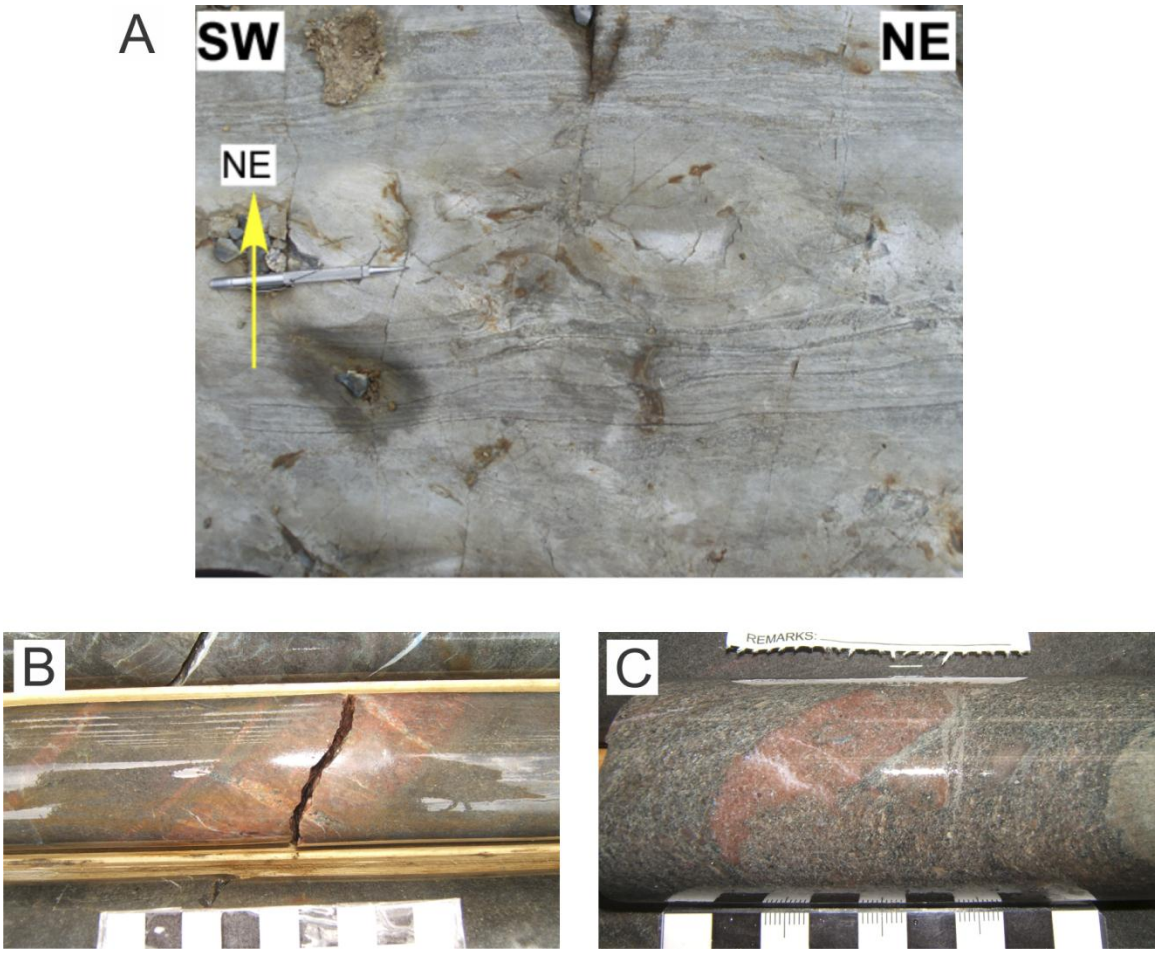

Figure 2.7: Examples of Timiskaming sediment encountered at Young-Davidson. A) Cross bedding in siltstone indicating younging to the northeast in the northern band of Timiskaming sedimentary rocks (Figure 2.2) in the Matachewan area (photo: Zhang pers. comm., 2011). A) Altered syenite dike crosscutting relatively fresh fine grained sandstone; Qtz ± Cb ± Chl veins crosscut the dike. Scale bar in cm. B) Sheared Timiskaming sediments with possible syenitic clast containing minor carbonate stringers, other clast types present within this rock. Scale bar in cm.

Zhang et al. (2012) has interpreted this younging reversal as evidence of large scale open folding of the volcanic and sedimentary assemblages in the Matachewan area during D_1 deformation.

Rare syenite clasts are present in the Timiskaming sediments. In drill core, identification as a true sedimentary clast is problematic because syenite dikes of all sizes are known to intrude the Timiskaming sediments (e.g., Figure 2.7B). Since these clasts are commonly hosted within sheared sedimentary sections, they could be explained by deformation resulting in boudinaged dikes (e.g., Figure 2.7C). However, boulders of syenite have been identified in a basal conglomerate in Timiskaming sediment (Zhang et al., 2012), which supports the characterization of syenite as clasts in

sheared Timiskaming sediments intersected by drill core. At the site where syenite boulders are identified, quartz veins crosscut both the sedimentary matrix and the syenite boulders, but are unmineralized. U-Pb age dating of these syenite boulders indicates that they are coeval with the Young-Davidson syenite (Zhang, unpubl. data). Syenite boulders in basal conglomerate in the Matachewan area is consistent with the general formational model from the rest of the Abitibi: that Timiskaming sedimentation and felsic plutonism were roughly coeval and associated with generation of the major crustal scale deformation zones CLLDZ and PDDZ (Robert and Poulsen, 1997). These relationships indicate that even with the dominant intrusive relationship between syenite and Timiskaming sediments at Matachewan, some phases of syenite are pre-Timiskaming. Similarly, at other syenite-associated gold deposits, there is often a close temporal relationship between intrusive and sedimentary rocks, outlined by Robert (1997; 2001).

2.4.4 Young-Davidson Syenite

The Young-Davidson syenite is an east-west trending intrusion that was emplaced roughly along the contact between the mafic-ultramafic volcanic rocks of the Tisdale assemblage to the south and Timiskaming sedimentary rocks to the north (Figure 2.3). The main syenite body is an elongate intrusion measuring ~1 km east-west and ~300 m north-south and is dipping approximately 75 º to the south (Edmunds, 2009). The U-Pb zircon-age of the Young-Davidson syenite is 2678.8 ± 1.6 Ma (Zhang et al., 2012), which is coeval with Timiskaming sedimentation (2680 to 2675 Ma; Ayer et al., 2002). The U-Pb zircon-age of a porphyritic syenite intrusion north of Young-Davidson is 2677 ± 1.3 Ma, which is consistent with the age of Young-Davidson (Zhang et al., 2012). The age of Young-Davidson is slightly older than the Cairo stock (U-Pb age from zircon: 2676 ± 1.7 Ma; Berger 2006) found northeast of Young-Davidson (discussed below) however both intrusions show deformation and alteration characteristics consistent with an overprint by the CLLDZ. Since the portions of the Cairo stock affected by the CLLDZ have been dated at 2676 ± 1.7 Ma (Berger, 2006) the maximum age of deformation along the CLLDZ is 2676 ± 1.7 Ma. Intrusive contacts of the Young-Davidson syenite with volcanic and sedimentary rocks are commonly deformed proximal to the CLLDZ. Porphyritic textures and the coeval nature of syenite and sedimentary rocks indicates that syenite has intruded at relatively shallow depths (Robert and Poulsen, 1997). Based on the distribution, orientation and crosscutting relationships of veins within syenite, sediment and volcanic rocks as well as foliation preserved in the sediments and volcanics in proximity of the syenite, Zhang et al. (2012)

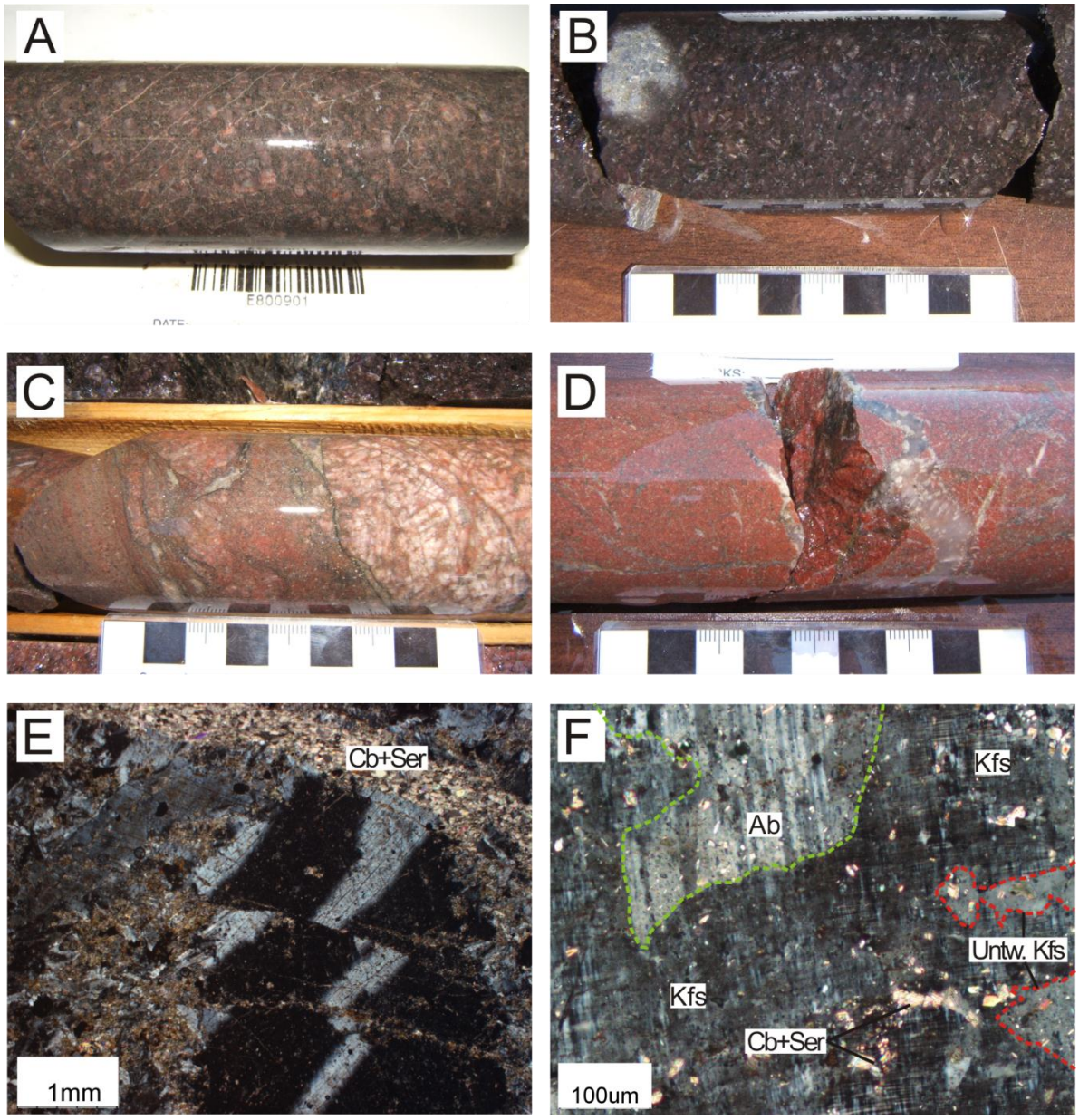

Figure 2.8: Syenite in drill core at Young-Davidson. A) Fresh porphyritic syenite, minor carbonate alteration, and crosscut by minor carbonate stringers. 47.6 mm width drill core. B) Mafic syenite with Bt altered to Chl in groundmass and elongate purple Na-feldspars. Scale bar in cm. C) Deformed contact between different phases of syenite within the intrusion: Left - Chl-bearing massive syenite, Right - coarse trachytic syenite. Contact is deformed. Scale bar in cm. D) Potassic-hematite altered massive syenite with deformed quartz-Fe-carbonate veins. Scale bar in cm. E) Photomicrograph of least-altered porphyritic syenite with brittle deformation of feldspar phenocrysts, fine-grained Cb-Chl-Ser in groundmass and carbonate vein to top right. Cross polarized light. F) Feldspar replacement in fresh to weakly altered syenite. Tartan twinned microcline is overprinted by untwinned feldspar, and subsequently overprinted by carbonate and weak sericitization. Cross polarized light.

has determined that the intrusion of the Young-Davidson syenite was pre to syn-D_1 and temporally related to Timiskaming sedimentation, pre-dating development of the CLLDZ.

The Young-Davidson syenite is a multiphase intrusion that includes different textures: fine to coarse-grained (< 500 μm to > 2 cm), porphyritic, trachytic, massive, and mafic to felsic in composition (Figure 2.8; detailed below). All intrusive rocks within the Young-Davidson stock can be classified as alkali-feldspar syenite, syenite or quartz-syenite depending on the relative proportions of quartz and K- and Na-feldspars. The variation between different textural types of syenite can be summarized as a product of grain size, abundance of feldspar phenocrysts and orientation of feldspar lathes (in trachytic samples). All studied samples of syenite from Young-Davidson contain some alteration. Least-altered syenite (Figure 2.8A) consists of approximately 40-50% K-feldspar, 20-30% Na-feldspar, up to 10% perthite, and the rest of the rock consisting of alteration minerals; amphibole and biotite grains are rarely observed. In least-altered syenite, optically continuous albite-twinned feldspar is replaced by untwinned feldspar that is commonly turbid. Perthite grains commonly occur as 2 to 3 mm rounded aggregates of two or more perthite grains within the syenite; potentially an autolith indicating multiple intrusive phases. Mafic syenite is occasionally intersected in drill core and contains euhedral elongate purple-brown Na-feldspar phenocrysts hosted in a biotite (altered to chlorite) and carbonate groundmass (Figure 2.8B).

Quartz-rich feldspar porphyries (QFP) are also present at the Young-Davidson mine site, however they are relatively rare, their relationship to mineralization is unknown and they were not examined in this study. Syenite is commonly crosscut by other syenite phases containing differing textures or alteration characteristics (e.g., Figure 2.8C). Syenite is also rarely crosscut by lamprophyre dikes. Potassic-hematite altered syenite xenoclasts in lamprophyre have been sampled; however, since the studied xenoclasts do not contain any sulfides, it is not clear whether or not the dikes are pre- or post-mineralization. At the very least we can conclude that lamprophyre post-dates potassic alteration of the syenites.

2.4.5 Other Intrusions

Several other coarse-grained felsic plutonic bodies have intruded Timiskaming sedimentary rocks and mafic volcanic rocks north of Young-Davidson (Figure 2.2). The largest intrusion in the area is the Cairo stock, which is located northeast of the town of Matachewan. It is a grey-pink to earthy-red, medium to coarse-grained syenite that intruded the Timiskaming sedimentary rocks and Tisdale volcanic rocks. The intrusion contains perthite, green amphibole, minor biotite and accessory titanite,

apatite, quartz and magnetite and minor albite as an alteration rim on perthite grains (Berger, 2006). The U-Pb (zircon) age of the Cairo stock is 2676 ± 1.7 Ma, dated by Berger (2006), which is roughly coeval with Timiskaming sedimentation, the Young-Davidson syenite and other intrusive rocks in the Kirkland Lake area (Ayer et al., 2005).

The Ryan Lake intrusion hosts porphyry-style Mo-Cu-Au mineralization north of Young-Davidson and west of the Cairo stock, between the Montreal River and Mistinigon Lake (Sinclair, 1979). This intrusion is coarse-grained and porphyritic intrusion that has a Re-Os (molybdenite) age of 2682 ± 11 Ma (Linnen, unpubl. data). Since quartz-veins in the intrusion are largely stockwork with no consistent orientations and the intrusion generally lacks the penetrative S_2 foliation found closer to the CLLDZ, the influence of the CLLDZ is thought to be absent from the Cu-Mo-Au mineralization associated with this intrusion (Zhang et al., 2012). This intrusion also lacks characteristic earth-red potassic-hematite alteration and pyrite-dominated mineralization styles that are observed in the Young-Davidson syenite.

Other syenite intrusions are located north of the map area in Figure 2.2; one of which has been dated by Zhang et al. (2012) at 2677.8 ± 1.3 Ma, which is similar to the age of the Young-Davidson syenite and Cairo stock. These intrusions are barren of Au mineralization but en-echelon quartz veins are locally present. Barite and Cu-Pb bearing fluorite veins have been identified in these intrusions, but are considered late and coeval with late barite-bearing veins found at Young-Davidson (Zhang et al., 2012).

2.5 Alteration, Veining and Mineralization

A total of 238 polished thin sections were used to characterize the alteration and mineralization at Young-Davidson using reflected and transmitted light microscopy supplemented by SEM analysis. A general alteration, vein and mineralization paragenesis for syenite and volcanic rocks based on these observations is presented in Figure 2.14.

2.5.1 Alteration – Distribution and timing

Study of alteration characteristics for each host rock and each phase of syenite is warranted since sediments, volcanics and syenite all potentially host mineralization and multiple intrusive phases of

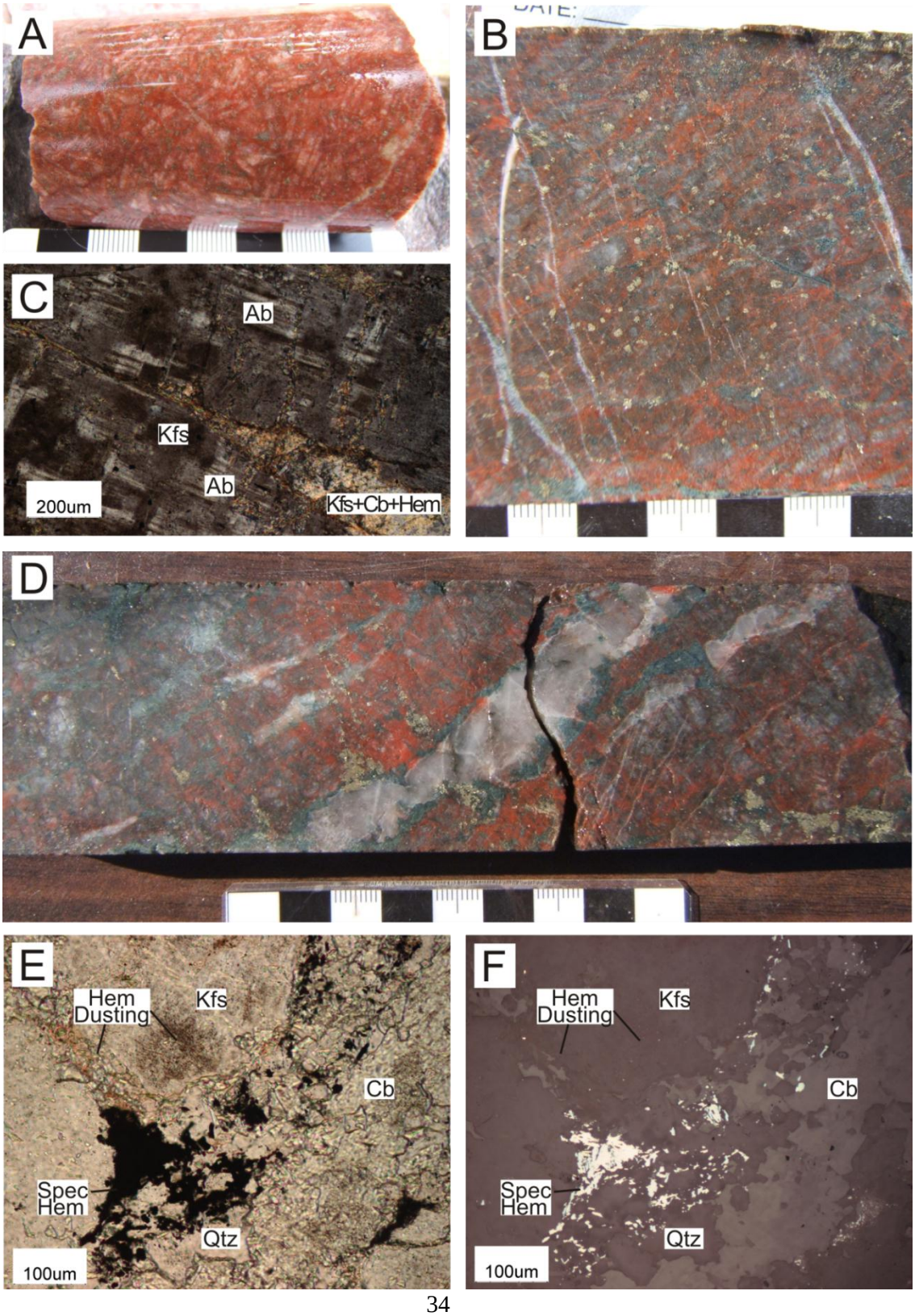
A
B
C
Ab
Kfs
Ab
Kfs+Cb+Hem
200um
D
E
Hem
Dusting
Kfs
Cb
Spec
Hem
Qtz
100um
F
Hem
Dusting
Kfs
Cb
Spec
Hem
Qtz
100um

Figure 2.9: Features of altered syenite at Young-Davidson. A) Gold-bearing intensely potassic-hematite-pyrite altered coarse trachytic syenite, minor carbonate associated with pyrite. Scale bar in cm. B) Potassic-hematite alteration in groundmass between larger feldspars. Minor chloritization and pyritization associated with fractures, weak late brittle carbonate stringers. Scale bar in cm. C) Photomicrograph showing typical albite-overprint pattern in syenite. Optically continuous albite-twins are replaced by untwinned feldspar and crosscut by later carbonate alteration. Cross polarized light. D) Potassic-hematite alteration halo surrounding Qtz-Cb-Chl veins in coarse trachytic syenite. Abundant pyrite associated with this vein. Scale bar in cm. E) Specular hematite (black) and flecks of fine-grained hematite associated with fine-grained carbonate-feldspar alteration in the groundmass. Plane polarized light. F) Same as E: Specular hematite associated with carbonate-feldspar alteration in the groundmass. Reflected plane polarized light.

syenite exist. There are at least 4 main alteration styles in the Young-Davidson syenite: potassic-hematization, sulfidation, carbonatization and chloritization. Gold distribution in the syenite is most strongly associated with potassic-hematite alteration and pyritization. Carbonatization is pervasive and is found in nearly all rocks at Young-Davidson. Based on XRD analyses (Naderi et al., 2012) and a subset of iron-carbonate stained thin section blocks (presented in Appendix I), syenite and volcanic rocks at Young-Davidson contain calcite and ankerite as the dominant carbonate phases. Timiskaming sedimentary rocks commonly contain alteration characteristics similar to the syenite; this is well developed at the contact between sediment and intensely altered syenite. Timiskaming sediments are also commonly potassic-hematite altered in haloes around quartz ± carbonate veins. Minor carbonate-chlorite alteration is found in the matrix of the sediment away from veins.

Syenite

Potassic-hematite alteration in syenite is manifested as the replacement of albite-twinned feldspars by untwinned feldspar containing abundant fine-grained hematite mineral inclusions (Figure 2.9C). The incorporation of hematite mineral inclusions into the feldspar tends to darken feldspars in plane polarized light and results in a brick red colored hand sample. The incorporation of hematite flecks in feldspar grains has been observed by Plümper and Putnis (2009) and is interpreted as the result of multiple feldspar re-equilibration during magmatic-hydrothermal fluids circulating during granitoid emplacement. K-feldspar has also developed in the groundmass where fine-grained feldspar, carbonate ± chlorite ± sericite contains fine hematite flecks that cause brick red staining in the groundmass (Figure 2.9E and F). Therefore although weakly altered syenites can contain Na-feldspar overprint textures, the feldspar replacement textures are enhanced in samples that have been intensely potassic-hematite altered, with strong iron-staining and specular hematite in the altered groundmass (Figure 2.9A, E and F). Potassic-hematite alteration haloes are developed around V_3 veins, and are generally only visible in the syenite where the groundmass is weakly altered and Na-feldspars still

dominate the mineralogy (e.g., Figure 2.9D). Hematite and magnetite are the main iron-oxide phases in the syenite. Magnetite is commonly associated with carbonate alteration in the groundmass, however, it has been observed at the center of large, weakly altered feldspar grains in the absence of carbonate alteration, possibly indicating that it existed as a primary oxide phase.

Hematite, magnetite and pyrite have a very interesting textural relationship at Young-Davidson. The three phases coexist in some samples and overgrow one another in other samples. Hematite and magnetite coexist as inclusions within pyrite grains in potassic-hematite- pyrite altered syenite. Hematite most commonly has overprinted magnetite although the reverse relationship is also present, and inclusions of both occur inside vein and disseminated pyrite. Less commonly, the textural relationship between the two Fe-oxide minerals is ambiguous and the minerals coexist with relatively linear grain-grain boundaries. Potassic-hematite alteration alone does not indicate gold mineralization, but combined with the presence of pyrite, it has served as a good proxy for mineralization for exploration geologists at Young-Davidson.

Timiskaming Sedimentary Rocks

Potassic-hematite alteration in sedimentary rocks is best developed as alteration haloes around V_3 quartz-carbonate veins and large syenite intrusions. V_3 quartz-carbonate veins in sediments commonly contain pyrite, chalcopyrite and galena, and are associated with weak to moderate K-feldspar alteration haloes (Figure 2.10A). K-feldspar staining of vein alteration haloes shows near complete replacement of the sedimentary groundmass by K-feldspar (Figure 2.10B). Without staining, K-feldspar alteration haloes are observed as reddening of the sedimentary matrix in the vicinity of V_3 quartz-iron-carbonate veins (Figure 2.10C). In thin section K-feldspar and quartz grain-grain contacts are sutured. Based on pyrite textures and chemical mapping of pyrite grains in the sediments (Chapter 3; Martin et al., in prep.), sediment-hosted pyrite is a result of multiple episodes of hydrothermal pyritization. Pyrite associated with these potassic alteration haloes ranges from euhedral to subhedral, and commonly contains inclusion-zoned pyrite grains (Chapter 3; Martin et al., in prep.). Carbonate alteration is found throughout the sediments and is interpreted as part of the metamorphic mineral assemblage in regional studies of the Timiskaming assemblage in the Matachewan area (Berger, 2006). Carbonate staining of thin section blocks shows that vein-hosted and matrix carbonates are iron-bearing (Figure 2.13); however, detailed carbonate petrology has not

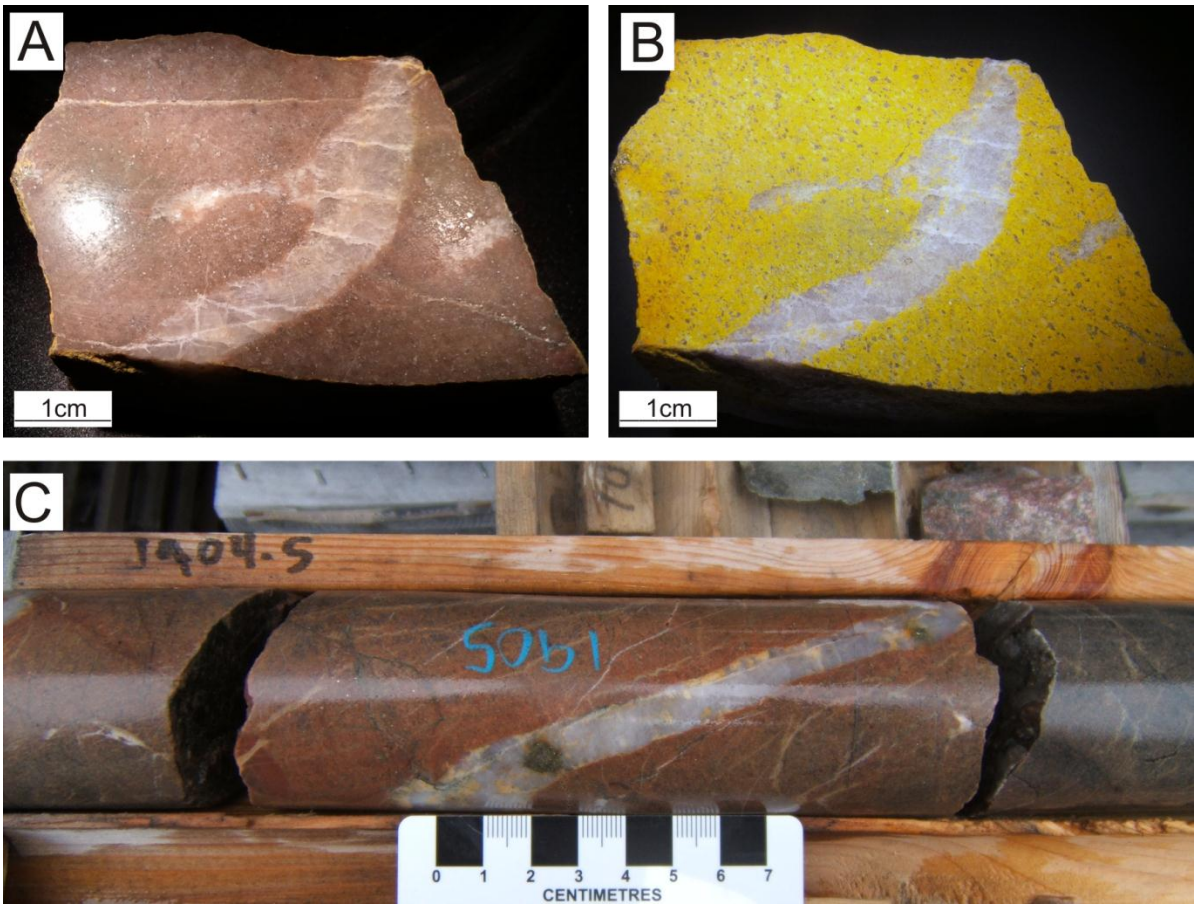

Figure 2.10: Vein-related alteration in Timiskaming sediments. A) Reddening of the sedimentary groundmass (potassic-hematite alteration) and abundant fine-grained disseminated pyrite in close proximity to a V_3 quartz-carbonate vein from the ore crosscut, UBZ. B) Stained sample from A: intense potassic (yellow)-hematite alteration in the sedimentary groundmass. C) Potassic-hematite alteration as reddening surrounding quartz-iron-carbonate vein in drill core.

been completed since thin sections have not been stained and analyzed.

Mafic Volcanic Rocks

Prior to the mineralization events the mafic volcanic rocks were of greenschist metamorphic grade and consisted of fine-grained foliated chlorite, carbonate and feldspar with accessory hematite and magnetite. Potassic alteration developed as K and Na addition where muscovite, Na-feldspar and minor amounts of K-feldspar replaced the fine-grained chlorite and quartz groundmass. Potassic alteration is coupled with intense pyritization. Rutile is abundant throughout altered volcanic rocks, and is the dominant Ti-bearing phase. In altered volcanic rocks, Fe-carbonate, albite, muscovite and

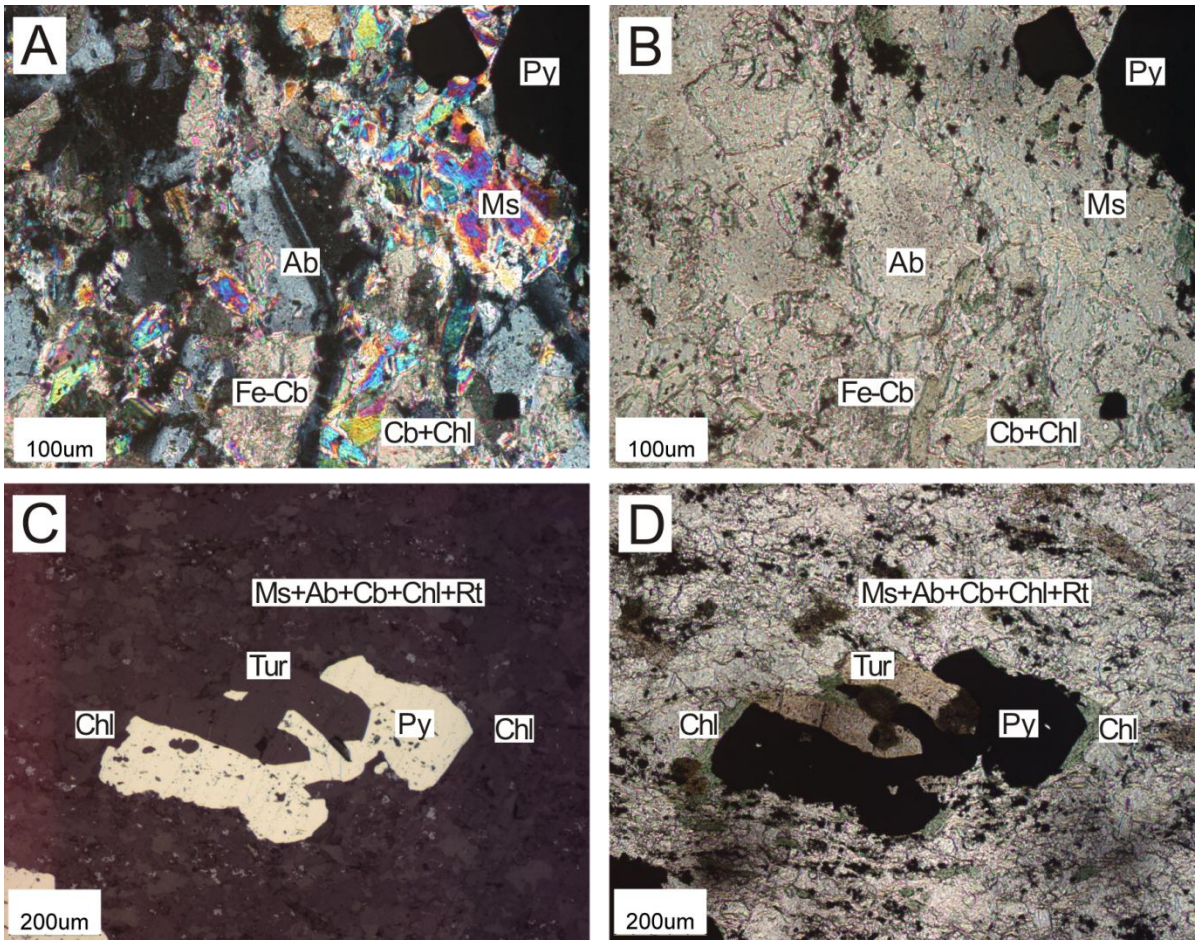

Figure 2.11: Gold-related alteration of mafic volcanic rocks. A,B) Coarsened volcanic groundmass associated with development of albite, iron-carbonate, muscovite, pyrite and minor chlorite. A) Cross polarized light. B) Plane polarized light. C,D) Anhedral inclusion-bearing pyrite in coarsened albitized groundmass, tourmaline overprinting pyrite in this section, minor chlorite halo on the pyrite grain. Abundant fine-grained rutile in the groundmass. C) Reflected plane polarized light. D) Plane polarized light.

pyrite grains coarsen and are more abundant, whereas the abundance of chlorite and quartz decreases. The most altered volcanic rocks contain ~8 wt% sulfur as pyrite, relatively coarse albite, iron-carbonate and muscovite, minor K-feldspar and accessory rutile and tourmaline (Figure 2.11). In mineralized volcanic rocks, magnetite and pyrite appear to coexist, but are not in contact. Instead, pyrite is present along some horizons whereas magnetite occurs along others. The boundaries between pyrite-bearing and magnetite-bearing zones do not show any significant replacement relationships, thus the relative timing of pyrite-magnetite is difficult to discern. In general, magnetite grains in the mineralized volcanic rocks tend to be euhedral whereas the pyrite is more typically anhedral and deformed with abundant inclusions. A late magnetite-alteration event probably best

explains the euhedral magnetite-bearing zones in mineralized basalts, and is consistent with addition of iron to mineralized volcanic rocks during gold-related alteration (discussed in Section 2.7.2). The tourmaline overprint of pyrite also indicates that a post-sulfidation alteration phase has generated tourmaline, and is potentially related to the magnetite (Figure 2.11).

2.5.2 Veining

Three main vein types hosted by syenite have been characterized in the Upper Boundary Zone (UBZ) based on structural mapping of the #9 ore crosscut (back star; Figure 2.4). Structural and crosscutting relationships are discussed in detail by Zhang et al. (2012) and are summarized below. Zhang et al. (2012) produced a structural map of the ore crosscut that outlines the structural relationships between the different vein sets and an excerpt is shown in Figure 2.12A with examples of each identified vein set in Figure 2.12B, C and D.

V_1 veins

V_1 veins are the earliest veins at Young-Davidson and consist of boudinaged quartz-iron-carbonate veins that are only present in the syenite. These veins are found in all zones of the deposit and display similar characteristics regardless of the zone. V_1 veins range from < 5 cm to > 20 cm in thickness and are strongly deformed. They are composed of 70-80% iron-carbonate (ankerite), 10-15% quartz, minor amounts of pyrite and K-feldspar, and are commonly rimmed by a thin chlorite ± pyrite halo (Figure 2.12B). Ore minerals associated with V_1 veins include trace amounts of galena, chalcopyrite, magnetite, molybdenite and gold as inclusions in pyrite. Since the V_1 veins are moderately to intensely deformed, K-feldspar grains in the veins could potentially represent wall rock fragments, however, tartan-twinned hydrothermal K-feldspar in these veins would imply a temperature of V_1 vein formation of > 300 ºC (Nesse, 2000). V_1 veins are boudinaged, folded, dipping to the southwest at moderate to high angles and are crosscut by V_3 veins and syn-D_1 thrust faults (Zhang et al., 2012). Based on these structural relationships, Zhang et al. (2012) has determined that V_1 veins were pre-D_1; coeval with syenite emplacement.

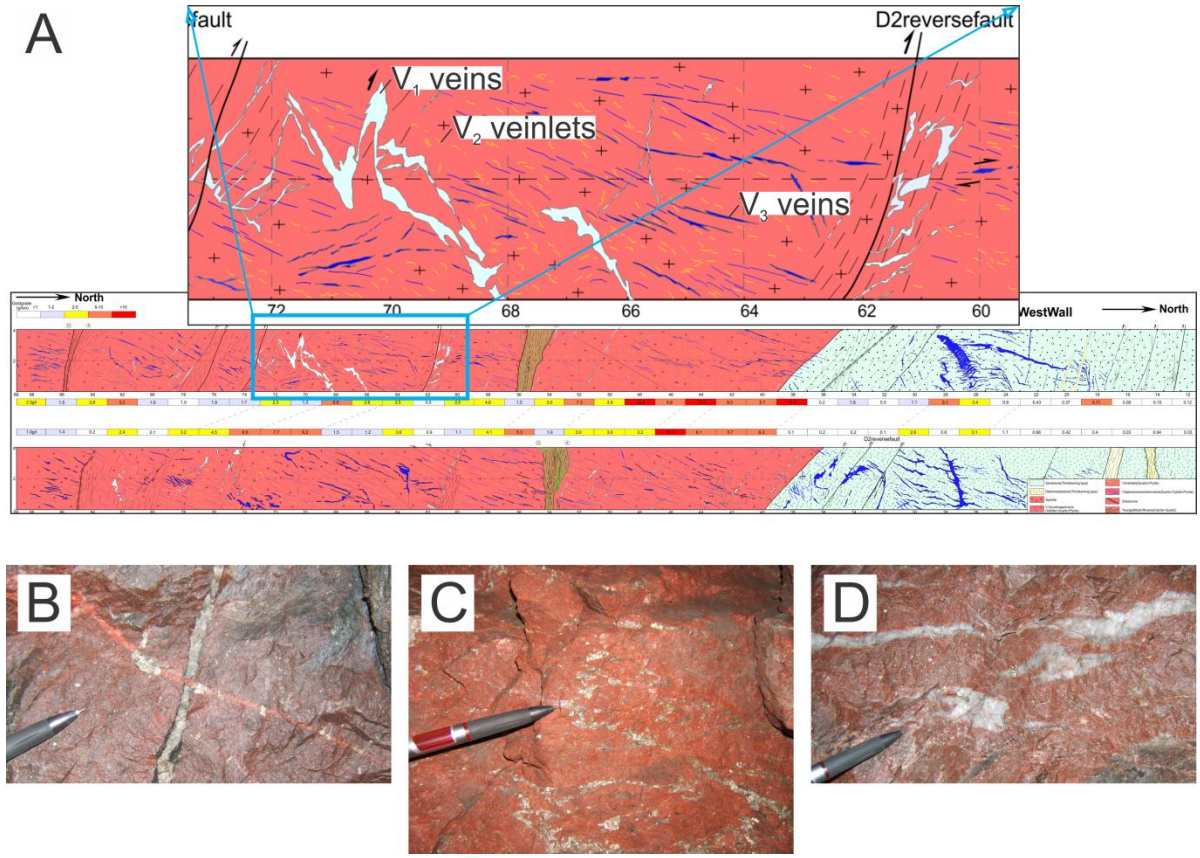

Figure 2.12: Structural map and examples of different vein types at the #9 ore crosscut. A) Structural map of the #9 ore crosscut highlighting vein types and contact relationship with the syenite (Modified from: Zhang et al., 2012). B) Steeply dipping boudinaged V_1 iron-carbonate vein with chlorite ± pyrite rim, crosscut by later planar V_3 K-feldspar altered vein. C) Moderately dipping quartz-pyrite veinlets, boudinaged, deformed, with abundant pyrite hosted in intensely altered syenite. D) V_3 quartz-carbonate veins, relatively planar, en-echelon, tension-gash type veins, minor associated pyrite.

V_2 veins

The second vein generation from the UBZ is boudinaged quartz-pyrite veinlets that are dominantly hosted in syenite. V_2 veinlets are < 2 cm to 10 cm in length and a few centimeters in width, are boudinaged and folded, and dip to the northeast at shallow to moderate angles. V_2 veins are composed of variable amounts of quartz and pyrite (locally up to 90% quartz or 90% pyrite) with accessory carbonate, chlorite and rutile. The main ore mineral in V_2 veins is pyrite that is corroded along fractures and contains abundant hematite, magnetite, rutile, chalcopyrite and gold as inclusions and additionally, gold along fractures. V_2 veins are the dominant gold-bearing vein type from the ore

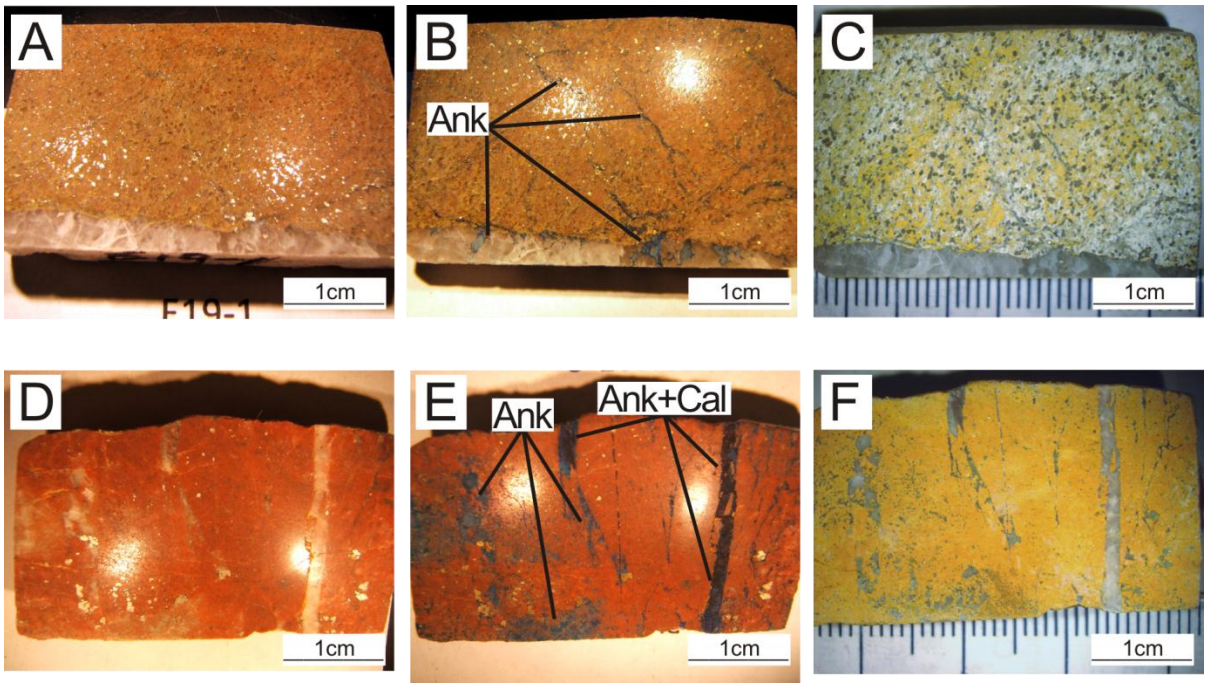

Figure 2.13: Staining of Timiskaming sediment sample E19-1 (A to C) and UBZ syenite sample RW45-3 (D to E). A) Unstained sediment. B) Iron-carbonate staining (blue). C) K-feldspar staining (yellow) with K-feldspar alteration through the sediment matrix proximal to V_3 quartz-carbonate vein. D) Unstained syenite. E) Iron-carbonate staining (blue) with iron-carbonate dominated V_3 veins and patches of alteration in the groundmass. F) K-feldspar staining (yellow) with K-feldspar dominating the syenite mineralogy.

crosscut and the UBZ. Based on the structural relationships these veins post-dated D_1 deformation and pre-dated or developed during the D_2 deformation (Zhang et al., 2012).

V_3 veins

The third vein generation from the UBZ, V_3, are large planar quartz-carbonate veins. They are commonly > 30 cm (locally > 2 m) in length and > 10 cm in width and are relatively planar compared to the older, more deformed, vein generations. These veins are composed of variable amounts of quartz and carbonate (either quartz or carbonate dominated) with accessory pyrite, K-feldspar and chlorite. The main ore mineral is pyrite that is generally euhedral and characteristically contains much less mineral inclusions compared to V_1 and V_2. Inclusions of galena, chalcopyrite and minor rutile in V_3 vein pyrite contrasts with the hematite-magnetite rich inclusion assemblage in V_2 vein pyrite. V_3 also commonly hosts galena, chalcopyrite, scheelite and occurrences of native free gold. During study of the ore crosscut, V_3 veins varied from carbonate dominated along one interval (i.e., 39 m-45 m) of

the ore crosscut and were quartz dominated along other intervals (i.e., 80 m-85 m). Tartan-twinned K-feldspar in V_3 veins in syenite and sediments suggest that the temperature of vein formation was > 300 ºC (Nesse, 2000), similar to the V_1 veins. Based on K-feldspar staining and petrography, potassic-hematite and pyrite alteration haloes are associated with V_3 veins in the syenite and sedimentary host rocks (Figure 2.9D and Figure 2.10B). The structural relationships documented at the ore crosscut allowed Zhang et al. (2012) to determine that the V_3 veins are structurally similar to V_2 veins; they post-date the D_1 deformation, are syn- to late-D_2 deformation, and are truncated by late east-west trending shear zones dated at ~2665 Ma (Zhang et al., 2012 and ref. therein). During core logging, without the large-scale crosscutting relationships available at the ore crosscut, classifying each vein as either V_2 deformed quartz-pyrite veinlets or V_3 planar quartz-carbonate ± pyrite veins proved problematic. If the vein was deformed, dominated by pyrite and generally matched the size range of V_2 from the ore crosscut, then that vein has been called a V_2 vein. If the vein was larger with brittle features (less deformed), dominated by quartz or carbonate and lacking pyrite then we termed that vein a V_3 vein. In practice, however, V_2 veins usually contain some quantity of quartz, and thus without the crosscutting relationships it is difficult to conclusively classify veins as V_2 or V_3 when core logging. Further difficulty arose from the similarities in vein orientations (less crosscutting relationships) and the fact that both veins are associated with similar alteration types that developed during the same deformation event.

Other vein types

Several other vein types have been identified at Young-Davidson during core logging from other zones of the deposit. These veins are mineralogically distinct from the three sets identified at the ore crosscut. Relating each vein to the structural and temporal framework developed at the ore crosscut was problematic during core logging because crosscutting relationships between these veins and the well-defined veins were generally absent. Other vein types found at Young-Davidson include barite-fluorite, carbonate-hematite-magnetite, quartz-chlorite, quartz-tourmaline and late brittle carbonate veins, stringers and fault-fill. With the exception of a sediment-hosted quartz-tourmaline vein locality intersected east of the current resource, other vein types are not mineralized.

Late brittle, brecciated barite veins in the syenite contain variable amounts of barite, fluorite, quartz, carbonate, specular hematite, galena, chalcopyrite and pyrite. Locally within volcanic rocks,

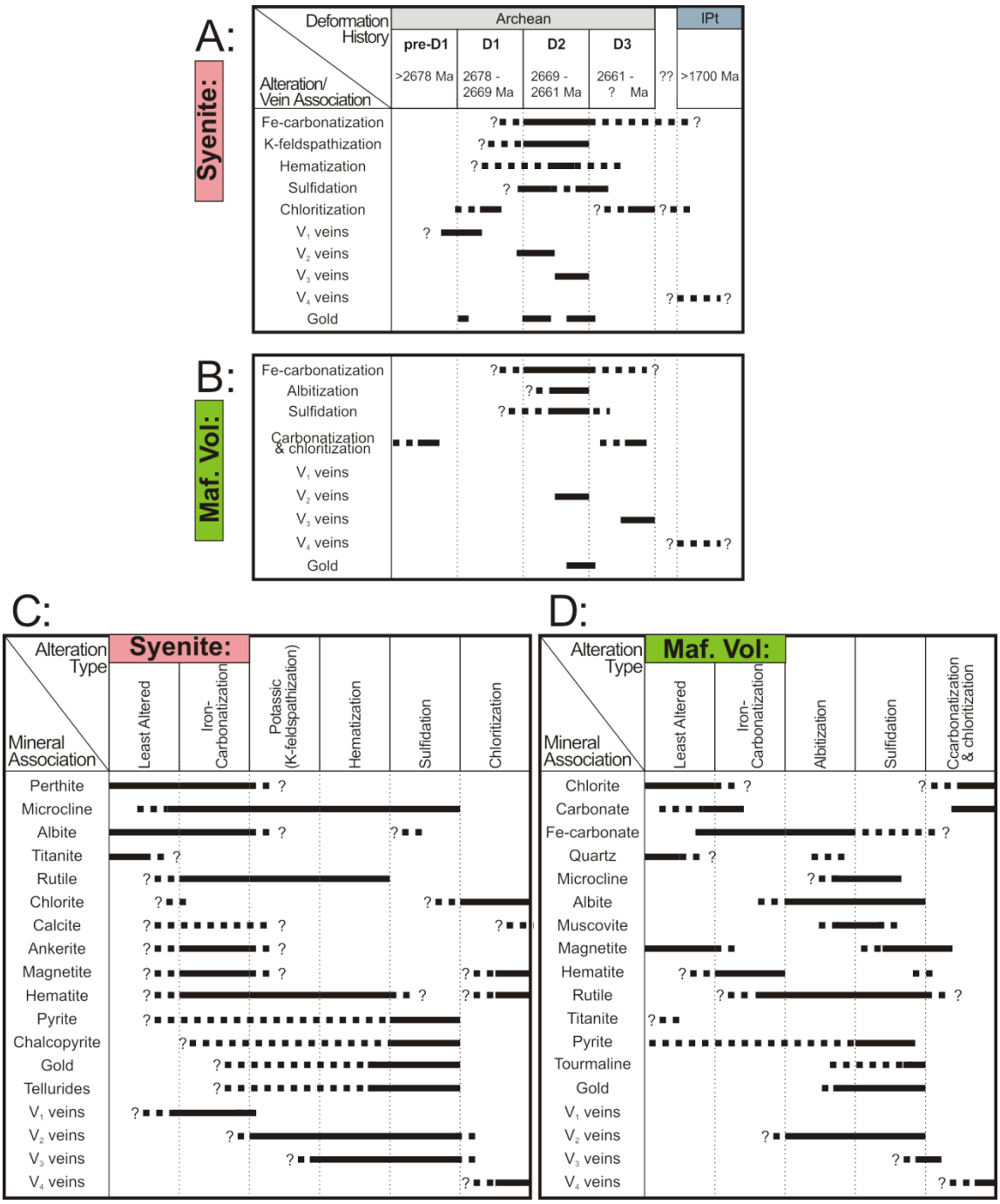

Figure 2.14: A) Generalized vein and alteration paragenesis for syenite showing temporal relationships between veins and major alteration styles. B) Generalized vein and alteration paragenesis for mafic volcanic rocks showing temporal relationship between veins and major alteration styles. C) and D) Mineral paragenesis relationship for each listed alteration type. Left to right represents general temporal relationship, however, some alteration types are repetitive (as seen in A and B) and relationships are meant to show appearance or disappearance of certain minerals from the alteration assemblage. C - Syenite paragenesis and D - mafic volcanic paragenesis. Solid lines - dominant alteration styles/minerals present at that time/during that phase of alteration. Dotted lines - minor component; introduction of or disappearance of alteration styles/alteration minerals. Age data from Zhang et al., 2012.

these veins are composed of nearly 100% barite, and crosscut all foliations. Barite veins at Young-Davidson are considered late and are likely coeval with other barite veins and occurrences located elsewhere in the Matachewan area (Lovell, 1967; Berger, 2006).

Carbonate-hematite-magnetite veins represent a small group of veins at Young-Davidson that are related to locally pervasive carbonate-hematite-magnetite alteration. One locality of carbonate-hematite-quartz veins at the ore crosscut in the UBZ contains hydrothermal monazite grains that have been dated at ~1730 Ma (Zhang et al., 2012). These veins do not contain gold mineralization, but are located within a zone in the UBZ that hosts significant disseminated and V_2 vein style mineralization. The age date from this vein is interesting with respect to potential remobilization because it shows that around 1730 Ma there was thermal reactivation in the area that has potentially remobilized gold from older mineralization. Since gold has not been identified with these veins sets to date, they are not considered to be important for controlling gold distribution.

Quartz-tourmaline veins are the most common 'other' vein type at Young-Davidson. Tourmaline is commonly present in planar quartz ± carbonate veins in syenite and sedimentary rocks. These veins are mineralogically similar to gold-bearing veins found at other gold deposits in the Abitibi where the presence of tourmaline is a strong indication of gold mineralization (e.g., Robert et al., 1995; McCuaig and Kerrich, 1998; Beaudoin and Pitre, 2005). Quartz-tourmaline veins are generally composed of 60-70% quartz, 25-30% tourmaline and accessory iron-carbonate, chalcopyrite and chlorite. Several syenite-hosted quartz-tourmaline veins have been sampled and petrography on each sample has not identified any associated gold mineralization. These veins lack hydrothermal K-feldspar, and similarly have not generated alteration haloes in the syenite. The only intersection of Tourmaline-bearing vein-related gold mineralization found to date is the intersection of deformed conglomerate with intense quartz-tourmaline veining and tourmaline flooding, east of the syenite at depth. In these veins gold occurs as inclusions and along cracks in deformed pyrite grains. This area is on-strike along the CLLDZ with syenite-hosted mineralization from the Lower Boundary Zone of the syenite, east of the defined resource. The mineralization is interesting because the tourmaline-gold association is similar to gold-bearing veins found elsewhere along the CLLDZ (e.g., Sigma; Olivo et al., 2006) and because it is rare at Young-Davidson. The tourmaline-gold association of these sedimentary examples is also similar to the tourmaline-gold association in altered volcanic rocks east of the mineralized syenite; however, in volcanic rocks tourmaline is found as a late stage alteration product whereas in the sediments tourmaline and gold are directly related to vein emplacement.

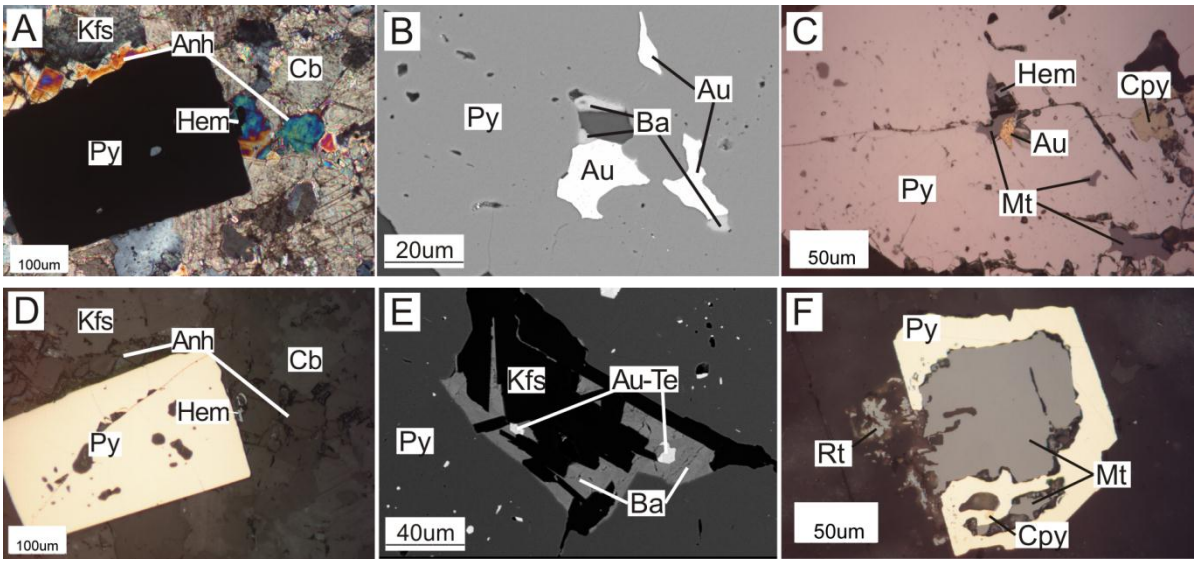

Figure 2.15: Oxidized mineral assemblages at Young-Davidson. A and D) Pyrite-anhydrite-carbonate-hematite assemblage associated with barren V_3 vein. A) Cross polarized light. D) Reflected plane polarized light. B) BSE image of V_2 vein-hosted mineralization from the UBZ; pyrite hosted Au associated with barite. C) Disseminated mineralization hosted within hematite-magnetite-bearing fractured pyrite grain. Reflected plane polarized light. E) BSE image of V_2 vein-hosted barite-K-feldspar-Au-Te mineralization. F) Pyrite overprint of magnetite, same sample as from C). Reflected plane polarized light.

2.5.3 Gold Mineralization

Two textural types of gold mineralization have been identified in the syenite based on transmitted and reflected light petrography of ore crosscut and drill core samples, supplemented by SEM analysis. Gold is intimately associated with disseminated pyrite and vein pyrite (V_1, V_2 and V_3). The only exception for the gold-pyrite association is where gold is present as native free-gold grains in V_3 quartz-carbonate veins or associated with other sulfides (galena, chalcopyrite) in these veins. Petrographic analysis of the different stages of mineralization has delineated two textural types of pyrite based on the inclusion composition, grain morphology and the vein association. Type 1 pyrite generally contains abundant inclusions of oxide minerals and has corroded and fractured grain boundaries. By contrast, type 2 pyrite is relatively free of oxide mineral inclusions and has euhedral grain boundaries. The first type of syenite-hosted gold mineralization is as inclusions and along fractures in type 1 pyrite hosted by V_1 veins, V_2 veins and disseminated pyrite. The second type of syenite-hosted gold mineralization is associated with V_3 veins where gold occurs along fractures in type 2 iron-oxide free pyrite grains and as free gold along quartz-carbonate grain boundaries. The

following section will discuss different phases of mineralization and the textural features of the gold-hosting pyrite at Young-Davidson.

Type 1 pyrite in V_1 veins contains inclusions of magnetite, chalcopyrite, galena, telluride minerals, gangue minerals and gold (Figure 2.16B). One specific example of V_1 mineralization contains euhedral pyrite with irregular gangue mineral inclusion patterns (Figure 2.16A). Chemical mapping of this euhedral type 1 by Martin et al. (Chapter 3; in prep.) has shown that this type of pyrite is a

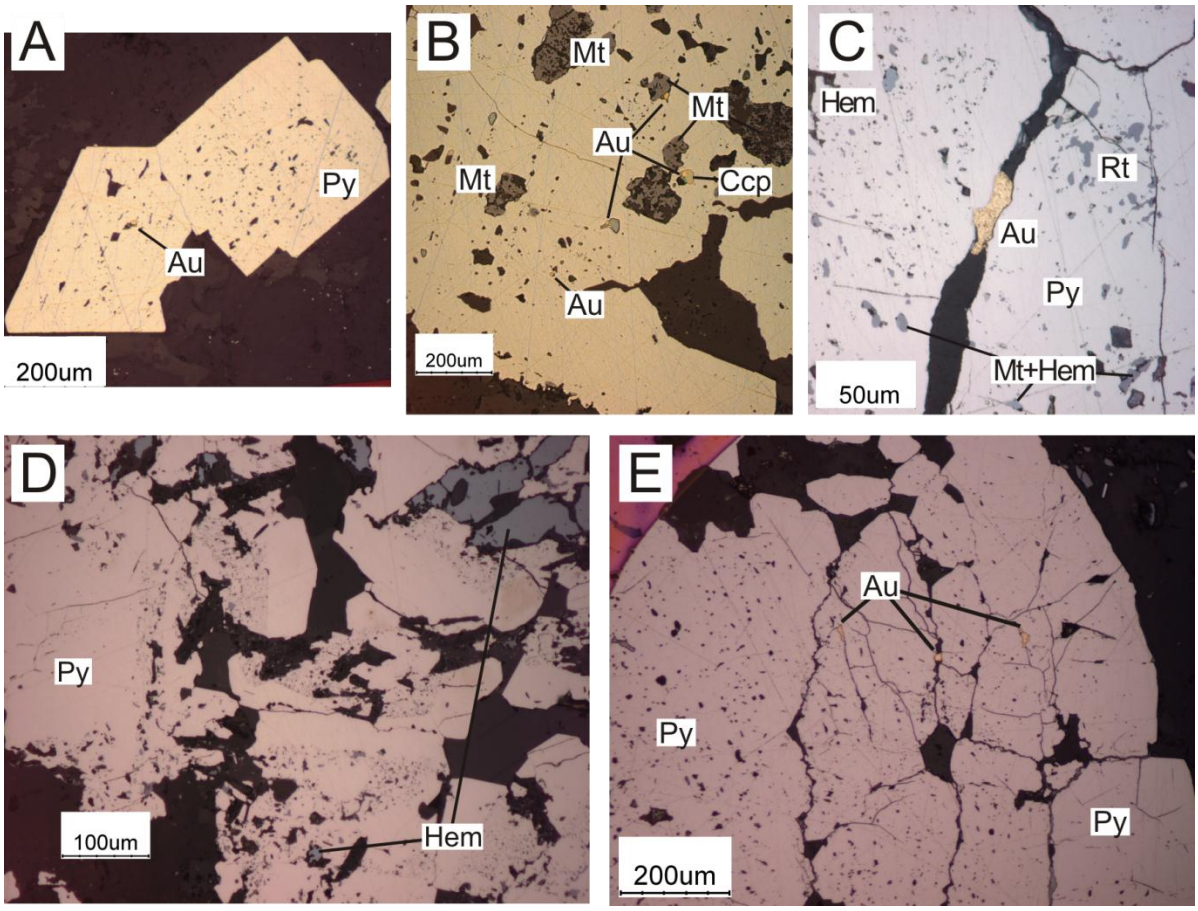

Figure 2.16: Features of type 1 pyrite related gold mineralization. A) Euhedral V_1 vein-hosted type 1 pyrite with carbonate and gold inclusions associated with 'invisible' hydrothermal overgrowths (Chapter 3; Martin et al., in prep.). Reflected plane polarized light. B) Corroded V_1 vein-hosted type 1 pyrite with Mt, Ccp, gangue and Au inclusions. Reflected plane polarized light. C) Native gold grain found along crack in V_2 vein hosted type 1 pyrite that hosts abundant Hem, Mt and Rt inclusions. Reflected plane polarized light. D) Dissolved corroded nature of V_2 vein pyrite with irregular inclusion patterns and inclusion rich and inclusion poor zones. Reflected plane polarized light. E) Type 1 pyrite from V_2 vein with corroded gold-bearing fractures. Reflected plane polarized light.

combined result of pyrite dissolution and Co-Ni-bearing hydrothermal pyrite overgrowth events. Telluride, galena and gold inclusions within type 1 pyrite in V_1 veins are associated with the overgrowths, and were introduced with the Co-Ni-bearing fluid that overprinted the original deformed and corroded pyrite grains (Chapter 3; Martin et al., in prep.).

Type 1 pyrite in V_2 veins is commonly corroded along fractures and is characteristically enriched in hematite and magnetite inclusions (Figure 2.16C and D). The hematite-magnetite inclusion pattern within this stage of pyrite is ambiguous as hematite and magnetite occur as coexisting inclusions within the pyrite, and occur outside of the pyrite grains where both hematite replacement of magnetite and magnetite replacement of hematite are observed. Type 1 pyrite in V_2 veins is not observed to have replaced magnetite or hematite; rather, the iron-oxide bearing textures in V_2-hosted type 1 pyrite grains are interpreted as oxidation of pyrite to corrode the grains and deposit iron-oxides (Figure 2.16D). In V_2 veins, gold is present as inclusions and more commonly along fractures and cracks in the pyrite where it is associated with oxides and gangue minerals (Figure 2.16C and E).

Type 1 disseminated pyrite grains are similar to type 1 pyrite in V_2; they contain abundant hematite, magnetite and rutile inclusions, irregular grain-grain boundaries and are commonly fractured (Figure 2.15C). The concentration of type 1 disseminated pyrite is highest in coarse-grained trachytic syenite that has undergone pervasive potassic-hematite-pyrite alteration in zones crosscut by abundant V_2 and V_3 veins. Gold is present as inclusions in the disseminated type 1 pyrite in these zones. Several examples of unmineralized disseminated type 1 pyrite grains exist in zones containing mineralized type 1 pyrite, perhaps suggesting that there have been multiple pyritization events, some of which were gold-bearing. In detail, textural evidence from pyrite-oxide relationships suggests that both sulfidation and oxidation have occurred; where pyrite has overgrown oxide grains and was subsequently oxidized to cause corrosion.

Type 2 pyrite grains are found in V_3 veins and as disseminated grains in zones with abundant carbonate between large feldspars in the syenite. V_3 veins are relatively planar and were developed during the late D_2 deformation associated with the CLLDZ. In the studied examples of V_3 vein mineralization, gold occurs as inclusions in type 1 disseminated pyrite in alteration haloes, as inclusions and along outer boundaries of type 2 pyrite grains (Figure 2.17B), along fractures in type 2 pyrite grains (gold appears to be after pyrite; Chapter 3; Martin et al., in prep.), along quartz-carbonate grain boundaries within V_3 veins (Figure 2.17A) and finally, with recrystallized quartz

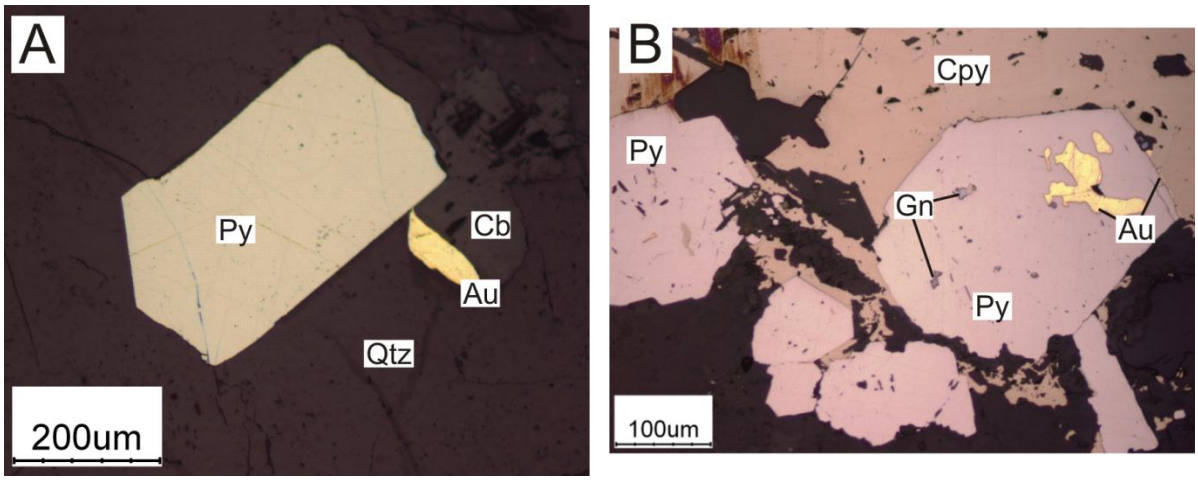

Figure 2.17: Features of type 2 pyrite related gold mineralization. A) Euhedral oxide-inclusion free type 2 pyrite hosted in V_3 quartz-carbonate vein with gold mineralization along quartz-carbonate grain boundary. Reflected plane polarized light. B) Euhedral oxide-inclusion-free type 2 pyrite hosting gold at the edge of a chalcopyrite-bearing V_3 vein. Reflected plane polarized light.

grains along the boundaries of larger quartz grains. Type 2 pyrite is generally euhedral and is distinguished from type 1 pyrite by a lack of hematite-magnetite mineral inclusions (Figure 2.17).

Gold mineralization hosted by volcanic rocks is associated with albite, iron-carbonate and pyrite alteration and quartz-iron-carbonate veins. Quartz-iron-carbonate-pyrite veins in these zones host abundant gold as fine to coarse native gold inclusions in pyrite, along fractures in pyrite and also in quartz and carbonate in the vein. The mineralization characteristics these veins are similar to those from V_3-hosted mineralization examples in the syenite. Gold grains were generally not observed in intensely pyritized volcanic wall rock samples (including a sample containing 9 g/t Au). The lack of visible grains in these samples can either be explained by a nugget effect in the assay (where gold is dominantly in veins) or by invisible gold as sub-microscopic inclusions in pyrite. Since we have identified abundant gold in the associated quartz-iron-carbonate veins and the 9 g/t analysis is mainly from vein-free samples (e.g., Figure 2.6B), the possibility of very fine pyrite-hosted gold exists. Coexisting vein-hosted and pyrite-replacement styles of mineralization in Tisdale assemblage mafic volcanic rocks has been observed in the Kirkland Lake area (Ispolatov et al., 2008 and ref. therein). Therefore, although the vast majority of observed gold was from veins, pyrite-replacement styles of mineralization at Young-Davidson potentially also represent a significant source of gold from volcanic rocks. Disseminated pyrite grains in mineralized volcanic rocks are texturally similar to type 1 syenite-hosted grains but lack hematite and magnetite inclusions and only contain rutile,

chalcopyrite carbonate and silicate minerals as inclusions. These grains are commonly fractured and also texturally zoned; with inclusion-bearing and inclusion poor zones.

2.6 Geochemistry

A total of 279 samples have been analyzed for whole rock, major and trace element geochemistry; 221 analyses from drill core, 33 analyses from the underground ore-crosscut and 25 analyses from surface exposures. The majority of analyses are of syenite, which is the dominant host of mineralization at Young-Davidson. Syenite samples were collected in order to characterize the geochemical changes from least-altered to mineralized and to determine deposit scale geochemical trends from different zones of the deposit, along two main cross sections X-X' and Y-Y', seen in Figure 2.5. Samples were also collected from volcanic rocks to characterize the geochemical changes from least-altered to mineralized. Effort was made to avoid veins during sampling, however due to the abundant nature of veining at Young-Davidson, it is inevitable that some of the samples contain vein material. Samples were analyzed at Geoscience Laboratories (GeoLabs) in Sudbury, Ontario and Activation Laboratories (ActLabs) in Ancaster, Ontario. At GeoLabs, major elements were analyzed by XRF and trace elements by fused pellet ICP-MS. At ActLabs, both major and trace elements were analyzed by fused pellet ICP-MS. To assess the agreement of major element data produced from ICP-MS and XRF methods, ActLabs was instructed to perform both XRF and ICP-MS whole rock analyses on a subset of samples. Major element data produced from ICP-MS data is within 5% of the data produced from XRF on the same samples. Therefore major element data produced from ICP-MS methods is considered equivalent to that produced by XRF methods (ActLabs Group of Companies, 2011). Since data was obtained using two labs, a subset of samples analyzed at GeoLabs were reanalyzed at ActLabs for comparison. Major element data produced from each lab is precise to 25% and trace element data from each lab is precise to 80%, indicating relatively poor agreement of data from the two labs, likely arising from different analytical procedures at each lab. Internal lab standards were utilized during geochemical testing at each lab to ensure accuracy and to check and correct for instrument drift. Therefore, mass balance calculations will be performed using only data from ActLabs, whereas geochemical plots (scatter plots Figure 2.18 and geochemical contouring Figure 2.19) will utilize data from both labs in a semi-quantitative manner to look at trends. In

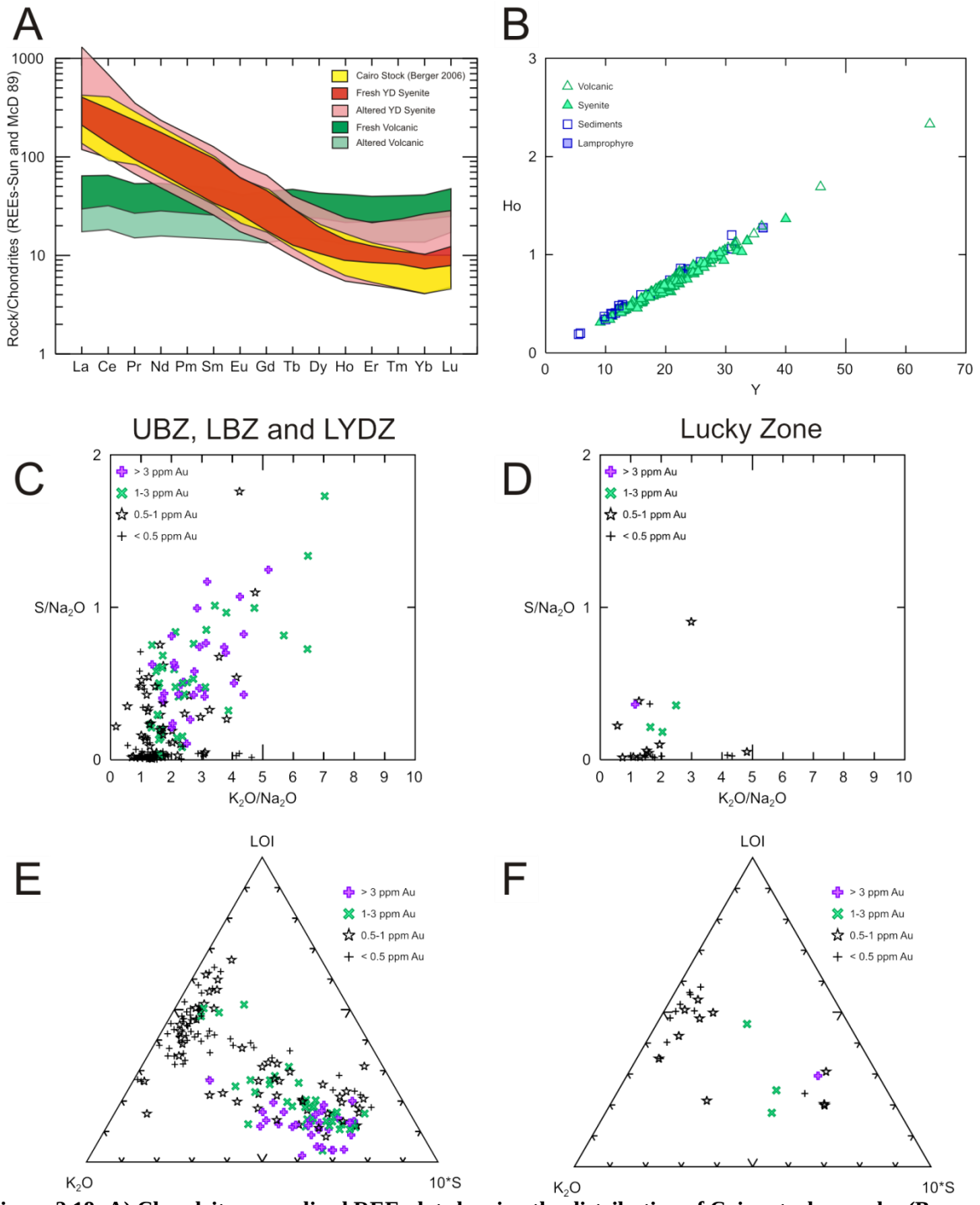

Figure 2.18: A) Chondrite normalized REE plot showing the distribution of Cairo stock samples (Berger, 2006), fresh and altered Young-Davidson syenite and fresh and altered volcanic rocks (this study). Alteration of volcanic rocks indicates mass gain and dilution of the immobile REEs during alteration. The main field of fresh Young-Davidson syenite mainly overlaps with Cairo stock samples and is enriched in LREEs relative to the Cairo stock. B) Binary plot of Ho vs Y demonstrating HREE and Y

immobility for use in mass balance calculations. Figures C-F utilize syenite analyses only. C) Binary plot of syenite alteration indices for the UBZ, LBZ and LYDZ showing Au-bearing samples are enriched in K_2O and S relative to the depleted Na_2O. D) Binary plot of syenite alteration indices for the LZ showing Au-bearing samples contain less K_2O and S enrichment compared to the UBZ, LBZ and LYDZ; potentially a function of vein-dominated styles of mineralization. E) Ternary plot of LOI vs K_2O vs 10*S for the UBZ, LBZ and LYDZ; gold grade correlates with sulfur. F) Ternary plot of LOI vs K_2O vs 10*S for the LZ; gold grade correlates with sulfur, but contains less S than the other zones of mineralization.

addition to major and trace element geochemistry, total S was determined by infrared absorption from both labs, and As, Au, Br, Cr, Ir, Sc and Se were analyzed by INAA at ActLabs.

2.6.1 Syenite Geochemistry

Representative geochemical analyses of least-altered syenite are tabulated in Table 2.1, altered and mineralized syenite in Table 2.2, and a complete dataset is provided in Appendix D. Based on geochemical analyses and carbonate staining of thin section blocks, least-altered syenite generally contains weak to moderate calcite and ankerite (carbonate and iron-carbonate) alteration that is associated with thin carbonate and iron-carbonate stringers. Since carbonate alteration is generally pervasive, variations in alteration are mostly due to varying intensities of potassic-hematite-pyrite alteration. Least-altered syenite samples generally contain 1.7 - 6.99 wt% LOI, 2.68 - 6.72 wt% CaO, 2.95 - 7.43 wt% Fe_2O_{3t}, 3.93 - 8.05 wt% K_2O and generally < 0.66 wt% S. High LOI in least-altered samples is attributed to CO_2 degassing from carbonates during LOI analysis. The abundances of chondrite-normalized REE show a steep negative slope (Figure 2.18A). It is also noteworthy that the REE pattern of the syenite lacks an Eu anomaly. The REE patterns from fresh Young-Davidson syenites (red on Figure 2.18A) also show similarities to REE patterns from the Cairo stock (yellow on Figure 2.18A), indicating that the two are likely part of the same magmatic suite. This data supports the early interpretation of the Young-Davidson syenite as a distal dike to the Cairo stock by Lovell (1967). Syenite-hosted gold mineralization is characterized by albite-twinned feldspar replacement by untwinned K-feldspar during potassic-hematite-pyrite alteration. Figure 2.18C and D highlights enrichments in K and S relative to depletions in Na during gold-related alteration. Gold values are best correlated with sulfur (Figure 2.18E), which supports the textural relationship between gold and pyrite in most gold-bearing rocks. There are a few outlier data points that warrant discussion; specifically those that contain low sulfur yet are mineralized. These points can be attributed to V_3 vein styles of mineralization that are relatively sulfide-free whereas samples with elevated S that contain no mineralization can be attributed to the presence of barren pyrite or sulfate minerals.

Similarly, a comparison of samples from the Lucky Zone (Figure 2.18D and F) with samples from all other zones (Figure 2.18C and E) indicates that mineralization in the Lucky Zone is associated with lower S and K_2O enrichments, which suggests that the mineralization from this zone likely occurs as V_3 veins. Barite and anhydrite are the main sulfate phases that have been identified in the syenite. Trace amounts of fine-grained barite have been identified with carbonate alteration in intense potassic-hematite altered syenite. Trace barite has also been identified with gold inclusions in V_2 veinlets (Figure 2.15B and E). Anhydrite has been identified in barren pyrite-bearing quartz-carbonate veins (Figure 2.15A and D).

The spatial distribution of Au, Ba, K_2O and S along two N-S cross sections is presented in Figure 2.19. The location of each cross section was selected such that each zone of mineralization was intersected for study. The cross section through 22790 mE intersects mineralization in the LYDZ at the west end of the deposit whereas the 23240 mE cross section intersects mineralization in the LZ and LBZ in the central portion of the deposit (Figure 2.4). Mineralization from the UBZ was studied during underground ore-crosscut mapping in conjunction with the structural study by Zhang et al. (2012; Figure 2.12A). The data presented in Figure 2.19 also incorporates the ore shapes as modeled by Northgate (now AuRico) geologists (Edmunds pers. comm., 2008). Sample points have been projected to the 2D cross section surface and, using the software package Surfer ™ (Version 10), contoured with the Kriging interpolation method with search ellipse: anisotropism = 2 and slope = 75-80˚. The specified search ellipse was designed to interpolate data up-dip between drill holes essentially following the syenite contact and the zone of mineralization as indicated by the ore trace. The goal of using the specified Kriging parameters was to orient the long axis of the search ellipse along the direction of the least data density; between adjacent drill holes rather than along the drill holes. The end result has generated contours that are preferentially elongated up-dip, mirroring the zone of mineralization and preferentially searching from neighboring drill holes. Since the present sampling method was largely of relatively vein-free samples, and the AuRico dataset represents a total analysis including veins and wall rock over a specified interval, correlation of the present data with AuRico analyses would indicate that gold is disseminated in the wall rock. Conversely, a lack of correlation with AuRico data might indicate vein-hosted styles of mineralization are more important than disseminated styles (e.g., Figure 2.20). In the LYDZ at the west end of the deposit Ba, K_2O and S highs generally overlap with the zone of mineralization (Figure 2.19A). Similarly, in the LBZ there

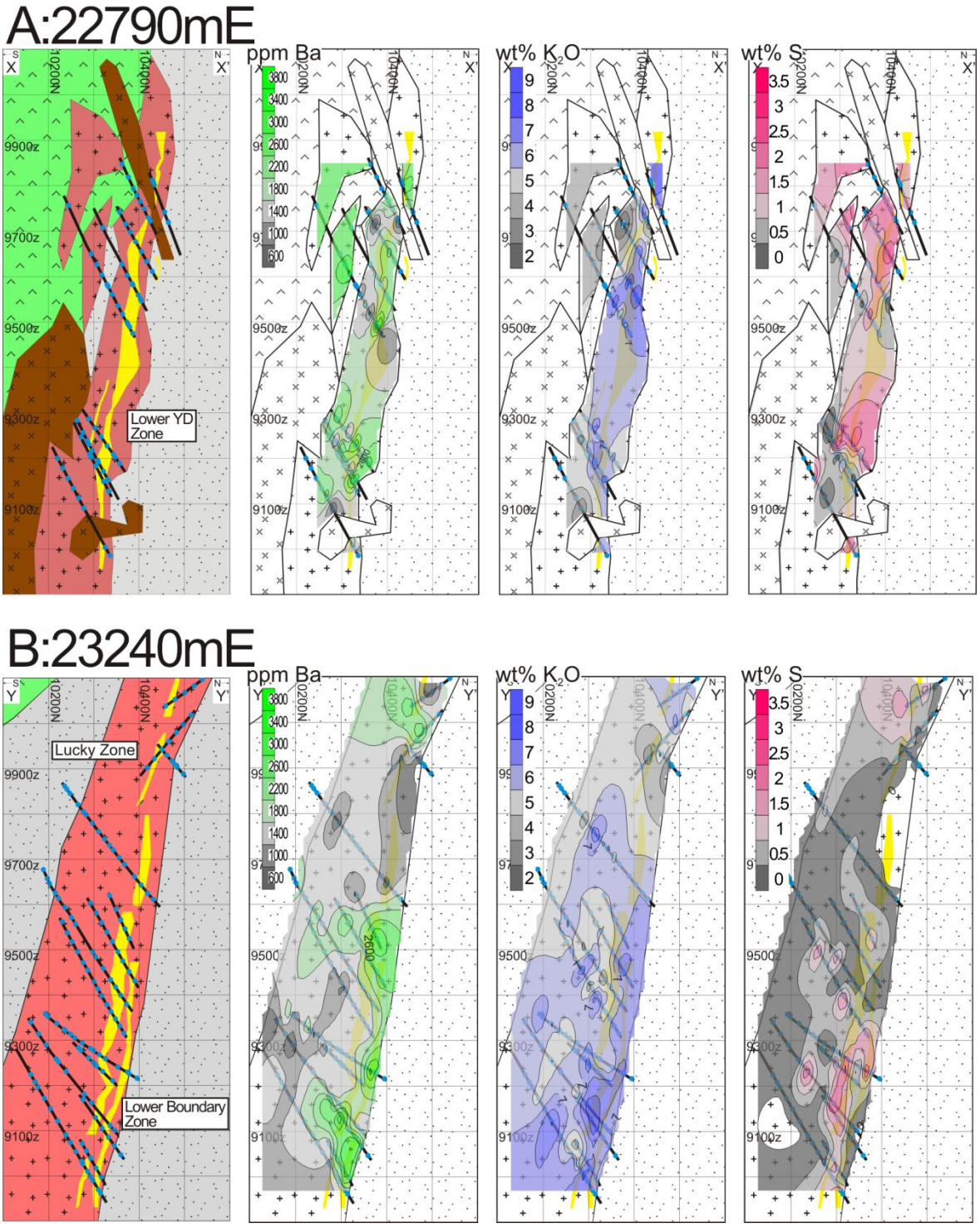

Figure 2.19: Geochemical contours from relatively vein-free samples along two N-S cross sections at Young-Davidson. A) 22790 mE intersecting LYDZ mineralization. Ore trace is shown in yellow on all figures. In general there is a cross-section wide correlation between Au, K_2O and S. Ba also shown interesting spatial overlap with K_2O and S highs; likely related to both. B) 23240 mE intersecting LZ and LBZ mineralization. Geochemical trends are better represented due to higher data density. Correlation between Au, K_2O, S and Ba is similar to that found on 22790 mE section.

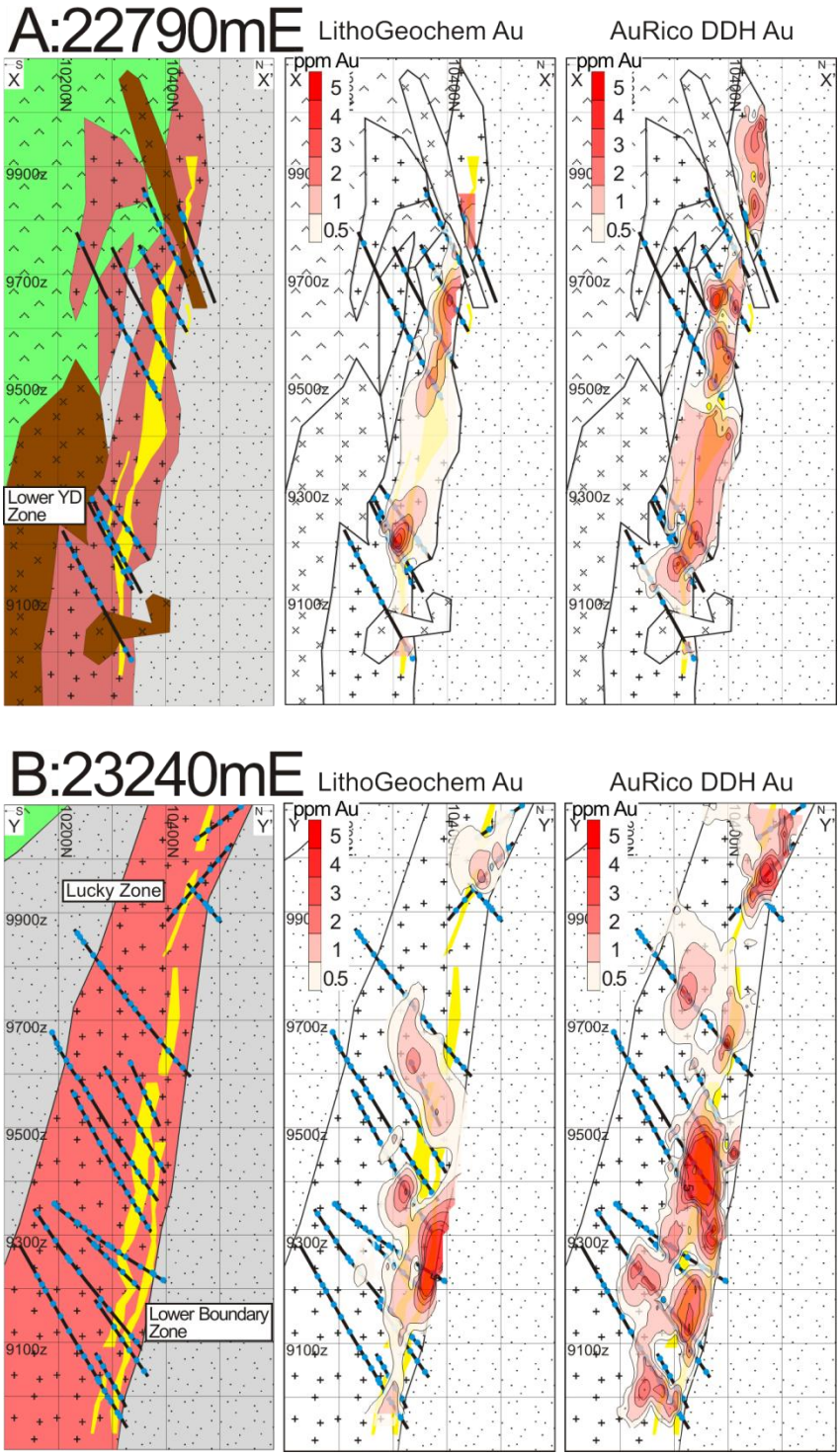

Figure 2.20: Gold contours along two N-S cross sections at Young-Davidson, complimentary to Figure 2.19. The ore trace is shown in yellow on all figures. LithoGeochem Au section represents contoured gold values from the analyses of relatively vein-free samples obtained in this study. AuRico DDH Au cross section represents contoured gold values from DDH analyses from the AuRico database. A) 22790 mE intersecting LYDZ mineralization. B) 23240 mE intersecting LZ and LBZ mineralization.

is strong correlation between Ba, K_2O, S and zones of gold mineralization (Figure 2.19B). By contrast, at the top of Figure 2.19B in the LZ, there is poor correlation between Ba, K_2O, S and the zone of mineralization. Therefore the LZ is potentially host to mineralization that is different from what is present in the LBZ or the LYDZ. It is also worth noting that the data density for the LZ is significantly less than what is available in the LBZ and LYDZ (i.e., 3 drill holes for LZ, 11 for LBZ and 9 for LYDZ). The spatial relationships between zones presented in Figure 2.19 are also consistent with data presented in Figure 2.18C, D, E and F where samples from the LZ are less enriched in S and K_2O than samples from all other zones. The relatively strong spatial correlation of Ba with K_2O and the ore trace in the LYDZ and the LBZ is interesting. At the Macassa mine in Kirkland Lake, Tesfaye (1992) found that Ba was uniformly distributed with K-feldspar alteration in the syenite groundmass, and was generally unrelated to gold mineralization. At Young-Davidson, Ba shows moderate correlation with K_2O in whole rock analyses. Very fine barite grains have been identified in carbonate ± K-feldspar alteration in the groundmass of mineralized syenite samples and interestingly, very fine-grained barite has also been found with gold in V_2 pyrite hosted mineralization (Figure 2.15B and E) indicating at least some Ba was present in the mineralizing fluids.

2.6.2 Volcanic Geochemistry

Representative geochemical analyses of least-altered mafic volcanic rock are tabulated in Table 2.1, altered and mineralized volcanic rocks in Table 2.2, and a complete dataset in Appendix D. Based on geochemical analyses and carbonate staining of thin section blocks, least-altered volcanic rocks generally contain weak to moderate chlorite-carbonate alteration that is associated with thin iron-carbonate and carbonate stringers and minor early pyrite. Fresh volcanic samples generally contain 6 - 8 wt% LOI, 4.63 - 5.19 wt% CaO, 16.59 - 16.63 wt% Fe_2O_{3t}, 0.1 - 0.7 wt% K_2O and generally < 0.15 wt% S. The slope of the chondrite normalized REE line shown in Figure 2.18A is relatively flat and is consistent with a MORB affinity. Fresh volcanic rocks are enriched in REE's relative to the mineralized counterparts; a result of the mass gain, determined by mass balance calculations presented in the following section. Mineralization in volcanic rocks correlates best with pyrite, albite and iron-carbonate alteration. The strong pyrite association is similar to what is observed in the syenite, however, in general mineralization in volcanic rocks occurs in small sheared intersections with intense alteration, commonly < 10 m in width.

Table 2.1: Representative geochemical analyses of selected fresh host rocks. Analyses at lower detection limit are indicated with 'ldl'

		Fresh Syenite							Fresh Volcanic		
SampleID	**Det***	800901	800902	800985	803310	803341	803343	803356	800916	800920	800924
Al_2O_3	**0.01 %**	14.14	14.12	14.77	13.9	13.62	13.55	16.73	13.14	11.75	12.05
CaO	**0.01 %**	4.3	4.42	2.95	3.84	3.62	6.72	2.76	4.63	5.19	6.03
$Fe_2O_{3(T)}$	**0.01 %**	4.59	4.68	3.74	3.7	4.59	4.6	4.31	16.59	16.63	15.53
K_2O	**0.01 %**	5.82	5.86	7.4	4.91	5.38	5.8	8.05	0.1	0.7	0.92
LOI	**%**	3.51	5.84	4.22	5.42	2.84	5.72	1.7	5.95	7.85	10.7
MgO	**0.01 %**	2.13	2.73	1.53	1.85	3.23	2.21	2.03	4.81	2.2	5.12
MnO	**0.001 %**	0.086	0.101	0.066	0.091	0.086	0.107	0.09	0.254	0.265	0.169
Na_2O	**0.01 %**	4.43	4.33	4.03	4.76	4.38	3.37	3.65	3.16	2.62	2.57
P_2O_5	**0.01 %**	0.29	0.33	0.18	0.21	0.33	0.36	0.29	0.16	0.27	0.16
S	**0.01 %**	0.12	0.08	0.15	0.1	0.22	0.18	0.1	0.15	0.15	0.12
SiO_2	**0.01 %**	59.54	57.59	61.38	61.36	59.25	58.04	58.89	48.47	50.22	43.89
TiO_2	**0.001 %**	0.407	0.385	0.289	0.329	0.439	0.461	0.443	1.629	1.508	1.507
Ag	**0.5**	1.9	1.3	1	0.8	1.4	1.2	2.9	0	1	0.5
As	**0.5**	8.2	6.5	2.9	2.2	4.3	3.7	2.4	0	18.4	12.1
Au	**0.002**	0.082	0.05	0.065	0.041	0.04	0.082	0.142	0.019	0.018	0.051
Ba	**3**	1510	2194	2225	1717	2953	2363	2340	38	113	101
Bi	**0.1**	3.8	0.6	0.5	1.7	1.1	1.2	1	0	0	0
Ce	**0.05**	136	125	91.9	98	156	164	162	25.4	39.5	19.4
Co	**1**	11	11	7	9	15	14	5	44	28	47
Cr	**5**	79	219	90	93	182	130	37	40	0	38
Cu	**10**	220	200	190	190	50	60	160	2	40	80
Dy	**0.01**	3.61	3.75	2.69	2.3	3.93	4.22	4.88	6.26	10.8	5.98
Er	**0.01**	1.87	1.79	1.43	1.13	1.72	1.81	2.42	3.85	6.53	3.59
Eu	**0.005**	2.2	2.31	1.45	1.6	2.81	3	3.06	1.68	2.28	1.23
Ga	**1**	21	21	21	20	21	21	24	18	21	18
Gd	**0.01**	6.33	6.34	4.13	4	7.47	7.77	8.31	5.22	9.11	4.95
Hf	**0.1**	6.1	6.1	6.8	3.4	6.9	7	8.1	2.8	5.2	2.7
Ho	**0.01**	0.65	0.66	0.49	0.41	0.66	0.7	0.87	1.29	2.33	1.21
La	**0.05**	65.5	64.8	47.8	50.9	79.3	84.2	88.2	10.5	15.1	6.95
Lu	**0.002**	0.27	0.261	0.274	0.162	0.23	0.237	0.35	0.661	1.2	0.628
Nb	**0.2**	9.2	10.6	9.6	5.5	11	11	13	5.1	8.6	4.1
Nd	**0.05**	50.4	53.4	34.5	38.5	69.2	71.2	68.1	14.4	25	13.1
Ni	**20**	20	50	20	30	80	70	5	40	5	40
Pb	**5**	37	35	22	25	35	42	68	0	0	0
Pr	**0.01**	13.3	14.1	9.66	10.6	18.4	19	18.4	3.18	5.05	2.52
Rb	**1**	154	140	160	109	159	129	142	2	21	29
Sb	**0.2**	1.9	2.2	3.3	1.6	1.7	1.6	1.7	1.1	1.3	1.1
Sc	**0.1**	8.3	9.1	5.7	6.9	9	8.2	7.8	38	32.6	38.3
Sm	**0.01**	8.96	9.48	5.81	6.35	11.9	12.5	12	4.54	7.31	3.89
Sr	**2**	1080	1165	1723	1246	2248	1724	909	59	55	95
Ta	**0.01**	0.51	0.53	0.53	0.29	0.62	0.6	0.61	0.28	0.5	0.27
Tb	**0.01**	0.83	0.81	0.53	0.47	0.89	0.96	1.04	0.94	1.74	0.91
Th	**0.05**	16.5	23.6	24.8	8.27	19.9	20.5	25.4	0.84	1.17	0.88
Ti	**7**	4070	3850	2890	3290	4390	4610	4430	16290	15080	15070
Tl	**0.05**	1.07	1	1.01	0.86	1.26	0.89	1.17	0	0.14	0.18
Tm	**0.005**	0.249	0.254	0.223	0.158	0.239	0.243	0.351	0.616	1.02	0.563
U	**0.01**	4.77	7.53	4.63	3.26	6.74	6.29	8.33	0.19	0.34	0.21
V	**5**	88	101	88	72	82	84	86	354	33	327
W	**0.5**	0.5	13.6	10.5	2.2	0.8	2.9	9.7	0	1.2	3.4
Y	**0.5**	18.9	20	15.3	12.6	19.4	20.4	26.4	36	64	34.7
Yb	**0.01**	1.84	1.68	1.53	1.04	1.48	1.53	2.22	3.9	6.93	3.83
Zn	**30**	60	90	50	60	90	90	100	110	170	120
Zr	**1**	284	281	311	153	304	307	409	114	218	113

***ppm unless specified**

Table 2.2: Representative geochemical analyses of selected altered host rocks. Analyses at lower detection limit are indicated with 'ldl'

		Altered Syenite							Altered Volcanic		
SampleID	**Det***	800976	803338	803363	800907	803370	803389	800940	800918	800923	800927
Al_2O_3	**0.01 %**	15.99	16.09	16.63	13.66	14.27	15.62	12.8	11.72	10.62	12.21
CaO	**0.01 %**	2.47	3.06	3.47	7.32	3.71	4.77	4.86	14.59	10.16	7.18
$Fe_2O_{3(T)}$	**0.01 %**	3.44	4.26	4.33	3.68	2.98	5.18	3.43	16.71	12.93	14.8
K_2O	**0.01 %**	9.13	8.55	7.59	9.19	7.51	8.69	5.85	2.02	1.59	1.93
LOI	**%**	4.2	4.93	3.94	7.66	5.19	4.93	6.86	15.14	16.03	15.28
MgO	**0.01 %**	0.92	1.39	1.21	1.68	1.45	1.53	2.3	1.39	3.54	3
MnO	**0.001 %**	0.064	0.099	0.068	0.105	0.097	0.076	0.094	0.159	0.218	0.191
Na_2O	**0.01 %**	3.36	3.57	3.03	2.22	3.16	2.76	3.67	0.37	3.57	3.75
P_2O_5	**0.01 %**	0.16	0.27	0.28	0.24	0.25	0.39	0.18	0.09	0.09	0.13
S	**0.01 %**	1.78	1.82	0.32	1.2	1.59	2.35	0.16	2.11	4.19	6.53
SiO_2	**0.01 %**	60.11	57.38	57.59	52.06	60.53	55.2	58.69	35.13	38.88	38.68
TiO_2	**0.001 %**	0.319	0.373	0.422	0.457	0.227	0.485	0.379	1.12	0.959	1.457
Ag	**0.5**	2	3.5	7.1	2.2	2.3	2.2	1.7	0	0	0.8
As	**0.5**	2.7	4.3	0	3.7	3.6	7.6	3	8.7	4.8	30.5
Au	**0.002**	1.54	3.61	8.18	0.904	1.64	2.72	0.693	0.396	4.68	9.33
Ba	**3**	2518	2900	2570	1299	2081	2610	1119	87	204	136
Bi	**0.1**	0.5	0.6	5.3	1.2	0.5	0.1	5.4	0	0	0
Ce	**0.05**	78.1	146	174	193	156	189	124	14.9	11.2	16.2
Co	**1**	7	8	8	15	6	9	11	61	42	49
Cr	**5**	24	33	31	163	15	34	73	14	32	25
Cu	**10**	20	70	110	190	60	80	510	230	100	120
Dy	**0.01**	2.6	3.76	4.89	3.85	3.85	4.77	3.25	4.34	3.79	5.07
Er	**0.01**	1.25	1.73	2.47	1.96	1.81	2.11	1.69	2.74	2.27	3.12
Eu	**0.005**	1.47	2.58	2.9	2.7	2.4	3.23	1.92	0.997	0.832	1.15
Ga	**1**	22	20	25	20	21	21	18	19	17	18
Gd	**0.01**	4.13	6.49	8.38	7.57	6.86	9.29	5.27	3.68	2.75	4.15
Hf	**0.1**	8.2	4.5	8.5	5.7	7.5	6.1	4.9	2.1	1.7	2.5
Ho	**0.01**	0.44	0.64	0.89	0.68	0.65	0.83	0.61	0.91	0.81	1.07
La	**0.05**	35.9	77	91.2	119	79.6	86.8	59.7	5.49	4.12	5.6
Lu	**0.002**	0.193	0.248	0.349	0.318	0.267	0.286	0.261	0.512	0.42	0.572
Nb	**0.2**	9.9	6.8	13.3	12.7	10.5	10	8	3.1	2.5	3.8
Nd	**0.05**	35.2	62.4	65.4	63.3	57.7	75.3	49.5	9.95	7.64	10.8
Ni	**20**	5	5	5	30	5	5	30	40	20	30
Pb	**5**	14	31	50	64	35	38	27	0	0	0
Pr	**0.01**	9.26	16.6	17.3	17.6	15.7	19.6	13.7	2.01	1.43	2.16
Rb	**1**	158	142	217	181	123	140	132	74	58	61
Sb	**0.2**	2.5	2	2.5	2.7	1.8	1.5	5.3	2.8	2	1.4
Sc	**0.1**	3.4	5.7	6.7	9.9	4.5	7.2	7.8	40.9	34.6	36.2
Sm	**0.01**	6.15	10.4	11.3	10.2	9.66	13.6	8.07	3.01	2.26	3.36
Sr	**2**	927	1270	1089	514	1578	593	439	137	188	131
Ta	**0.01**	0.67	0.4	0.66	0.54	0.58	0.55	0.41	0.19	0.14	0.23
Tb	**0.01**	0.53	0.81	1.03	0.88	0.9	1.11	0.68	0.69	0.58	0.81
Th	**0.05**	20.9	12.3	25.4	23.2	36.5	14.7	16.2	0.43	0.33	0.5
Ti	**7**	3190	3730	4220	4570	2270	4850	3790	11200	9590	14570
Tl	**0.05**	0.87	1.05	1.42	1.09	0.66	1.02	0.93	0.52	0.27	0.39
Tm	**0.005**	0.187	0.243	0.366	0.273	0.254	0.275	0.256	0.442	0.363	0.513
U	**0.01**	3.33	4.11	5.97	11	3.09	2.64	5.14	0.19	0.11	0.16
V	**5**	32	79	94	67	26	84	80	346	279	349
W	**0.5**	15.6	19.4	9.5	34	474	40.9	16.5	27.4	73.8	20.7
Y	**0.5**	13.4	19.1	24.6	19.6	19.1	22.3	18.4	27.5	22.3	30.4
Yb	**0.01**	1.21	1.56	2.44	1.88	1.66	1.86	1.68	3.03	2.47	3.43
Zn	**30**	30	50	50	90	40	60	60	120	50	30
Zr	**1**	413	203	401	263	333	298	216	83	71	100

***ppm unless specified**

2.7 Mass Balance

Mass balance calculations have been performed using the Isochon method of Grant (1986) and the method of Maclean (1990) to compare geochemistry of least-altered samples to the mineralized equivalents. Least-altered syenites have been identified based on hand samples, petrography and geochemistry. True unaltered syenite has not been observed at Young-Davidson; instead, least-altered syenite is weakly carbonate-chlorite altered (3-6% LOI from carbonate) with chlorite, carbonate and magnetite in the groundmass. Least-altered syenite also contains minor feldspar alteration with feldspar overprint textures and trace sulfide mineralization. Least-altered volcanic samples are fine-grained chlorite-carbonate-bearing (6-8% LOI) greenschist grade metamorphosed basalts with minor veins and trace pyrite. The Isochon method is presented first; this calculation is best applied when the least-altered rock can be directly related to mineralized rock through petrography, stratigraphy and geochemistry (Grant, 1986). A limitation of the Isochon method when considering the polyphase Young-Davidson intrusion is identifying the least-altered equivalent of the mineralized sample; efforts must be made to compare the geochemistry of similar textured syenites since compositional variations in the precursor will affect the results of any geochemical calculations. The second method chosen to calculate elemental changes is from Maclean (1990) where a single element is considered immobile and used to calculate a mass factor that is then applied to the altered geochemistry. The least-altered samples and immobile elements must be well characterized for this method to produce good results, similar to the Isochon method. To calculate mass changes with the Isochon method, geochemical data from the altered sample (C_i) is scaled and then plotted against the identically-scaled geochemical data from the least-altered sample (C_o). The Isochon is defined by drawing a line of best fit through a group of immobile elements that passes through the origin. The slope of the Isochon corresponds to the mass factor, which is used to calculate the unit change (in g/100 g for major elements and $g/10^6$ g for trace elements) for each element in the rock, from the fresh to altered host rock.

The linear relationship between Ho and Y for all host lithologies at Young-Davidson is presented in Figure 2.18B. This diagram demonstrates that for all host lithologies at Young-Davidson, Ho and Y have either remained immobile during alteration or are geochemically coupled during alteration. Further binary REE vs REE plots for all REEs (presented in Appendix E) show linear trends with high correlation coefficients ($R^2 > 0.80$) indicating that for syenite REEs have remained relatively immobile and likely reside in a refractory phase. By contrast, for volcanic rocks, all REE's are immobile, with REE vs REE plots showing high correlation coefficients ($R^2 > 0.95$ for volcanic

rocks; Appendix E). The assumption of REE immobility is consistent with other studies on the alteration systematics for gold deposits from the Abitibi (McCuaig and Kerrich, 1998) and as Grant (2005) notes, identical C_i/C_o ratio's for a group of immobile elements used to define the isochon is sufficient for element immobility in the compared samples. Ropchan et al. (2002) also noted that REE transport requires formation of complexes with F, Cl, CO_3 or PO_4, and since gold transport was likely in the form of thio-sulfide complexes, the gold-bearing solution should not have interacted with REE's during alteration. Interestingly, van Middlesworth and Wood (1998) have noted many other possible ligands for the REEs in hydrothermal solutions, including SO_4^{2-}. Anhydrite has been identified barren vein sets, so SO_4^{2-} likely existed during some phase of hydrothermal alteration; however, it does not appear to have played any role in complexing REEs during gold-related alteration. This in turn suggests that the transport of gold was by relatively reduced fluids. The linear interelement trends presented here can be interpreted as element immobility during alteration, however, as Grant (1986) outlines, an Isochon is best defined when it is based on species that have different geochemical characteristics. Therefore, linear REE vs REE trends could also indicate coupled geochemical behavior of these elements during alteration or that all REEs reside in a single phase. The REEs have been chosen for the aforementioned reasons and will be used in the Grant (1986; 2005) method to define the Isochon, whereas Y (which commonly lies long the Isochon) and Ti are assumed immobile for the Maclean (1990) method (discussed below).

2.7.1 Syenite

Two examples of least-altered and mineralized syenite have been chosen for comparison. Since the Young-Davidson intrusion consists of different textural types of syenite, multiple precursor samples have been used in these calculations to check for consistency between different examples of syenite alteration; a complete set of Isochon diagrams are presented in Appendix E. The first least-altered sample, 800901, is a coarse biotite-chlorite-magnetite-bearing syenite from between the LZ and the LBZ on the central cross section (as labeled; Figure 2.5B), approximately 250 m above the gold-bearing alteration zone. This sample contains minor carbonate stringers and weak carbonate alteration (LOI = 3.51%) that is typical of least-altered syenite at Young-Davidson. Isochon diagrams showing the scaled major and trace element chemistry of sample 800901 and the potassic-hematite altered and mineralized sample 800976 are shown in Figure 2.21A1. The second least-altered sample, 803343, is a porphyritic to trachytic chlorite-magnetite-plagioclase-bearing syenite (LOI = 5.72%) located below

the mineralized zone in the LYDZ on the western cross section (as labeled; Figure 2.5A). Isochon diagrams showing the scaled major and trace element chemistry of sample 803343 and the mineralized sample 803342 are shown in Figure 2.21A2. The calculated mass changes for Grant mass balance calculations for each sample are presented in Figure 2.21B and Table 2.3. Notable enrichments have been highlighted. The mass changes for Maclean mass balance calculations assuming Y and Ti immobility are presented in Figure 2.22 and Table 2.4 and 2.5.

Gold-related syenite alteration is associated with gains of up to 133 g/100 g K_2O and up to 2100 g/100 g S, reflecting the tendency of gold to occur in pyrite-bearing potassic altered syenite. Other notable enrichments include: up to 140 g/10^6 g Ba and up to 4400 g/10^6 g W. Mineralized syenite also tends to be depleted in CaO, MgO, P_2O_5, Co, Cr, Ni, Sc, V and Zn. The SiO_2 increase in these samples can be attributed to V_2 and V_3 veins in vicinity of the altered sample and considering the gains in Al_2O_3, K_2O and Na_2O, development of feldspars in the altered sample. Enrichments of Na_2O for both syenite samples is interesting because in general gold-related alteration is characterized by untwinned feldspar replacement of albite-twinned feldspars, and development of fine-grained K-feldspar in the altered groundmass. Based upon a small set of SEM analyses, we have determined that the untwinned feldspar is K-feldspar but because we have not analyzed every occurrence of twinned-feldspar replacement, it is possible that in some cases the untwinned feldspar is Na-feldspar, since hydrothermal Na-feldspars may lack twinning (Nesse, 2000). Also, since white mica is seldom found in altered syenite the Na and K alteration is associated with feldspar alteration rather than development of micaceous minerals. The Na- and K-feldspar overprint of groundmass feldspars coupled with development of fine-grained feldspars and carbonate in vein haloes could account for the coupled enrichments of Na and K that occurs with syenite alteration, and would be consistent with the Na and K enrichments in gold-related volcanic alteration (discussed below). Interestingly there are relatively minor changes in the total iron content (Fe_2O_{3t}) of both examples of syenite alteration, suggesting that minor amounts of iron have been introduced to the syenite during gold-related alteration. This in turn suggests that the introduction of S to mineralized syenite was from iron-poor fluids that may have overprinted pre-existing iron-bearing minerals in the syenite to produce pyrite. The results from Maclean mass balance calculations for syenite alteration, presented in Figure 2.22 Table 2.4 and 2.5, are generally consistent with the Isochon method.

A

1) Syenite

C_o 800901 vs C_i 800976

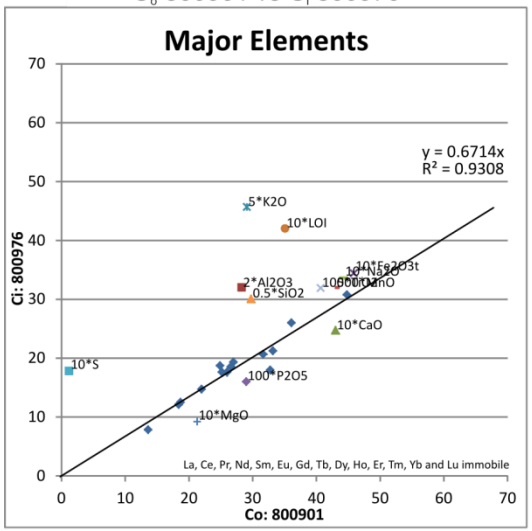

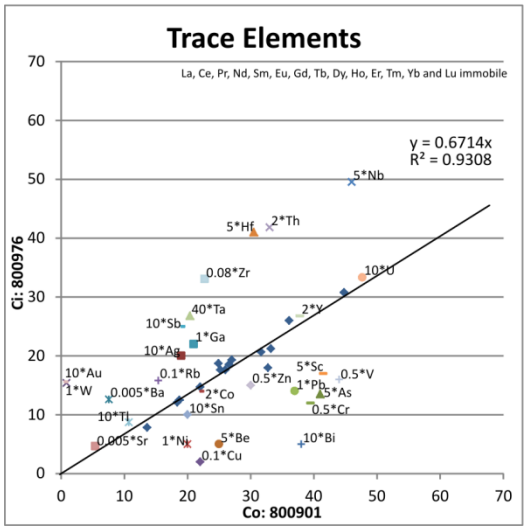

2) Porphyritic Syenite

C_o 803343 vs C_i 803342

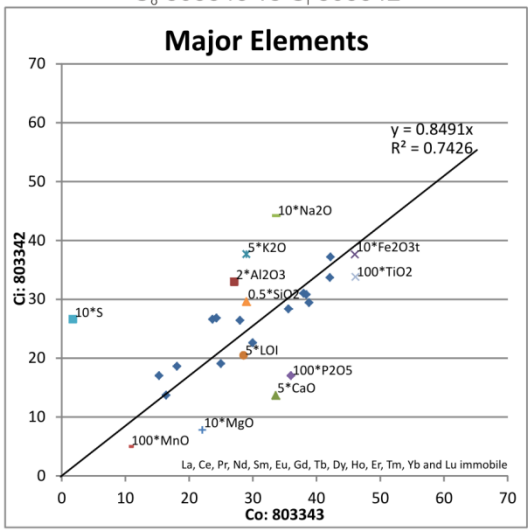

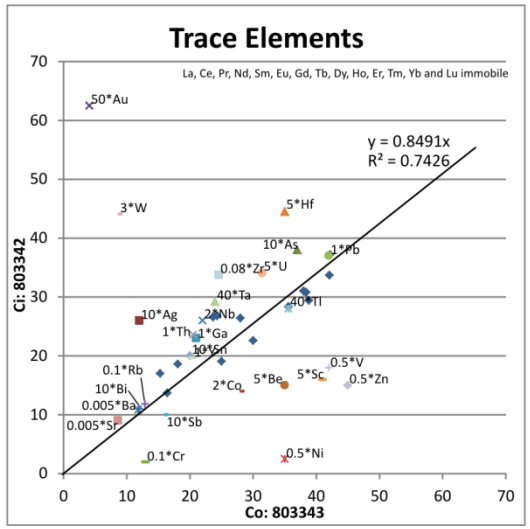

3) Volcanic:

C_o 800921 vs C_i 800923

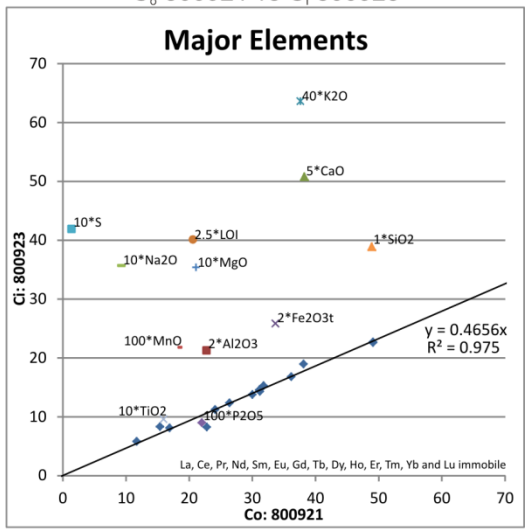

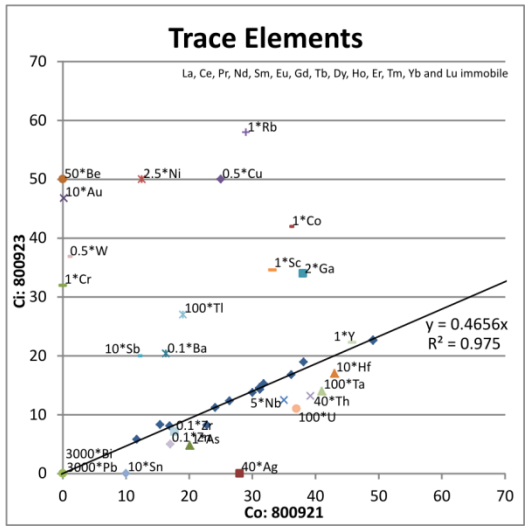

B

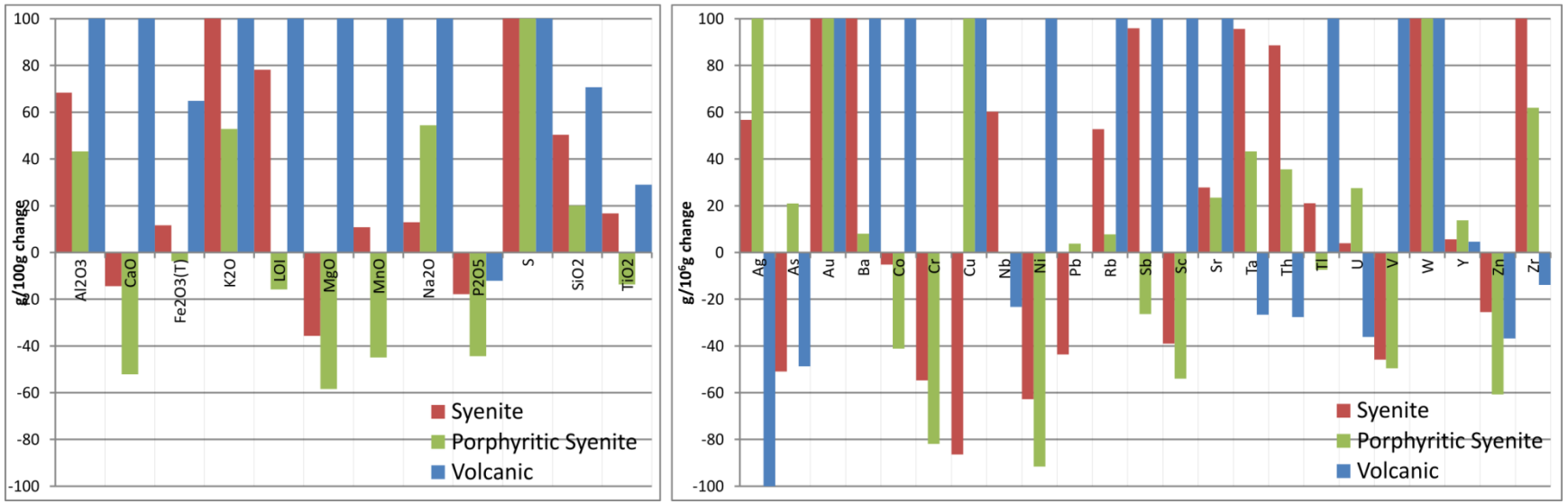

Figure 2.21: A) Example Isochon diagrams for mass balance between: 1) least-altered syenite 800901 and potassic-hematite altered and mineralized syenite 800976, 2) least-altered porphyritic syenite 803343 and potassic-hematite altered and mineralized syenite 803342 and 3) least-altered volcanic 800921 and albitized-iron-carbonate altered and mineralized volcanic rock 800923. C_o and C_i have been scaled by a factor labeled on each data point. The slope of the Isochon and the R^2 correlation coefficient are shown on each figure. Elements at or near detection limits have been omitted from these calculations.

B) Mass gains/losses in g/100 g for major elements and g/10^6 g for trace elements. Changes from 800901 to 800976 are shown in red, 803343 to 803342 are shown in green and volcanic rocks 800921 to 800923 are shown in blue. For volcanic alteration, all major elements except Al, Fe, P, Si and Ti show >100 g/100 g increases. All samples show gains of >2000 g/100 g in S. Gold-related alteration at Young-Davidson is associated with mass gains for the present samples.

Table 2.3: Tabulated mass balance data for Isochon mass balance samples presented in Figure 2.21A and B

	Syenite								Volcanic			
Element	**Co:800901**	**Ci:800976**	**ΔC**	**Δg/100g**	**Co:803343**	**Ci:803342**	**ΔC**	**Δg/100g**	**Co:800921**	**Ci:800923**	**ΔC**	**Δg/100g**
Al_2O_3	14.14	15.99	9.68	68.43	13.55	16.48	5.86	43.24	11.38	10.62	11.43	100.43
CaO	4.3	2.47	-0.62	-14.44	6.72	2.73	-3.50	-52.16	7.65	10.16	14.17	185.25
$Fe_2O_{3(T)}$	4.59	3.44	0.53	11.63	4.6	3.76	-0.17	-3.73	16.84	12.93	10.93	64.91
K_2O	5.82	9.13	7.78	**133.65**	5.8	7.53	3.07	**52.90**	0.94	1.59	2.47	**263.29**
LOI	3.51	4.2	2.75	78.22	5.72	4.09	-0.90	-15.79	8.25	16.03	26.18	317.32
MgO	2.13	0.92	-0.76	-35.67	2.21	0.78	-1.29	-58.43	2.11	3.54	5.49	260.34
MnO	0.086	0.064	0.01	10.84	0.107	0.05	-0.05	-44.97	0.183	0.218	0.29	155.85
Na_2O	4.43	3.36	0.57	12.97	3.37	4.42	1.84	54.47	0.93	3.57	6.74	724.47
P_2O_5	0.29	0.16	-0.05	-17.82	0.36	0.17	-0.16	-44.39	0.22	0.09	-0.03	-12.14
S	0.12	1.78	2.53	**2109.31**	0.18	2.66	2.95	**1640.40**	0.14	4.19	8.86	**6327.96**
SiO_2	59.54	60.11	29.99	50.37	58.04	59.16	11.63	20.04	48.91	38.88	34.60	70.73
TiO_2	0.407	0.319	0.07	16.74	0.461	0.338	-0.06	-13.65	1.596	0.959	0.46	29.05
Element	**800901**	**800976**	**ΔC**	**Δg/10^6g**	**803343**	**803342**	**ΔC**	**Δg/10^6g**	**800921**	**800923**	**ΔC**	**Δg/10^6g**
Ag	1.9	2	0.99	52.07	1.2	2.6	1.86	155.17	0.7	0	-0.70	-100.00
As	8.2	2.7	-4.30	-52.43	3.7	3.8	0.78	20.95	20.1	4.8	-9.79	-48.71
Au	0.082	1.54	2.14	**2613.16**	0.082	1.25	1.39	**1695.30**	0.014	4.68	10.04	**71696.76**
Ba	1510	2518	2127.68	140.91	2363	2168	190.29	8.05	163	204	275.14	168.80
Co	11	7	-0.89	-8.07	14	7	-5.76	-41.11	36	42	54.21	150.57
Cr	79	24	-44.33	-56.11	130	20	-106.45	-81.88	0	32	68.73	-
Cu	220	20	-191.11	-86.87	60	160	128.43	214.06	50	100	164.78	329.55
Nb	9.2	9.9	5.24	56.98	7.0	2.5	-0.05	-0.35	13	11	-1.63	-23.29
Ni	20	5	-12.78	-63.88	70	5	-64.11	-91.59	5	20	37.96	759.11
Pb	37	14	-16.77	-45.34	42	37	1.58	3.75	0	0	0.00	0.00
Rb	154	158	74.26	48.22	129	118	9.97	7.73	29	58	95.57	329.55
Sb	1.9	2.5	1.71	90.09	1.6	1	-0.42	-26.39	1.2	2	3.10	257.96
Sc	8.3	3.4	-3.39	-40.82	8.2	3.2	-4.43	-54.04	33.2	34.6	41.11	123.83
Sr	1080	927	259.21	24.00	1724	1808	405.31	23.51	56	188	347.78	621.04
Ta	0.51	0.67	0.46	89.79	0.6	0.73	0.26	43.29	0.41	0.14	-0.11	-26.66
Th	16.5	20.9	13.69	82.99	20.5	23.6	7.29	35.58	0.98	0.33	-0.27	-27.68
Tl	1.07	0.87	0.19	17.46	0.89	0.7	-0.07	-7.37	0.19	0.27	0.39	205.21
U	4.77	3.33	0.04	0.85	6.29	6.81	1.73	27.51	0.37	0.11	-0.13	-36.15
V	88	32	-41.77	-47.47	84	36	-41.60	-49.53	92	279	507.23	551.33
W	0.5	15.6	22.04	**4407.37**	2.9	14.7	14.41	**496.98**	1.8	73.8	156.71	**8705.84**
Y	18.9	13.4	0.46	2.43	20.4	19.7	2.80	13.73	45.8	22.3	2.10	4.57
Zn	60	30	-16.66	-27.77	90	30	-54.67	-60.74	170	50	-62.61	-36.83
Zr	284	413	312.65	110.09	307	422	190.00	61.89	177	71	-24.51	-13.85

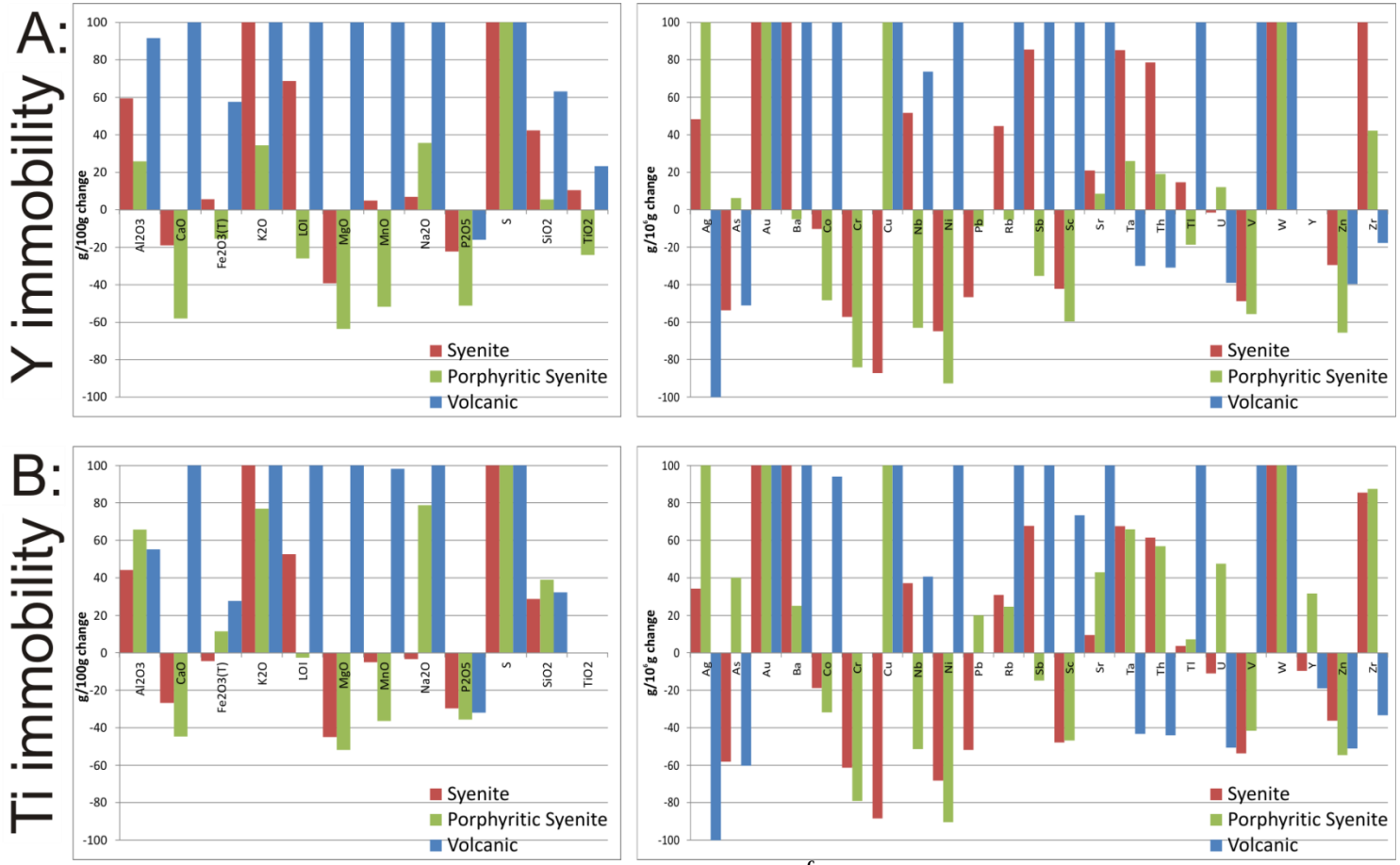

Figure 2.22: Maclean method mass gains/losses in g/100 g for major elements and g/10^6 g for trace elements. Changes from 800901 to 800976 are shown in red, 803343 to 803342 are shown in green and volcanic rocks 800921 to 800923 are shown in blue. Gold-related alteration at Young-Davidson is associated with mass gains for the present samples. Calculations using Maclean method are consistent with those from the Isochon method. A) Y immobility. All samples show gains of > 1400 g/100 g in S. For volcanic alteration, all major elements except Al, Fe, P, Si and Ti show >100 g/100 g increases. Results are tabulated in Table 2.4. B) Ti immobility. All samples show gains of > 1700 g/100 g in S. Volcanic alteration is associated with gains of > 100 g/100 g for all major elements except Al, Fe, P and Si. Calculations assuming Ti immobility are generally consistent with the results obtained using Y immobility, presented in part A. Results are tabulated in Table 2.5.

Table 2.4: Tabulated mass balance data for Maclean mass balance calculations assuming Y immobility with mass changes presented in Figure 2.22A

	Syenite								Volcanic			
Element	**Co:800901**	**Ci:800976**	**ΔC**	**Δg/100g**	**Co:803343**	**Ci:803342**	**ΔC**	**Δg/100g**	**Co:800921**	**Ci:800923**	**ΔC**	**Δg/100g**
Al_2O_3	14.14	15.99	22.55	59.50	13.55	16.48	17.07	25.95	11.38	10.62	21.81	91.67
CaO	4.3	2.47	3.48	-18.98	6.72	2.73	2.83	-57.93	7.65	10.16	20.87	172.77
$Fe_2O_{3(T)}$	4.59	3.44	4.85	5.71	4.6	3.76	3.89	-15.36	16.84	12.93	26.56	57.69
K_2O	5.82	9.13	12.88	**121.26**	5.8	7.53	7.80	**34.44**	0.94	1.59	3.27	**247.40**
LOI	3.51	4.2	5.92	68.77	5.72	4.09	4.24	-25.96	8.25	16.03	32.92	299.06
MgO	2.13	0.92	1.30	-39.08	2.21	0.78	0.81	-63.45	2.11	3.54	7.27	244.57
MnO	0.086	0.064	0.09	4.96	0.107	0.05	0.05	-51.61	0.183	0.218	0.45	144.66
Na_2O	4.43	3.36	4.74	6.98	3.37	4.42	4.58	35.82	0.93	3.57	7.33	688.40
P_2O_5	0.29	0.16	0.23	-22.18	0.36	0.17	0.18	-51.10	0.22	0.09	0.18	-15.98
S	0.12	1.78	2.51	**1992.16**	0.18	2.66	2.75	**1430.29**	0.14	4.19	8.61	**6046.76**
SiO_2	59.54	60.11	84.78	42.40	58.04	59.16	61.26	5.55	48.91	38.88	79.85	63.26
TiO_2	0.407	0.319	0.45	10.55	0.461	0.338	0.35	-24.08	1.596	0.959	1.97	23.41
Element	**800901**	**800976**	**ΔC**	**Δg/10^6g**	**803343**	**803342**	**ΔC**	**Δg/10^6g**	**800921**	**800923**	**ΔC**	**Δg/10^6g**
Ag	1.9	2	2.82	48.47	1.2	2.6	2.69	124.37	0.7	0	0.00	-100.00
As	8.2	2.7	3.81	-53.56	3.7	3.8	3.94	6.35	20.1	4.8	9.86	-50.95
Au	0.082	1.54	2.17	**2548.89**	0.082	1.25	1.29	**1478.56**	0.014	4.68	9.61	**68555.99**
Ba	1510	2518	3551.51	135.20	2363	2168	2245.04	-4.99	163	204	418.98	157.04
Co	11	7	9.87	-10.24	14	7	7.25	-48.22	36	42	86.26	139.61
Cr	79	24	33.85	-57.15	130	20	20.71	-84.07	0	32	65.72	0.00
Cu	220	20	28.21	-87.18	60	160	165.69	176.14	50	100	205.38	310.76
Nb	9.2	9.9	13.96	51.78	7.0	2.5	2.59	-63.02	13	11	22.59	73.78
Ni	20	5	7.05	-64.74	70	5	5.18	-92.60	5	20	41.08	721.52
Pb	37	14	19.75	-46.63	42	37	38.31	-8.77	0	0	0.00	0.00
Rb	154	158	222.85	44.71	129	118	122.19	-5.28	29	58	119.12	310.76
Sb	1.9	2.5	3.53	85.59	1.6	1	1.04	-35.28	1.2	2	4.11	242.30
Sc	8.3	3.4	4.80	-42.22	8.2	3.2	3.31	-59.59	33.2	34.6	71.06	114.04
Sr	1080	927	1307.49	21.06	1724	1808	1872.24	8.60	56	188	386.12	589.49
Ta	0.51	0.67	0.95	85.29	0.6	0.73	0.76	25.99	0.41	0.14	0.29	-29.87
Th	16.5	20.9	29.48	78.66	20.5	23.6	24.44	19.21	0.98	0.33	0.68	-30.84
Tl	1.07	0.87	1.23	14.68	0.89	0.7	0.72	-18.55	0.19	0.27	0.55	191.86
U	4.77	3.33	4.70	-1.53	6.29	6.81	7.05	12.11	0.37	0.11	0.23	-38.94
V	88	32	45.13	-48.71	84	36	37.28	-55.62	92	279	573.01	522.84
W	0.5	15.6	22.00	**4300.60**	2.9	14.7	15.22	**424.91**	1.8	73.8	151.57	**8320.63**
Y	18.9	13.4	18.90	0.00	20.4	19.7	20.40	0.00	45.8	22.3	45.80	0.00
Zn	60	30	42.31	-29.48	90	30	31.07	-65.48	170	50	102.69	-39.59
Zr	284	413	582.51	105.11	307	422	436.99	42.34	177	71	145.82	-17.62

Table 2.5: Tabulated mass balance data for Maclean mass balance calculations assuming Ti immobility with mass changes presented in Figure 2.22B

	Syenite								Volcanic			
Element	**Co:800901**	**Ci:800976**	**ΔC**	**Δg/100g**	**Co:803343**	**Ci:803342**	**ΔC**	**Δg/100g**	**Co:800921**	**Ci:800923**	**ΔC**	**Δg/100g**
Al_2O_3	14.14	15.99	20.40	44.28	13.55	16.48	22.48	65.88	11.38	10.62	17.67	55.31
CaO	4.3	2.47	3.15	-26.71	6.72	2.73	3.72	-44.59	7.65	10.16	16.91	121.03
$Fe_2O_{3(T)}$	4.59	3.44	4.39	-4.38	4.6	3.76	5.13	11.48	16.84	12.93	21.52	27.78
K_2O	5.82	9.13	11.65	**100.15**	5.8	7.53	10.27	**77.07**	0.94	1.59	2.65	**181.50**
LOI	3.51	4.2	5.36	52.67	5.72	4.09	5.58	-2.48	8.25	16.03	26.68	223.37
MgO	2.13	0.92	1.17	-44.89	2.21	0.78	1.06	-51.86	2.11	3.54	5.89	179.21
MnO	0.086	0.064	0.08	-5.05	0.107	0.05	0.07	-36.27	0.183	0.218	0.36	98.25
Na_2O	4.43	3.36	4.29	-3.23	3.37	4.42	6.03	78.89	0.93	3.57	5.94	538.85
P_2O_5	0.29	0.16	0.20	-29.61	0.36	0.17	0.23	-35.59	0.22	0.09	0.15	-31.92
S	0.12	1.78	2.27	**1792.53**	0.18	2.66	3.63	**1915.55**	0.14	4.19	6.97	**4880.81**
SiO_2	59.54	60.11	76.69	28.81	58.04	59.16	80.69	39.02	48.91	38.88	64.71	32.29
TiO_2	0.407	0.319	0.41	0.00	0.461	0.338	0.46	0.00	1.596	0.959	1.60	0.00
Element	**800901**	**800976**	**ΔC**	**Δg/10^6g**	**803343**	**803342**	**ΔC**	**Δg/10^6g**	**800921**	**800923**	**ΔC**	**Δg/10^6g**
Ag	1.9	2	2.55	34.30	1.2	2.6	3.55	195.51	0.7	0	0.00	-100.00
As	8.2	2.7	3.44	-57.99	3.7	3.8	5.18	40.08	20.1	4.8	7.99	-60.26
Au	0.082	1.54	1.96	**2296.13**	0.082	1.25	1.70	**1979.12**	0.014	4.68	7.79	**55532.95**
Ba	1510	2518	3212.62	112.76	2363	2168	2956.95	25.14	163	204	339.50	108.28
Co	11	7	8.93	-18.81	14	7	9.55	-31.80	36	42	69.90	94.16
Cr	79	24	30.62	-61.24	130	20	27.28	-79.02	0	32	53.26	0.00
Cu	220	20	25.52	-88.40	60	160	218.22	263.71	50	100	166.42	232.85
Nb	9.2	9.9	12.63	37.29	7.0	2.5	3.41	-51.29	13	11	18.31	40.82
Ni	20	5	6.38	-68.10	70	5	6.82	-90.26	5	20	33.28	565.69
Pb	37	14	17.86	-51.72	42	37	50.46	20.15	0	0	0.00	0.00
Rb	154	158	201.59	30.90	129	118	160.94	24.76	29	58	96.53	232.85
Sb	1.9	2.5	3.19	67.88	1.6	1	1.36	-14.76	1.2	2	3.33	177.37
Sc	8.3	3.4	4.34	-47.74	8.2	3.2	4.36	-46.77	33.2	34.6	57.58	73.44
Sr	1080	927	1182.72	9.51	1724	1808	2465.94	43.04	56	188	312.88	458.71
Ta	0.51	0.67	0.85	67.61	0.6	0.73	1.00	65.94	0.41	0.14	0.23	-43.17
Th	16.5	20.9	26.67	61.61	20.5	23.6	32.19	57.02	0.98	0.33	0.55	-43.96
Tl	1.07	0.87	1.11	3.74	0.89	0.7	0.95	7.27	0.19	0.27	0.45	136.50
U	4.77	3.33	4.25	-10.93	6.29	6.81	9.29	47.67	0.37	0.11	0.18	-50.52
V	88	32	40.83	-53.61	84	36	49.10	-41.55	92	279	464.32	404.70
W	0.5	15.6	19.90	**3880.69**	2.9	14.7	20.05	**591.36**	1.8	73.8	122.82	**6723.36**
Y	18.9	13.4	17.10	-9.54	20.4	19.7	26.87	31.71	45.8	22.3	37.11	-18.97
Zn	60	30	38.28	-36.21	90	30	40.92	-54.54	170	50	83.21	-51.05
Zr	284	413	526.93	85.54	307	422	575.57	87.48	177	71	118.16	-33.24

2.7.2 Volcanic

The least-altered volcanic sample 800921 is a chlorite-carbonate-quartz ± feldspar bearing greenschist-grade metamorphosed basalt that is compared with the albitized, iron-carbonatized and pyritized volcanic sample 800923. Least-altered mineralogy consists of very fine-grained foliated chlorite, quartz and minor feldspar with minor deformed quartz ± carbonate lenses. Trace amounts of early pyrite, abundant fine-grained rutile and magnetite are also found in the least-altered sample. Results of the Isochon mass balance calculation are presented in Figure 2.21A3 and B and show that for volcanic rocks there is significant mass gain associated with gold-related volcanic alteration. There are also gains in nearly all major elements in the volcanic rocks with respect to the fresh sample. Gains in MgO can be attributed to development of abundant coarse grained iron-carbonate consisting of ankerite and potentially iron-dolomite. The chemical composition of carbonate minerals has not been evaluated in detail; therefore the proportion of Mg and Fe in these carbonates is not known. Based on XRD analyses from altered syenite (Naderi et al., 2012), the identified carbonate minerals are consistent with the dolomite group, and since they are iron-bearing (as shown from iron-carbonate staining) we can conclude that they potentially include ankerite and/or iron-dolomite. Therefore, considering the least-altered mineralogy, MgO, MnO and some portion of Fe_2O_{3t} from the least-altered rock have been enhanced in coarse-grained iron-carbonate that developed during gold-related alteration. Gains in MgO could also be influenced by late stage elongate zoned tourmaline grains that replace pyrite (e.g., Figure 2.11C and D). Lastly, minor amounts of late stage chloritization occurs along pyrite grain boundaries and as fine grains through the altered volcanic groundmass and could explain retention of some Mg (Figure 2.11). Addition of Na_2O, K_2O, Al_2O_3 and SiO_2 are attributed to development of coarse-grained Na-feldspars and muscovite with lesser amounts of fine-grained K-feldspar. Increases in Fe_2O_{3t} can be attributed to development of iron-carbonate (as indicated from carbonate staining) and, when considering the 6000 g/100 g gains of S in mineralized volcanic rocks, pyrite. Relatively large (> 60 g/100 g) gains of Fe_2O_{3t} in mineralized volcanic rocks contrasts with the modest Fe_2O_{3t} changes for mineralized syenite, and indicate that iron was introduced to the volcanic rocks during mineralization. Volcanic rocks also show significant increases in Ba, W, Co, Cu, Ni and V and depletion in Ag, As, Th and U. The results from Maclean mass balance calculations for volcanic rocks, presented in Figure 2.22 Table 2.4 and 2.5, are generally consistent with the Isochon method.

2.8 Discussion

The gold mineralization at Young-Davidson possesses characteristics that are similar to other syenite-hosted gold deposits and also similar to typical orogenic gold deposits from the southern Abitibi greenstone belt. Iron-carbonate and K-feldspar alteration in the Young-Davidson syenite is generally consistent with the typical syenite-hosted gold alteration styles outlined by Robert (2001). Robert (2001) further details zoned carbonate alteration that consists of carbonate at the periphery to Fe-carbonate in the mineralized zone. Based on the iron-carbonate stained samples in this study, all samples (including barren and mineralized) contain iron-bearing carbonates suggesting: that the zoning is absent, that we have not sufficiently sampled the periphery to mineralization or that iron-carbonates are ubiquitous and the carbonate alteration is generally pervasive. Iron-carbonate alteration is particularly well developed in mineralized volcanic host rocks. The deposit-wide correlation of K_2O with gold mineralization at Young-Davidson supports a porphyry model where potassic alteration is found in the core of the deposit with other alteration styles dominating at the periphery. However, as Dubé and Gosselin (2007) have noted, the mine-scale alteration styles at orogenic gold deposits are related to the composition of the host rocks, their competence and metamorphic grade and as McCuaig and Kerrich (1998) note, there is a large range in physicochemical compositions for fluids responsible for orogenic styles of mineralization. Volcanic rocks along strike of the CLLDZ also contain alkali-enriched alteration styles characterized by development of albite, muscovite and K-feldspar. Mineralization in volcanic rocks is best developed in narrow intensely deformed and pervasively altered shear zones containing abundant pyrite; consistent with Tisdale volcanic-hosted alteration and mineralization that is spatially associated with the CLLDZ and syenite intrusions in the Kirkland Lake area (e.g., Anoki deposit; Ispolatov et al., 2008). The large disseminated style of mineralization in the syenite can therefore be explained by a competency contrast where hydrothermal fluids were dispersed in veins and porosity generated from deformation of the syenite whereas in the volcanic rocks fluids were localized along small shear zones. Therefore, zones of pervasive of potassic-hematite alteration in the syenite and alteration surrounding sediment- and syenite-hosted veins could have resulted from a typical metamorphic fluids associated with the deformation zone. Similarly, the alkali enrichments observed in volcanic rocks could be a result of typical orogenic fluids, or could be related to the nearby intrusions.

In a structural context, gold mineralization in the Young-Davidson syenite is associated with veinlets and veins that developed during the D_2 deformation and has potentially been remobilized into

late-D_2 V_3 quartz-carbonate veins. The earliest styles of mineralization are interpreted to be V_1, V_2 or disseminated styles of mineralization. These mineralization styles are commonly dominated by type 1 pyrite-associated gold, where inclusions of gold occur in pyrite grains that host inclusions of hematite and magnetite. Gold may occur as microscopic native gold grains in the inclusion-rich zones, or as part of a single poly-phase mineral inclusion consisting of some combination of hematite, magnetite, chalcopyrite and gold. Gold is also present along fractures in the earlier styles of mineralization, suggesting that there has been some remobilization from inclusion stages of gold, or at least that sulfidation is not the only control for gold precipitation. In the later veins, gold correlates with galena, chalcopyrite and tellurides, and occurs as free gold or along fractures in type 2 pyrite. In addition, the type 2 pyrite grains found in these later veins are characteristically void of hematite-magnetite inclusions, suggesting that the hematite-magnetite bearing pyrite grains in V_1, V_2 and disseminated pyrite have undergone either different precipitation mechanisms, or have been influenced by different fluids after their deposition. Based on the structural work by Zhang et al. (2012), we can conclude that each vein has formed with influence from regional structural events. Therefore, although syenite alteration styles and mineralogy of the early veins support a magmatic-hydrothermal model the observed textures and vein relationships suggest that the magmatic fluid was externally derived, and has potentially mixed with typical metamorphic fluids. If the earliest mineralization style is as inclusions in disseminated pyrite, V_1 and V_2 veins, then deformation and later hydrothermal fluids remobilized gold into V_3 styles of mineralization.

The hematite-gold relationship at Archean syenite-associated deposits has long been questioned (Hattori and Cameron, 1986; Cameron and Hattori, 1987; Neumayr et al., 2008). Some exploration geologists have noted the correlation between gold and hematite and have used this as a successful exploration tool (Cameron and Hattori, 1987 and ref. therein) whereas other researchers have determined that the gold-hematite (-K-feldspar) correlation is likely from rheological contrasts with the competent intrusions that also happen to contain hematite (Tesfaye, 1992). Feldspar overprinting textures are observed even in fresh rocks where the overprinting feldspar has incorporated fine-grained hematite mineral inclusions; this texture is interpreted as sub-solidus re-equilibration event from fluid infiltration in weakly altered felsic intrusions (Plümper and Putnis, 2009). Therefore the feldspar overprinting textures observed in phenocrysts and coarse-grained feldspars at Young-Davidson is consistent with an origin as a primary alteration that is related to emplacement of the syenite and feldspar re-equilibration during cooling. Since the deposit wide correlation of gold and

potassic-hematite-pyrite alteration is so consistent, it is likely that although this alteration style is magmatic, the feldspar replacement textures were enhanced during gold-related alteration. Similarly, ore zones consist of coarse-grained alkali feldspars in a fine-grained groundmass of iron-carbonate, K-feldspar, hematite and pyrite. Fine-grained hematite occurs as dustings in carbonate or feldspar grains (similar to the dusting in larger feldspars) in the altered groundmass, or as mineral inclusions in pyrite or as 'free' specular hematite associated with the carbonate.

Many examples of pyrite grains with zones of oxide minerals that lack crystallographic orientation are observed, and can be interpreted in 2 ways: 1) poikiolitic pyrite grains have formed from sulfidation of earlier oxides and hematite-magnetite grains are preserved as inclusions in the overprinting pyrite; or 2) pyrite grains developed with the magmatic-hydrothermal system, and have been dissolved by oxidizing fluids, which left residual hematite-magnetite grains with irregular orientations and distributions in the pyrite. Disseminated pyrite textures commonly contain evidence for pyrite overgrowth of Fe-oxide minerals since the inclusions are preserved in inclusion rich zones, surrounded by inclusion poor pyrite. Conversely, oxide-inclusion textures from type 1 pyrite grains in V_2 veins suggest some component of pyrite dissolution; inclusion patterns are highly irregular and the pyrite contains evidence of dissolution (e.g., Figure 2.16D). Similarly, the absence of oxides in type 2 pyrite associated mineralization suggests different pyrite-precipitation mechanisms. Therefore at Young-Davidson, there is evidence for repetitive cycles of sulfidation and pyrite dissolution such that pyrite has been deposited (potentially incorporating primary oxide grains) and then has subsequently been deformed and corroded, and then also potentially overprinted by further pyritization.

The controls of gold mineralization at a wide variety of deposits are typically changes in fO_2, fS_2, pH and temperature (Gibert et al., 1998). The experimental conditions used by Gibert et al. (1998) are similar to the mineral assemblages at Young-Davidson, and therefore the dominant complex determined experimentally for each temperature range and fluid composition can be semi-quantitatively applied to the mineralization at Young-Davidson. For hydrothermal solutions buffered by pyrite, pyrrhotite, magnetite, hematite, quartz, K-feldspar and muscovite, the dominant gold-complex for temperatures 250 ºC to 400 ºC and P = 500 bars is $AuHS^0$ whereas $AuHS_2^-$ is dominant for pH above 5.5 (Gibert et al., 1998; Stefánsson and Seward, 2004). The chloride species $AuCl_2^-$ is only found to be important in hydrothermal brines poor of H_2S at temperatures below 350 ºC; however, above 400 ºC the chloride complex is dominant even in sulfide-bearing hydrothermal fluids (Gibert et al., 1998; Stefánsson and Seward, 2003). Since the presence of tartan twinned K-feldspars

suggests that V_1 through V_3 veins formed at > 300 ºC and gold is dominantly associated with pyrite, transport of gold at Young-Davidson was likely dominated by the thio-sulfide complex, but also potentially influenced from the chloride complex. Therefore, the gold mineralization type 1 pyrite that contains abundant oxide inclusions and gold (in V_1, V_2 and disseminated styles) could have resulted from destabilization of the thio-sulfide complex during sulfidation of the wall rock. The small addition of iron to the syenite during alteration compared with the large gains in S generally supports pyritization as a depositional mechanism. Conversely, in V_3 veins, where gold is more associated with tellurides, galena and chalcopyrite, transport was likely from the chloride complex and gold precipitation occurred by other means.

Cooling is often cited as an improbable control for gold mineralization in Archean lode gold deposits because strong temperature gradients do not exist at the scale of a single deposit (McCuaig and Kerrich, 1998). Similarly, it can often be shown that changes in fO_2, fS_2 and pH from fluid interaction with wall rocks are more likely the main controls for gold precipitation at orogenic gold deposits. However, in a magmatic-metamorphic system, hot fluids derived from an underlying magma would cool upon intersection with a relatively low temperature metamorphic fluid. As Williams-Jones (2009) notes, a decrease of 50 ˚C in a hydrothermal fluid with $AuCl_2^-$ dominating in the temperature range 500 ˚C to 300 ˚C will cause most of the gold to precipitate. In addition, mixing oxidized magmatic-hydrothermal fluids with reduced metamorphic fluids would cause oxidation of sulfide and reduction of sulfate, the net effect depending on the relative abundance of each fluid. If a metamorphic fluid dominates and there is sufficient H_2S in solution after the initial decrease in temperature and oxidation, the solubility of gold may increase due to increased stability of the bisulfide complex (Williams-Jones et al., 2009). Typical metamorphic fluids can range in temperature from 200 ˚C to 420 ˚C depending on the local conditions (McCuaig and Kerrich, 1998). Since a fluid exsolved from underlying magmas would be at higher temperatures than the metamorphic counterparts, fluid mixing may have invoked cooling to precipitate gold from solution. Cooling would also have precipitated pyrite, and this mechanism could account for disseminated styles of mineralization with pervasive alteration. These observations require magmatic-hydrothermal activity overlapped with introduction of metamorphic fluids from the CLLDZ. Multiple intrusive phases of syenite at Young-Davidson generally support long-lived magmatic-hydrothermal activity in the area, and the likely source of oxidized magmatic fluids is a deeper, potentially larger magma chamber.

2.9 Conclusions

Gold mineralization at Young-Davidson shows strong correlation with pyrite, veining and potassic-hematite alteration. The characteristics of the mineralization and geochemistry presented in this chapter suggest that the mineralization at Young-Davidson has been influenced by the CLLDZ, but also possesses many characteristics that are consistent with the syenite-associated model of formation. The multi-host nature of mineralization suggests that the CLLDZ has in part influenced the mineralization at Young-Davidson. Therefore the proposed formational model is of a mixed magmatic-metamorphic hydrothermal origin where alteration styles and mineralizing fluids possess characteristics of both magmatic and metamorphic fluids. There also appears to have been repetitive mineralizing events at Young-Davidson such that there are different temporal and textural styles of mineralization throughout the deposit. Additional characterization of the physicochemical fluid conditions through stable isotopes, fluid inclusions and mineral-chemical methods may better help in understanding the origins of the mineralizing fluids.

Chapter 3

Mineral-chemical and sulfur isotopic constraints on genesis of the syenite-hosted gold mineralization at the Young-Davidson deposit, Matachewan, Ontario

3.1 Introduction

The syenite-hosted Young-Davidson gold deposit is located in the southern Abitibi greenstone belt of the Canadian Shield, Ontario, Canada. This portion of the southern Abitibi is home to several well characterized mafic-hosted shear-related gold deposits, commonly named quartz-carbonate vein deposits, orogenic, mesothermal and/or lode gold deposits. These deposits are hosted by a variety of lithologies and are spatially related to Timiskaming sedimentary rocks, felsic intrusions and regional scale deformation zones such as the Porcupine-Destor deformation zone (PDDZ) and the Cadillac-Larder-Lake deformation zone (CLLDZ)(Figure 3.1)(Dubé and Gosselin, 2007). Intrusion-related gold-deposits from the Abitibi have been classified as a unique deposit type where mineralization is associated with emplacement of the felsic intrusions and pre-dates major structural development (Robert, 2001). Many quartz-carbonate vein deposits are associated with felsic intrusions, and the role of the intrusion in mineralization remains controversial. At some deposits gold is spatially related to intrusions but is dominantly hosted in veins within other rock types (e.g., Hollinger-McIntyre and Ross; Robert and Poulsen, 1997) whereas mineralization at other deposits is hosted mostly within the felsic intrusions and contains evidence for oxidizing mineralizing fluids, and mineralization styles that have been overprinted by regional structures (e.g., Upper-Beaver, Beattie and Young-Davidson; Robert and Poulsen, 1997). The role of intrusions in these deposits has been interpreted in two ways: 1) mineralization is localized in the intrusion during deformation because of favorable rheological and geochemical contrasts; or 2) gold is related to the magmatic-hydrothermal system associated with emplacement of the intrusion and has subsequently been overprinted by regional deformation (Robert, 2001). The overprint of mineralization by structural events, localization of gold dominantly in syenite, oxidized mineral assemblages and magmatic $\delta^{34}S$ signatures are commonly cited as evidence for a genetic relationship between the intrusions and gold (Sinclair, 1982; Cameron and Hattori, 1987; Robert and Poulsen, 1997; Robert, 2001).

The Young-Davidson gold deposit is dominantly hosted by coarse-grained porphyritic to trachytic syenite that intruded at or near the contact between Timiskaming meta-sedimentary rocks and Tisdale meta-volcanic rocks (hereafter referred to as sedimentary and volcanic rocks, respectively; Figure 3.2 and Figure 3.3). The Young-Davidson syenite and neighboring rocks are interpreted to lie along the western extension of the regional scale CLLDZ (Zhang et al., 2012) that affected similar rocks in the Kirkland Lake area (Ispolatov et al., 2008). The majority of the defined resource at Young-Davidson is hosted by syenite; however, gold is also concentrated in intensely altered and deformed volcanic and sedimentary rocks that host quartz and quartz-carbonate veins. Petrographic and structural analysis has shown that syenite-hosted gold mineralization is correlated to distinct vein sets

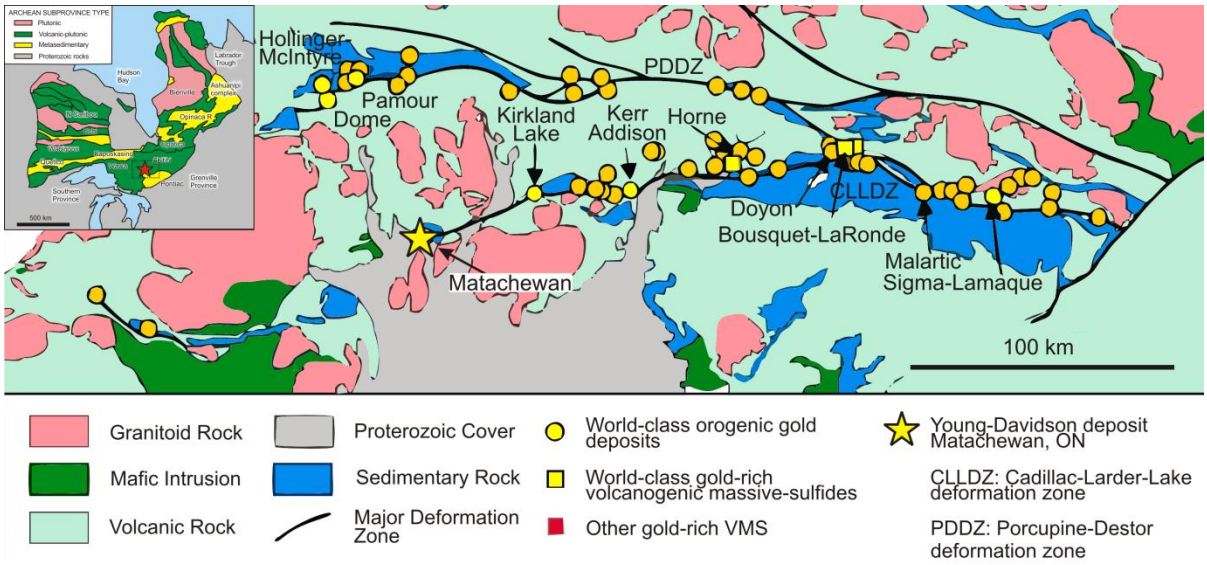

Figure 3.1: World class gold deposits in the southern Abitibi greenstone belt, Canada. (Modified from Dubé and Gosselin, 2007)

associated with movements along the CLLDZ during D_2 (Zhang et al., 2012; Chapter 2; Martin et al., in prep.). Lithogeochemical study of the syenite-hosted Young-Davidson deposit (Chapter 2; Martin et al., in prep.) has shown that gold mineralization is associated with potassic-hematite-pyrite altered syenite that is crosscut by quartz-pyrite and quartz-carbonate veins, and has been enriched in S, K_2O, Ba and W. Volcanic-hosted mineralization at Young-Davidson is associated with strongly deformed and intensely albite-iron-carbonate-pyrite altered basalts that are crosscut by quartz-iron-carbonate veins and characterized by strong enrichments in Na_2O, K_2O, S, Ba and W (Zhang et al., 2012; Chapter 2; Martin et al., in prep.). Gold mineralization in the Young-Davidson syenite is interpreted to contain alteration and mineralization characteristics that are consistent with intrusion-associated deposits and also with typical orogenic-gold deposits (Chapter 2; Martin et al., in prep.). In order to further evaluate the source of the mineralizing fluids, this study will characterize the mineral chemistry of rutile, pyrite and gold, and the sulfur isotopic composition of pyrite to place further constraints on the fluid source and depositional mechanisms for gold mineralization at the Young-Davidson deposit.

Pyrite is a common sulfide mineral in a range of hydrothermal mineral deposit types owing to its high stability under a wide range of physicochemical conditions. Studies have shown that gold mineralization at nearly all orogenic gold deposits from around the world (Canada, Australia) is in some part dependent on pyrite mineralization (e.g., McCuaig and Kerrich, 1998; Dubé and Gosselin, 2007). Pyrite is known to acquire unique geochemical signatures from the precipitating fluids; the resulting chemical differences can be explained by different physicochemical conditions or fluid

sources. The study of pyrite chemistry commonly consists of bulk analyses where pyrite grains are separated for sulfur isotopic and trace element analysis on a sample by sample basis; with best efforts to separate different stages of pyrite. Bulk pyrite analyses are currently the best way to evaluate $\Delta^{33}S$ and $\delta^{34}S$ simultaneously; these two values must be evaluated together in order to draw meaningful interpretation of fractionated sulfides (e.g., Hu et al., 2003 and ref. therein). An inherent problem with bulk pyrite analyses at hydrothermal ore deposits is that these methods cannot distinguish different hydrothermal phases of pyrite, even with the best separation techniques (e.g., Ho et al., 1995). Consequently unless one hydrothermal phase dominates the analyzed grain, the resulting chemical/isotopic signature will reflect some mixture of each phase. An ideal method of studying hydrothermal pyrite chemistry is to perform in situ analysis of the pyrite grains; however, such analyses are often time consuming, labor intensive and costly. Similarly, although methods for simultaneously acquiring $\Delta^{33}S$ and $\delta^{34}S$ from in situ analyses have been developed (Hu et al., 2003), they have not been widely applied in sulfur isotopic studies. Craig et al. (1998) demonstrated that chemical zoning of pyrite can be recognized through point and map analyses on a wavelength-dispersive electron-microprobe (EMP). These analyses have advantages over other elemental mapping methods (LA-ICP-MS, SEM and etching): 1) sample preparation is quick and straightforward; 2) analyses are non-destructive; 3) machine conditions may be modified as needed to reduce detection limits; 4) detection limits for common pyrite-substituting elements are adequate for most studies (i.e., < 100-400 ppm); and 5) rapid collection of high quality data at a relatively low cost. The main disadvantage of this method compared to LA-ICP-MS is that the suite of elements is restricted and detection limits are higher (i.e., ~10 ppm or less for LA-ICP-MS; Zhao et al., 2011). The gold mineralization at Young-Davidson is associated with variably textured pyrite grains with complex inclusion patterns. Consequently, a detailed study of the gold-associated pyrite grains at Young-Davidson was undertaken to determine the chemical characteristics of the gold-associated and gold-barren pyrite grains.

Rutile is stable over a large range of physicochemical conditions and is commonly the dominant Ti-bearing phase in many ore-related alteration zones (Zack et al., 2004). Substitution of Fe, Nb, Al, Ta, Sn, Cr, W and Sb for Ti in rutile is well documented whereas elevated levels of W and Sb in rutile has been correlated with vein-hosted gold mineralization in orogenic gold deposits (Rice et al., 1998; Clark and Williams-Jones, 2004; Scott and Radford, 2007; Dostal et al., 2009). Substitution of elements for Ti in rutile grains is still poorly understood; current research shows that it is dependent on fluid chemistry, temperature, pressure, the TiO_2 polymorph and fluid redox conditions (Rice et al.,

1998; Triebold et al., 2011). The incorporation of elements into rutile during hydrothermal alteration combined with relatively high stability under variable hydrothermal conditions makes it a good candidate for mineral-chemical studies. Clark and Williams-Jones (2004) and Scott and Radford (2007) analyzed rutile compositions from barren and ore-related host rocks at a variety of hydrothermal mineral deposits. For Archean Cu-Zn-(Au) VMS deposits from the Abitibi, Clark and Williams-Jones (2004) showed that rutile grains in VMS-related alteration zones are consistently enriched in Sn, and to a lesser extent Cu, W and Sb, compared to rutile in least-altered rocks. Similarly, for Archean mesothermal gold deposits from the Abitibi, rutile in gold-related alteration zones is enriched in W with lesser amounts of Sb and V compared to grains in least-altered rocks (Clark and Williams-Jones, 2004). Scott and Radford (2007) analyzed a number of rutile grains associated with barren, altered and gold-bearing host rocks at the Big Bell gold deposit in Western Australia, and observed that grains associated with gold mineralization in metamorphosed basalts were characteristically enriched in V, Fe, W and Sb. The main objective of the study by Clark and Williams-Jones (2004) was to characterize typical ore-associated rutile enrichments for a number of deposits in the Abitibi to assess the potential of rutile compositions as vectors towards mineralization. Thus, rutile from deposits where the controls on mineralization are more controversial can be analyzed and their chemistry can be compared with the data acquired by Clark and Williams-Jones (2004) to check for similarities. For example, Clark and Williams-Jones (2004) analyze rutile compositions at the Troilus Au-Cu deposit and the Montauban Au-Cu deposit, where each possesses multiple formational models based on contrasting mineralization and alteration characteristics. They determined that ore-associated rutile grains at the Troilus Au-Cu deposit contained elevated Sb and W; since Sb is atypical of Au-porphyry systems and W is common in mesothermal systems, the implications are that hydrothermal fluids with characteristics of orogenic deposits fluids have influenced the gold-related rutile grains at the Troilus deposit. Similarly, at Montauban, the lack of Sn with elevated W in ore-related rutile grains provides evidence for mesothermal, rather than VMS, styles of Au-mineralization (Clark and Williams-Jones, 2004). Since rutile is common in barren and mineralized rocks at Young-Davidson it presents an opportunity to evaluate the composition of rutile grains as a vector towards mineralization (i.e., compare the chemistry of barren-associated rutile with mineralization-associated rutile) and to place further controls on the composition of the fluids that may have precipitated gold.

The use of rutile chemistry as a vector towards mineralization will be evaluated for Young-Davidson (Clark and Williams-Jones, 2004; Scott and Radford, 2007). Similarly, pyrite chemistry and

isotopic composition will be used to evaluate the composition of the mineralizing fluids (Roberts, 1982; Craig et al., 1998; Rice et al., 1998; Simon et al., 1999; Clark and Williams-Jones, 2004; Scott and Radford, 2007; Dostal et al., 2009; de Almeida et al., 2010; Pitcairn et al., 2010). The analyses of rutile, pyrite and gold chemistry will be used to evaluate a fluid source and depositional mechanisms, and contribute to the formation models outlined in the geochemical and structural studies by Martin et al. (Chapter 2; in prep.) and Zhang et al. (2012), respectively.

3.1.1 History and Mineralization

Historical production from Young-Davidson was dominantly from syenite-hosted gold mineralization characterized by quartz veins and disseminated pyrite in zones of potassic alteration. Gold production has also been from quartz-carbonate veins in volcanic and sedimentary rocks at Young-Davidson. Since acquisition of Young-Davidson by Northgate Minerals Corporation in late 2005, drilling has expanded the underground resource (as of 2011) to 14.6 million tonnes (measured and indicated) at an average grade of 2.03 g/t Au and an underground reserve of 39.1 million tonnes (proven and probable) at an average grade of 2.79 g/t Au (AuRico, 2011). In 2011, Northgate Minerals Corporation was acquired by the current owner-operator AuRico Gold Corporation. Gold mineralization at Young-Davidson has been subdivided into 4 main zones by AuRico geologists: Upper Boundary Zone (UBZ), Lower Boundary Zone (LBZ), Lucky Zone (LZ) and the Lower YD Zone (LYDZ; Figure 3.4).

Gold is present in all of the lithologies at Young-Davidson and its abundance is spatially correlated with pyrite abundance. In the syenite gold mineralization is best developed in zones of intense veining, potassic-hematite alteration and sulfidation. In volcanic rocks gold mineralization is characterized by narrow shear zones with intense albite-Fe-carbonate alteration and up to 8 wt% sulfur as pyrite. The majority of gold mineralization is as native gold grains (containing up to 20% silver) with less abundant gold-telluride and gold-silver-telluride minerals. In the syenite gold occurs as inclusions and along cracks in vein-hosted pyrite or in disseminated pyrite in potassic-hematite-pyrite altered vein haloes. Gold-bearing pyrite grains are commonly corroded, fractured and contain abundant hematite-magnetite-rutile mineral inclusions. Lesser amounts of gold is present as free gold along quartz-carbonate grain boundaries associated with euhedral, oxide-free pyrite grains hosted in large planar quartz-carbonate veins.

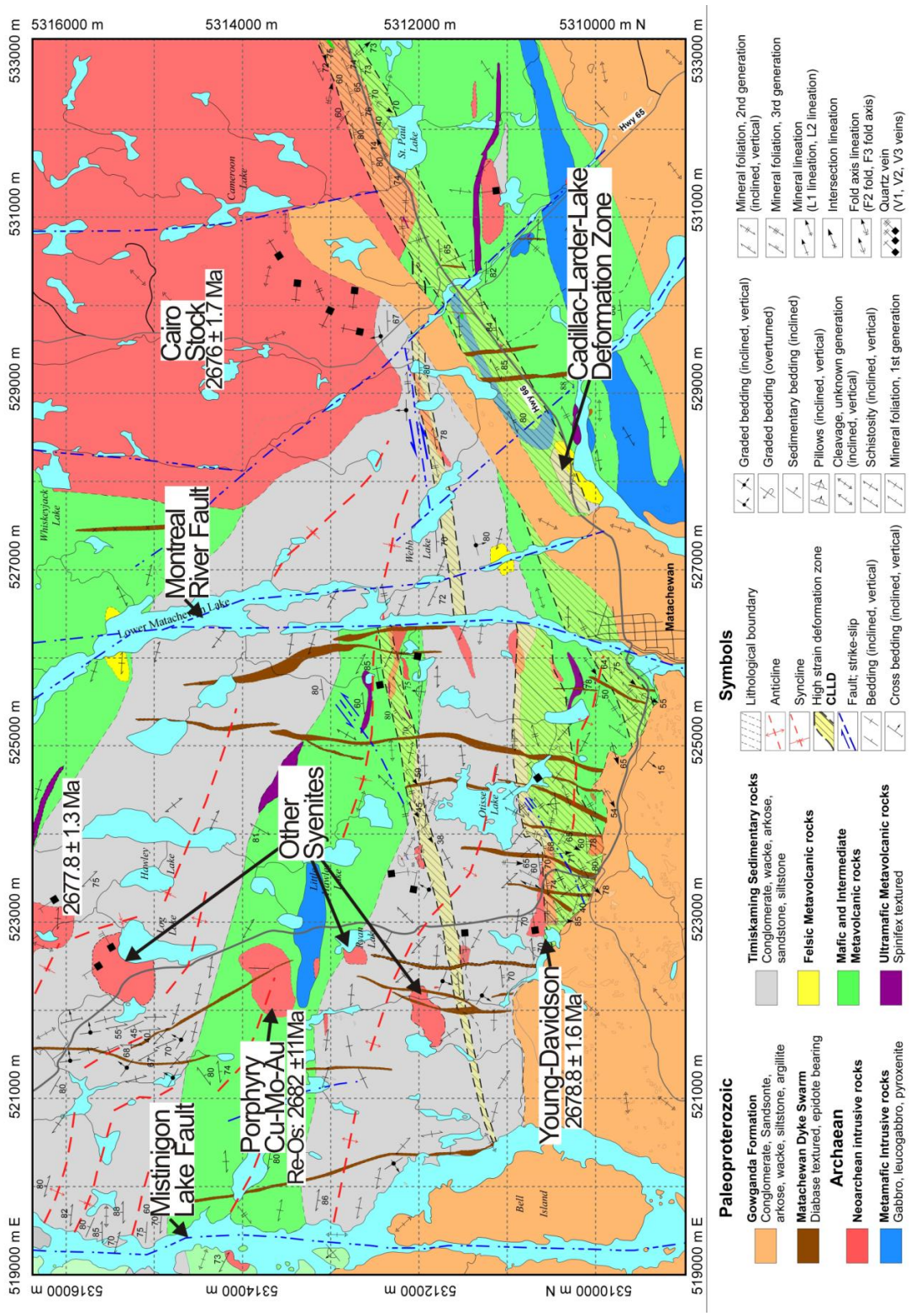

Figure 3.2: General geology of the Matachewan area (modified from Zhang et al., 2012). Cairo U-Pb age from Berger (2006), Young-Davidson and north intrusion U-Pb ages from Zhang et al. (2012), and Ryan Lake (porphyry Cu-Mo-Au) Re-Os molybdenite age from R.L. Linnen (unpubl. data).

3.1.2 General Geology

The general geology of the Matachewan area is shown in Figure 3.2 where roughly east-west trending, southward-dipping units of Archean-aged greenschist-grade sedimentary and volcanic rocks have been intruded by syenite, then subsequently crosscut by north-south trending diabase dikes of the Matachewan swarm and overlain by relatively horizontal Proterozoic sediments of the Cobalt Group. The main structural feature in the Matachewan area is the east-west striking regional-scale Cadillac-Larder-Lake deformation zone (CLLDZ). Intense D_2 deformation generated a penetrative S_2 foliation that is generally restricted to areas affected by the CLLDZ, although in the northern portion of the map area, small gold-bearing shear zones are interpreted as splays off of the CLLDZ (Zhang et al., 2012). A minor component of late brittle left-lateral movement developed along the N-S trending Mistinigon Lake fault and the Montreal River fault which are west and east of Young-Davidson, respectively (Figure 3.2; Lovell, 1967; Ayer et al., 2002).

Ultramafic and mafic volcanic rocks are the oldest rocks in the Matachewan area. These rocks were formerly known as the Larder-Lake but are now part of the Tisdale assemblage (Zhang et al., 2012), deposited at 2710 to 2703 Ma (Ayer et al., 2002). At Young-Davidson, the Tisdale assemblage consists of basalt with lesser ultramafic and felsic volcanic rocks (Lovell, 1967; Berger, 2006; Zhang et al., 2012). Undeformed mafic and ultramafic flows found north of the mine site away from the deformation zone in Figure 3.2 preserve primary pillow and spinifex textures, respectively. These rocks have been metamorphosed to greenschist-grade and are generally very fine to fine-grained, dark-green to green-grey in color, and composed of chlorite, carbonate, iron-carbonate, magnetite, hematite, rutile, pyrite, quartz and feldspar. At the mine site (Figure 3.3) volcanic rocks are weakly to strongly deformed and host varying intensities of quartz-iron-carbonate veining and albite-iron-carbonate alteration. Veins are commonly folded and, where intensely deformed, nearly all primary structures are destroyed; S_1 is nearly completely transposed to S_2.

Timiskaming sedimentary rocks consist of clastic and chemical sedimentary rocks that unconformably overly the Tisdale assemblage and, based on the youngest detrital zircon ages, were deposited from 2687 to 2675 Ma (Ayer et al., 2002). The superposition of gold deposits with Timiskaming sediments, felsic intrusions and corridors of intense deformation is a result of sedimentation and plutonism associated with accretion and regional orogenesis (Ayer et al., 2002). In the Matachewan area, the timing relationship between Timiskaming sediments and syenite is ambiguous. Syenite clearly intruded the sediments, however, at select locations (and potentially in

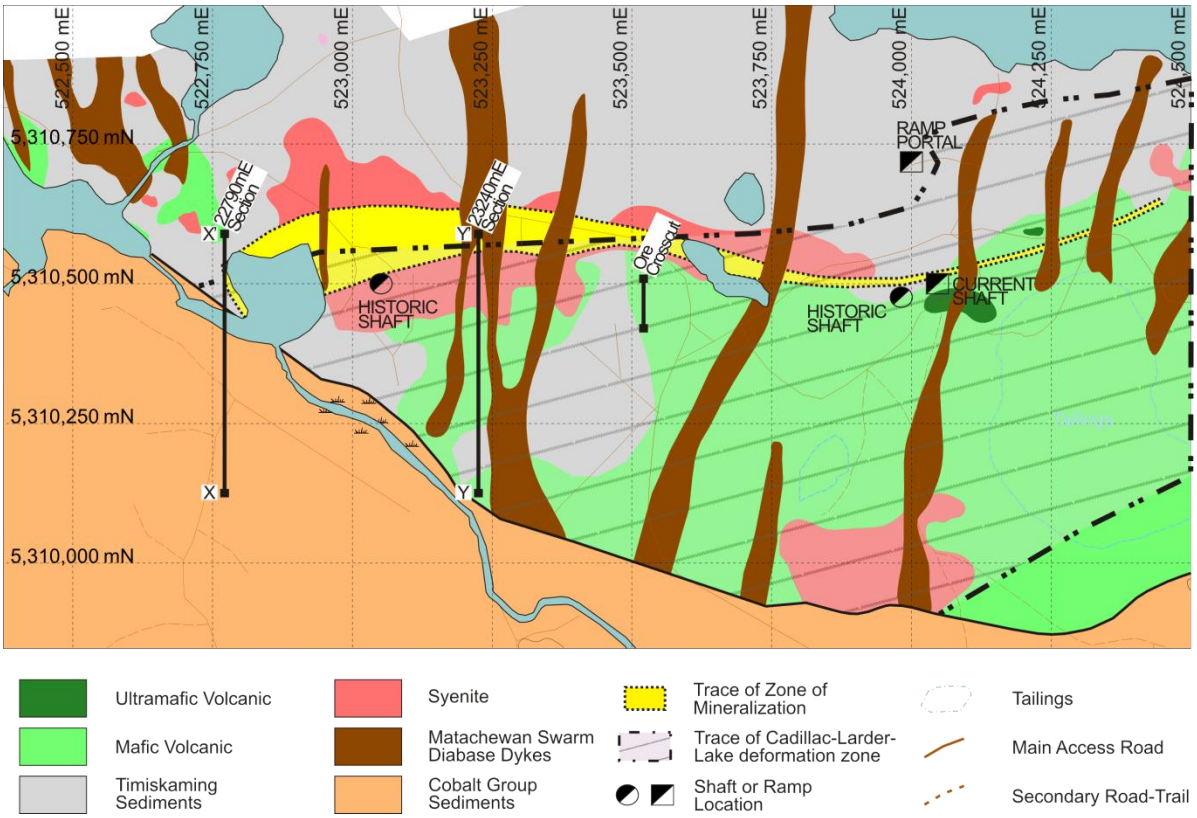

Figure 3.3: Mine-scale geologic map of Young-Davidson showing the distribution of major Archean rock types and the location of the CLLDZ (Zhang et al., 2012). Historic and current shaft/ramp locations are shown and labeled. Mineralization is highlighted in yellow and the location of the two N-S vertical cross sections from are shown in red. Grid is in meters, 50 m x 50 m (Modified after Lucas, 2008 and Zhang et al., 2012)

drill core) syenite is present as clasts within the sediments (Zhang et al., 2012). These timing relationships are similar to other syenite-associated gold deposits from the Abitibi and confirm both the shallow depth of emplacement and the coeval nature of plutonism and Timiskaming sedimentation (Robert, 2001 and ref. therein). At Matachewan, the Timiskaming sediments consist of grey to grey-green conglomerate, sandstone, fine sandstone, siltstone and mudstone that may be reddish-brown in color proximal to the CLLDZ and syenite. Sediments are generally composed of < 15 vol%, 5 mm to 10 cm subrounded, sedimentary or volcanic clasts set in a fine-grained (< 100 μm) matrix of quartz, carbonate, Na- and K-feldspar and chlorite. Undeformed sediments commonly host trace pyrite whereas elevated levels of pyrite are associated with shearing and quartz-carbonate veining. Distal from the CLLDZ in the northern portion of Figure 3.2 clasts are generally subrounded whereas closer to the CLLDZ in the southern portion of Figure 3.2 they tend to be ellipsoidal and elongated parallel to the major penetrative S_2 foliation (Zhang et al., 2012). Several syenite intrusions

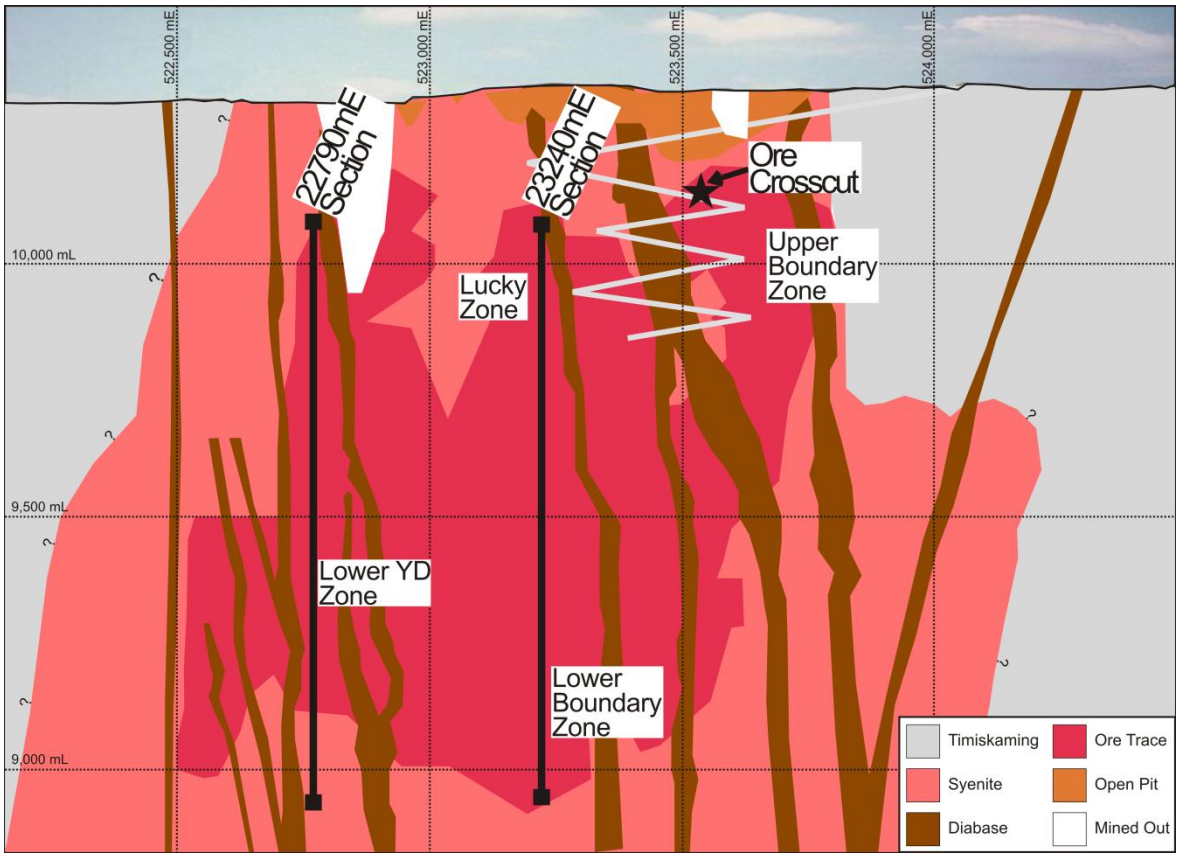

Figure 3.4: Long section through the Young-Davidson deposit (looking north) showing location of the Upper Boundary Zone (UBZ), Lower Boundary Zone (LBZ), Lucky Zone (LZ) and Lower YD Zone (LYDZ). The location of the studied ore crosscut is indicated with the black star. The location of the two N-S geological cross sections at 22790 mE and 23240 mE from Figure 3.3 is shown with vertical black lines. (Based on unpublished data from Edmunds, 2012)

are found in the Matachewan area; the largest of which is the Cairo stock (Figure 3.2). A Cu-Mo-Au-bearing porphyritic intrusion and several barren syenite intrusions are found north of Young-Davidson, and generally contain brittle extensional quartz-carbonate veining. The Young-Davidson syenite has been U-Pb (zircon) dated at 2678.8 ± 1.6 Ma by Zhang et al. (2012) and is roughly coeval with northern syenite intrusions and the Cairo stock (as labeled; Figure 3.2). The intrusive rocks in the Matachewan area are also roughly coeval with Timiskaming sedimentation (2680 to 2675 Ma; Ayer et al. 2002).The Young-Davidson syenite is fine to coarse-grained (< 500 μm to > 2 cm), trachytic to porphyritic textured and mafic to felsic in composition. Young-Davidson syenite generally consists of 40-60% K-feldspar, 20-30% plagioclase, 5-10% carbonate (locally as iron-carbonate), up to 5-10% pyrite in mineralized zones and a fine-grained groundmass consisting of feldspar, quartz, carbonate, chlorite with accessory magnetite, hematite, rutile, pyrite, zircon, barite,

apatite and anhydrite. Porphyritic syenite is generally composed of 10-40% coarse euhedral plagioclase and perthite phenocrysts hosted in a fine-grained groundmass of Na- and K-feldspar, carbonate, magnetite and chlorite with accessory magnetite, hematite, rutile, quartz, zircon, and apatite. Trachytic syenite consists of > 80% coarse-grained elongate altered Na- and K-feldspars, and a fine-grained groundmass of feldspar, carbonate, chlorite with accessory magnetite, hematite, rutile, quartz, zircon, and apatite. Sulfides are either absent or a trace constituent of least-altered syenite. Primary igneous mafic minerals and oxides (i.e., amphibole, titanite, magnetite) are absent in 'least-altered' rocks; the absence of these minerals in all studied samples is interpreted to reflect alteration even in fresh looking samples.

3.1.3 Veining and Alteration

The main alteration styles found in syenite are potassic-hematization, sulfidation, carbonatization and chloritization. The alteration paragenesis presented in Figure 3.6A and B shows the general temporal relationship for the different veining and alteration events, whereas Figure 3.6C and D shows the general mineral paragenesis between alteration types. The most important gold-related alteration is sulfidation developed in zones of intense veining and potassic-hematite alteration. Iron-carbonate and carbonate alteration is generally ubiquitous; varying intensities are related to the abundance of carbonate veins and stringers. The three main vein types that crosscut syenite have been characterized by structural mapping of the #9 ore crosscut found in the Upper Boundary Zone (UBZ) (Figure 3.4). Structural and crosscutting relationships are discussed in detail by Zhang et al. (2012) and are summarized below. Zhang et al. (2012) produced a structural map of the ore crosscut during the structural study; this map outlines the structural relationship between the different vein sets and an excerpt is shown in Figure 3.5A with examples of each identified vein set in Figure 3.5B, C and D.

The earliest V_1 vein generation consist of < 5 cm to > 20 cm boudinaged iron-carbonate veins that dip southwest at moderate to high angles. V_1 veins are dominantly quartz and iron-carbonate with trace amounts of K-feldspar, pyrite, chalcopyrite, galena, molybdenite, gold and are rimmed by chlorite (Figure 3.5B). Tartan-twinned K-feldspars hosted within these veins suggests relatively high (> 300 ºC) temperatures of vein formation (Nesse, 2000). The second V_2 vein generation consists of < 2 cm to 10 cm boudinaged quartz-pyrite veinlets that dip to the northeast at shallow to moderate angles (Figure 3.5C). V_2 veins contain varying proportions of pyrite and quartz with accessory

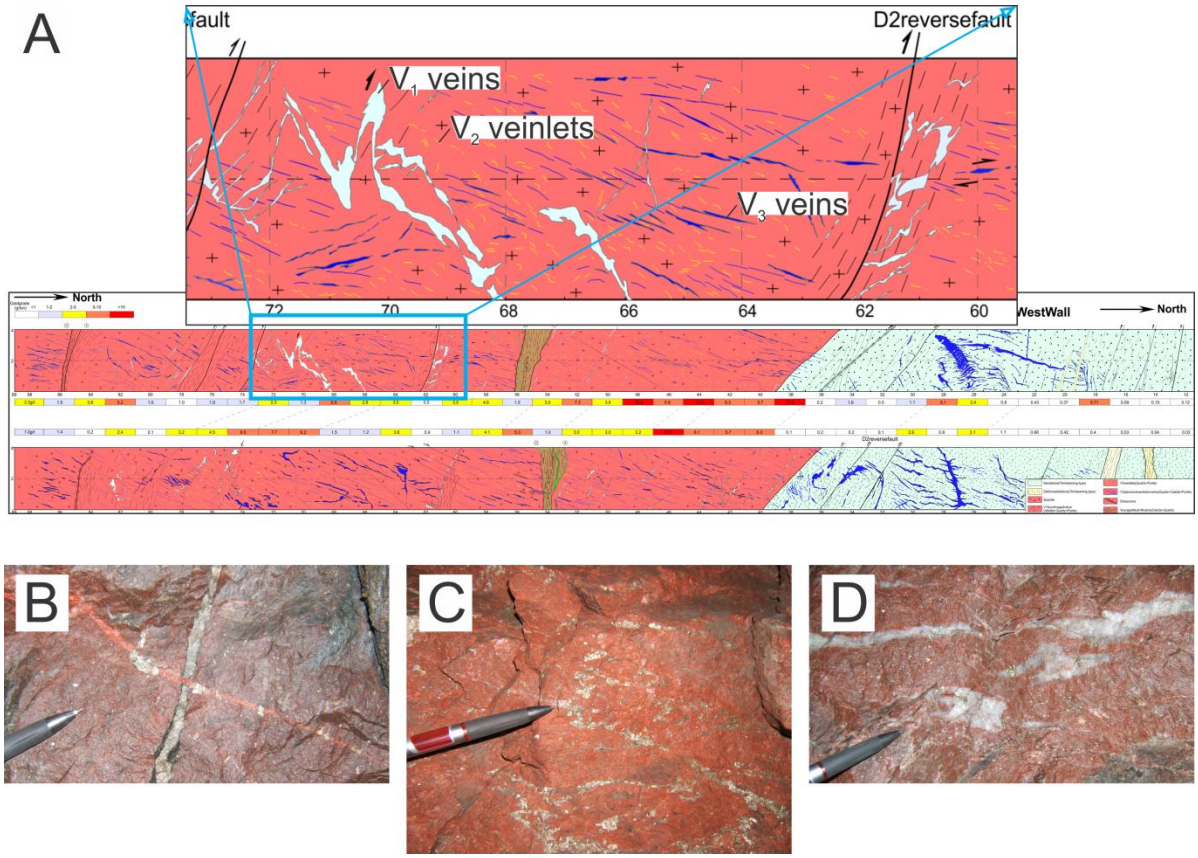

Figure 3.5: Structural map and examples of different vein types at the #9 ore crosscut. A) Structural map of the #9 ore crosscut highlighting vein types and contact relationship with the syenite (Modified from: Zhang et al., 2012). B) Steeply dipping boudinaged V_1 iron-carbonate vein with chlorite ± pyrite rim, crosscut by later planar V_3 K-feldspar altered vein. C) Moderately dipping quartz-pyrite veinlets, boudinaged, deformed, with abundant pyrite hosted in intensely altered syenite. D) V_3 quartz-carbonate veins, relatively planar, en-echelon, tension-gash type veins, minor associated pyrite.

carbonate, and are the dominant host of gold mineralization where gold is as inclusions and along cracks in the vein-hosted pyrite grains. The youngest V_3 vein generation consists of generally large > 30 cm (locally > 5 m) quartz-carbonate veins that form sub-parallel to en-echelon vein arrays (Figure 3.5D). V_3 veins are composed of varying proportions of quartz and carbonate, and contain accessory K-feldspar and pyrite and trace galena, chalcopyrite, scheelite and gold. V_2 and V_3 veins formed during the early to mid D_2 deformation whereas V_1 veins were emplaced either during syenite emplacement or during the D_1 deformation (Figure 3.6A; Zhang et al., 2012). Due to the high intensity of alteration at the ore crosscut, correlating wall rock alteration with a specific vein set was difficult. Study of drill core from zones where alteration intensities are generally lower reveals potassic-hematite alteration haloes on V_3 (and potentially V_2) quartz-pyrite-carbonate veins.

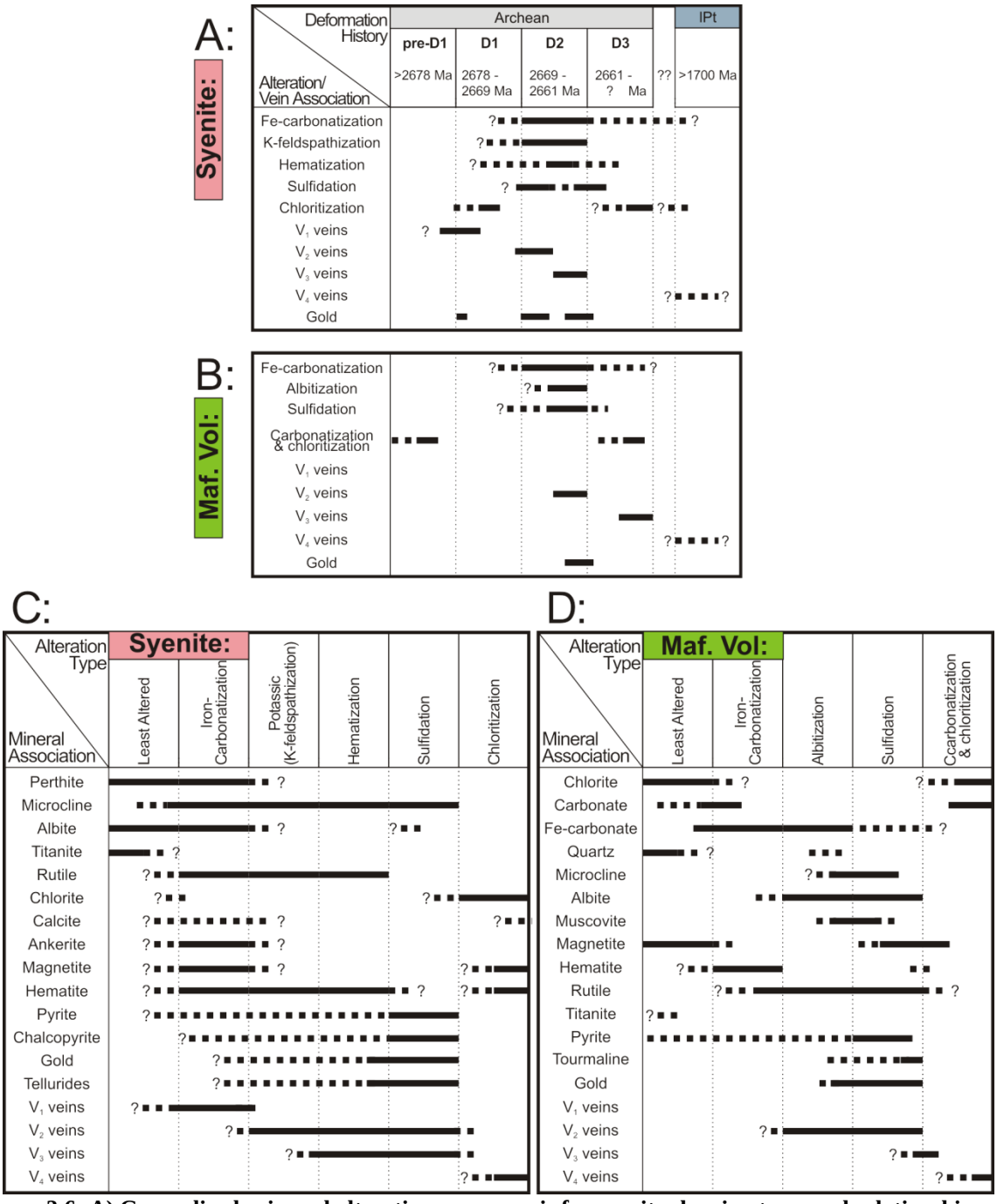

Figure 3.6: A) Generalized vein and alteration paragenesis for syenite showing temporal relationship between veins and major alteration styles. B) Generalized vein and alteration paragenesis for mafic volcanic rocks showing temporal relationship between veins and major alteration styles. C) and D) Mineral paragenesis relationship for each listed alteration type. Left to right represents general temporal relationship, however, some alteration types are repetitive (as seen in A and B) and relationships are meant to show appearance or disappearance of certain minerals from the alteration assemblage. C - Syenite paragenesis and D - mafic volcanic paragenesis. Solid lines - dominant alteration styles/minerals present at that time/during that phase of alteration. Dotted lines - minor component; introduction of or disappearance of alteration styles/alteration minerals. Timing data from Zhang et al., 2012.

Potassic-hematite alteration in syenite is characterized by an overprint of optically continuous albite-twinned Na-feldspar by untwinned K-feldspar that has incorporated abundant fine (< 2 μm) hematite mineral inclusions (Chapter 2; Martin et al., in prep.). K-feldspar alteration is also observed along altered fractures through larger feldspars, and as fine grains in the carbonate groundmass. Incorporation of hematite in K-feldspar during alteration tends to stain K-feldspars in thin section and generate brick red hand samples. The K-feldspar alteration is accompanied by a hematite overprint of magnetite, and locally specular hematite is present in the altered groundmass, indicating relatively oxidized fluid conditions. Pyrite is commonly associated with the carbonate and iron-carbonate between larger feldspars whereas rare fine (<100 μm) pyrite is observed within larger feldspar phenocrysts.

Sediments are commonly potassic-hematite-pyrite altered in haloes around V_3 quartz-carbonate veins, and where the sediments are in close contact with altered syenites. Sedimentary rocks also contain carbonate and iron-carbonate, however the relationship of each to mineralization is poorly characterized. Sediment-hosted gold is as native gold inclusions in euhedral pyrite associated with V_3 vein alteration haloes. Mineralized volcanic rocks are characterized by intense pyrite, albite and iron-carbonate alteration in localized sheared sections with quartz-carbonate veins. Abundant gold mineralization is hosted by quartz-iron-carbonate veins and in zones of pervasive pyritization in the volcanic wall rock. Gold is as fine native gold grains spatially associated with and hosted in pyrite in these intensely altered sections.

3.2 Rutile, Pyrite and Gold textures

3.2.1 Rutile

Rutile has been selected to evaluate as an indicator mineral because: 1) rutile is found in both barren and mineralized wall rocks; 2) different textural types of rutile have been identified; 3) rutile is found as inclusions in mineralized pyrite grains; and 4) studies of rutile compositions at gold deposits in the Abitibi have shown that ore related rutile grains are chemically enriched in specific elements compared to grains found in barren host rocks (Clark and Williams-Jones, 2004).

With the exception of magnetite, primary magmatic Fe-Mg silicate (amphibole, biotite) and Fe-Ti oxide minerals (titanite, ilmenite) are absent in nearly all studied samples of Young-Davidson syenite.

Chlorite-altered-biotite has been found in weakly altered maroon mafic syenite, but generally this phase of syenite represents a small portion of the Young-Davidson intrusion. In the neighboring Cairo stock titanite, magnetite and amphibole are the primary Ti-Fe-Mg bearing phases (Berger, 2006) however at Young-Davidson, relict rhomboid-shaped clusters of rutile, carbonate and chlorite are present in least-altered syenite (Figure 3.7A and B). Based on the least-altered Cairo mineralogy and the rhomboid shaped rutile clusters in Young-Davidson syenite, the primary Ti-bearing and Fe-Mg bearing phases are thought to be a combination of titanite and amphibole. Magnetite grains found at the center of feldspar grains from weakly altered syenite potentially represent magmatic Fe-oxide grains, however these grains lack characteristic Ti-exsolution textures. Carbonate-associated magnetite grains are commonly corroded and fractured, with hematite replacement found along outer edges and along cracks, however, euhedral magnetite grains have also been found with carbonate in altered syenite, and are likely not magmatic. One textural type of rutile is spatially related to hematite replacement of magnetite (e.g., Figure 3.7C); however since the rutile generally is not in contact with magnetite grains, the temporal relationship between magnetite and rutile can only be inferred by the spatial association. All syenite-hosted rutile grains can be characterized based on their relative grain textures, vein and pyrite association. Four general textural types of rutile have been delineated: 1) granular rutile; 2) pseudomorphic rutile; 3) residual hematite-magnetite rutile; and 4) pyrite-hosted rutile.

Individual rutile grains in pseudomorphic clusters are commonly fine-grained and range in size from < 10 μm to 20 μm. The clusters are bladed rhombohedral-shaped aggregates of rutile, carbonate and chlorite that can be > 500 μm across (Figure 3.7A and B). These mineral-aggregate-pseudomorphs are dominantly composed of rutile with < 30% carbonate and lesser chlorite. The rutile grains in these aggregates are interpreted as remnants of primary Ti-Fe bearing minerals that have been consumed during alteration. Pseudomorphic rutile tends to occur in samples with weak alteration intensities whereas granular rutile is more often located in zones containing abundant pyrite, veining and intense carbonate and hematite-potassic alteration styles.

Granular rutile grains range from 20 μm to 100 μm across, are roughly equant and are commonly either associated with pyrite, hosted in veins or located in the fine-grained altered syenite groundmass (e.g., Figure 3.7D). Granular grains are generally associated with areas of extensive alteration and are

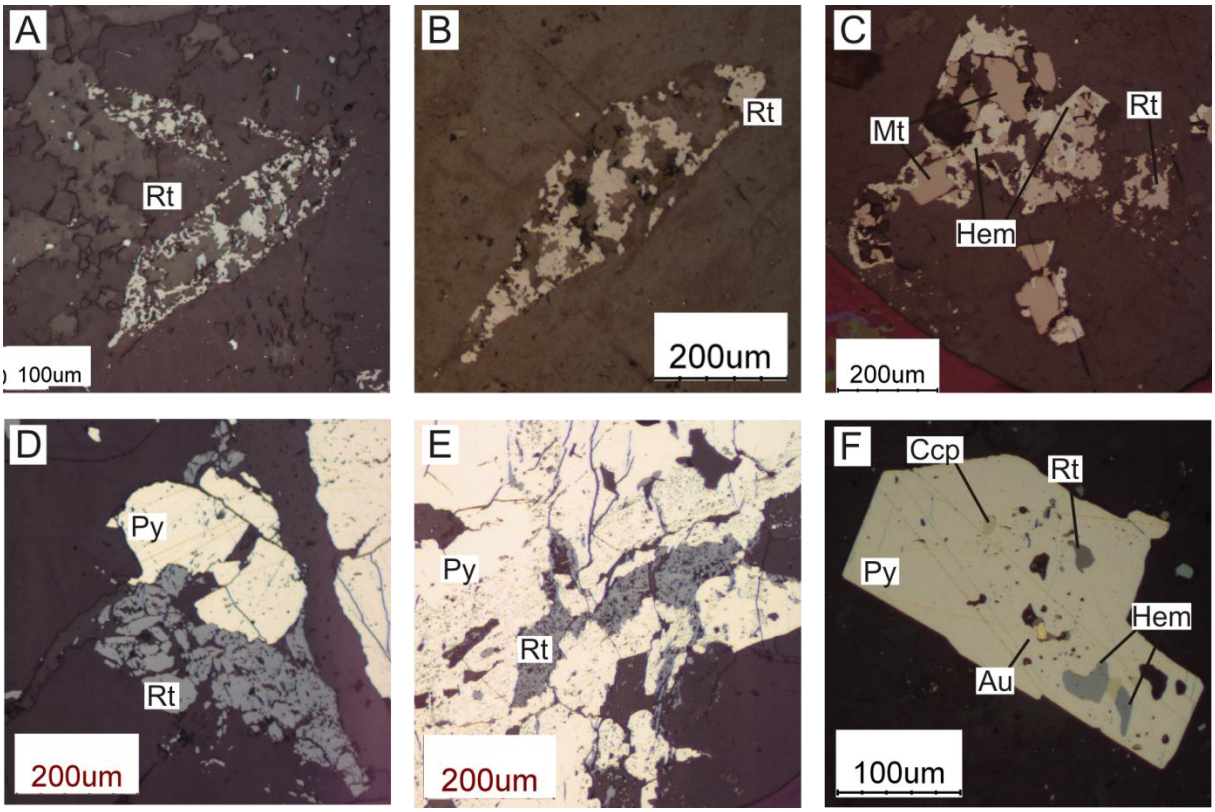

Figure 3.7: Typical syenite-hosted rutile textures. A) Pseudomorphic rutile; relict rhombid-shaped cluster of rutile, carbonate and minor chlorite. Reflected plane polarized light. B) Same as A; pseudomorphic rutile. Reflected plane polarized light. C) Rutile associated with hematite replacement of magnetite. Reflected plane polarized light. D) Pyrite-associated coarse granular rutile, rutile appears to be after pyrite. Reflected plane polarized light. E) Rough-textured pyrite-hosted rutile associated with gold mineralization (elsewhere in this Py-vein). Reflected plane polarized light. F) Fine-grained rutile-hematite-ccp inclusion assemblage in gold-hosting pyrite. Reflected plane polarized light.

interpreted to be a result of hydrothermal alteration in the syenite groundmass. Rutile grains associated with hematite-magnetite are relatively rare and are only preserved where hematite has replaced magnetite in samples that are weakly altered and lack pyrite (Figure 3.7C).

Mafic volcanic rocks contain abundant very fine-grained (< 10 μm) rutile that is found along foliation and evenly distributed through volcanic samples. The lower grain size limit for rutile grains with the present EMP machine conditions is 15 μm to 20 μm; grains smaller than this commonly fail data quality checks (discussed in Section 3.3). Since volcanic hosted rutile is very fine-grained, analysis of these grains with the present conditions generally yielded poor results, and thus volcanic-hosted rutile was not analyzed in this study. Since mineralized volcanic rocks can be correlated with the least-altered precursor within a few 10's of meters, it would be interesting to note the chemical

changes in rutile from unmineralized to mineralized zones; however, the fineness of rutile in these samples warrants modified analytical methods.

3.2.2 Pyrite

Pyrite was chosen for analysis because: 1) gold mineralization shows a strong spatial and temporal association with pyrite in most of the studied samples; 2) pyrite is present in both barren and mineralized rocks; 3) two textural types of pyrite are recognized based on inclusion composition and grain textures (Chapter 2; Martin et al., in prep.); and 4) studies of other mineral deposits have shown that pyrite chemistry and heterogeneities need to be characterized in order to fully understand complex pyrite textures (Craig et al., 1998; Craig, 2001).

Pyrite is the dominant ore-associated sulfide in mineralized rocks at Young-Davidson. All mineralized host rocks contain elevated concentrations of sulfur compared to the unmineralized equivalent (Chapter 2; Martin et al., in prep.). The studied examples of Timiskaming sediments are from zones containing quartz-carbonate veins proximal to mineralized syenite. Therefore the pyrite textures in these zones are the result of hydrothermal pyrite deposition. Pyrite grains from these zones can either contain abundant fine-grained carbonate and quartz inclusions with irregular orientations (e.g., Figure 3.8A) or contain euhedral textured rims surrounding inclusion-bearing pyrite (Figure 3.8B). Sedimentary samples commonly contain > 1-2% fine-grained (< 300 μm) euhedral disseminated pyrite grains. In volcanic rocks, at least one stage of hydrothermal pyrite existed prior to the main gold-related stage of pyritization. The initial pyrite stage is visible in drill core as euhedral to subhedral inclusion filled pyrite grains that are foliated and reoriented into 'pyrite stringers', consisting of a number of pyrite grains in a string concordant with the major foliation. These grains are also commonly associated with boudinaged quartz-carbonate veins that are interpreted to represent pre-D_2 volcanic-hosted quartz-carbonate veins (Chapter 2; Martin et al., in prep.). In the syenite, disseminated and vein-hosted pyrite grains have extremely heterogeneous textures; at the microscopic scale, in a single sample, pyrite textures range from euhedral to anhedral, weakly to strongly fractured, corroded and mineral-inclusion zoned (Figure 3.8C, D and E). Vein hosted pyrite is commonly fractured corroded (Figure 3.8D). In general, syenite-hosted pyrite grains range from < 50 μm to > 4 mm in size, are anhedral to euhedral, occur in all vein sets and are disseminated in the associated alteration haloes. Based on inclusion assemblages, grain morphology and vein association,

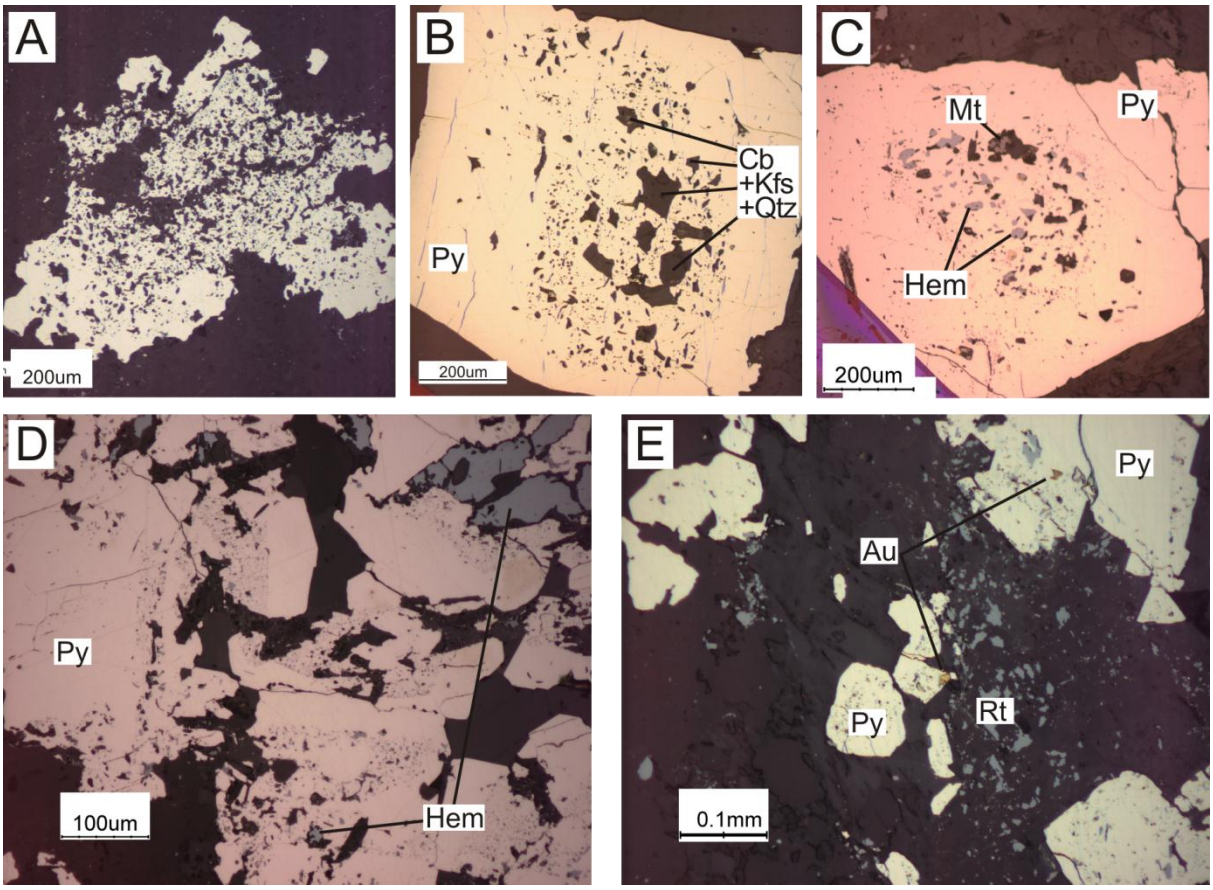

Figure 3.8: Sediment and syenite hosted pyrite textures. A) Corroded pyrite in Timiskaming sediments. Reflected plane polarized light. B) Hydrothermal pyrite rim around inclusion rich pyrite near V_3 vein in Timiskaming sediments. Reflected plane polarized light. C) Inclusion zoned disseminated pyrite in syenite; hematite and magnetite inclusions in the core. Reflected plane polarized light. D) Corroded, fractured and inclusion zoned hematite-bearing pyrite. Reflected plane polarized light. E) Oxide-inclusion hosting pyrite grains with gold mineralization. Reflected plane polarized light.

two textural types of pyrite are recognized.

Type 1 pyrite is present in V_1 veins, V_2 veins and as disseminated pyrite in the groundmass of altered syenite. Type 1 pyrite grains are anhedral, corroded, fractured and commonly contain abundant hematite, magnetite and rutile inclusions. Hematite and magnetite are present either as poly-phase mineral inclusions inside pyrite, or as isolated mono-phase inclusions with no clear relationship to one another other than being located in the same oxide-inclusion rich zone of that pyrite grain (Figure 3.8C). Pyrite-hosted oxide inclusions are usually subhedral to anhedral and have an irregular distribution through type 1 pyrite grains (Figure 3.8C). Rare euhedral magnetite inclusions have also been observed in some gold-bearing type 1 pyrite grains (Figure 3.9B). Even though type 1 pyrite

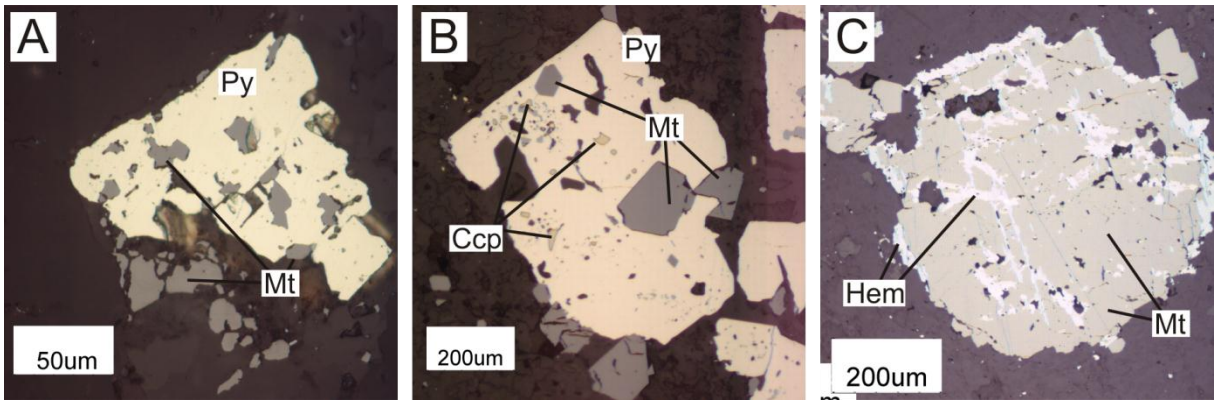

Figure 3.9: Corroded pyrite and oxidized mineral assemblages in syenite. A) Magnetite after pyrite. Reflected plane polarized light. B) Corroded pyrite with euhedral magnetite inclusions, hematite, chalcopyrite and gold inclusions. Reflected plane polarized light. C) Corroded magnetite; hematite after magnetite along boundaries and fractures. Reflected plane polarized light.

grains are consistently anhedral, it does not appear as if any one mineral phase has replaced pyrite; commonly corroded fractures are lined by silicate or carbonate minerals rather than sulfide or oxide minerals. Inclusion-rich and inclusions-poor zones in pyrite also commonly lack crystallographic orientation, whereas if the zones were generated during pyrite overprint of oxide grains, some crystallographic control to the inclusion distribution would be expected.

Type 2 pyrite grains are present in V_3 veins and disseminated in the groundmass with carbonate alteration. Type 2 pyrite grains are commonly fractured, similar to type 1 pyrite grains. However, type 2 grains characteristically lack oxide inclusions and have euhedral to subhedral grain boundaries. Type 2 pyrite grains are typically hosted in larger quartz-carbonate veins that also host galena and chalcopyrite. In the studied examples of type 2 pyrite associated mineralization, gold is either as free gold along quartz-carbonate grain boundaries, or is found along fractures crosscutting pyrite where the pyrite texturally pre-dates the gold (Figure 3.10A and B).

Sedimentary rocks generally contain a mixture of type 1 and type 2 pyrite. Hydrothermal overgrowths of earlier pyrite are present in vein alteration haloes (Figure 3.8B), where inclusion rich cores are rimmed by inclusion poor zones. Gold is generally associated with the euhedral hydrothermal pyrite in these haloes. Gold is also associated with subhedral pyrite in sheared sediments; shear and vein related pyrite are interpreted to be hydrothermal in origin (Figure 3.15C). In the volcanic rocks, abundant gold is contained in quartz-iron-carbonate veins where the gold-pyrite relationships are similar to type 2 pyrite-associated V_3 mineralization styles in the syenite. In the

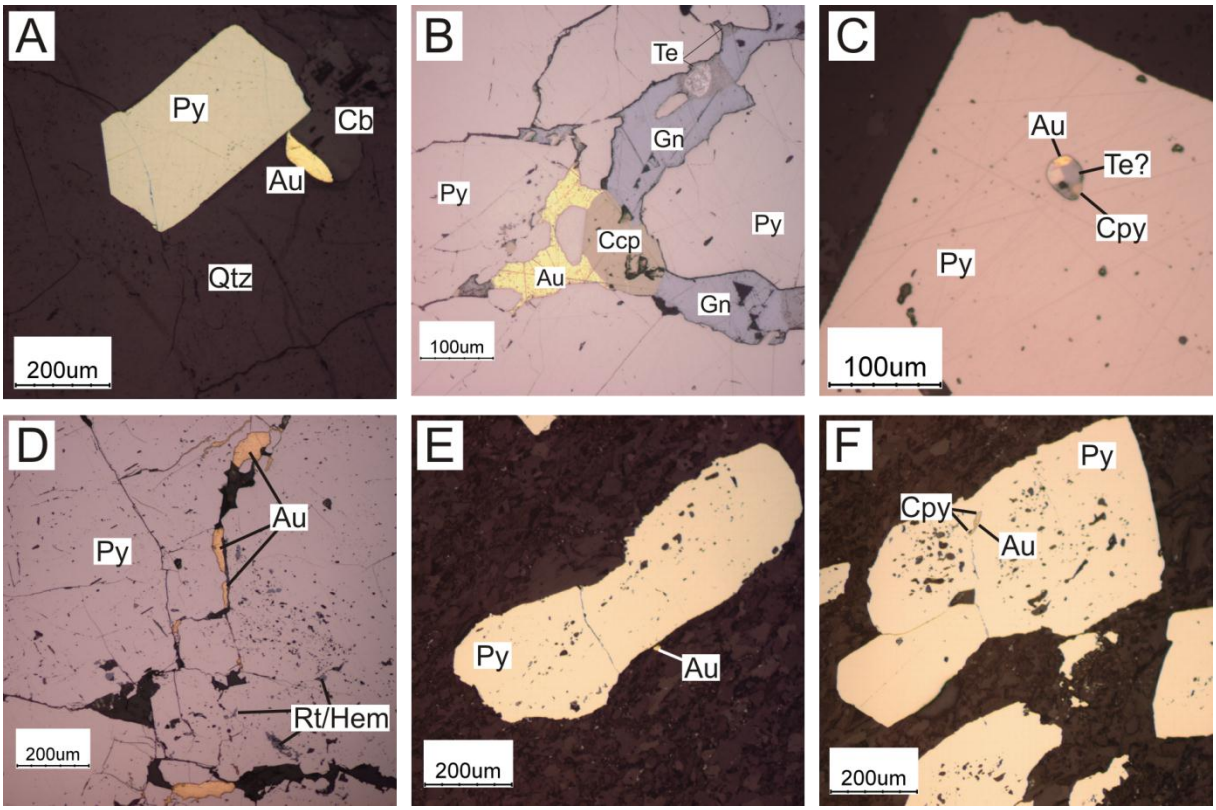

Figure 3.10: Pyrite-gold textures at Young-Davidson. A) V_3 vein hosted free gold along quartz-carbonate grain boundary, related to type 2 pyrite. Reflected plane polarized light. B) Gold associated with chalcopyrite, galena, and tellurides along fracture in oxide-inclusion free V_3 vein pyrite. Reflected plane polarized light. C) Gold-telluride-chalcopyrite inclusion in type 2 disseminated pyrite, V_3 alteration halo. Reflected plane polarized light. D) Gold along fractures in type 1 oxide-bearing pyrite in V_2 vein in syenite. Reflected plane polarized light. E) Fine-grained gold inclusion spatially related to deformed corroded pyrite in albitized volcanic rocks. Reflected plane polarized light. F) Fine-grained chalcopyrite-gold inclusion in corroded inclusion-bearing pyrite in albitized volcanic rocks. Reflected plane polarized light.

volcanic wall rock, pyrite-gold relationships are less clear mainly due to lower amounts of observable gold (i.e., gold was not petrographically abundant in the altered wall rock). Where gold has been observed, it occurs as very fine (< 10 μm) native gold grains associated with type 1 pyrite (Figure 3.10E and F). Volcanic-hosted pyrite grains are foliated and deformed and contain abundant inclusions of fine-grained feldspar, quartz and carbonate minerals rather than the hematite-magnetite inclusions that characterizes type 1 mineralized pyrite in syenite (Figure 3.10E and F).

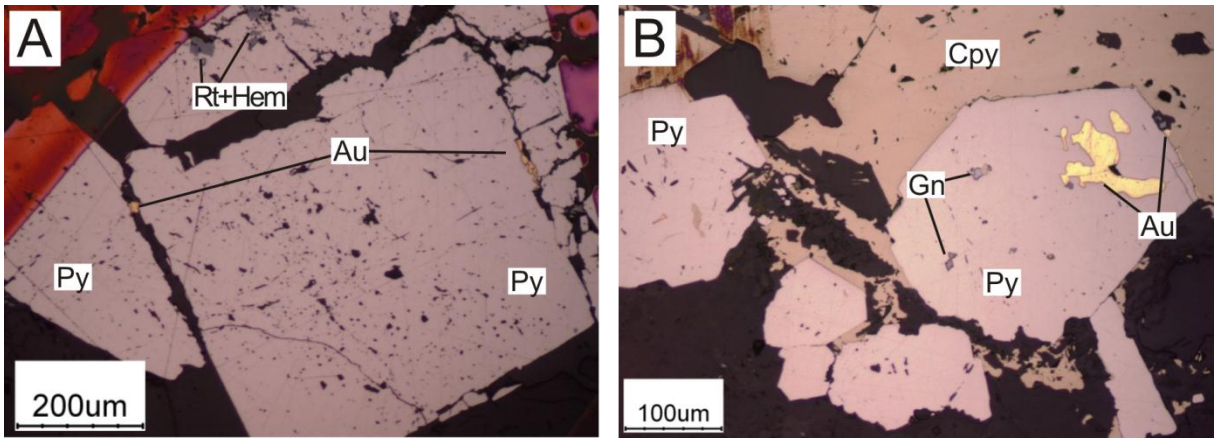

Figure 3.11: Type 1 and type 2 pyrite associated gold. A) Gold along fractures in oxide-bearing pyrite. Reflected plane polarized light. B) Gold inside type 2 pyrite and along pyrite boundary in chalcopyrite-bearing V_3 vein. Reflected plane polarized light.

3.2.3 Gold

The chemical compositions of gold inclusions were determined because: 1) gold is associated with different textural types of pyrite hosted within distinct vein types; 2) metal associations for the latest vein generation differ from those for the first two vein types; and 3) studies of gold mineralization in the Abitibi have shown that differences in Au:Ag in gold inclusions from different textural styles of mineralization can be explained by contrasting fluid properties and depositional mechanisms (Olivo and Williams-Jones, 2002).

The first type of gold mineralization is associated with V_1, V_2 and disseminated pyrite that is generally corroded and hosts abundant hematite and magnetite inclusions. Gold mineralization associated with type 1 pyrite is fine-grained (typically < 25 μm) and occurs as inclusions or along fractures in pyrite that is host to hematite, magnetite, rutile and minor chalcopyrite mineral inclusions (e.g., Figure 3.7F, Figure 3.9B, Figure 3.10D and Figure 3.11A). Rare occurrences of gold-silver-tellurides are present in corroded pyrite in V_2 veins, however, in general they represent a small subset of the studied samples. Native gold grains in type 1 pyrite occur along fractures or are as fine inclusions spatially related to fractures. The presence of hematite and magnetite as inclusions inside pyrite is commonly a good indicator for gold mineralization.

Gold mineralization associated with type 2 pyrite in V_3 quartz-carbonate veins is associated with scheelite, galena, chalcopyrite and telluride minerals. In this style of mineralization gold is as native

free gold along quartz-carbonate grain boundaries in V_3 veins (Figure 3.10A), along fractures in the oxide-free pyrite (Figure 3.10B) or as inclusions in the pyrite and along the edge of euhedral pyrite grains (Figure 3.11B). Gold mineralization in V_3 veins can also be with recrystallized quartz along quartz grain boundaries or with pristine undeformed quartz associated with pyrite pressure shadows. The association of gold with scheelite, galena, chalcopyrite and tellurides combined with the occurrence of free gold (i.e., gold occurrence independent of pyrite) suggests contrasting controls for gold precipitation when compared to the earlier styles of mineralization.

3.3 Microanalytical Methodology

Rutile grains were analyzed with the Cameca SX50 electron microprobe at the University of Toronto, Ontario, which is equipped with 3 tunable wavelength dispersive spectrometers. Rutile grains were analyzed for Cr, V, Fe, W, Ti, Cu, Ni, Nb, Sn, Sb and Si. The microprobe was operated at 20 kV and 50 nA with a 1 μm beam size and the following count times: 20 seconds for Cr, V, Fe, W, Ti, Cu and Ni; 40 seconds for Nb, Sn and Sb; and 80 seconds for Si. The background count times were as follows: 20 seconds for Cr, V, Fe, W, Ti, Cu and Ni; 40 seconds for Nb, Sn and Sb; and 80 seconds for Si. Elemental analysis of > 20 μm rutile grains at these conditions produced good results with oxide totals between 98.5% and 101.5% (depending on grain morphology) and detection limits better than 0.05 elemental % for each element. Analytical precision tested by duplicate analyses is better than 10% and accuracy tested by repeat analysis of lab standards is better than 10%. Grain morphology played an important role in the collection of quality data for these tests. Ideal rutile grains are larger than 20 μm in all orientations and are generally close to equant; these grains are commonly translucent, light brown and easily identifiable at 10x magnification in plane polarized light. Pseudomorphic rutile, as detailed above, is finer and generally yield poorer results (i.e., oxide totals < 98.5% or > 101.5%), however approximately 50% of analyses passed the oxide-totals check. Results from rutile analyses are presented in Table 3.1 and Table 3.2 and discussed in Section 3.4.1.

All textural and vein associated types of pyrite were analyzed with the Cameca SX100 electron microprobe at the University of Michigan, Michigan, USA, which is equipped with five wavelength-dispersive spectrometers. Since pyrite textures are extremely variable at Young-Davidson, point analyses and elemental maps were collected to understand the spatial distribution of elements within pyrite grains (ideally with point analyses after map collection). Pyrite was analyzed for Fe, S, Co, Ni,

As, Au, Te, Pb and Cu. The microprobe was operated with the following machine conditions: 20 kV; 100 nA; 1 μm beam size; counting 10 seconds for Fe and S, 20 seconds for Au and Te, 30 seconds for Ni, Co and Cu, 120 seconds for As and 240 seconds for Pb. Background counting times were identical to peak count times. Long counting times are required for low (< 300 ppm) detection limits of each element in pyrite. Elemental maps of As, Co and Ni were acquired for each textural and vein associated types of pyrite (i.e., type 1 and type 2 pyrite in V_1, V_2, V_3 veins or disseminated pyrite). Craig et al. (1998) also showed that the spatial distribution of Co, Ni and As in pyrite can resolved by using specialized EMP machine conditions: high voltages (20-25 kV), high beam currents (100-400 nA) and extremely long counting times (6-24 hours). Because of time and microprobe limitations, we utilized slightly modified machine conditions of: 20-25 kV, 100-200 nA and run times of 1-4 hours for each map. In addition to As, Co and Ni, maps, Fe and S maps and BSE images were collected to constrain the boundaries of As, Co and Ni maps to the extent of pyrite grains (i.e., make sure the mapped grain is pyrite). Results from pyrite point analyses are tabulated in Table 3.3 and results from pyrite mapping are presented in Figure 3.14 to Figure 3.17 and discussed in Section 3.4.2.

Bulk sulfur isotopic analyses of pyrite hosted in each vein set from the UBZ were obtained at the McGill Stable Isotope Lab by Dr. Boswell Wing, McGill, Ontario. All sulfur isotope data is reported relative to Vienna Cañon Diablo Troilite (V-CDT). The analytical conditions used for these analyses are similar to those utilized by Johntson et al. (2005 and ref. therein) and the analytical reproducibility for the analysis procedure is estimated to be better than 0.1 ‰ for $\delta^{34}S$ values and 0.01 ‰ for $\Delta^{33}S$. Results from bulk pyrite sulfur isotopic analysis are discussed in Section 3.4.2.

Different petrographic styles of gold mineralization, outlined above, were analyzed with the Cameca SX50 electron microprobe at the University of Toronto, Ontario, which is equipped with 3 tunable wavelength dispersive spectrometers. Gold grains were analyzed for Au, Ag, Fe, Cu, Pb, Se, Te, Hg, Bi, Ti and Si. The machine was operated at 20 kV and 20 nA with a 1 μm beam size, counting 20 seconds for Au, Ag, Fe, S, Cu, Pb, Se, Te, Hg, Bi and 40 seconds for Si and Ti. Background counting times were 20 seconds for Au, Ag, S, Fe, Cu, Pb, Se, Te, Hg, Bi and 40 seconds for Si and Ti. Analysis of gold inclusions with these conditions produced good results with elemental totals between 98.5% and 101.5% and detection limits better than 0.1 elemental % except for Pb at 0.5 elemental %. After a number of analyses, the concentrations of Se, Hg, Bi, Pb, Te and Ti were at or below detection limits and were removed from subsequent analyses to reduce counting times. Since the majority of gold inclusions found in the studied sections were < 50 μm (more commonly ≤

10 μm) in size, the influence of host pyrite grains on the gold analysis was tested by performing a 45 μm transect with 5 μm step size starting in a pyrite grains, across the boundary of a gold grain hosted within pyrite, and ending in gold (Figure 3.20). This test showed that the influence of pyrite in the gold analysis just 5 μm away from the gold boundary was negligible; the combined amount of Fe and S in the analysis was < 2 elemental %. Therefore we determined that the minimum analyzable inclusion size with the present machine conditions is approximately 10 μm. Results from gold inclusion testing are tabulated in Table 3.4 and discussed in Section 3.4.3.

3.4 Results

3.4.1 Rutile

Table 3.1 shows the average composition of rutile grains from each thin section analyzed in this study. The average composition of syenite-hosted rutile at Young-Davidson is: 96.7 wt% TiO_2, 0.70 wt% WO_3, 0.61 wt% V_2O_3, 0.50 wt% FeO, 0.35 wt% Cr_2O_3, 0.35 wt% Nb_2O_5, 0.03 wt% Sb_2O_3 and 0.02 wt% SnO_2. Data presented in Table 3.1 does not discriminate rutile by textural type and represents average rutile compositions for each thin section. The 4 textural types of rutile discussed in Section 3.2.1 can be further subdivided based on the presence (Au-associated) or absence (Au-barren) of gold in each sample. Au-associated grains are in samples either containing gold or intense alteration whereas Au-barren grains are in samples that contain no gold and lack the associated alteration characteristics. Average compositions for each textural type of rutile in Au-associated and Au-barren rocks are shown in Table 3.2. Pyrite-hosted rutile grains that are directly associated with gold show the highest enrichments in W, Cr, V, Fe and Sb. The Fe enrichments are highest in pyrite-hosted rutile grains; which may be explained by fluorescence from the surrounding pyrite grain. However, Fe enrichment of ore-related rutile grains has been observed at other orogenic gold deposits (e.g., Scott and Radford, 2007). In general granular, pseudomorphic and hematite-magnetite related rutile grains contain elevated W, Cr and V in gold-related grains compared to gold-barren grains. Niobium contents in rutile are interpreted to reflect the earliest phases of hydrothermal alteration where magmatic Nb rich titanite and magnetite were consumed, and the Nb was retained in the resulting rutile grains. The inverse relationship between Nb and W presented in Figure 3.12A can therefore be interpreted in 2 ways: 1) rutile grains have been depleted in Nb and enriched in W during progressive hydrothermal alteration; or 2) there have been multiple alteration events, where primary magmatic titanite and magnetite grains have been consumed in Au-barren alteration phases whereas later Au-related alteration has consumed amphibole and simultaneously enriched grains in W. The linear relationship between V and W presented in Figure 3.12B shows that pyrite-hosted grains, granular grains and a few pseudomorphic grains contain coupled enrichments of V and W. A comparison of the data from Au-bearing and Au-barren zones from Table 3.2 shows that there is considerable overlap between compositions for each textural type, and for grains from mineralized and non-mineralized zones. Discrimination diagrams for Au-associated and Au-barren rutile grains from typical orogenic gold deposits have been developed by Clark and Williams-Jones (2004) and are presented with the current dataset in Figure 3.12C. Because of the strong enrichments of V and

Table 3.1: Average rutile composition for each sample used in this study. The reported value is an average for all analyses from each thin section. ldl indicates lower detection limit.

SampleID	WO_3	Cr_2O_3	V_2O_3	FeO	Nb_2O_5	TiO_2	Cu_2O	NiO	SnO_2	Sb_2O_3	SiO_2	Oxide
Avg Det.Lim (%)	0.07	0.02	0.03	0.02	0.03	0.03	0.02	0.02	0.02	0.02	0.01	Totals
802803 (n=4)	0.35	0.13	0.41	0.44	0.13	97.96	ldl	ldl	ldl	ldl	ldl	99.41
802807 (n=2)	0.26	0.58	0.22	1.12	1.78	95.38	0.02	ldl	0.07	0.09	ldl	99.53
802809 (n=4)	0.37	0.36	0.31	0.29	0.09	97.72	ldl	ldl	ldl	ldl	0.03	99.13
802822 (n=4)	ldl	ldl	0.30	0.39	ldl	98.72	ldl	ldl	0.03	ldl	ldl	99.44
802826 (n=3)	ldl	0.06	0.55	0.30	0.30	98.00	ldl	ldl	0.02	ldl	ldl	99.24
802838 (n=5)	0.28	0.20	0.05	0.62	0.15	98.29	ldl	ldl	ldl	0.02	ldl	99.61
802839 (n=4)	1.22	1.13	0.45	0.50	0.12	95.79	ldl	ldl	0.05	ldl	ldl	99.25
802841 (n=6)	0.13	1.69	0.34	0.81	0.07	96.31	ldl	ldl	0.02	0.05	ldl	99.42
802842 (n=2)	0.47	0.48	0.57	0.39	0.71	96.61	ldl	ldl	0.08	0.09	ldl	99.39
802857 (n=1)	ldl	0.06	0.21	0.46	0.30	97.64	ldl	ldl	ldl	0.04	ldl	98.71
802858 (n=2)	0.91	0.17	0.09	1.29	1.06	95.25	ldl	ldl	ldl	0.17	ldl	98.95
802860 (n=9)	0.38	0.31	0.09	0.54	0.30	98.19	ldl	ldl	ldl	ldl	ldl	99.82
802861 (n=3)	0.83	0.20	0.17	0.83	0.39	97.06	ldl	ldl	ldl	0.22	ldl	99.69
802864 (n=4)	0.90	0.98	0.31	1.07	0.32	95.56	ldl	ldl	0.02	ldl	ldl	99.15
802870 (n=14)	0.20	0.06	0.72	0.41	0.53	97.96	ldl	ldl	ldl	0.02	ldl	99.90
802927 (n=1)	0.19	0.10	0.67	0.31	0.56	96.88	ldl	ldl	ldl	0.08	ldl	98.79
802929 (n=4)	0.59	0.29	0.55	0.47	0.30	96.15	ldl	ldl	0.04	0.03	ldl	98.41
802934 (n=16)	0.40	0.29	0.94	0.31	0.46	96.42	ldl	ldl	ldl	0.03	ldl	98.85
802936 (n=3)	0.08	0.28	0.68	0.25	0.45	96.71	ldl	ldl	0.06	ldl	ldl	98.51
803326 (n=4)	0.45	0.06	0.55	0.57	0.52	96.62	ldl	ldl	ldl	ldl	ldl	98.76
803331 (n=3)	0.29	0.11	0.09	0.64	0.11	98.41	ldl	ldl	ldl	ldl	ldl	99.65
803336 (n=3)	0.08	0.30	0.53	0.28	0.45	97.63	ldl	ldl	ldl	ldl	ldl	99.27
803337 (n=4)	0.38	ldl	0.28	0.69	0.36	97.35	ldl	ldl	ldl	ldl	0.02	99.05
803338 (n=2)	ldl	0.03	0.87	0.22	0.27	97.37	ldl	ldl	ldl	ldl	ldl	98.76
803342 (n=4)	0.12	0.04	0.89	0.32	0.64	96.68	ldl	ldl	0.04	ldl	ldl	98.72
803346 (n=2)	0.32	0.25	0.43	0.37	0.19	96.45	ldl	ldl	0.03	ldl	ldl	98.05
803352 (n=1)	0.19	0.27	0.23	0.40	0.13	98.32	ldl	ldl	ldl	ldl	ldl	99.54
803354 (n=1)	0.16	0.03	0.79	0.20	0.38	96.92	ldl	ldl	ldl	ldl	ldl	98.48
803360 (n=15)	0.35	0.11	0.75	0.42	0.59	96.78	ldl	ldl	0.02	ldl	ldl	99.02
802866A (n=7)	0.37	0.39	0.38	0.56	0.11	97.93	ldl	ldl	ldl	0.03	ldl	99.77
802866B (n=2)	0.15	0.27	0.44	0.25	0.04	97.57	ldl	ldl	ldl	ldl	ldl	98.72
803323A (n=3)	0.15	0.19	0.60	0.22	0.11	98.23	ldl	ldl	ldl	ldl	ldl	99.49
803323B (n=4)	0.23	0.18	0.79	0.34	0.21	97.74	ldl	ldl	ldl	ldl	ldl	99.48
803355A (n=4)	0.56	0.36	0.82	0.22	0.41	96.82	ldl	ldl	0.02	ldl	ldl	99.22
803355B (n=1)	0.21	0.29	0.53	0.22	0.41	97.50	ldl	ldl	ldl	ldl	ldl	99.15
RE41-1 (n=10)	0.18	0.14	0.66	0.31	0.28	97.55	ldl	ldl	ldl	ldl	ldl	99.13
RE41-2 (n=8)	4.21	0.92	1.74	1.10	0.09	91.09	ldl	ldl	ldl	0.06	ldl	99.22
RE51-2 (n=5)	0.15	0.08	0.64	0.30	0.48	97.53	ldl	ldl	ldl	0.03	ldl	99.22
RW39-1 (n=4)	4.82	1.82	1.16	1.08	0.09	91.14	ldl	ldl	0.02	0.11	ldl	100.25
RW41-1 (n=2)	3.15	0.94	1.26	0.64	0.21	92.98	ldl	ldl	0.08	ldl	ldl	99.26
RW41-2 (n=4)	3.12	0.84	1.20	0.82	0.14	93.52	ldl	ldl	0.03	0.07	ldl	99.73
RW43-2 (n=5)	1.70	0.49	0.92	0.86	0.23	95.91	ldl	ldl	0.05	0.05	ldl	100.21
RW45-1 (n=7)	0.79	0.26	0.83	0.24	0.28	97.36	ldl	ldl	ldl	0.03	ldl	99.79
RW49-1 (n=3)	0.76	0.29	1.01	0.42	0.59	96.38	ldl	ldl	0.02	0.02	ldl	99.48
RW49-2 (n=12)	2.60	0.35	1.40	0.91	0.29	94.13	ldl	ldl	0.04	0.05	ldl	99.76
RW49-3 (n=1)	ldl	0.04	0.87	0.18	0.31	97.70	ldl	ldl	ldl	ldl	ldl	99.11
RW75-1 (n=1)	ldl	0.06	0.37	0.42	0.59	97.92	ldl	ldl	0.03	ldl	ldl	99.37
RW87-2 (n=6)	0.35	0.45	0.67	0.32	0.60	97.71	ldl	ldl	0.02	ldl	ldl	100.12

Table 3.2: Average composition of each textural type of rutile found in gold-bearing and gold-barren syenite

Textural Type	Det Lim	WO_3 % 0.07	Cr_2O_3 % 0.02	V_2O_3 % 0.03	FeO % 0.02	Nb_2O_5 % 0.03	TiO_2 % 0.03	Cu_2O % 0.02	NiO % 0.02	SnO_2 % 0.02	Sb_2O_3 % 0.02	SiO_2 % 0.01	Oxide Totals
Au-Associated													
Granular (n=51)		0.73	0.26	0.79	0.46	0.39	96.87	0.00	0.00	0.02	0.02	0.00	99.54
Pseudomorphic (n=34)		0.30	0.17	0.71	0.26	0.35	97.45	0.00	0.00	0.01	0.01	0.00	99.26
Coarse pseudomorph (n=7)		0.28	0.24	0.55	0.29	0.27	97.26	0.00	0.00	0.02	0.02	0.00	98.94
Pyrite hosted (n=22)		4.20	1.18	1.42	1.30	0.06	91.36	0.00	0.00	0.03	0.07	0.00	99.63
Average Au-Associated:		1.38	0.46	0.87	0.58	0.27	95.73	0.00	0.00	0.02	0.03	0.00	99.34
Au-Barren													
Granular (n=50)		0.21	0.33	0.60	0.45	0.44	97.08	0.00	0.00	0.02	0.02	0.00	99.15
Pseudomorphic (n=34)		0.43	0.36	0.50	0.41	0.33	97.43	0.00	0.00	0.02	0.02	0.00	99.50
Coarse pseudomorph (n=8)		0.33	0.26	0.27	0.61	0.55	97.00	0.01	0.00	0.02	0.04	0.02	99.09
Hem-Mt residual (n=11)		0.55	0.08	0.23	0.72	0.28	97.50	0.00	0.00	0.01	0.08	0.00	99.47
Pyrite hosted (n=2)		0.94	0.67	0.27	1.05	0.11	96.96	0.00	0.00	0.02	0.03	0.00	100.05
Average Au-Barren:		0.49	0.34	0.37	0.65	0.34	97.19	0.00	0.00	0.02	0.04	0.00	99.45

Cr, data for Young-Davidson tends to be scattered towards the Fe-Cr-V apex. Pyrite-associated rutile grains are consistently enriched in W (Figure 3.12C) however, are comparatively depleted in Sb (strongly enriched in V and Cr) compared to other orogenic gold deposits (Clark and Williams-Jones, 2004). Hematite-magnetite associated rutile grains generally contain the highest Sb enrichments. The broad chemical overlap for all textural and gold associated types of rutile grains indicates that even rutile from 'least-altered' syenite samples has been influenced by fluids typical of orogenic lode gold deposits. This is likely related to the lack of ‘least-altered’, i.e., all samples are altered and thus contain W and Sb. Clark and Williams-Jones (2004) determined that, in general, background concentrations for the current elements in rutile are likely to be at or below detection limits, and that any measurable concentration of each element with the EMP represents some hydrothermal enrichment process. The broad overlap of rutile compositions also suggests that different textural types of rutile within zones of pervasive alteration cannot be distinguished chemically. We also must note that the substitution of elements into rutile is dependent on a number of physicochemical criteria, and more importantly is dependant on the specific polymorph of TiO_2 (Triebold et al., 2011). Since we find different textural types of rutile we must also consider the possibility that the textural types actually represent different polymorphs of TiO_2 in the syenite. Therefore, since the present dataset potentially includes multiple TiO_2 polymorphs, this should be included in any conclusions or interpretations drawn from the data.

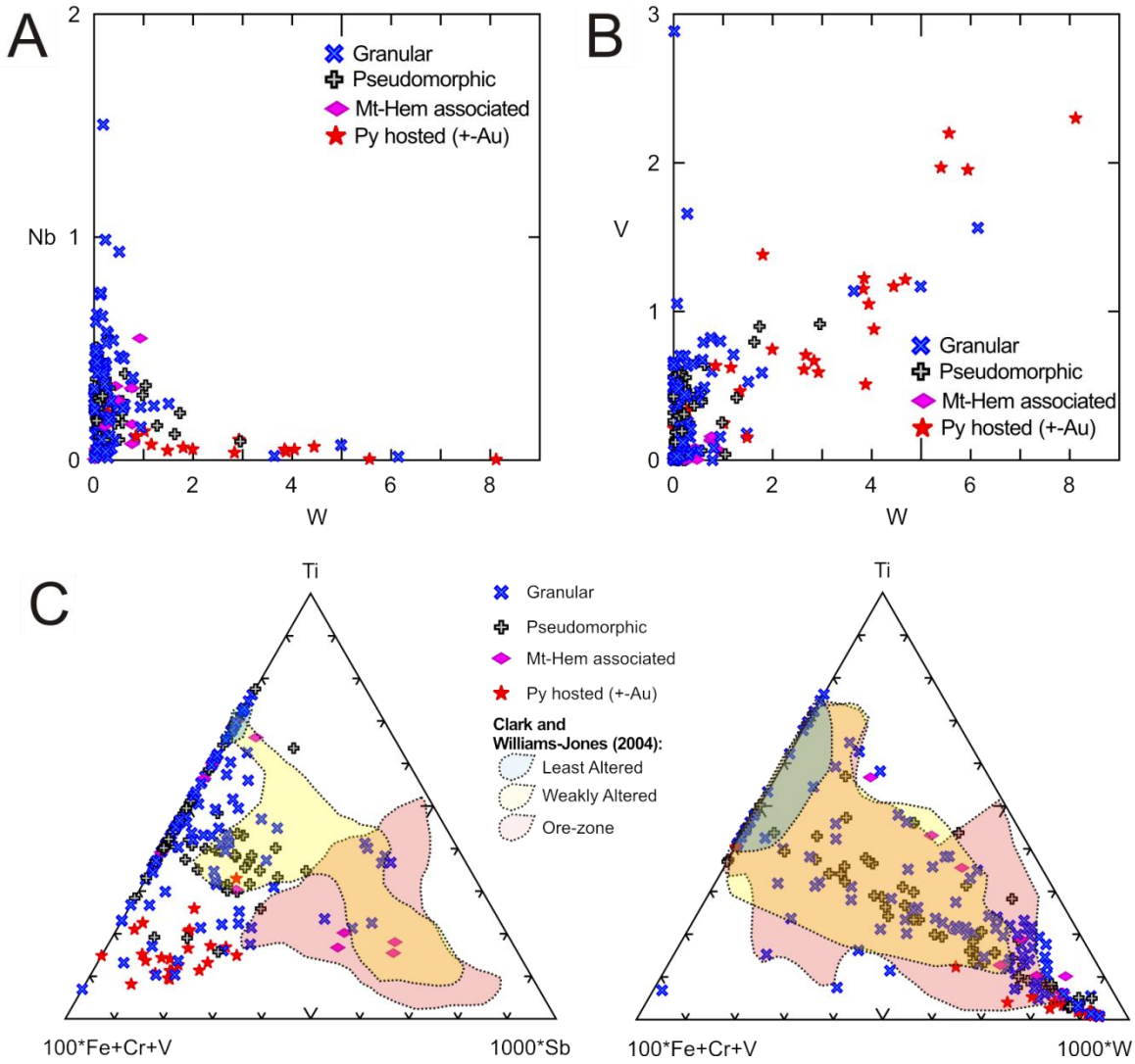

Figure 3.12: Geochemical characteristics of rutile grains at Young-Davidson. A) Nb vs W (elemental %) for each textural type of rutile; inverse Nb-W relationship could represent Nb loss during alteration. B) V vs W (elemental %) for each textural type of rutile; coupled V-W enrichment in rutile related to pyritization and groundmass alteration. C) Discrimination diagrams developed by Clark and Williams-Jones for rutile grains at orogenic gold deposits. Traced fields indicate regions for typical orogenic gold deposits from the Abitibi. Rutile grains at Young-Davidson show considerable W enrichment whereas they contain less Sb and instead contain significant quantities of V.

3.4.2 Pyrite

The results of pyrite point analyses are tabulated in Table 3.3 and presented in Figure 3.13. Pyrite textures, inclusion assemblages and vein association are the main criteria distinguishing type 1 from type 2 pyrite; in some samples both types are present and have been analyzed. Point analyses were

initially collected under the assumption of either isochemical or concentric-zoned pyrite grains. With this approach, points were chosen based on inclusion patterns; analyzing zones identified by inclusion abundance or core-rim relationships where inclusion zoning was absent. After a number of point analyses we found that the concentration of Au, Te and Pb was commonly at or below detection limits (Au < 390 ppm, Te < 298 ppm and Pb < 313 ppm); therefore further point analyses were limited to Co, Ni, As and Cu.

The data for point analysis is presented in Table 3.3 where the average analysis for each textural type of pyrite in each sample is presented. In general type 1 pyrite grains contain up to 1.234% Co, 0.39% Ni, 0.16% As and 0.03% Cu and type 2 pyrite grains up to 1.52% Co, 0.43% Cu, 0.43% As and 0.25% Ni. The main fields of each textural type of pyrite plotted on the Ni-Co-As ternary diagram in Figure 3.13 do not chemically corroborate the textural characterization. Results from these analyses are difficult to interpret due to inconsistent core-rim relationships, and > 1000 ppm variation of each element with the same grain. Therefore chemical maps were collected to determine the spatial variation of each element within pyrite (Craig et al., 1998; Craig, 2001).

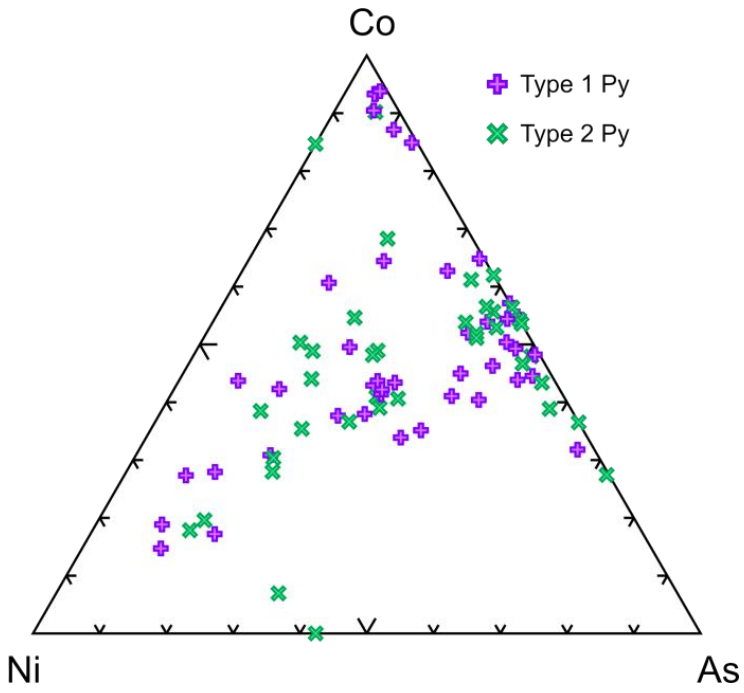

Figure 3.1: Compositional discrimination of different textural types of pyrite mineralization at Young-Davidson; Ni-Co-As compositions from different textural types of pyrite mainly overlap.

Table 3.3: Average pyrite compositions from each analyzed sample, pyrite grouped by textural type. ldl indicates lower detection limit.

SampleID	Pyrite Type	Fe %	S %	Ni %	Co %	As %	*Cu %	Elemental Totals
Avg Det.Lim (%)		0.024	0.056	0.011	0.011	0.007	0.007	
Volcanic:								
800916 (n = 4)	**1**	46.27	53.94	**ldl**	0.091	0.062	0.008	100.37
800919A (n=3)	**1**	46.54	53.44	0.041	**ldl**	**ldl**	**ldl**	100.03
800923B (n=7)	**1**	46.34	53.34	0.017	**ldl**	**ldl**	**ldl**	99.70
800927B (n=1)	**1**	46.35	53.33	**ldl**	**ldl**	**ldl**	-	99.69
Sediments:								
E21-3 (n = 3)	**2**	45.84	54.04	0.127	0.088	0.052	0.024	100.17
Syenite Drill Core:								
800940 (n = 2)	**2**	46.32	53.77	**ldl**	0.079	0.053	0.022	100.25
802803 (n = 3)	**1**	47.22	53.60	0.020	0.072	0.074	-	100.98
802809 (n = 2)	**1**	47.20	53.58	**ldl**	0.071	0.076	-	100.93
802809 (n = 2)	**2**	47.11	53.55	0.035	0.099	0.077	-	100.87
802822 (n = 1)	**2**	45.62	53.48	0.061	1.524	0.105	-	100.79
802825 (n = 13)	**1**	45.91	53.82	0.085	0.431	0.064	0.015	100.33
802826 (n = 3)	**1**	47.27	53.64	**ldl**	0.079	0.075	-	101.07
802826 (n = 1)	**2**	47.12	53.67	**ldl**	0.069	0.073	-	100.93
802838 (n = 2)	**1**	47.07	53.63	0.062	0.088	0.074	-	100.93
802838 (n = 2)	**2**	46.80	53.46	0.115	0.424	0.254	-	101.05
802841 (n = 3)	**1**	47.11	53.61	0.122	0.124	0.076	-	101.04
802842 (n = 1)	**1**	46.94	53.54	0.065	0.107	0.073	-	100.73
802842 (n = 2)	**2**	47.03	53.54	0.031	0.081	0.076	-	100.75
802940 (n = 4)	**2**	46.02	53.95	0.078	0.067	0.052	0.018	100.19
803307 (n = 4)	**1**	46.09	53.83	0.207	0.126	0.054	0.009	100.31
803307 (n = 4)	**2**	45.98	53.53	0.067	0.156	0.036	0.008	99.77
RE53-1 (n=3)	**1**	46.44	53.42	0.033	**ldl**	**ldl**	**ldl**	99.90
RE73-1 (n = 6)	**2**	46.06	54.33	0.039	0.068	0.061	0.089	100.64
RE87-1 (n = 4)	**1**	46.29	53.88	0.105	0.128	0.052	0.018	100.47
RW47-1 (n = 3)	**2**	46.25	54.05	0.057	0.113	0.054	0.016	100.54
RW53-1 (n = 5)	**1**	46.11	54.10	0.021	0.162	0.053	0.014	100.47
RW53-1 (n = 4)	**2**	45.69	53.76	0.072	0.105	0.053	0.013	99.69
YD06-3626 (n=8)	**1**	46.82	53.53	0.065	**ldl**	**ldl**	**ldl**	100.41
Regional Syenite:								
R27-3 (n = 4)	**2**	45.85	53.77	0.041	0.095	0.117	0.038	99.92
R59-1 (n=1)	**2**	46.40	53.36	0.020	**ldl**	**ldl**	**ldl**	99.78

*** - not analyzed**

Reflected light photomicrographs and corresponding Co and Ni elemental maps of different textural and vein associated types of pyrite are shown in Figure 3.14 to Figure 3.18. In each figure, the reflected light image is presented on the left, with the corresponding EMP maps presented on the right. In each map, brighter grey areas outline the distribution of increased concentrations of each element in that pyrite grain. With the present machine conditions we found that the EMP can successfully resolve spatial variations of Co and Ni in pyrite at concentrations > 600-1000 ppm. The

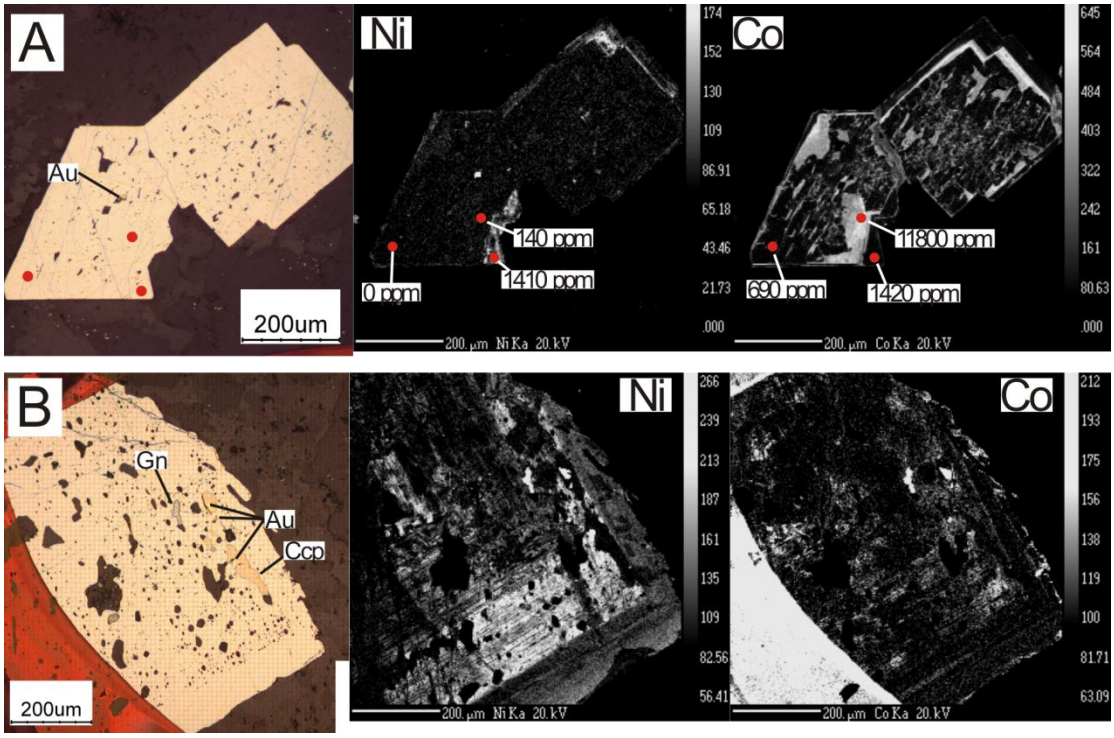

Figure 3.14: Reflected plane polarized light photomicrographs and corresponding EMP chemical maps of type 1 pyrite in V_1 veins. A) Euhedral V_1 vein hosted pyrite from sample where V_1 vein is crosscut by quartz-carbonate vein. Complex Co-zoning patterns indicate initial stage of Co-poor pyrite has been corroded and overgrown by Co-rich hydrothermal phase (with which gold is associated) and then finally overprinted by a Co-poor and Ni-rich phase of hydrothermal pyrite. B) Typical magnetite-bearing type 1 pyrite from V_1 veins. Original Ni-poor pyrite at center has been overgrown by a gold-associated Ni-rich phase, then finally overprinted by a final barren inclusion free Ni-poor pyrite phase.

results from As mapping were less successful because As, counted with the As La line, showed interference from Mg (Mg Kα and Mg Kβ peaks; Henderson, pers. comm 2011). To address this issue we attempted to map the As Kα peak instead. In general, Young-Davidson pyrite ranges from < 500-4200 ppm As (avg 687 ppm), which is relatively low compared to other gold deposits where up to 6 wt% As may correlate with invisible gold in pyrite (Fleet et al., 1993). We found that the combination of low As contents, short mapping runtimes and generally low counts-per-second from the As Kα peak resulted in high detection limits for As on As Kα maps, and consequently no visible As variations in the resulting map. Therefore As maps have been omitted from the results presented in this section. Chemical maps presented in Figure 3.14 to Figure 3.18 have been digitally enhanced using Corel PhotoPaint x5 ™; contrast bracketing was modified to highlight any chemical zoning in each pyrite grain. Following chemical maps, point analyses were collected in different chemical zones of zoned pyrite grains, and where available, the point location and concentration of each element is indicated on each map.

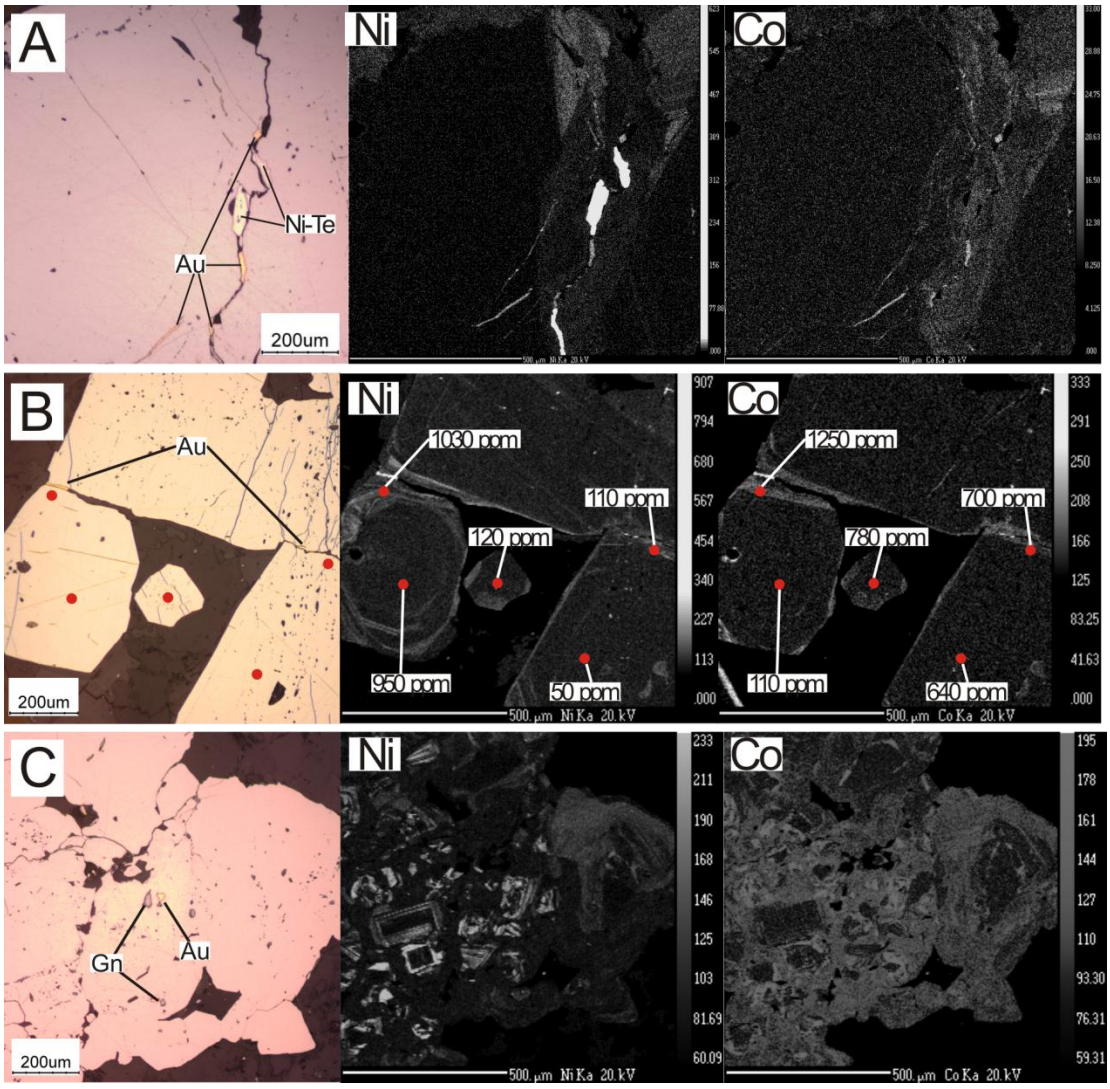

Figure 3.15: Reflected plane polarized light photomicrograph and corresponding EMP chemical maps of type 1 pyrite in V_2 veins. A) Type 1 pyrite in mineralized V_2 vein showing Ni and Co enrichment along a Au + Ni-Te bearing fracture in the pyrite. Fracture is enriched relative to the rest of the grain and all gold found in the pyrite along this fracture is associated with the Ni-Co enrichment. B). Type 1 pyrite in V_2 vein with Au along fractures, enrichment of Co and Ni in the Au-associated fractures within the pyrite grain. C) Type 1 pyrite from sediment hosted V_2 vein showing complex Ni and Co zoning; Ni appears to consist of concentric crystallographically oriented zoning patterns that are welded together by Co-rich hydrothermal overgrowths.

Cobalt and nickel maps of type 1 pyrite associated with V_1 veins are shown in Figure 3.14A and B where pyrite from separate V_1 veins from different locations shows complex Co and Ni hydrothermal overgrowth patterns. The euhedral pyrite grain in Figure 3.14A has textural characteristics of type 2 pyrite; however, chemical mapping reveals an early Co-Ni poor phase of corroded pyrite that has been overprinted by at least 2 episodes of Co-Ni rich hydrothermal pyrite. Gold mineralization in this grain is associated with the Co-rich hydrothermal pyrite found in the center of the grain, and was

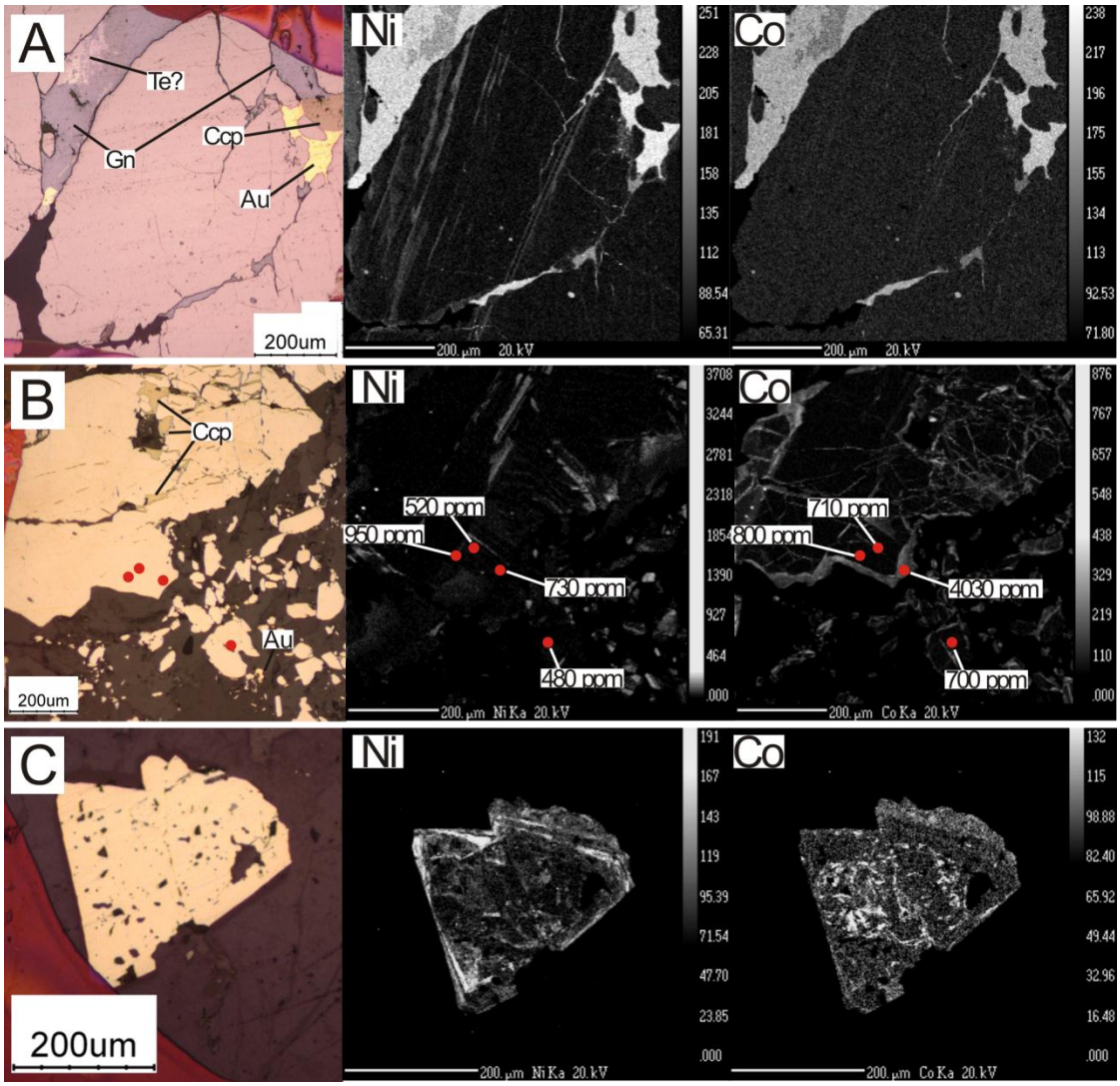

Figure 3.16: Reflected plane polarized light photomicrograph and corresponding EMP chemical map of type 2 pyrite associated with V_3 veins. A) Type 2 pyrite crosscut by Au-Pb-Cu-Te mineralization in V_3 vein; Linear Ni-wisps are crosscut by gold mineralization in this sample. B) Type 2 pyrite on edge of quartz-carbonate vein, Co-Ni enrichments along edges of pyrite grain, gold is associated with fine pyrite in the vein (bottom right). C) Type 2 pyrite in V_3 vein showing variable Ni contents in different stages of the mineralizing fluids.

potentially deposited with the Co-rich pyrite, or from dissolution of the earlier pyrite grain (Figure 3.14A). Similarly in Figure 3.14B the center of the pyrite grain is Ni-poor, and Au is associated with the Ni-rich band towards the outer portion of the grain. Based on these V_1 pyrite maps, V_1 veins are interpreted to contain Co-Ni-poor magmatic-hydrothermal pyrite that has been overprinted by Co-Ni-bearing hydrothermal fluids that deposited gold. Figure 3.14A also highlights the utility of chemical mapping in understanding hydrothermal pyrite textures. Point analyses on V_1 zoned pyrite grains

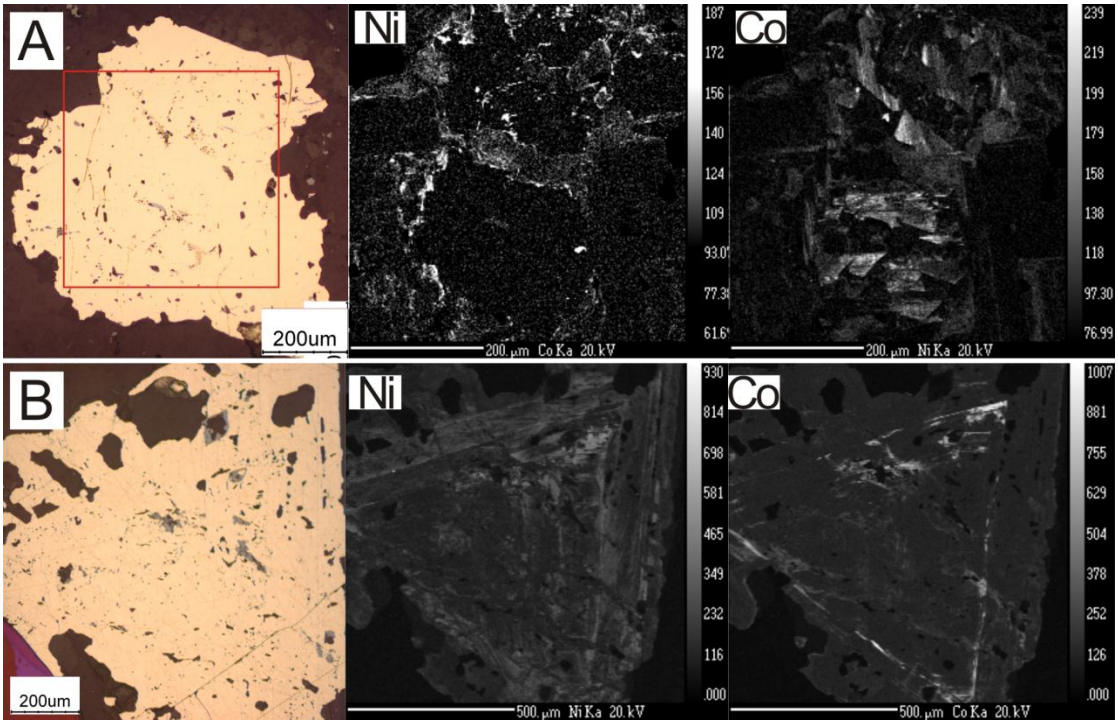

Figure 3.17: Reflected plane polarized light photomicrographs and corresponding EMP chemical maps of type 1 disseminated pyrite. A) Mineralized type 1 pyrite in V_3 alteration halo with extremely chaotic Co and Ni zoning patterns; Au appears to coincide with Ni enrichment between Ni-poor domains. B) Anhedral type 1 corroded from barren V_3 vein sample; embayment into pyrite crosscut crystallographically controlled Co-zoning patterns.

indicate up to 12,000 ppm Co in Co-rich pyrite overgrowths whereas up to 1400 ppm Ni is present in Ni-rich zones of pyrite (Figure 3.14A).

Cobalt and nickel maps of type 1 pyrite grains from V_2 veins are shown in Figure 3.15. Chemical maps presented in Figure 3.15A show that fracture-related Au and Ni-Pb-Te mineralization is associated with Co-Ni enrichment along the mineralized fracture, and Ni enrichment along the top of the pyrite grain towards the outside of the vein. This relationship suggests that gold mineralization is associated with later Co-Ni-bearing fluids along a fracture in pyrite that occurred after an initial Co-Ni poor phase of pyrite deposition. Figure 3.15B shows type 1 pyrite hosted in a V_2 vein where gold is associated with Co-Ni enrichments along fractures and outer boundaries of the pyrite. This relationship is similar to that presented in Figure 3.15A, however, in this case the central pyrite grain contains minor Ni enrichment as linear wisps through the grain. By contrast, Figure 3.15C shows a Timiskaming-hosted V_2 vein where gold and galena are present as inclusions in a fractured anhedral pyrite grain. The sediment hosted grains show complex Ni zoning patterns that indicate early texturally euhedral phases of pyrite grew in the presence of Ni-rich fluids. These initial euhedral

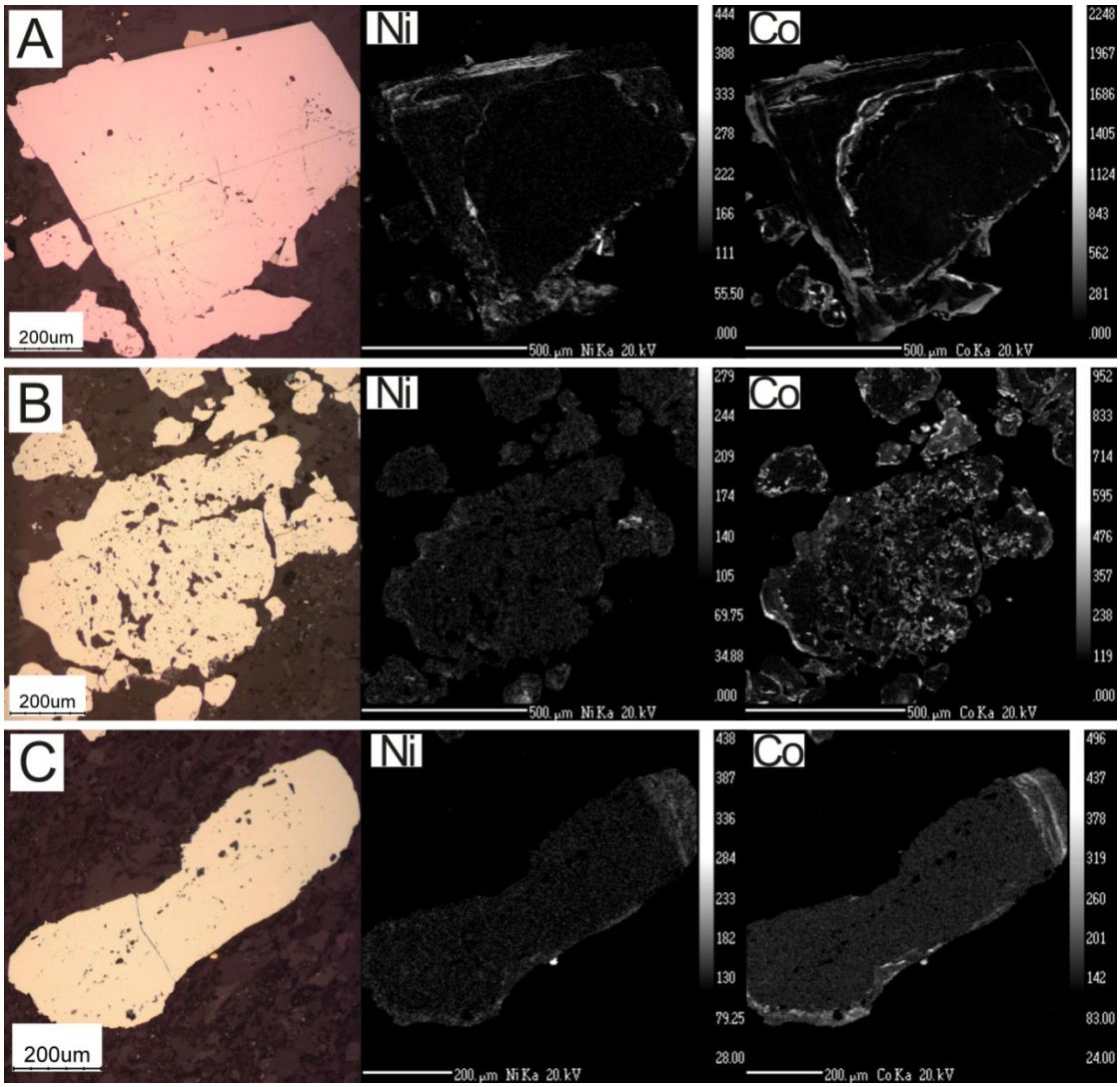

Figure 3.18: Reflected plane polarized light photomicrograph and corresponding EMP chemical maps of type 1 volcanic-hosted pyrite. A) Euhedral inclusion free pyrite grain from weakly altered sample showing abundant Co-Ni zoning patterns. B) Corroded pyrite from mineralized sample showing chaotic Co zoning patterns, and relatively minor Ni-zoning. C) Anhedral pyrite grain with minor Co-Ni zoning associated with fine-grained gold inclusion outside the pyrite grain.

grains were subsequently enveloped by hydrothermal pyrite that is Co-enriched relative to the initial euhedral Ni-rich phases as the Co-poor rectangle-shaped domains spatially coincide with Ni-enrichments. Figure 3.15C shows that sedimentary pyrite textures have undoubtedly been influenced by metamorphic Co-Ni bearing hydrothermal fluids, and large complex textured grains are the combined result of several hydrothermal events.

Cobalt and nickel maps of type 2 pyrite from V_3 veins are shown in Figure 3.16. Type 2 pyrite grains contain Co and Ni enrichments similar to type 1 pyrite and earlier vein generations. Gold mineralization in type 2 pyrite grains has crosscut linear Ni-enrichments inside pyrite grains, indicating that gold mineralization is not associated with pyrite growth in this V_3 vein (Figure 3.16A). Figure 3.16B shows a fractured pyrite grain associated with a V_3 vein where gold occurs as free gold amongst the fine-grained pyrite to the lower right. The pyrite in this example has been fractured and is chemically enriched along grain boundaries and fractures; however, gold mineralization has occurred in the vein rather than associated with the pyrite. In general, both fractured and subhedral type 2 pyrite grains from V_3 veins show some component of chemical enrichment by Co and Ni bearing fluids (Figure 3.16B and C).

Cobalt and nickel maps of syenite-hosted disseminated pyrite are shown in Figure 3.17. Disseminated pyrite textures from a single sample are highly variable; euhedral to anhedral, corroded, fractured, inclusions rich and inclusion poor grains can all occur in the same thin section. The pyrite grain in Figure 3.17A hosts gold, hematite and chalcopyrite mineral inclusions that are associated with areas of chaotic Co-Ni enrichment within the grain. By contrast, the grain mapped in Figure 3.17B is unmineralized and shows chemical zoning that suggests that fluid compositions changed during pyrite deposition. The euhedral concentric zoning within the grain has also been crosscut by gangue minerals embayed into the grain suggesting pyritization has been followed by some component of pyrite dissolution, even in unmineralized samples.

Cobalt and nickel maps of volcanic hosted pyrite grains are shown in Figure 3.18. The chemical maps presented in Figure 3.18A are of pyrite from a weakly altered sample. This grain shows that with weak alteration and deformation, separate hydrothermal phases of pyrite can be identified. Similarly, the maps in Figure 3.18B are of pyrite associated with weak alteration and deformation. This grain shows little Ni-zoning but considerable Co around the outside edges of the pyrite grain. Finally, the pyrite grain from Figure 3.18C is from an intensely altered sample and has minor Ni-enrichment around the rim, but considerable Co-enrichment around the rim. In general, the chemical heterogeneities are greatest in volcanic-hosted pyrite grains from weakly altered samples. In pervasively altered samples, it appears as if the pyrite grains have been homogenized to a certain extent, with final stages of hydrothermal overprint. Pyrite from sedimentary rocks, volcanic rocks and syenite all contain similar Co-Ni enrichments, suggesting similar fluids have controlled pyrite

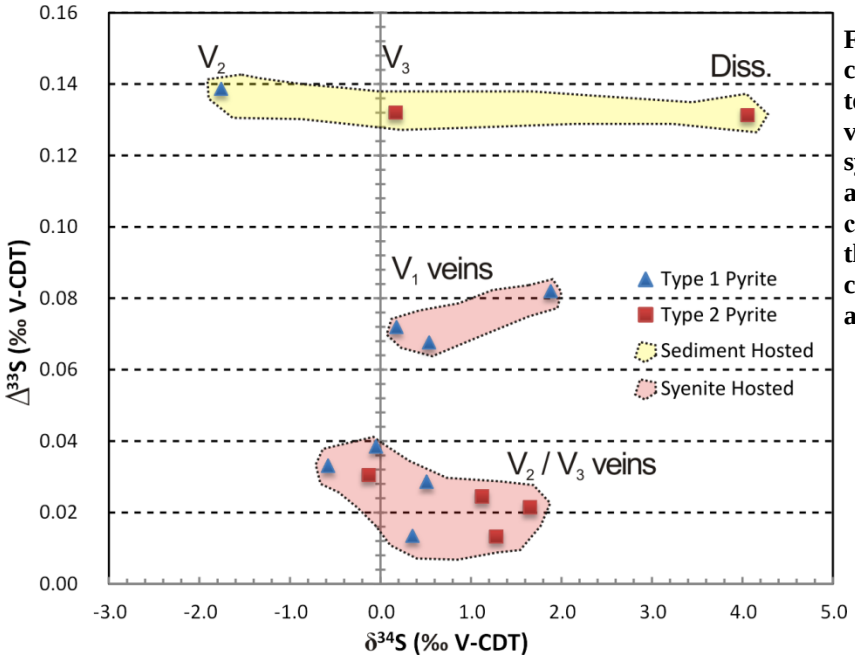

Figure 3.2: Bulk sulfur isotopic composition of different textural types of pyrite from veins hosted in sediments and syenite from the UBZ study area. In general type 2 pyrite contains higher $\delta^{34}S$ values than type 1, however, there is considerable overlap between all analyzed phases of pyrite.

deposition in all lithologies.

Bulk sulfur isotopic analyzes of syenite and sediment hosted pyrite grains are shown in Figure 3.19. Vein-associated pyrite grains from the syenite range from -0.6‰ to 1.9‰ $\delta^{34}S$ indicating a dominantly magmatic source of sulfur (Figure 3.19). Sedimentary hosted pyrite grains show increased deviation from the magmatic $\delta^{34}S$ value representing origination from a non-magmatic source. Deviation from 0‰ in $\Delta^{33}S$ for all pyrite analyses indicates some component of sulfur that has interacted with the reduced Archean atmosphere. The combined $\Delta^{33}S$ and $\delta^{34}S$ isotopic compositions of the pyrite at Young-Davidson indicate that the source of sulfur is likely a mixture of igneous and sedimentary sulfur. Electron microprobe mapping of pyrite grains has shown that the grains are chemically zoned and since the sulfur isotope analyses are bulk analyses, there may be sulfur isotopic variation within individual pyrite grains. Addressing this question is beyond the scope of the current study.

3.4.3 Gold

The results of gold grain analysis are shown in Table 3.4 and Figure 3.21. Gold mineralization is subdivided based on the vein type and associated pyrite textures. Syenite-hosted gold grains are found as inclusions and along fractures in type 1 pyrite in V_1, V_2, disseminated pyrite, along fractures in

Table 3.4: Average gold grain compositions in elemental %, grouped by vein and pyrite association. ldl indicates lower detection limit.

Sample ID	Gold Association	Si	Au	Ag	S	Fe	Cu	Pb	Se	Totals
Avg Det.Lim (%)		0.02	0.24	0.14	0.05	0.04	0.05	0.35	0.05	
RW53-1.1 (n= 1)	V_1 vein	0.05	89.45	10.42	0.13	1.23	ldl	ldl	ldl	101.27
RW39-1 (n= 6)	V_2 and Free	0.11	92.26	7.95	0.09	0.13	ldl	ldl	ldl	100.54
RE45-1 (n= 1)	V_2 vein	0.13	91.58	7.96	0.08	0.62	0.08	ldl	ldl	100.44
RE45-1A (n= 6)	V_2 vein	0.05	92.08	7.95	0.14	0.58	ldl	ldl	ldl	100.79
RW43-2 (n= 5)	V_2 vein	0.05	93.26	7.37	0.11	0.26	ldl	ldl	ldl	101.05
RW45-2.1 (n= 1)	V_2 vein	0.10	89.50	9.87	0.24	1.05	ldl	ldl	ldl	100.76
RW45-2.2 (n= 1)	V_2 vein	0.05	92.59	6.55	0.21	0.86	0.06	ldl	ldl	100.34
RW49-2 (n= 6)	V_2 vein	0.09	90.55	9.73	0.15	0.63	ldl	ldl	ldl	101.15
YD06-01A-3493A (n= 1)	V_2 vein	0.32	91.36	7.15	0.15	0.35	0.15	ldl	0.06	99.55
YD06-01A-3626 (n= 12)	V_2 vein	0.05	92.74	8.15	0.07	0.21	ldl	ldl	ldl	101.21
W25-2 (n= 1)	V_2 vein	0.13	94.74	3.57	0.24	1.62	0.09	ldl	ldl	100.40
802926 (n= 14)	V_2-V_3 vein	0.03	89.82	10.89	0.07	0.18	ldl	ldl	ldl	101.00
802884 (n= 15)	V_3 Free	0.10	85.04	15.11	0.06	0.06	ldl	ldl	ldl	100.37
802866B (n= 1)	V_3 vein	0.44	84.74	13.01	0.20	0.84	ldl	ldl	0.07	99.31
E19-2.1 (n= 1)	V_3 vein	0.09	88.11	12.02	0.15	0.68	ldl	ldl	ldl	101.05
RW41-2 (n= 5)	V_3 vein	0.06	91.37	8.15	0.11	0.66	ldl	ldl	ldl	100.35
YD06-01-3769 (n= 3)	V_3 vein	0.06	87.91	11.55	0.43	0.42	ldl	ldl	ldl	100.37

type 2 pyrite in V_3 veins and as free gold along quartz-carbonate grain boundaries in V_3 veins. Since most gold mineralization at Young-Davidson consists of very fine inclusions inside pyrite, Fe and S were analyzed to measure influence of the surrounding pyrite. In order to determine the smallest grain size that was possible to analyze with these methods, a 45 µm transect with 5 µm step size was

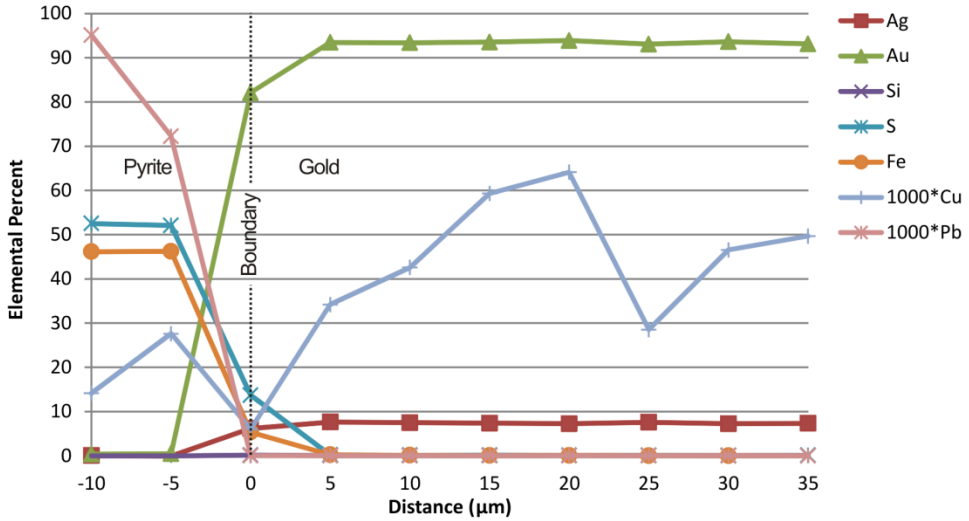

Figure 3.20: Results of a 45 µm transect across a gold-pyrite grain boundary indicating that the influence of pyrite 5 µm from the gold-pyrite grain boundary with the present machine conditions is negligible.

analyzed, beginning in pyrite and ending in the center of a relatively large gold inclusion (Figure 3.20). The influence of pyrite is negligible 5 μm from the gold-pyrite boundary (i.e., combined Fe and S in analysis is < 2 elemental %), and therefore the smallest gold inclusion that we are able to analyze with these machine conditions is approximately 10 μm in diameter. The results from gold analysis show that free gold in V_3 veins and along fractures in pyrite hosted in V_3 veins is enriched in Ag relative to gold associated with V_1, V_2 and disseminated pyrite (Figure 3.21). It is also apparent that, although tellurides are associated with gold in some samples, the majority of gold at Young-Davidson is as native gold grains hosted in pyrite or V_3 veins.

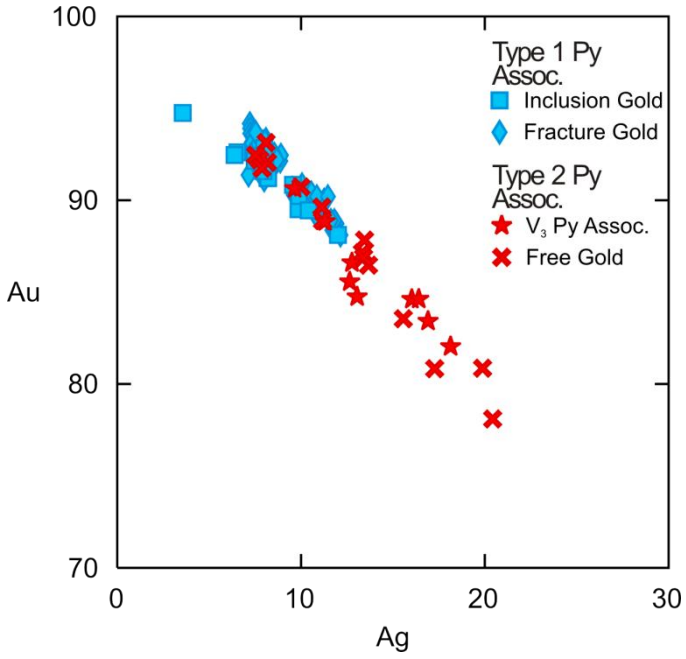

Figure 3.3 Au vs. Ag for texturally distinct styles of gold mineralization associated with different pyrite types. V_3 vein and free gold are enriched in Ag relative to inclusion and fracture gold grains. V_3 and free gold are also texturally late and tend to be associated with tellurides, galena and chalcopyrite whereas inclusion and fracture gold is associated with corroded magnetite-hematite bearing pyrite grains in the earlier vein sets.

3.5 Discussion

In general, the enrichments of W, V, Fe and Sb in rutile grains at Young-Davidson are consistent with the elemental enrichments in rutile at orogenic gold deposits in the Abitibi (Clark and Williams-Jones, 2004), orogenic gold deposits from Australia (Scott and Radford, 2007) and from gold-scheelite-bearing veins in Bolivia (Rice et al., 1998). Scott (2005) noted that Cu-Au porphyry-associated rutile grains from several deposits in Australia are characteristically V-enriched in ore zones compared to grains outside of ore zones. This led Scott (2005) to conclude that rutile compositions can be used to vector towards mineralization in Cu-Au porphyry deposits in Australia. Similarly, Clark and Williams-Jones (2004) have shown that W and Sb in rutile can be used to vector towards mineralization in orogenic gold deposits from the Abitibi greenstone belt, Canada. Since intrusion-associated gold deposits are also known to have a W association (Hart, 2007) the elevated W and V concentrations in gold-associated rutile grains at Young-Davidson are potentially explained by rutile interaction with intrusion-related hydrothermal fluids in addition to orogenic fluids. The Sb contents of rutile at Young-Davidson are atypical of porphyry systems (Clark and Williams-Jones, 2004) and, combined with the high W contents and the association of gold and scheelite in late quartz-carbonate veins, suggests that the gold-related rutile grains at Young-Davidson have interacted with fluids typical of orogenic gold deposits.

An interesting consideration for the rutile analyses is the mechanism for highly-charged cation substitution into the rutile structure. Rice et al. (1998) provides a detailed characterization on rutile in a gold-scheelite-bearing vein from Bolivia. They detail W substitution in rutile such that coupled substitution of the highly charged W^{6+} cation with an undercharged cation (Fe^{2+}, Fe^{3+} or V^{3+}) is necessary to maintain electro neutrality. The calculated stoichiometry for rutile from the present study, grouped by W and V rich and W and V poor, is tabulated in Table 3.5, with the complete dataset presented graphically in Figure 3.22. Stoichiometry has been calculated assuming 6 oxygens and cation valences of Fe^{3+}, V^{3+}, Sb^{5+} and W^{6+}. Rice et al. (1998) propose double substitutions such that $2Ti^{4+} \rightarrow Fe^{3+}+M^{5+}$ (where M is the metal with corresponding valence) has occurred to maintain electrical neutrality. Based on this assumption, the Fe:M ratio is 1:1 and the (Fe+M):Ti ratio is 1:-1. Based on the normalized cations calculated from the data collected in this study, the proposed double substitution for Young-Davidson rutile grains is either: 1) $V^{3+}+W^{6+} \rightarrow 2Ti^{4+}$ (Figure 3.22A and B); or 2) $2V^{3+}+W^{6+} \rightarrow 3Ti^{4+}$ (Figure 3.22C and D). For the first case, the normalized cation plot in Figure 3.22A shows a 1.14:1, V:W ratio whereas Figure 3.22B shows a 1:-1.44 (V+W):Ti ratio. Alternatively for the second case, the normalized cation plot in Figure 3.22D shows a 1.76:1, 2V:W

Table 3.5: Calculated stoichiometry for typical W and V rich and W and V poor rutile grains

	W and V Rich									W and V poor							
SampleID	**RW49-2**	**RW41-2**	**RW49-2**	**RE41-2**	**RE41-2**	**802907A**	**RW41-1**	**RE41-2**	**RW39-1**	**802864**	**802857**	**803307B**	**803307B**	**803307B**	**802841**	**802809**	**802838**
TestID	P1001-32-2	P1001-5-2	P1001-32-1	P1001-019-3	P1001-019-3	P1111-47-2	MP015-1	P1001-018-1	MP010-1	P1007-18-2	P1007-5-1	P1111-9-2	P1111-9-1	P1111-8-2	RT-107-1	RT-090-2	RT-102-1
Cr2O3	0.245	1.087	0.556	1.486	1.593	0.123	1.860	0.799	1.875	0.541	0.060	0.000	0.074	0.043	0.749	0.939	0.191
Cu2O	0.000	0.000	0.000	0.000	0.000	0.000	0.000	0.000	0.000	0.000	0.000	0.000	0.000	0.000	0.000	0.000	0.000
Fe2O3	3.290	1.741	1.807	1.149	1.242	1.762	1.066	2.161	0.911	0.476	0.456	0.428	0.427	0.399	0.505	0.124	0.411
Nb2O3	0.000	0.000	0.000	0.000	0.000	0.414	0.096	0.000	0.086	0.615	0.299	0.181	0.223	0.210	0.035	0.000	0.049
NiO	0.000	0.000	0.000	0.000	0.000	0.000	0.000	0.000	0.000	0.000	0.000	0.000	0.000	0.000	0.000	0.000	0.000
Sb2O5	0.069	0.104	0.077	0.111	0.105	0.036	0.026	0.089	0.122	0.000	0.040	0.000	0.000	0.000	0.090	0.000	0.000
SiO2	0.000	0.000	0.000	0.000	0.000	0.000	0.000	0.000	0.000	0.000	0.000	0.000	0.000	0.000	0.000	0.000	0.000
SnO2	0.051	0.056	0.061	0.028	0.000	0.037	0.154	0.026	0.029	0.000	0.000	0.000	0.000	0.000	0.000	0.000	0.000
Ta2O5	0.000	0.000	0.000	0.000	0.000	0.000	0.000	0.000	0.000	0.000	0.000	0.000	0.000	0.000	0.000	0.000	0.000
TiO2	82.692	86.915	86.587	86.085	86.268	87.715	88.093	88.629	89.701	97.630	97.638	99.471	99.033	99.477	98.369	98.118	99.202
V2O3	3.383	2.298	2.872	3.233	2.895	3.058	1.718	1.787	1.719	0.236	0.213	0.208	0.177	0.157	0.130	0.106	0.000
WO3	10.239	7.748	7.493	7.017	6.811	6.686	6.292	5.901	5.606	0.000	0.000	0.000	0.000	0.000	0.000	0.000	0.000
Oxide Totals	99.973	99.971	99.453	99.115	98.928	99.832	99.304	99.391	100.048	99.560	98.778	100.330	99.980	100.304	99.973	99.318	99.899
Cations normalized to 6 oxygens (Ti3O6 assumed)																	
Cr	0.008	0.036	0.019	0.050	0.053	0.004	0.062	0.026	0.061	0.017	0.002	0.000	0.002	0.001	0.024	0.030	0.006
Cu	0.000	0.000	0.000	0.000	0.000	0.000	0.000	0.000	0.000	0.000	0.000	0.000	0.000	0.000	0.000	0.000	0.000
Fe3+	0.035	0.018	0.019	0.012	0.013	0.019	0.011	0.023	0.009	0.005	0.005	0.004	0.004	0.004	0.005	0.001	0.004
Nb	0.000	0.000	0.000	0.000	0.000	0.009	0.002	0.000	0.002	0.013	0.006	0.004	0.005	0.004	0.001	0.000	0.001
Ni	0.000	0.000	0.000	0.000	0.000	0.000	0.000	0.000	0.000	0.000	0.000	0.000	0.000	0.000	0.000	0.000	0.000
Sb5+	0.001	0.001	0.001	0.001	0.001	0.000	0.000	0.001	0.001	0.000	0.000	0.000	0.000	0.000	0.001	0.000	0.000
Si	0.000	0.000	0.000	0.000	0.000	0.000	0.000	0.000	0.000	0.000	0.000	0.000	0.000	0.000	0.000	0.000	0.000
Sn	0.001	0.001	0.001	0.000	0.000	0.001	0.003	0.000	0.000	0.000	0.000	0.000	0.000	0.000	0.000	0.000	0.000
Ta	0.000	0.000	0.000	0.000	0.000	0.000	0.000	0.000	0.000	0.000	0.000	0.000	0.000	0.000	0.000	0.000	0.000
Ti	2.656	2.744	2.745	2.735	2.743	2.762	2.778	2.786	2.795	2.961	2.977	2.983	2.981	2.983	2.965	2.972	2.985
V3+	0.116	0.077	0.097	0.110	0.098	0.103	0.058	0.060	0.057	0.008	0.007	0.007	0.006	0.005	0.004	0.003	0.000
W6+	0.113	0.084	0.082	0.077	0.075	0.073	0.068	0.064	0.060	0.000	0.000	0.000	0.000	0.000	0.000	0.000	0.000
Totals:	2.930	2.962	2.963	2.985	2.983	2.969	2.982	2.960	2.987	3.003	2.998	2.997	2.998	2.998	3.000	3.007	2.997

Assumptions and Molar Masses

# of Oxygens	**Cr2O3**	**Cu2O**	**FeO**	**Nb2O3**	**NiO**	**Sb2O5**	**SiO2**	**SnO2**	**Ta2O5**	**TiO2**	**V2O3**	**WO3**	**Fe2O3**
6	**151.99**	**143.091**	**71.846**	**233.811**	**74.6928**	**323.511**	**291.512**	**150.709**	**409.894**	**79.88**	**149.881**	**231.85**	**159.692**

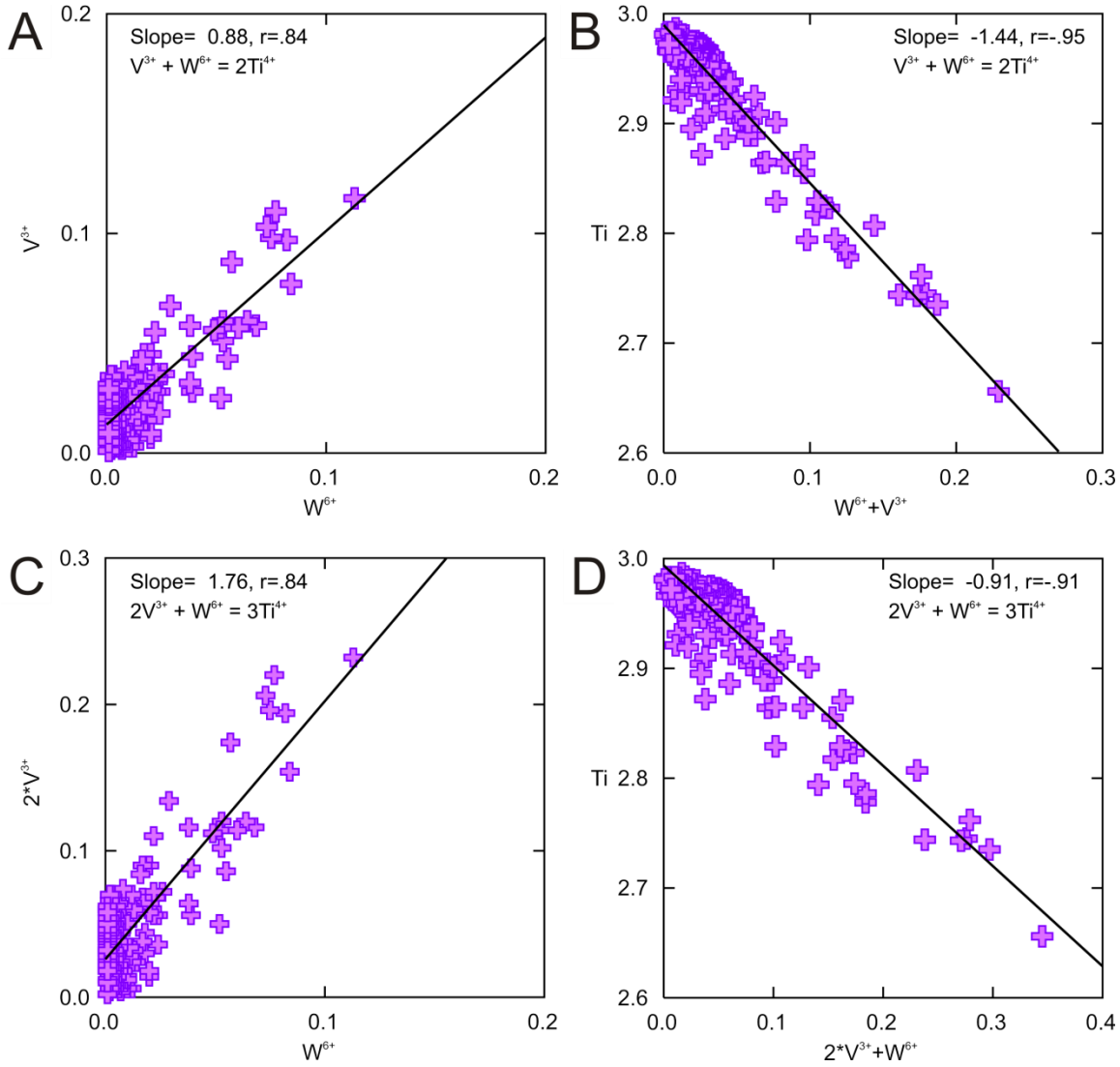

Figure 3.22: Cation plots for normalized rutile data, assuming 6 oxygens and the valences outlined above. A and B) Assuming a substitution scheme for Ti of $V^{3+}+W^{6+}\rightarrow 2Ti^{4+}$. C and D) Assuming a substitution scheme for Ti of $2V^{3+}+W^{6+}\rightarrow 3Ti^{4+}$.

ratio whereas Figure 3.22D shows a 1.1:-1, (2V+W):Ti ratio. Since there are many other valence possibilities for V, Fe, Sb and W, this data qualitatively supports coupled substitution of W and V, however, the substitution is likely much more complex than this simplified version. Additionally, Rice et al. (1998) and Scott (2005) have identified chemical zoning in the hydrothermal rutile grains. Based on BSE images observed during EMP analysis, significant zoning as observed by Rice et al. (1998) is absent from the rutile analyzed in this study. The study by Triebold et al. (2011) has also shown that the substitution of each element in rutile varies by TiO_2 polymorph; there are systematic

differences in the Cr, V, Fe, and Nb substitutions into the 3 TiO_2 polymorphs anatase, brookite and rutile. A problem with this is that differentiation of the 3 polymorphs by optical microscopy is essentially impossible (Triebold et al., 2011). Based on a subset of whole rock XRD analyses, rutile and potentially anatase have been identified in altered syenite (Naderi, pers. comm. 2012), however, further in situ testing is warranted to determine which TiO_2 polymorphs are present at Young-Davidson. Therefore since the analyzed rutile grains at Young-Davidson likely encompass different polymorphs, the results presented in this study only qualitatively support interaction of these rutile grains with hydrothermal fluids that are characteristic of orogenic lode gold deposits.

Pyrite textures at Young-Davidson suggest that multiple fluid events controlled the sulfide morphology and either directly controlled gold deposition or acted to redistribute gold. The oxide-hosting textures of many pyrite grains throughout the syenite can be interpreted as poikiolitic pyrite grains where pyrite has encompassed earlier magnetite and hematite grains during pyrite growth. Alternatively fluids could have dissolved pyrite and deposited oxide minerals in the secondary porosity. Chemical mapping of pyrite grains has shown that dissolution did occur within pyrite grains. Additionally, the common orientation of dissolved domains within pyrite can be interpreted as either dissolution or pyrite growth under some stress (e.g., Figure 3.14A). Therefore pyrite grains may contain variable dissolution characteristics depending on the physical stress: along grain boundaries, along fractures or additionally within the pyrite grain. Pyrite grains that host oxide inclusions in crystallographically controlled zones are believed to form by sulfidation where pyrite has consumed oxide grains. Gold mineralization in these examples is either directly hosted with the oxide mineral inclusions in these pyrite grains (Mt-Hem-Au inclusion), or is found as native gold inclusions associated with the oxide-rich zone within the pyrite grain. By contrast, fracture controlled styles of mineralization appear to be related to pyrite dissolution rather than pyrite growth and the association of gold to oxides is spatial rather than genetic. The corroded nature of pyrite grains and the abundance of hematite and magnetite at Young-Davidson with contrasting overprinting relationships indicate that there were likely multiple fluids with different physicochemical conditions. For example, in type 1 pyrite where gold inclusions are associated with magnetite and hematite rich zones inside the pyrite grain, pyrite precipitation appears to control gold mineralization. In contrast, where pyrite is corroded and hosts gold along fractures, other fluid mechanisms must control the observed style of mineralization. Oxide-bearing pyrite grains that are corroded suggest that at least 2 physicochemically distinct fluids have interacted with the syenite; the first to precipitate pyrite with oxide grains, and the

second to dissolve the pyrite along fractures. Additionally, since not all pyrite hosts oxide grains, there must be other pyrite precipitation mechanisms for those grains. Similarly, although sulfur isotopic compositions do not adequately delineate the textural types of pyrite (i.e., pyrite grains are zoned and all $\delta^{34}S$ values are approximately 0‰), the $\Delta^{33}S$ composition of pyrite suggest that there have been two sulfur sources. Although this does not necessarily imply 2 distinct fluids, the simplest explanation is that there have been 2 fluid sources. Pyrite chemical mapping results confirm that multiple fluids have influenced pyrite (and gold) mineralization at Young-Davidson since we observe Co-Ni poor and Co-Ni rich hydrothermal phases of pyrite. Additionally where there is chemical zoning and gold mineralization, gold shows spatial association with distinct hydrothermal events. Therefore, a single fluid - single control model for gold mineralization at Young-Davidson does not sufficiently describe the observed mineralization styles.

The chemical pyrite textures presented in Figure 3.14 to Figure 3.18 show that syenite hosted pyrite grains contain elemental enrichments of Co and Ni. Pyrite mapping results presented in this study also confirm the complexity of pyrite textures in this deposit, and suggest that a textural study of pyrite (and potentially other hydrothermal sulfide minerals) at hydrothermal ore deposits is incomplete without considering the chemical textures. Studies by Ho et al. (1994; 1995) show that Co, Ni, Zn and Cu in pyrite grains are derived from mafic wall rock and that the low amounts of Co, Ni, Zn and Cu in granitoid-hosted pyrite grains, at Dargues Reef and Cowarra, Australia, reflect the generally low abundance of these elements felsic intrusive rocks. Therefore the implication of high Co and Ni in distinct zones in Young-Davidson pyrite is that Co-Ni poor magmatic-hydrothermal fluids and Co-Ni rich metamorphic fluids either mixed or each were dominant during stages of the mineralizing history. In general, V_1, V_2 and disseminated pyrite cores contain very low Co-Ni enrichments whereas towards the outside of the grains and along fractures, moderate to strong Co-Ni enrichments may exist; suggesting that the earliest pyrite grains were magmatic-hydrothermal in origin, with subsequent stages of pyrite containing hydrothermal mixing with metamorphic fluids. Bulk sulfur isotopic analyses of pyrite grains suggest that the fluid source for pyrite was magmatic since the data clusters around the magmatic value of 0 ‰ (Figure 3.19). In situ SIMS analyses on vein-hosted and disseminated pyrite grains by R.L. Linnen (unpubl. data) has shown grain-scale variations of $\delta^{34}S$ in pyrite grains. Since $\delta^{34}S$ within a single pyrite grain can vary, the dominantly magmatic signature is interpreted to reflect mass-dominance of the magmatic phase. Therefore the chemical controls for mineralization are associated with deposition of pyrite that contains signatures

of both magmatic-hydrothermal and metamorphic fluids and corrosion of pyrite by some other mechanism.

The presence of hematite and magnetite in the wall rock prior to gold-related hydrothermal alteration is a convenient model for explaining the style of mineralization at Young-Davidson; this model is commonly invoked for other orogenic lode gold models from elsewhere in the Abitibi (McCuaig and Kerrich, 1998). A problem with this explanation is that, apart from the general spatial relationship between pyrite, gold and hematite-magnetite inclusions, evidence for progressive sulfidation of hematite and magnetite is not observed at Young-Davidson. In least-altered rocks, a hematite overprint of magnetite is the dominant relationship indicating a relatively oxidizing fluid, whereas in mineralized rocks pyrite contains inclusions of hematite and magnetite, but does not clearly show overprinting textures other than hosting the grains as inclusions. The mineralization styles at Young-Davidson are potentially better-explained by a fluid mixing model where oxidized magmatic fluids mixed with relatively reduced and sulfur-bearing metamorphic fluids to cause destabilization of the bisulfide complex and deposit gold. Type 1 oxide-bearing pyrite grains texturally support this model where gold deposition is either synchronous with oxide-overprint by pyrite or with simultaneous oxide-pyrite deposition. Corroded gold-hosting fractures are potentially also explained by fluid mixing, with a low H_2S magmatic fluid dominating in the mixing to cause pyrite consumption. This mechanism can also account for destabilizing the bisulfide complex.

3.6 Conclusions

The variable gold-pyrite-oxide textures combined with multiple vein sets, magmatic-hydrothermal alteration styles and volcanic hosted mineralization at Young-Davidson indicate that mineralization is controlled by intrusion-associated and typical orogenic mechanisms. The textures and chemistry of rutile, pyrite and gold grains indicate that intrusion-associated fluids and typical metamorphic fluids have influenced the ore-associated minerals at Young-Davidson. There appear to be multiple controls on mineralization at Young-Davidson, invariably all linked to pyrite. Gold precipitation occurs where pyrite overprinted pre-existing magnetite and hematite, or where pyrite and oxides precipitated simultaneously. Gold mineralization also occurs where pyrite was corroded and dissolved. The chemistry of gold inclusions also potentially suggests that gold in the latest vein set has been transported and/or deposited by mechanisms that differ from those in the earlier vein sets and

disseminated styles of mineralization. Additionally, gold mineralization generally correlates with the grain-scale variations in Co and Ni in the earliest vein sets whereas gold mineralization crosscuts Co-Ni enrichments in the later vein sets. The interpretation of bulk pyrite chemical and isotopic analyses is difficult without considering grain-scale chemical and sulfur isotopic variations since a textural study of hydrothermal pyrite (and potentially other sulfides) is incomplete without considering grain-scale chemical variations.

Chapter 4
Discussion and Conclusions

4.1 Discussion

The dominant gold-transporting complexes are $AuHS^0$, $Au(HS)_2^-$, $AuCl_2^-$ and $AuOH^0$, governed by the solubility equations 4.1 to 4.4, depending on the composition and physicochemical conditions of the hydrothermal fluids (Seward, 1973; Gibert et al., 1998; McCuaig and Kerrich, 1998; Stefánsson and Seward, 2003; Stefánsson and Seward, 2004). Studies on gold speciation in hydrothermal fluids

$$Au + H_2S + HS^- = Au(HS)_2^- + 0.5H_2 \quad 4.1$$

$$Au + H_2S = AuHS^0 + 0.5H_2 \quad 4.2$$

$$Au + 2Cl^- + H^+ = AuCl_2^- + 0.5H_2 \quad 4.3$$

$$Au + H_2O = AuOH + 0.5H_2 \quad 4.4$$

$$Fe_3O_4 + 6H_2S + O_2 = 3FeS_2 + 4H_2O \quad 4.5$$

$$Fe_2O_3 + 4H_2S + 0.5O_2 = 3FeS_2 + 4H_2O \quad 4.6$$

$$FeCO_3 + 2H_2S = 2FeS_2 + CO_2 + 2H_2O \quad 4.7$$

$$H_2S = HS^- + H^+ \quad 4.8$$

$$H_2O = 0.5O_2 + 2H^+ \quad 4.9$$

$$CaCO_3 + H^+ = HCO_3^- + Ca^{2+} \quad 4.10$$

$$FeCO_3 + H^+ = HCO_3^- + Fe^{2+} \quad 4.11$$

generally agree that the $AuHS^0$ and $Au(HS)_2^-$ complexes dominate at relatively low temperatures (250 ºC to 400 ºC) in acidic to neutral sulfide-bearing aqueous solutions whereas the $AuCl_2^-$ complex dominates at higher temperatures (> 400 ºC) even in sulfide-bearing fluids (Seward, 1973; Gibert et al., 1998; Stefánsson and Seward, 2003; Stefánsson and Seward, 2004). Studies of typical orogenic gold-associated fluids have constrained the mineralizing fluids to 1-3 kbar, 160 ºC to 700 ºC, near neutral pH, in the H_2O-CO_2 ± CH_4 ± H_2S ± N_2 system with 0-35 wt% (generally ≤6 wt%) equivalent NaCl (McCuaig and Kerrich, 1998). In general systematic fluid inclusion studies for syenite-associated deposits have not been completed; however, Robert (2001) suggests that there are similarities between the mineralization in Archean examples and intrusion associated deposits from much younger terranes. Therefore by drawing from fluid studies of much younger deposits, we can infer potential physicochemical characteristics of intrusion-associated fluids: aqueous carbonic, higher temperatures (likely > 400 ºC), oxidized and potentially experienced boiling (phase separation) (Hattori and Cameron, 1986; Lang and Baker, 2001; Hart, 2007). Since the Archean atmosphere was reducing, the main source for oxidized hydrothermal fluids is thought to be from oxidized intrusions (Cameron and Hattori, 1987). Therefore by using the solubility figures presented by Gibert et al.

(1998) for aqueous sulfide-bearing solutions in equilibrium with pyrite-magnetite-hematite and quartz-Na-feldspar-paragonite, we can conceptualize the solubility of gold under different physicochemical conditions at Young-Davidson. Cooling or the removal of H_2S from hydrothermal solutions is the main mechanism cited for controlling gold precipitation, depending on the deposit type. The two main fluids considered below are relatively oxidized high temperature intrusion-related fluids and relatively reduced and lower temperature S-bearing metamorphic fluids. From Figure 4.2 and reactions 4.1 to 4.3, 4.10 and 4.11 we can conclude that pyritization (oxidation), boiling (fluid immiscibility), acid neutralization, dilution and cooling are efficient means of decreasing gold solubility in gold-bearing hydrothermal fluids. Each mechanism will be discussed below with supporting or contrasting evidence from Young-Davidson.

The pyritization of iron-bearing host rocks is commonly cited as evidence for gold deposition from sulfidation (McCuaig and Kerrich, 1998). In this mechanism gold is deposited in alteration haloes surrounding quartz veins where primary Fe-bearing oxides and silicates are consumed to produce Fe-sulfides (pyrite) by reactions 4.5 and 4.6. Deposition of pyrite removes H_2S from the hydrothermal fluids and results in decreased gold solubility by reactions 4.1 and 4.2. In this model since the fluids are S-bearing and Fe in the original rock is converted to pyrite during alteration, gains in S associated with no changes in Fe are expected. Mass balance calculations presented in Section 2.7 show that syenite-hosted gold-related alteration contains substantial increases in S and relatively minor changes in Fe. Conversely, for volcanic-hosted mineralization, S and Fe are strongly enriched indicating that pyritization is likely not an important gold-precipitating mechanism. In the syenite, this style of mineralization may be important in V_2-V_3 alteration haloes where oxide-bearing and chaotic Co-Ni-zoned pyrite grains containing gold are found on the edge of the veins. However, in samples where gold inclusions are located along fractures and crosscutting pyrite grains, precipitation of gold cannot be explained by this mechanism. Similarly, since evidence for oxidizing and pyrite-corroding fluids has been observed at Young-Davidson, there are potentially multiple mineralizing fluids all of which were not reduced.

The ascent of aqueous or aqueous-carbonic fluids in the porphyry environment can cause fluid immiscibility with coexisting vapors and aqueous brines, depending on the initial composition of the fluid (Heinrich et al., 2004). During liquid-vapor immiscibility, H_2S is strongly partitioned into the vapor phase, which depletes H_2S from the residual liquid and would cause decreased gold solubility by reaction 4.1 and 4.2 (Gibert et al., 1998; Heinrich et al., 2004; Heinrich, 2007). Although fluid

immiscibility may be produced from ascent of S-bearing magmatic-hydrothermal fluids (Heinrich, 2007), immiscibility may also be induced in S-bearing metamorphic fluids from pressure variations due to seismic pumping along fault zones (e.g., Bowers, 1991). The concept of seismic pumping is discussed in detail by Sibson et al. (1975) where faulting is shown to be capable of moving significant quantities of fluids from one crustal environment to another. Since the Young-Davidson syenite is closely associated with the regional scale deformation zone, and V_2 and V_3 veins developed during the D_2 deformation, it is likely that these veins experienced pressure variations from structural movements associated with the deformation zone. The criteria outlined by Sibson et al. (1975) to indicate episodic vein formation in seismically active areas include: cemented vein breccias, compositional layering of veins, laminated veins and crystal growth zoning. Quartz textures in V_3 veins at Young-Davidson indicate moderate strain since their formation: undulose extinction, sub grain development, sub grain rotation and sutured grain boundaries. In V_3 veins, gold has precipitated along fractures in pyrite, along recrystallized quartz boundaries, in pyrite pressure shadows with pristine undeformed quartz and along quartz-carbonate grain boundaries. In the volcanic-hosted quartz-iron-carbonate veins, iron-carbonate lines the edges of the vein whereas sutured quartz-grains elongated normal to the vein margins dominate the center portion of the vein. Gold occurs along quartz-carbonate grain boundaries and in pyrite pressure shadows associated with unstrained quartz grains. Therefore episodic vein formation may have influenced the volcanic-hosted quartz-Fe-carbonate veins, however textural evidence for episodic vein formation is not observed in syenite-hosted V_3 veins, potentially owing to destruction of these textures with subsequent fluid events or recrystallization. Sector-zoned pyrite grains can potentially be explained by periodic fluid infiltration events, however McCuaig and Kerrich (1998) noted that the above mechanisms will only occur in fluid conduits; thus this mechanism does not adequately explain disseminated styles of mineralization in the syenite. Since seismic pumping may have caused fluid infiltration events it can potentially explain the observed chemical zoning in pyrite in V_1, V_2 and V_3 veins where pyrite in veins pre-dates gold.

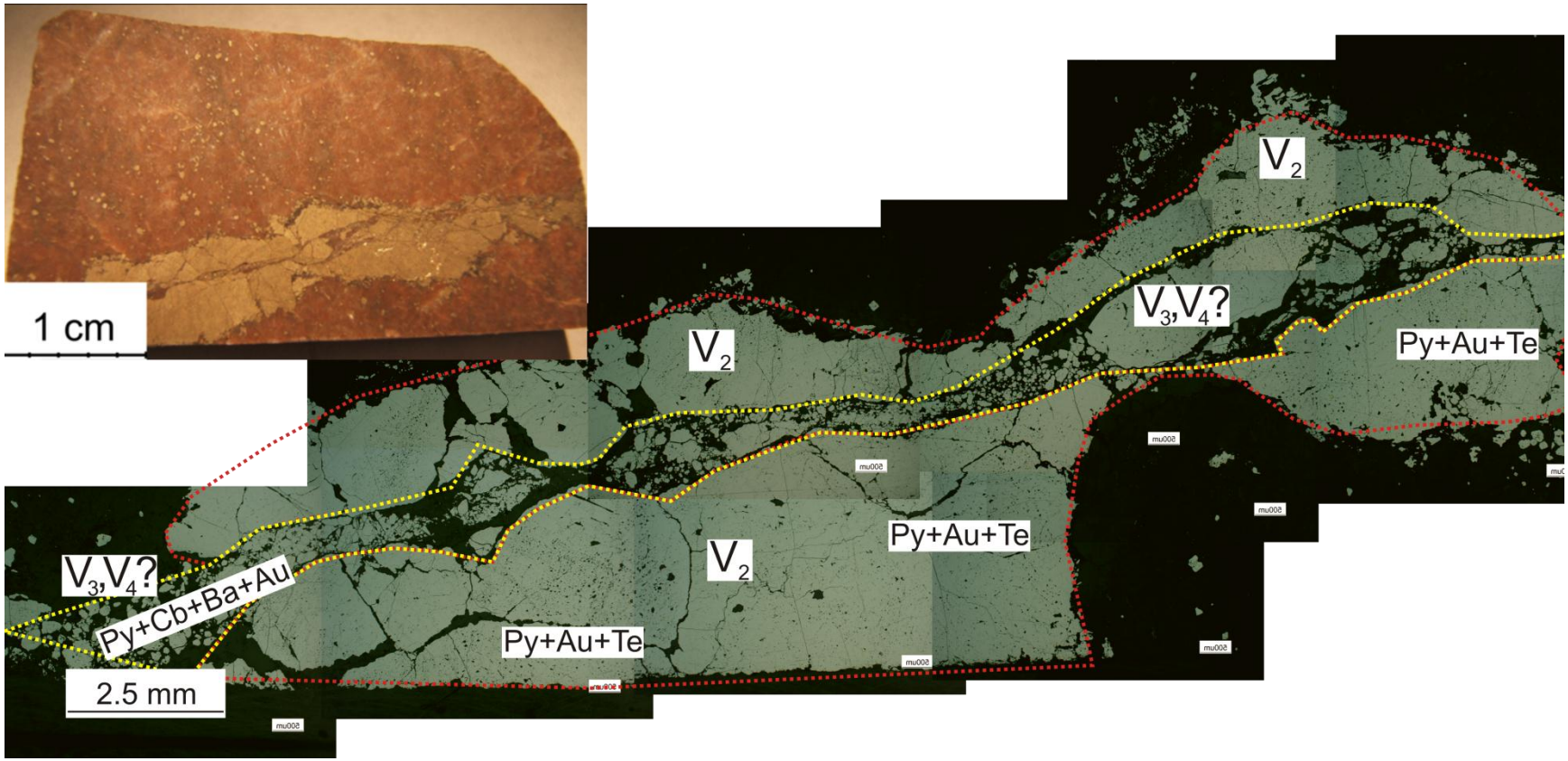

Figure 4.1: Syenite hosted V_2 vein with reactivation down the center of the vein. Pyrite, barite, carbonate, quartz makeup the center vein whereas the outside vein is mostly pyrite with abundant gold and telluride minerals.

V_1 and V_2 veins commonly contain pyrite with a Co-Ni poor core that can be interpreted as the primary magmatic-hydrothermal pyrite. Therefore, gold mineralization associated with Co-Ni rich overgrowths on Co-Ni poor magmatic pyrite indicates that a Co-Ni rich fluid infiltrated and deposited pyrite and gold. Figure 4.1 shows a syenite-hosted V_2 vein that has been reactivated down the center of the vein. This example shows that the textures contained within a single vein at Young-Davidson can contain characteristics from multiple hydrothermal and tectonic events. Similarly the presence of many other vein types at Young-Davidson suggests long-lived systems with many tectonic events that have caused fluid infiltration. The potential for multiple fluids with different temperatures and compositions warrants further detailed study of the fluid composition for each vein set. Co-Ni zoning relationships in V_1, V_2 and V_3 vein-hosted pyrite suggest multiple hydrothermal fluid events and confirm the idea of seismic pumping to draw Co-Ni rich fluids into the Young-Davidson syenite. However, without a detailed fluid inclusion and isotopic study of the veins at Young-Davidson, we can only suggest pressure-induced fluid immiscibility as a depositional mechanism for gold at Young-Davidson.

Acid neutralization could be important for Young-Davidson for acidic magmatic-hydrothermal solutions. The pH of typical orogenic fluids is near neutral whereas the pH for magmatic-hydrothermal solutions can be weakly to moderately acidic. Acid neutralization by reactions 4.10 and 4.11 would tend to consume free H^+, increase the pH and cause increased dissociation of H_2S by reaction 4.8. Since the H_2S will be consumed from the hydrothermal fluids the solubility of gold is decreased, and gold precipitation is promoted. Therefore if an acidic gold-bearing fluid either intersects a carbonate rich horizon or a more alkaline fluid, gold precipitation may occur. At Young-Davidson carbonate minerals are ubiquitous and found throughout mineralized and unmineralized syenite. Since large-scale carbonate alteration is most likely related to hydrothermal fluids from the CLLDZ, for this model to have contributed to mineralization, carbonate alteration must precede or be relatively contemporaneous with acidic gold-bearing fluids. This model could be possible if a deeper late magmatic-hydrothermal source of mineralizing fluids is called upon, since the CLLDZ and large-scale carbonate alteration developed after emplacement of the syenite intrusion.

Dilution of a gold and H_2S-bearing hydrothermal fluid by mixing with a sulfur-poor hydrothermal fluid would reduce the activity of H_2S in the resulting fluid and reduce the solubility of gold. A common source for sulfur poor fluids cited for porphyry and epithermal deposits are meteoric fluids that happen to also be oxidized (Heinrich, 2007). In the Archean the most probable source for

oxidized hydrothermal fluids are felsic intrusions (Hattori and Cameron, 1986) whereas reduced CO_2 and sulfur-rich fluids are generated from metamorphic devolatilization reactions during deformation events (Phillips, 1993). The bulk sulfur isotopic composition of pyrite grains suggests that deposition of pyrite was from a fluid that has either interacted with two sources, or was from two separate fluids with the dominant fluid being magmatic. Chemical zoning in pyrite suggest an early magmatic-hydrothermal pyrite phase that was followed by Co-Ni bearing pyrite. In many examples of pyrite overgrowth, gold mineralization tends to be associated with the Co-Ni bearing pyrite rather than the Co-Ni poor pyrite. Therefore although fluid mixing appears to be present at Young-Davidson, dilution of a sulfur-rich fluid does not appear to control gold mineralization since nearly all phases of mineralization are associated with pyrite.

Cooling is a common mechanism cited for gold precipitation in the porphyry-epithermal environments as the solubility of gold as the chloride complex $AuCl_2^-$ is strongly temperature dependent (Seward, 1973; Stefánsson and Seward, 2003; Stefánsson and Seward, 2004). However, McCuaig and Kerrich (1998) noted that cooling is not a main control for mineralization in most orogenic gold deposits since strong temperature gradients do not exist at the scale of a single deposit. Similarly, it can often be shown that changes in fO_2, fS_2 and pH from fluid interaction with wall rocks are more likely the main controls for gold precipitation at orogenic gold deposits. However, in a magmatic-metamorphic system, hot fluids derived from an underlying magma would cool upon intersection with a relatively low temperature metamorphic fluid (yellow plus; Figure 4.2A to B). As Williams-Jones (2009) notes, a 50 ˚C drop in temperature in the interval 500 ˚C to 300 ˚C will cause 95% of the gold in solution complexed as $AuCl_2^-$ to precipitate. In addition, the mixing of oxidized magmatic-hydrothermal fluids with reduced metamorphic fluids would cause oxidation of sulfide and reduction of sulfate, the net effect depending on the relative abundance of each fluid. If there is sufficient H_2S in solution after the initial decrease in temperature and oxidation, the solubility of gold may increase due to increased stability of the bisulfide complex (Williams-Jones et al., 2009). Oxygen isotope thermometry indicates V_3 veins formed at temperatures > 330 ˚C (Naderi et al., 2012) and tartan twinned K-feldspar in all vein generations indicates high temperature (> 300 ˚C; Nesse, 2000) hydrothermal fluids were present during all episodes of vein formation. Typical metamorphic fluids can range in temperature from 200 ˚C to 420 ˚C depending on the local conditions (McCuaig and Kerrich, 1998). Since a fluid exsolved from underlying magmas would be at higher temperatures than the metamorphic counterparts, fluid mixing may have invoked cooling to

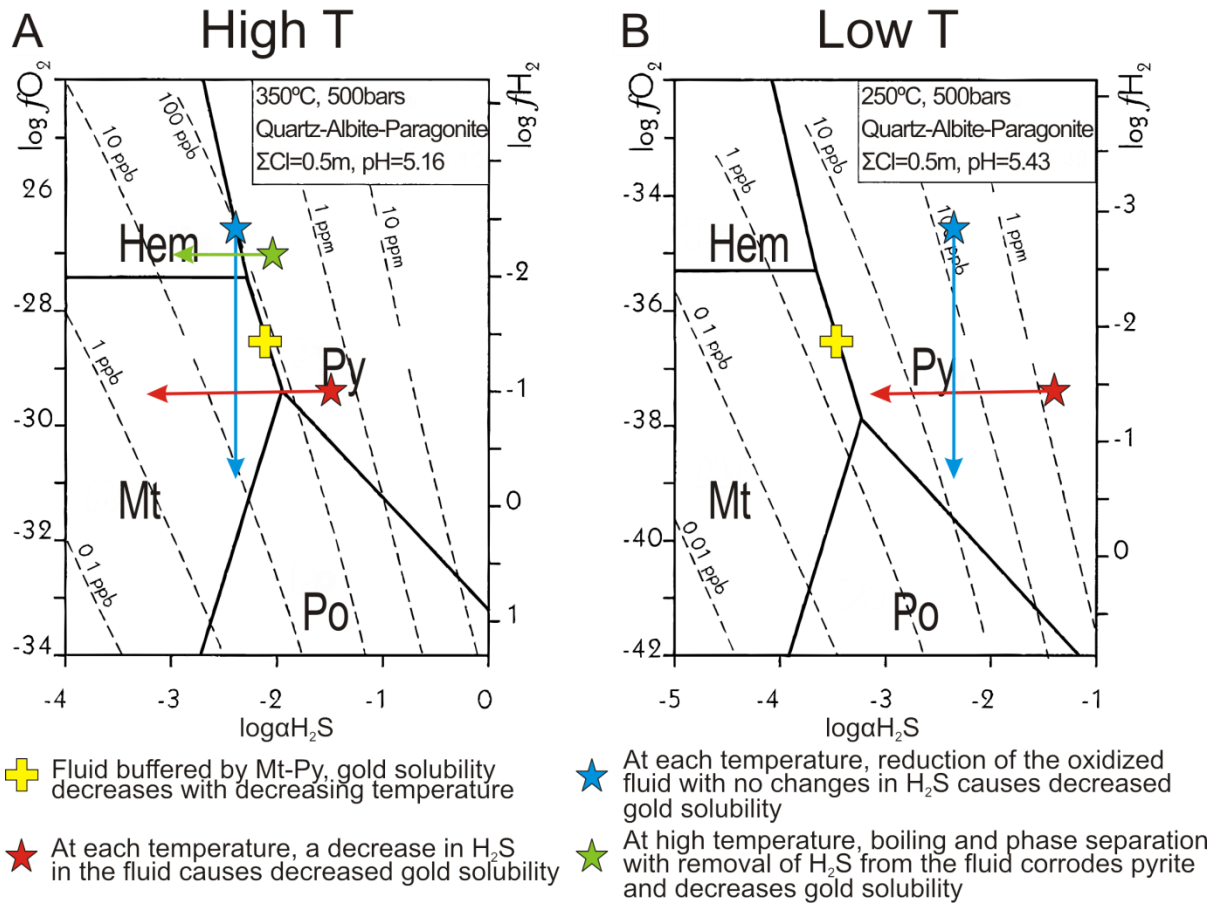

Figure 4.2: The solubility of gold at A) high (350 ºC) and B) low (250 ºC) temperatures in the quartz-albite-paragonite system, calculated as a function of fO_2 and aH_2S (modified from: Gibert et al., 1998). The labeled fluid reaction pathways are mechanisms by which the fluid at Young-Davidson may have precipitated gold.

precipitate gold from solution. Cooling would also have precipitated pyrite, and this mechanism could account for disseminated styles of mineralization with pervasive alteration. Similarly, high vein temperatures and magmatic sulfur isotopic compositions indicate that the magmatic fluid dominated; therefore reduced sulfide from metamorphic fluids was oxidized to prevent increased solubility with decreasing temperature.

Figure 4.2 can be used to propose hypothetical fluid pathways to explain the mineralization observed at Young-Davidson. A magmatic-hydrothermal system is represented in Figure 4.2A (likely at temperatures > 350 ˚C) by a fluid in the pyrite stability field at relatively high fO_2 and temperature (blue star; Figure 4.2A). Similarly, a metamorphic fluid is represented by the red star in Figure 4.2A at lower fO_2 and containing higher H_2S. Fluids associated with the deformation zone infiltrating pore

spaces and migrating into veins may have interacted with iron-rich carbonates or oxide minerals in the syenite to reduce the H_2S in the fluid by pyritization and precipitate gold as shown by the red pathway at both temperatures. This mechanism could potentially explain disseminated styles of mineralization in coarse-grained trachytic syenite where gold is intimately associated with oxide grains in pyrite. If pressure induced immiscibility occurred during vein generating events, H_2S would be removed and by the red pathway in Figure 4.2, gold deposition would occur without co-precipitation of pyrite. By contrast, if mixing of the magmatic and metamorphic fluids occurred there would be two main effects: 1) cooling of magmatic fluids to precipitate gold from the chloride complex; and 2) oxidation of the reduced sulfur from metamorphic fluids to destabilize the bisulfide complex. The observed textures at Young-Davidson could result from magmatic-hydrothermal controls, metamorphic controls, or some combination of the two fluids, depending on the location in the system and the prevailing conditions for each case of mineralization. Pyrite chemistry and isotopic compositions indicate that magmatic and metamorphic fluids existed during mineralization, and the influence of metamorphic fluids may control mineralization hosted along fractures in vein-hosted pyrite and in vein alteration haloes. Based on the metal associations in the latest vein generations, chloride may have also been present in the hydrothermal fluids to account for co-deposition of Au, Pb, Cu and Te.

4.2 Conclusions

The geochemical, petrographic and mineral chemical characteristics of the syenite-hosted mineralization at Young-Davidson contain signatures that support influence from both magmatic and metamorphic fluids. Gold mineralization is associated with pyrite that is hosted in distinct structurally correlatable vein sets found in zones of intense alteration and disseminated pyrite. Pyrite chemical variations indicate that Co-Ni-bearing fluids are associated with gold. Gold-pyrite-oxide textures indicate multiple phases of mineralization, perhaps repetitive sequences of reduced sulfidizing fluids mixing with oxidized magmatic fluids. The multiphase nature of the intrusion suggests multiple intrusive episodes, however, detailed crosscutting relationships are largely absent and detailed radiometric age dating of different phases of syenite would likely yield identical ages within error. An integrated magmatic-metamorphic model best describes the mineralization at Young-Davidson, and

supports the characterization of this syenite-associated mineralization as a distinct deposit type where the intrusion hosts mineralization styles that are distinct from typical orogenic gold deposits.

References

Actlabs Group of Companies.2011. Canadian schedule of services and fees [online]. Available from http://www.actlabs.com/files/Canada_2012.pdf. [cited 09 2011].

AuRico. 2011. 2011 Reserves and Resources Summary [online]. Available from http://www.auricogold.com/download-document/515-2011-reserves-resources.html [cited 03 2012].

Ayer, J., Amelin, Y., Corfu, F., Kamo, S., Ketchum, J., Kwok, K. and Trowell, N. 2002. Evolution of the southern Abitibi greenstone belt based on U-Pb geochronology; autochthonous volcanic construction followed by plutonism, regional deformation and sedimentation. Precambrian Research, **115**, pp 63-95.

Ayer, J.A., Thurston, P.C., Bateman, R., Dubé, B., Gibson, H.L., Hamilton, M.A., Hathway, B., Hocker, S.M., Houlé, M.G., Hudak, G., Ispolatov, V.O., Lafrance, B., Lesher, C.M., MacDonald, P.J., Péloquin, A.S., Piercey, S.J., Reed, L.E. and Thompson, P.H. 2005. Overview of results from the Greenstone Architecture Project: Discover Abitibi Initiative; Ontario Geological Survey, Open File Report 6154, 146p.

Bailey, E.H. and Stevens, R.E. 1960. Selective staining of K-feldspar and plagioclase on rock slabs and thin sections. The American Mineralogist, **45**, pp 1020-1025.

Bateman, R. and Bierlein, F. 2007. On Kalgoorlie (Australia), Timmins–Porcupine (Canada), and factors in intense gold mineralization. Ore Geology Reviews, **32**, pp 187-206.

Beaudoin, G. and Pitre, D. 2005. Stable isotope geochemistry of the Archean Val-d'Or (Canada) orogenic gold vein field. Mineralium Deposita, **40**, pp 59-75.

Berger, B.R. 2006. Geological synthesis along Highway 66 from Matachewan to Swastika; Ontario Geological Survey, Open File Report 6177, 125p.

Bowers, T.S. 1991. The deposition of gold and other metals: Pressure-induced fluid immiscibility and associated stable isotope signatures. Geochimica et Cosmochimica Acta, **55**, pp 2417-2434.

Cameron, E. and Hattori, K. 1987. Archean gold mineralization and oxidized hydrothermal fluids. Economic Geology, **82**, pp 1177-1191.

Clark, J.R. and Williams-Jones, A.E. 2004. Rutile as a potential indicator mineral for metamorphosed metallic ore deposits. Unpubl. rept., 17p.

Craig, J.R. 2001. Ore-mineral textures and the tales they tell. Canadian Mineralogist, **39**, pp 937-956.

Craig, J.R., Vokes, F.M., and Solberg, T.N. 1998. Pyrite: Physical and chemical textures. Mineralium Deposita, **34**: 82-101.

de Almeida, C.M., Olivo, G.R., Chouinard, A., Weakly, C., and Poirier, G. 2010. Mineral Paragenesis, Alteration, and Geochemistry of the Two Types of Gold Ore and the Host Rocks from the Carlin-Type Deposits in the Southern Part of the Goldstrike Property, Northern Nevada: Implications for Sources of Ore-Forming Elements, Ore Genesis, and Mineral Exploration. Economic Geology, **105**, pp 971-1004.

Dinel, E., Fowler, A.D., Ayer, J., Still, A., Tylee, K., and Barr, E. 2008. Lithogeochemical and Stratigraphic Controls on Gold Mineralization within the Metavolcanic Rocks of the Hoyle Pond Mine, Timmins, Ontario. Economic Geology, **103**, pp 1341-1363.

Dostal, J., Kontak, D.J., and Chatterjee, a.K. 2009. Trace element geochemistry of scheelite and rutile from metaturbidite-hosted quartz vein gold deposits, Meguma Terrane, Nova Scotia, Canada: genetic implications. Mineralogy and Petrology, **97**, pp 95-109.

Dubé, B. and Gosselin, P. 2007. Greenstone-hosted quartz-carbonate vein deposits (orogenic, mesothermal, lode gold, shear-zone-related quartz-carbonate or gold-only deposits). [online]. Mineral Deposits of Canada, available from: http://gsc.nrcan.gc.ca/ [cited 09-2009].

Dubé, B., Gosselin, P., Hannington, M., Mercier-Langevin, P., and Galley, A. 2007. Gold-rich volcanogenic massive sulphide deposits. *in* Mineral deposits of Canada: a synthesis of major deposit-types, district metallogeny, the evolution of geological provinces, and exploration methods. *edited by* W.D. Goodfellow. St. John's, NL, pp. 75-94.

Edmunds, C. 2009. Technical report on underground and open pit mineral resource estimates, Young-Davidson property, Matachewan, Ontario. Northgate Minerals Corporation 43-101 report, 92p.

Evans, L. 2007. Technical report of the lower boundary zone, lucky zone and lower YD zone mineral resource estimates, Young-Davidson property, Matachewan, Ontario. Northgate Minerals Corporation 43-101 report, 88p.

Fleet, M.E., Chryssoulis, S.L., MacLean, P.J., Davidson, R., and Weisener, C.G. 1993. Arsenian pyrite from gold deposits; Au and As distribution investigated by SIMS and EMP, and color staining and surface oxidation by XPS and LIMS. Canadian Mineralogist, **31**, pp 1-17.

Geoscience Laboratories. 2011. Schedule of fees and services [online]. Available from http://www.mndm.gov.on.ca/mines/ogs/labs/geobroc.pdf [cited 09-2010].

Gibert, F., Pascal, M.-L., and Pichavant, M. 1998. Gold solubility and speciation in hydrothermal solutions: Experimental study of the stability of hydrosulphide complex of gold (AuHS°) at 350 to 450 °C and 500 bars. Geochimica et Cosmochimica Acta, **62**, pp 2931-2947.

Grant, J.A. 1986. The Isocon diagram - a simple solution to Gresens' equation for metasomatic alteration. Economic Geology, **81**, pp 1976-1982.

Grant, J.A. 2005. Isocon analysis: A brief review of the method and applications. Physics and Chemistry of the Earth, **30**, pp 997-1004.

Hart, C.J.R. 2007. Reduced intrusion-related gold systems. *In* Mineral Deposits of Canada: A Synthesis of Major Deposit-Types, District Metallogeny, the Evolution of Geological Provinces, and Exploration Methods: Geological Association of Canada, Mineral Deposits Division, Special Publication *Edited by* W.D. Goodfellow. Geological Association of Canada, St. John's, NL, pp. 95-112.

Hattori, K. and Cameron, E. 1986. Archaean magmatic sulphate, Nature, **319**, pp 45-47.

Heinrich, C.A., Driesner, T., Stefánsson, A., and Seward, T.M. 2004. Magmatic vapor contraction and the transport of gold from the porphyry environment to epithermal ore deposits, Geology, **32**, pp 761-764.

Heinrich, C.A. 2007. Fluid-fluid interactions in magmatic-hydrothermal ore formation. Reviews in Mineralogy & Geochemistry, **65**, pp 363-387.

Ho, S.E., McNaughton, N.J., and Groves, D.I. 1994. Criteria for determining initial lead isotopic compositions of pyrite in Archaean lode-gold deposits: A case study at Victory, Kambalda, western Australia. Chemical Geology, **111**, pp 57-84.

Ho, S.E., McQueen, K.G., McNaughton, N.J., and Groves, D.I. 1995. Lead isotope systematics and pyrite trace element geochemistry of two granitoid-associated mesothermal gold deposits in the southeastern Lachlan fold belt. Economic Geology, **90**, pp 1818-1830.

Hodgson, C.J. 1989. The structure of shear-related, vein-type gold deposits: A review. Ore Geology Reviews, **4**, pp 231-273.

Hu, G., Rumble, D., and Wang, P. 2003. An ultraviolet laser microprobe for the in situ analysis of multisulfur isotopes and its use in measuring Archean sulfur isotope mass-independent anomalies. Geochimica et Cosmochimica Acta, **67**, pp 3101-3117.

Ispolatov, V., Lafrance, B., Dubé, B., Creaser, R., and Hamilton, M. 2008. Geologic and structural setting of gold mineralization in the Kirkland Lake-Larder Lake gold belt, Ontario. Economic Geology, **103**, pp 1309-1340.

Johnston, D.T., Wing, B.A., Farquhar, J., Kaufman, A.J., Strauss, H., Lyons, T.W., Kah, L.C., and Canfield, D.E. 2005. Geochemistry: Active microbial sulfur disproportionation in the mesoproterozoic. Science, **310**, pp 1477-1479.

Kerrich, R. and Watson, G.P. 1984. The Macassa mine Archean lode gold deposit, Kirkland Lake, Ontario; geology, patterns of alteration, and hydrothermal regimes. Economic Geology, **79**, pp 1104-1130.

Lang, J.R. and Baker, T. 2001. Intrusion-related gold systems: the present level of understanding. Mineralium Deposita, **36**, pp 477-489.

Lovell, H.L., 1967. Geology of the Matachewan area. Ontario Department of Mines, Geological Report 51, 61p.

Lucas, K., 2008. Report on the 2007 Geological Mapping on the Young-Davidson Property. unpubl. rept. for Northgate Minerals Ltd., 25p.

MacLean, W.H. 1990. Mass change calculations in altered rock series. Mineralium Deposita, **25**, pp 44-49.

McCuaig, T.C. and Kerrich, R. 1998. P-T-t-deformation-fluid characteristics of lode gold deposits: evidence from alteration systematics. Ore Geology Reviews, **12**, pp 381-453.

Naderi, N., Martin, R., Linnen, R.L., Zhang, J., Lin, S., and Banerjee, N. 2012. Alteration and isotopic vectoring at the syenite-hosted Young-Davidson gold deposit, Matachewan, Ontario. Goldschmidt 2012 Abstracts.

Nesse, W.D. 2000. Introduction to optical mineralogy. 3rd edition, 348 p. Oxford University Press, New York, Oxford.

Neumayr, P., Walshe, J., Hagemann, S., Petersen, K., Roache, A., Frikken, P., Horn, L., and Halley, S. 2008. Oxidized and reduced mineral assemblages in greenstone belt rocks of the St. Ives gold

camp, western Australia: Vectors to high-grade ore bodies in Archaean gold deposits? Mineralium Deposita, **43**, pp 363-371.

Olivo, G.R. and Williams-Jones, A.E. 2002. Genesis of the auriferous C quartz-tourmaline vein of the Siscoe Mine, Val d'Or district, Abitibi Subprovince, Canada: Structural, mineralogical and fluid inclusion constraints. Economic Geology, **97**, pp 929-947.

Olivo, G.R., Chang, F., and Kyser, T.K. 2006. Formation of the auriferous and barren north dipper veins in the Sigma Mine, Val d'Or, Canada: Constraints from structural, mineralogical, fluid inclusion, and isotopic data. Economic Geology, **101**, pp 607-631.

Phillips, G.N. 1993. Metamorphic fluids and gold. Mineralogical Magazine, **57**, pp 365-374.

Pitcairn, I.K., Olivo, G.R., Teagle, D.A.H., and Craw, D. 2010. Sulfide evolution during prograde metamorphism of the Otago and Alpine schists, New Zealand. The Canadian Mineralogist, **48**, pp 1267-1295.

Poulsen, K., Card, K., and Franklin, J. 1992. Archean tectonic and metallogenic evolution of the Superior Province of the Canadian Shield. Precambrian Research, **58**, pp 25-54.

Poulsen, K.H., Robert, F., and Dubé, B. 2000. Geological classification of Canadian gold deposits. Bulletin of the Geological Survey of Canada, pp 1-106.

Plümper, O. and Putnis, A. 2009. The complex hydrothermal history of granitic rocks: Multiple feldspar replacement reactions under subsolidus conditions. Journal of Petrology, **50**, pp 967-987.

Rice, C.M., Darke, K.E., Still, J.W., and Lachowski, E.E. 1998. Tungsten-bearing rutile from the Kori Kollo gold mine, Bolivia. Mineralogical Magazine, **62**, pp 421-429.

Robert, F. 1989. Internal structure of the Cadillac tectonic zone southeast of Val d'Or, Abitibi greenstone belt, Quebec. Canadian Journal of Earth Sciences, **26**, pp 2661-2675.

Robert, F., Boullier, A., and Firdaous, K. 1995. Gold-quartz veins in metamorphic terranes and their bearing on the role of fluids in faulting. Journal of Geophysical Research, **100**, pp 12,861-12,879.

Robert, F. and Poulsen, K.H. 1997. World-class Archean gold deposits in Canada: An overview. Australian Journal of Earth Sciences, **44**, pp 329-351.

Robert, F. 2001. Syenite-associated disseminated gold deposits in the Abitibi greenstone belt, Canada. Mineralium Deposita, **36**, pp 503-516.

Roberts, F.I. 1982. Trace element chemistry of pyrite: A useful guide to the occurrence of sulfide base metal mineralization. Journal of Geochemical Exploration, **17**, pp 49-62.

Ropchan, J.R., Luinstra, B., Fowler, A.D., Benn, K., Ayer, J., Berger, B., Dahn, R., Labine, R., and Amelin, Y. 2002. Host-rock and structural controls on the nature and timing of gold mineralization at the Holloway mine, Abitibi Subprovince, Ontario. Economic Geology, **97**, pp 291-309.

Scott, K.M. 2005. Rutile geochemistry as a guide to porphyry Cu-Au mineralization, Northparkes, New South Wales, Australia. Geochemistry: Exploration, Environment, Analysis, **5**, pp 247-253.

Scott, K.M. and Radford, N.W. 2007. Rutile compositions at the Big Bell Au deposit as a guide for exploration. Geochemistry: Exploration, Environment, Analysis, **7**, pp 353-361.

Seward, T.M. 1973. Thio complexes of gold and the transport of gold in hydrothermal ore solutions. Geochimica et Cosmochimica Acta, **37**, pp 379-399.

Sibson, R.H., Moore, J.M., and Rankin, A.H. 1975. Seismic pumping-a hydrothermal fluid transport mechanism. Journal of the Geological Society, **131**, pp 653-659.

Simon, G., Kesler, S.E., and Chryssoulis, S. 1999. Geochemistry and textures of gold-bearing Arsenian pyrite, Twin Creeks, Nevada: implications for deposition of gold in Carlin-Type deposits. Economic Geology, **94**, pp 405-421.

Sinclair, W.D. 1979. Copper-Molybdenum occurrences of the Matachewan area, Ontario. Geolical Survey of Canada, Regional and Economic Geology Division, 6p.

Sinclair, W.D. 1982. Gold deposits of the Matachewan Area, Ontario. *in* Geology of Canadian Gold Deposits: CIMM special volume 24. *edited by* Hodder, R.W., and Petruk, W., pp. 83-93.

Stefánsson, A. and Seward, T.M. 2003. Stability of chloridogold(I) complexes in aqueous solutions from 300 to 600°C and from 500 to 1800 bar. Geochimica et Cosmochimica Acta, **67**, pp 4559-4576.

Stefánsson, A. and Seward, T.M. 2004. Gold(I) complexing in aqueous sulphide solutions to 500°C at 500 bar. Geochimica et Cosmochimica Acta, **68**, pp 4121-4143.

Tesfaye, G. 1992. Ore-microscopic and geochemical characteristics of gold-tellurides-sulfide mineralization in the Macassa Gold Mine, Abitibi Belt, Canada. Mineralium Deposita, **27**, pp 66-71.

Triebold, S., Luvizotto, G.L., Tolosana-Delgado, R., Zack, T., and von Eynatten, H. 2011. Discrimination of TiO_2 polymorphs in sedimentary and metamorphic rocks. Contributions to Mineralogy and Petrology, **161**, pp 581-596.

van Middlesworth, P.E. and Wood, S.A. 1998. The aqueous geochemistry of the rare earth elements and yttrium. Part 7. REE, Th and U contents in thermal springs associated with the Idaho batholith. Applied Geochemistry, 13, pp 861-884.

Williams-Jones, A.E., Bowell, R.J., and Migdisov, A.A. 2009. Gold in solution. Elements, **5**, pp 281-287.

Zack, T., von Eynatten, H., and Kronz, A. 2004. Rutile geochemistry and its potential use in quantitative provenance studies. Sedimentary Geology, **171**, pp 37-58.

Zhang, J., Lin, S.F., Linnen, R., Martin, R., and Berger, B., 2012. Deformational history of the Matachewan area: new constraints on the tectonic evolution of the Cadillac–Larder Lake deformation zone, southern Abitibi greenstone belt. Precambrian Research, under review.

Zhao, H., Frimmel, H.E., Jiang, S., and Dai, B. 2011. LA-ICP-MS trace element analysis of pyrite from the Xiaoqinling gold district, China: Implications for ore genesis. Ore Geology Reviews, **43**, pp 142-153.

Appendices

Appendix A

Hand Sample Descriptions

The following tables contain brief hand sample descriptions for geochemistry samples taken from drill core for the two N-S cross sections. On the CD in the back insert of this thesis, the folder "2010 Photos" contains photos of all samples taken from drill core during the 2010 field season (sample series 803xxx and 800xxx).

If you accessed this thesis from a source other than the University of Waterloo, then you may not have been able to access the core photos. Please contact the author at rd2marti@uwaterloo.ca to obtain copies of these photos.

X-X' Cross section 22790mE				
Sample #	**Hole ID**	**Depth (m)**	**Purpose**	**Small Sample Description**
803303	YD07-56	701.5	TS & Chem	Fractured, chlorite altered sediments with QFe and Q veins, minor carb stringers. Looks weakly hematized.
803304	YD07-56	722.5	TS & Chem	Syenite dyke in the sediments, weakly potassic altered
803305	YD07-56	723	TS & Chem	Sediment with fine-grained specular hematite proximal to the syenite dyke
803306	YD07-56	753	TS & Chem	Chlorite and fe-carb altered syenite, no disseminated hematite grains, distinctly free of dark grains in the groundmass NOTE: the hematite altered zone ends at 762.7m
803307	YD07-56	743.5	TS	Is the Au in the veins or in the altered groundmass?
803308	YD07-56	775	TS & Chem	Sediment intruded by lamprophyre in this area. Contains abundant pyrite.
803309	YD07-56	803.5	TS	Sample contains a large QFe vein with minor pyrite. Also has a bright red halo around the vein with abundant chlorite and carbonate alteration in the groundmass.
803310	YD07-56	800	TS & Chem	Seemingly unaltered syenite with minor pyrite and very few dark minerals. Groundmass looks carbonate-chlorite altered and is wispy in nature.
803311	YD07-56	824.2	TS & Chem	Unmineralized syenite, no potassic alteration, minor carbonate alteration. No dark minerals found in the groundmass. Syenite dyke is crosscutting the sediments,
803312	YD07-56	851.4	TS	Interesting dark vein material, quartz + dark mineral. Seen a few times before, and associated with Au when seen before.
803313	YD07-56	855.9	TS & Chem	Dark brownish syenite. Very fresh looking with only weak fe-carb alteration. Few carb veins. Only G1 veins with Chl halo observed. Minor quartz-tourmaline veins.
803814A	YD07-56	865.9	TS	Ccp along fractures and at boundaries of deformed G1 veins and with chlorite in the groundmass
803314B	YD07-56	865.2	TS	Buff dark looking vein. Ductile deformed with corroded looking pyrite. Trachytic syenite right beside.
803314C	YD07-56	864.2	TS	Abundant fine Py in altered groundmass. Also a Q vein. Alteration halo around the Q-vein?
803315	YD07-56	877.3	TS & Chem	Moderately potassic, bright red. Chlorite and carbonate wisps throughout, groundmass is lighter than previous, very fine disseminated pyrite found throughout.
803316	YD07-56	1086.1	TS	Trying to find where mineralization in this 20g interval is found. Unit contains qtz veins with some py along boundaries and in halo's, and disseminated pyrite throughout. Does not look intensely KFS altered which leads me to believe that this is vein associated. Did not see the VG
803320	YD07-52	527.2	TS & Chem	Fine to medium-grained, pyrite blebs, minor carbonate veins, some chlorite along the shear. Pyrite associated with carbonate in the groundmass
803321	YD07-52	550.1	TS & Chem	Silicified sediment, minor quartz-iron-carbonate veins, very fine-grained disseminated pyrite grains throughout the stuff.
803322	YD07-52	578.2	TS & Chem	UMF, weak deformation and very little pyrite in general throughout this box. Weakly foliated with minor carbonate stringers, Locally there is abundant pyrite associated with carbonate and what looks like syenitic clasts

Sample #	Hole ID	Depth (m)	Purpose	Small Sample Description
803323	YD07-52	591.7	TS	Abundant quartz veining in a coarse porphyritic to trachytic groundmass of syenite. Large quartz veins, minor pyrite within those veins, Abundant disseminated pyrite. Galena found within one of the larger quartz veins, so potential for Au and remobilized Au with pyrite. 2 samples: A- galena in the quartz vein, B- disseminated pyrite in the groundmass
803324	YD07-52	612	TS & Chem	Coarse to medium-grained porphyritic syenite, very fine disseminated sulfides, moderately hematized with minor quartz stringers. Does not appear potassic altered. Fresh?
803325	YD07-52	629.1	TS & Chem	Sheared carbonate rich syenite/sediments, or a lamprophyre? Looks like there could be some carbonate phenocrysts within one of these sections
803326	YD07-52	650.6	TS & Chem	Very fine disseminated pyrite, chlorite along late fractures, minor quartz veining.
803327	YD07-52	662.5	TS & Chem	Sheared mafic flow, abundant pyrite. Possible sediments or QFP
803328	YD06-23	623.5	TS & Chem	Weakly hematized conglomerate with syenite fragments, sheared with minor pyrite. Chlorite along fracture planes. Pictures(2774-2776). Syenite clasts in the conglomerate.
803329	YD06-23	747.8	TS & Chem	Fine to medium-grained brownish red to dark maroon syenite, looks fresh but upon closer inspection looks like groundmass has carb + fine hematite. Disseminated magnetite or hematite present.
803330	YD06-23	775.5	TS & Chem	Foliated silicified sediment? Carb veins along foliation with minor chlorite, very little spotty pyrite mineralization. Locally fuschitic. Could it be a QFP? The rock is almost glassy. Pictures(2785-2789). sheared chloritic to fuschitic material.
803331	YD06-23	800	TS & Chem	Fine maroon red syenite, moderately carbonate altered and weakly hematized, quartz-iron carbonate veins, very minor to trace pyrite found, locally enriched
803332	YD06-23	826	TS & Chem	Lamprophyre like syenite, abundant pyrite with quartz veins. Second sample: alteration halo around a large pyrite grain in the groundmass, magnetic depletion in halo? TS
803333	YD06-23	829	TS & Chem	porphyritic with minor quartz veins, carbonate altered, weakly potassic altered
803334	YD06-23	851.2	TS & Chem	fine to medium-grained syenite, fine groundmass, minor quartz veins, quartz veins are abundant elsewhere in the box
803335	YD06-23	877.5	TS & Chem	Medium to coarse maroon syenite, very little to no hematite/potassic in this interval, carbonate alteration and stringers, lamprophyre? Biotite grains are present.
803336	YD06-23	901	TS & Chem	dirty chloritic and sulfide rich syenite, fractured and sheared and proximal to moderate hem/pot stuff, abundant pyrite, quartz veins in this region have hem/pot alteration halo
803337	YD06-23	927.5	TS & Chem	moderate hem/pot, disseminated py and quartz veins, abundant chlorite along fractures, fe-carb alteration, disseminated pyrite - has gold?

Sample #	Hole ID	Depth (m)	Purpose	Small Sample Description
803338	YD06-23	921.5	TS & Chem	strong hem/pot, coarse-grained trachytic syenite, moderate pyrite. This sample is above (up hole) sample 803337
803339	YD06-23	948.8	TS & Chem	moderate hem/pot, disseminated and vein pyrite, late chlorite along the shear planes, moderate amounts of carbonate stringers
803340	YD06-23	930.5	TS & Chem	coarse trachytic syenite with abundant fine pyrite in the interstities, minor quartz stringers
	YD06-21A	1149	TS & Chem	sheared mafic flow looking stuff, carbonate and chlorite with no pyrite,
803341	YD06-21A	1174.5	TS & Chem	Chlorite altered almost lamprophyric syenite, minor carbonate, extremely fresh looking. Possible magnetite altered? Definitely has magnetite in it, FRESH? But also possibly a different younger post alteration phase of syenite.
803342	YD06-21A	1200.3	TS & Chem	Coarse trachytic syenite with abundant sulfides and moderately potassic altered in the groundmass
	YD06-21A	1182.5	TS	Intrusive or alteration contact between the two phases of syenite?
803343	YD06-21A	1182.1	TS & Chem	Bottom of the fresh looking dark syenite unit
803344	YD06-21A	1182.8	TS & Chem	Top of the coarse trachytic hem/pot syenite unit
803345	YD06-21A	1224.5	TS & Chem	Greyish dead looking trachytic and porphyritic syenite, patchy earthy hematite alteration in places associated with very fine disseminated pyrite in the groundmass, syenite looks fresh here, color wise, but could just be subdued hematite/potassic alteration
803346	YD06-21A	1248.4	TS & Chem	Coarse - extremely coarse trachytic syenite. Abundant dirty carbonate-chlorite-sulfide between the larger feldspars. Megacrysts of feldspar show brittle deformation and are cut by the quartz veins
803347	YD06-21A	1273.7	TS & Chem	Coarse trachytic syenite, abundant fine and coarse pyrite, carbonate and chlorite found in between the feldspar grains, fractured.
803348	YD06-21A	1299.5	TS & Chem	Trachytic, porphyritic, abundant pyrite, no potassic alteration here, fresh with respect to that but still looks altered. Chlorite dominant alteration, but weakly altered
803349	YD07-34	682.5	TS & Chem	Weakly hematized fine-grained syenite or QFP, minor carbonate alteration and stringers, very fine pyrite disseminated, majority of pyrite in the sample is found along chlorite lined fractures crosscutting the groundmass
803350	YD07-34	776	TS & Chem	Syenite? Very fine-grained, near lamprophyre, abundant pyrite is fine and coarse-grained and disseminated, minor carbonate stringers, could be a chilled sediment?
803351	YD07-34	801	TS & Chem	Fresh looking trachytic syenite, abundant fine-grained sulfides, chlorite alteration is weak, but is the dominant alteration. Minor carbonate stringers throughout

Sample #	Hole ID	Depth (m)	Purpose	Small Sample Description
803352	YD07-34	821.8	TS & Chem	Medium porphyritic to trachytic syenite. Minor hem/pot alteration, but more fresh looking than anything. Minor fine-grained sulfides. Compare the alteration and geochemistry with sample 803353
803353	YD07-34	825	TS & Chem	Moderately hem/pot with abundant quartz veins, fine disseminated sulfides and sulfides found in the veins
803354	YD07-34	852.6	TS & Chem	coarse trachytic, fresh looking in areas. Weak hematite alteration starting in this sample. Feldspars look albitic (are white instead of pink). Weak hematite alteration in the spaces between the feldspars. Very fine-grained pyrite throughout, and chlorite-carbonate along shears within the sample
803355	YD07-34	861	TS	potassic halo around vein with sulfides, cut sample to see alteration away from the vein, Staining?
803356	YD07-34	865.5	TS & Chem	Grey, coarse trachytic syenite, minor sulfides, hematite in between the feldspar grains. Very fine to trace sulfides
803357	YD06-26	1150.2	TS & Chem	Coarse porphyritic syenite, groundmass is very fine-grained, albitic phenocrysts? Hem/pot alt in the groundmass? Some phenocrysts look potassic, minor carbonate stringers and carbonate alteration in the groundmass. Minor quartz veins
803358	YD06-26	1180	TS & Chem	Maroon syenite, lamprophyric almost, can see biotite grains, extremely unaltered, Groundmass contains some chlorite and carbonate, very minor sulfides and magnetite is probably present.
803359	YD06-26	1201	TS & Chem	Brownish red porphyritic syenite with 10% coarse phenocrysts, fresh looking with fine-grained glass groundmass, Looks foliated, sample is just below a sheared segment with abundant carbonate veins
803360	YD06-26	1208.7	TS & Chem	Intense hem/pot, trachytic to coarse-grained, abundant large quartz veins and quartz-py veins, abundant fine-grained disseminated pyrite in the groundmass, carbonate also in the groundmass
803361	YD06-26	1225	TS & Chem	coarse locally trachytic syenite, strongly hem/pot altered, looks recrystallized, pyrite with carbonate in the spaces between the feldspars, abundant pyrite mineralization in these interstitial spaces, vey minor specular hematite possible present
803362	YD06-26	1253.4	TS	Fe-carb-qtz vein (V1) with chlorite and sulfide mineral rim, Look for mineralization/moly along the vein boundary and within the vein
803363	YD06-26	1250	TS & Chem	Coarse trachytic syenite with black and pink feldspar phenocrysts, abundant chlorite and carbonate in the interstities, pyrite mineralization in the halo around a small quartz vein, potassic halo around this vein, in general weak pyrite mineralization here, chlorite alteration is dominant and is moderate

Sample #	Hole ID	Depth (m)	Purpose	Small Sample Description
803364	YD06-26	1276.5	TS & Chem	Medium to course trachytic syenite, increased sulfides in proximity to potassic increase, otherwise sulfides are found in the dark interstitial spaces along with chlorite and carbonate, does not look hem/pot altered, rather we have intense hem/pot alteration in the vicinity of quartz veins and along fractures. Pictures(2898-2900)
803365	YD06-26	1297.5	TS	2 samples for thin sections of the mineralization
803366	YD06-26	1298.8	TS & Chem	extremely coarse, chlorite altered, in close proximity to lamprophyric syenite intrusive, minor hem/pot alteration found, dirty black stuff in the interstities, crumbly
803367	YD06-21	1199.8	TS & Chem	Dark maroon syenite, coarse-grained, very little sulfides, no quartz veins, minor carbonate stringers, lamprophyric syenite? Is this stuff later than the main alteration, could explain the sharp contacts and the lack of veining/alteration in this phase of the intrusive. Could also be the least altered syenite.. ?
803368	YD06-21	1233.5	TS & Chem	Coarse trachytic syenite, dark brown to grey, abundant fine sulfides in the interstitial spaces, chlorite-carbonate in the interstitial spaces? Minor carbonate stringers throughout
803369	YD06-21	1249.5	TS & Chem	Megacrystic syenite, brownish grey with extremely fine-grained groundmass, near glassy, minor carbonate stringers and very minor pyrite. Stuff looks fresh, but also looks like a different phase of syenite
803370	YD06-21	1271.5	TS & Chem	Coarse syenite, moderate-strong hem/pot alteration, abundant pyrite found in the interstitial spaces, quartz veins are present in this location, alteration is pervasive
803371	YD06-21	1310.5	TS & Chem	coarse syenite, trachytic syenite, fine sulfides, moderate hem/pot alteration, locally veined
803372	YD06-21	1335.5	TS & Chem	coarse trachytic syenite, intense hem/pot alteration, abundant sulfides
803373	YD07-46	1250	TS & Chem	Chilled syenite/sediments, possible phenocrysts in there, quartz veining with alteration haloes
803374	YD07-46	1275.3	TS & Chem	Potassic altered sheared ugly sediments, also a considerable amount of carbonate in there, silicified? Probably some potassic alteration that's making it look this way
803375	YD07-46	1299.8	TS & Chem	Porphyritic syenite with minor quartz veins and medium hematite/potassic alteration, increased alteration in halo around the veins
803376	YD07-46	1325	TS & Chem	Coarse maroon stuff, but this stuff has some alteration around the quartz veins that crosscut it. Overall it is weakly potassic altered, and there are abundant fine-grained disseminated sulfides inside
803377	YD07-46	1351.2	TS & Chem	coarse porphyritic syenite, abundant glassy groundmass with very fine dark minerals, no sulfides found
803378	YD07-46	1375	TS & Chem	Porphyritic brown syenite, earthy brown color, sample contains disseminated hematite grains? Minor veins found within sample, minor to no potassic alteration
803379	YD07-46	1476.3	TS & Chem	Moderate hematite/potassic alteration, coarse-grained, abundant sulfides, sample is proximal to section with quartz veining, pyrite in the interstitial spaces is corroded looking
803380	YD07-46	1496.8	TS & Chem	Weakly hematized with very fine-grained sulfides, weak veining in this area, but there is abundant pyrite?

Sample #	Hole ID	Depth (m)	Purpose	Small Sample Description
803381	YD08-78A	648	TS & Chem	Fine syenite, moderate hem/pot alteration, abundant fine sulfides and sulfide stringers, sample is from the top of a mafic (syenite) section
803382	YD08-78A	678	TS & Chem	Trachytic syenite dyke in foliated fuschitic to chloritic sediments. Trace sulfide veinlets, minor carbonate and quartz stringers, moderate hem/pot alteration within the dyke, but not necessarily in the sheared sediments, though they are altered also. 1m Syenite dyke
803383	YD08-78A	699	TS & Chem	Strongly hem-pot altered, very fine-grained disseminated specular hematite and sulfides in the groundmass, minor amounts of veining, porphyritic, quartz veins
803384	YD08-78A	724	TS & Chem	Abundant fine-grained sulfides in the glassy aphanitic groundmass, sulifde stringers are present, large feldspar phenocrysts, minor carbonate stringers, does not look kfs altered, BUT brick red color, hematite only?
803385	YD08-78A	750	TS & Chem	trachytic with abundant fine sulfides in the interstitial spaces, quartz stringers present, hematite/potassic halo on the qtz veins, overall there is minor to trace hematite/potassic in the groundmass
803386	YD08-78A	774.5	TS & Chem	moderately hematized to weakly potassic syenite, fine-grained, carbonate stringers, qtz-kfs veins, abundant fine-grained sulfides and chlorite along fractures
803387	YD08-78A	800	TS & Chem	Sediment? Looks like sediment.. But mafic? Minor carbonate stringers, hematized potassic syenite dykes crosscut this stuff with little to none of the hematite/potassic in the host rock.. Interesting..
803388	YD07-55	549.5	TS & Chem	Coarse grey syenite, hematized in halo around the qtz veins, carbonate alteration dominates, sulfides are very fine-grained, minor quartz stringers crosscutting unit
803389	YD07-55	553.5	TS & Chem	coarse red syenite, quartz veins nearby, moderate to strong hematite/potassic alteration
803390	YD07-55	559.5	TS & Chem	medium to coarse trachytic syenite, carbonate stringers, very fine sulfides, dark minerals in the groundmass, biotite grains? Chlorite along fractures
803391	YD07-55	625	TS & Chem	Abundant fine-grained pyrite, sample is K2O altered but not veined, porphyritic, locally trachytic, groundmass appears red and altered and is associated with abundant very fine-grained sulfides
803392	YD07-55	648.3	TS & Chem	Sandstone, red to pink, hematite/potassic? Doesn't look like it. Minor carbonate stringers, minor disseminated pyrite around local quartz vein, sheared/foliated.

Y-Y' Cross section 23240mE				
Sample #	**Hole ID**	**Depth (m)**	**Purpose**	**Small Sample Description**
800901	YD07-56A	850.9	TS & Chem	dark syenite with minor carbonate stringers and feldspar phenocrysts, very fresh looking, biotite (?) grains present.
800902	YD07-56A	875	TS & Chem	medium to coarse syenite with minor purple feldspars, minor carbonate stringers and biotite grains
800903	YD07-56A	900	TS & Chem	medium to coarse syenite, minor carbonate stringers with chlorite along fractures, very minor pyrite, increased fe-carbonate alteration
800904	YD07-56A	926.3	TS & Chem	brown-red medium-grained syenite, minor carbonate stringers, disseminated pyrite, minor quartz-carbonate veins
800905	YD07-56A	952.3	TS	hematitic syenite dyke in relatively fresh syenite, disseminated pyrite and abundant carbonate stringers, minor quartz veins
800906	YD07-56A	954.1	TS & Chem	Fe-carbonate altered syenite, with fe-carb veins. Medium to coarse-grained, minor quartz in fe-carb vein
800907	YD07-56A	976	TS & Chem	weakly hematite altered syenite, fe-carb and q-fe-carb veins, looks like V3 veins and V1 veins
800913	YD06-11	423.3	TS & Chem	Weakly altered syenite, purple feldspars, weak fe-carb alteration, dark groundmass, no veining
800914	YD07-33D	1371	TS	LAMP containing SYN PEBBLE
800915	YD07-33D	1371	TS	LAMP containing SYN PEBBLE
800916	YD10-188	15	TS & Chem	VOLCANIC, fresh with carbonate stringers
800917	YD10-188	29	TS & Chem	VOLCANIC, increased carbonate stringers and pyrite
800918	YD10-188	37.5	TS & Chem	VOLCANIC, pyrite along foliation, decreased carbonate stringers
800919	YD10-194	30	TS	VOLCANIC, abundant disseminated pyrite in groundmass, 'albitized mineralized zone' quartz-fe-carb veins with abundant pyrite are mineralized
800920	YD10-217	9.5	TS & Chem	VOLCANIC, fresh volcanic with minor quartz-fe-carb veins
800921	YD10-217	16.2	TS & Chem	VOLCANIC, fresh volcanic, minor quartz-fe-carb veins
800922	YD10-217	32.5	TS & Chem	VOLCANIC, relatively fresh, minor pyrite and quartz fe-carb veins
800923	YD10-217	56.5	TS & Chem	VOLCANIC, brown foliated 'albitized' volcanic with abundant fine-grained pyrite along foliation, buff grey in color, no veins or stringers
800924	YD10-222	11.2	TS & Chem	Volcanic, relatively fresh, minor carbonate stringers
800925	YD10-222	25	TS & Chem	Volcanic, relatively fresh with patchy carbonate alteration throughout
800926	YD10-222	32.5	TS & Chem	Volcanic, weakly sheared with wisps of albite alteration, minor pyrite along foliation

Sample #	Hole ID	Depth (m)	Purpose	Small Sample Description
800927	YD10-222	36.5	TS & Chem	Volcanic, Buff brown, sheared with fine-grained pyrite along foliation, mineralized
800928	YD10-222	37	TS	Volcanic, quartz-fe-carb vein crosscutting the albitic alteration, abundant pyrite in vein, mineralized.
800929	YD07-41	802.3	TS & Chem	Coarse hematitic syenite, abundant fe-carb stringers. Chlorite filled shear planes present
800930	YD07-41	825.5	TS & Chem	medium-grained syenite, quartz-fe-carb veins have potassic halo
800931	YD07-41	852.5	TS & Chem	Dark fine-grained biotite rich syenite? Minor carbonate stringers. Lamprophyre like
800932	YD07-41	879.7	TS & Chem	coarse trachytic hematitic syenite, chlorite shears, minor disseminated pyrite
800933	YD07-41	903.2	TS	Dark colored quartz-fe-carb vein (V1?) with chlorite/pyrite rim. Possibly looking for moly here
800934	YD07-41	902	TS & Chem	light pink fine syenite with carbonate stringers chlorite along fractures
800935	YD07-41	925.7	TS & Chem	hematitic syenite with pyrite stringers, minor chlorite along fractures, light groundmass
800936	YD07-41	948.5	TS & Chem	Dark hematitic with minor carbonate stringers and chlorite alteration in the groundmass
800937	YD07-41	974.7	TS & Chem	Bright red hematitic fine to medium-grained syenite, minor chlorite in groundmass, fe-carb alteration, minor fe-carb stringers
800938	YD07-41	1000.1	TS & Chem	Fine to medium brown syenite with chlorite-carbonate alteration, minor to no veining
800939	R03A	147	TS & Chem	Coarse deformed syenite with minor kfs stringers, fe-carb crosscutting feldspars
800940	R03A	176.5	TS & Chem	Dark maroon syenite with abundant q-fe stringers, coarse-grained, chlorite-carbonate in groundmass
800941	R03A	197.5	TS & Chem	Fine to medium syenite, abundant quartz -fe-carb veins, some with pyrite, others with kfs-halo. Minor pyrite veinlets
800942	R03A	225.1	TS & Chem	Dark fine to medium syenite, quartz-kfs vein with some possible pyrite, chlorite-carbonate alteration in groundmass
800943	R03A	250	TS & Chem	Medium to fine-grained syenite with quartz-fe-carb veins and fine disseminated pyrite. Minor carbonate stringers. Possible patchy biotite
800944	YD07-33B	1301	TS & Chem	Coarse to medium syenite, minor hematitic alteration, fe-carb stringers, minor patchy chlorite in groundmass.
800945	YD07-33B	1322.7	TS X 2	Large quartz-pyrite vein, abundant pyrite within vein, minor pyrite in groundmass, coarse syenite.
800946	YD07-33B	1320.9	TS	Coarse trachytic hematitic syenite, moderate fine disseminated pyrite, minor chlorite in groundmass.
800947	YD07-33B	1349.5	TS & Chem	coarse red syenite, minor quartz veins, minor carbonate alteration, abundant pyrite in groundmass, minor carbonate stringers
800948	YD07-33B	1377.3	TS & Chem	Coarse red syenite, quartz veins, minor carbonate stringers, disseminated pyrite
800949	YD07-33B	1399.8	TS & Chem	Coarse syenite, weakly altered, pink from feldspars, chlorite-carbonate alteration in the groundmass.
800950	YD07-33B	1421.4	TS & Chem	Coarse hematitic syenite, minor quartz-fe-carb stringers, chlorite along fractures, minor pyrite
800951	YD07-33B	1447	TS & Chem	Fine to medium brown syenite, carbonate stringers, local fe-carb alteration. Minor chlorite along fractures
800952	R06	225.4	TS & Chem	Coarse sheared syenite, chlorite along shear planes, minor carbonate stringers crosscutting feldspars

Sample #	Hole ID	Depth (m)	Purpose	Small Sample Description
800953	R06	251.6	TS & Chem	Coarse red syenite, minor carbonate stringers, trace pyrite
800954	R06	276.3	TS & Chem	Fine to medium-grained porphyritic syenite, dark red to reddish brown, minor carbonate stringers, chlorite along fractures
800955	R06	300.1	TS & Chem	Fine to medium red syenite, abundant carbonate stringers, local carbonate-pyrite patches, weakly hematite altered? Minor disseminated pyrite
800956	R06	350	TS & Chem	Fine to medium red syenite with q-fe-carb veins, minor carbonate alteration in groundmass
800957	R06	375	TS & Chem	Fine to medium-grained dark red syenite, chlorite in groundmass, minor carbonate alteration
800972	YD07-53A	1429.6	TS & Chem	Fresh looking porphyritic syenite, dark groundmass with large white feldspar phenocrysts, possible minor fe-carb alteration in groundmass
800973	YD07-53A	1450.8	TS & Chem	Coarse brown porphyritic syenite, large white feldspar phenocrysts, minor chlorite lined fractures, trace disseminated pyrite
800974	YD07-53A	1473.4	TS & Chem	Red coarse trachytic syenite, hematite altered, disseminated pyrite in groundmass,
800975	YD07-53A	1475.6	TS	LAMP containing SYN PEBBLE
800976	YD07-53A	1500.3	TS & Chem	Bright red hematitic syenite, quartz veins throughout, with possible kfs rim, abundant disseminated pyrite in groundmass
800977	YD07-53A	1501.4	TS	VEIN?? (Lost TS block..)
800978	YD07-53A	1526.7	TS & Chem	Coarse syenite, minor fe-carb stringers, local quartz veins with kfs rim
800979	YD07-48	761.1	TS	V1 vein, sample to look for moly and Au in the vein. Turns out its ccp and galena. Nothing interesting here! Vein is highly deformed.
800980	YD07-48	763.5	TS & Chem	Coarse syenite with quartz veinlets, kfs around rim of veins. Abundant disseminated pyrite and what looks like V2 veins
800981	YD07-48	801	TS & Chem	Fine sandstone (syenite?) abundant carbonate stringers, minor hematite alteration
800982	YD07-48	826.5	TS & Chem	Medium-grained syenite (sandstone?) carbonate stringers and chlorite lined fractures
800983	YD07-48	850.6	TS & Chem	Very fine syenite (sandstone?) with abundant carbonate stringers, minor chlorite lined fractures
800984	YD07-48	873.1	TS & Chem	Light pink coarse syenite with abundant fe-carb stringers, hematite alteration and some disseminated pyrite
800985	YD06-16A	1117	TS & Chem	Coarse dark red syenite with chlorite-carbonate in groundmass, possible biotite in groundmass
800986	YD06-16A	1124	TS & Chem	Porphyritic syenite with minor chlorite in groundmass, disseminated pyrite
800987	YD06-16A	1150	TS & Chem	Coarse porphyritic syenite with fine-grained red groundmass, minor carbonate stringers
800988	YD06-16A	1174	TS & Chem	Red-brown porphyritic syenite, minor carbonate stringers, weak carbonate alteration
800989	YD06-16A	1325	TS & Chem	Medium brown coarse porphyritic syenite with carbonate along fractures, dark groundmass, unaltered?
800990	YD06-16A	1349.2	TS & Chem	Coarse trachytic hematitic syenite with minor chlorite along fractures, weak carbonate stringers and minor pyrite veinlets

Sample #	Hole ID	Depth (m)	Purpose	Small Sample Description
800991	YD06-16A	1350.1	TS	Coarse hematitic syenite with minor quartz-pyrite veining, and fe-carb-pyrite veins
800992	YD06-16A	1350.2	TS & Chem	Coarse trachytic hematitic syenite with minor chlorite along fractures, weak carbonate stringers
800993	YD06-16A	1371	TS & Chem	Coarse hematitic syenite with minor chlorite along fractures, weak fe-carb alteration
800994	YD06-26	1284.8	TS	Quartz-kfs vein crosscutting syenite and pyrite mineralization, abundant disseminated pyrite through rest of sample
800995	YD06-21A	1260	TS X 3	A: quartz vein with pyrite inside the vein, B:medium to coarse hematitic syenite with disseminated pyrite, C: chlorite-pyrite infill on fractures
800996	N/A	N/A	TS	Old rhyolite (dated by Jason) from mine site with the same age as the volcanic rocks
802801	YD06-10	496.0	Chem	geochem
802802	YD06-10	-	Chem	barite or G1 vein
802803	YD06-10	-	TS & Chem	q-fe carb vein with trace amounts of scheelite
802804	YD06-10	517.0	-	geochem
802805	YD06-10	-	-	q-fe carb vein with specular hematite
802806	YD06-10	-	-	tourmaline and G1 vein
802807	YD06-10	-	TS	q-fe carb vein containing tourmaline
802808	YD06-10	535.6	-	geochem
802809	YD06-10	-	TS	veins (2 fe-carb, 1 fluorite)
802810	YD06-10	543.9	Chem	geochem
802811	YD06-10	558.2	Chem	sample of biotite rich lower stuff, lamprophyr? Sheared. GEOCHEM
802812	YD06-10	567.0	TS	Chlorite rim on G1 fe-carb vein
802813	YD06-10	576.3	Chem	sediments, geochem
802814	YD06-16A	-	Chem	geochem
802815	YD06-16A	1194.1	Chem	geochem
802816	YD06-16A	1207.5	Chem	geochem
802817	YD06-16A	1211.4	TS	lamprophyr dike
802818	YD06-16A	1229.1	TS	q-fe vein with some tourmaline
802819	YD06-16A	1228.6	Chem	geochem
802820	YD06-16A	1231.5	TS	possible Au with q-fe vein
802821	YD06-16A	1244.2	TS x 2	disseminated specular hematite in the groundmass

Sample #	Hole ID	Depth (m)	Purpose	Small Sample Description
802822	YD06-16A	1250.2	TS	geochem
802823	YD06-16A	1257.4	Chem	magnetite vein
802824	YD06-16A	1258.4	Chem	geochem + disseminated pyrite
802825	YD06-16A	1263.3	TS	g1 vein with pyrite crosscut by something
802826	YD06-16A	1270.5	TS	pyrite in vein and groundmass
802827	YD07-33A	1145.8	Chem	geochem
802828	YD07-33A	1174.4	Chem	geochem
802829	YD07-33A	1202.2	Chem	geochem
802830	YD07-33A	1219.9	Chem	geochem
802831	YD07-33A	1234.5	Chem	geochem
802832	YD07-33A	1262.2	Chem	geochem
802833	YD07-33A	1289.2	Chem	geochem
802834	YD07-33A	1321.0	Chem	geochem
802835	YD07-33A	1356.1	Chem	geochem
802836	YD06-16A	1276.1	Chem	geochem
802837	YD06-16A	1291.5	Chem	geochem
802838	YD07-33A	1357.4	TS	abundant tourmaline in q-fe vein
802839	YD07-33A	1372.2	TS	Pyrite rich crosscutting feature
802840	YD07-33A	1375.5	Chem	geochem
802841	YD07-33A	1387.8	TS	dike
802842	YD07-33A	1387.9	TS	Q-fe vein
802843	YD07-33A	1399.5	Chem	geochem - fresh syenite
802844	YD07-33A	1424.5	Chem	geochem
802845	YD07-33A	1429.8	Chem	geochem and for primary oxides
802846	YD07-33A	1449.5	Chem	geochem
802847	YD07-33A	1463.5	Chem	geochem of the different syenite
802848	YD07-33A	1473.8	Chem	geochem
802849	YD07-33A	1483.2	TS	lamprophyr dike
802850	YD07-33A	1496.7	Chem	geochem
802851	YD07-33A	1507.0	Chem	geochem for upper part of the seds adjacent to the contact with the syenite

Sample #	Hole ID	Depth (m)	Purpose	Small Sample Description
802852	YD07-33A	1526.0	Chem	Geochem
802853	YD07-33E	1019.2	Chem	Geochem
802854	YD07-33E	1129.0	Chem	geochem
802855	YD07-33E	1135.7	TS & Chem	quartz-tourmaline vein
802856	YD07-33E	1148.0	-	cut the sample to crosscut the vein to see some interesting structure
802857	YD07-33E	1150.8	TS	tourmaline in the q-fe vein
802858	YD07-33E	1160.5	TS	tourmaline in q-fe vein
802859	YD07-33E	1159.0	1	geochem
802860	YD07-33E	1167.6	TS	G1 vein
802861	YD07-33E	1185.9	TS	tourmaline
802862	YD07-33E	1201.3	Chem	geochem
802863	YD07-33E	1208.9	Chem	geochem
802864	YD07-33E	1222.0	TS	spec hem within carbonate veins
802865	YD07-33E	1236.0	Chem	geochem
802866	YD07-33E	1251.0	TS x 2	py around q-fe vein
802867	YD07-33E	1255.8	TS	coarse cubic pyrite in coarse-grained syenite
802868	YD07-33E	1268.3	TS	tourmaline in q-fe vein
802869	YD07-33E	1274.3	TS	geochem + q-py veinlet
802870	YD07-33E	1281.0	TS	coroded disseminated pyrite
802871	YD07-33E	1302.2	Chem	Geochem of the maroon syenite
802872	YD07-33E	1321.8	TS	cool black quartz thing
802873	YD07-33E	1325.0	Chem	geochem
802874	YD07-33E	1391.0	Chem	geochem
802875	YD07-43	548.8	Chem	geochem
802876	YD07-43	556.1	Chem	geochem
802877	YD07-43	569.9	Chem	geochem
802878	YD07-43	599.1	Chem	geochem
802879	YD07-43	618.5	Chem	geochem
802880	YD07-43	626.8	Chem	geochem
802881	YD07-43	650.5	Chem	geochem

Sample #	Hole ID	Depth (m)	Purpose	Small Sample Description
802882	YD07-43	673.3	Chem	geochem
802883	YD07-43	690.5	Chem	geochem
802884	YD07-43	710.5	TS	Large brittle looking quartz-carbonate vein
802885	YD07-43	710.7	Chem	geochem
802886	YD07-43	725.3	Chem	geochem
802887	YD07-43	747.0	Chem	geochem
802888	YD07-43	765.5	Chem	geochem
802889	YD07-43	801.0	Chem	geochem
802890	YD07-43	824.4	Chem	geochem
802891	YD07-43	834.7	TS	Tourmaline
802892	YD07-43	848.5	Chem	geochem
802893	YD07-43	877.7	Chem	geochem
802894	YD07-33E	1404.2	Chem	geochem
802895	YD07-33E	1411.7	TS	cpy in vein
802896	YD07-33E	1419.2	TS	tourmaline
802897	YD07-56	946.0	Chem	geochem
802898	YD07-56	961.1	Chem	geochem
802899	YD07-56	993.0	Chem	geochem
802900	YD07-56	1021.0	Chem	geochem
802901	YD07-56	1042.6	Chem	geochem
802902	YD07-56	1049.2	TS	cpy + gal in q-fe vein
802903	YD07-56	1072.2	TS	G1 vein
802904	YD07-56	1072.9	TS	Cb + magnetite
802905	YD07-56	1062.5	Chem	geochem
802906	YD07-56	1087.1	Chem	geochem
802907	YD07-56	1097.8	TS x 2	pyrite in strong hem/pot alteration
802908	YD06-16C	1228.5	Chem	geochem
802909	YD06-16C	1255.0	Chem	geochem
802910	YD06-16C	1264.0	Chem	geochem - abundant pyrite
802911	YD06-16C	1265.0	Chem	geochem - fine disseminated pyrite

Sample #	Hole ID	Depth (m)	Purpose	Small Sample Description
802912	YD06-16C	1276.5	Chem	geochem
802913	YD06-16C	1294.2	Chem	geochem
802914	YD06-16C	1299.6	TS	q-fe vein and dissemianted pyrite
802915	YD06-16C	1319.5	TS	Galena
802916	YD06-16C	1221.0	Chem	geochem
802917	YD06-16C	1222.0	TS	pyrite
802918	YD06-16C	1327.0	TS	abundant disseminated pyrite around q-fe vein
802919	YD06-16C	1335.8	Chem	geochem
802920	YD06-16C	1340.0	TS	brown syenite contact
802921	YD06-16A	1233.4	TS	Scheelite
802922	YD07-33A	1424.0	TS	Scheelite
802923	YD07-56A	1006.0	Chem	geochem
802924	YD07-56A	1025.2	Chem	geochem
802925	YD07-56A	1042.1	Chem	geochem and Au in thin section
802926	YD07-56A	1044.1	TS	Au mineralization
802927	YD07-56A	1062.2	TS	Au mineralization
802928	YD07-56A	1064.0	Chem	geochem
802929	YD07-56A	1071.8	TS	scheelite
802930	YD07-56A	1083.2	Chem	geochem
802931	YD07-56A	1103.4	Chem	geochem
802932	YD07-56A	1112.5	-	scheelite
802933	YD07-56A	1121.0	Chem	geochem
802934	YD07-56A	1127.7	TS	Au in py
802935	YD07-56A	1137.5	Chem	geochem
802936	YD07-33B	1320.2	TS	scheelite
802937	YD06-21	1275.2	TS	Au mineralization
802938	YD06-21A	1085.5	TS	Q-fe-tourmaline vein
802939	YD06-21A	1201.5	TS	Au Mineralization
802940	YD06-21A	1241.5	TS x 2	Au Mineralization

Random Drill Core Sampling				
Sample Number	**Hole ID**	**Depth (m)**	**Purpose**	**Small Sample Description**
803301	YD10-225A	122.3	Geothermometer	Quartz-kfs-hem vein in Tseds
803302	YD10-225A	139	TS	Sheared chloritic syenite crosscutting red Tseds with abundant pyrite at contact
803317	YD10-225A	613.2	TS	
803318	YD10-225A	637.5	TS	Sheared syenitic fragment in the Tseds, minor pyrite and carbonate stringers within and crosscutting the pebble
803319	M1030-3	N/A	TS	Assay Data for sample R30-2
800908	YD10-225A	1240.8	TS ONLY	quartz-tourmaline veins with abundant pyrite in sediments, mineralized
800909	YD10-225A	1245.2	TS ONLY	abundant tourmaline and fe-carbonate in quartz-tourmaline vein from sheared sediment zone
800910	YD10-225A	1257	TS ONLY	pyrite and tourmaline in quartz-tourmaline vein from sheared sediment zone
800911	YD10-225A	1282.5	TS ONLY	Tourmaline-fe-carb quartz vein from tourmaline sediment zone
800912	YD10-225A	1280.4	TS ONLY	quartz-fe-carbonate vein with small pyritizied sediment fragment within.

Appendix B

Surface Sample Location Maps

This appendix contains a surface map showing the location and name of each sample and an excel file containing the UTM coordinates and a brief description of each surface sample.

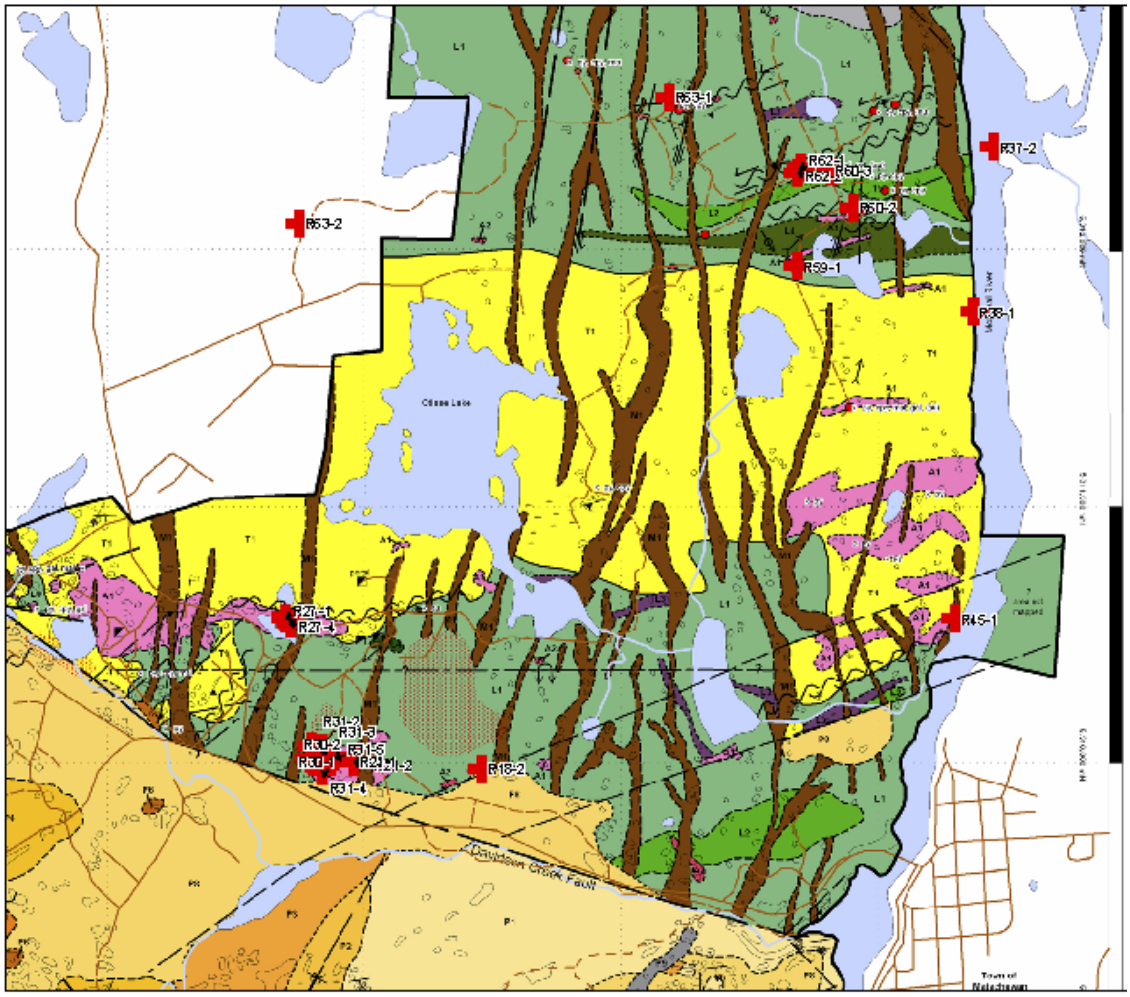

The above figure (modified after Lucas, 2008) shows the location and name of each surface sample. A high resolution version of this image has also been included on the CD in the back insert of this thesis, named "Maps - Surface Sample Locations.pdf"

UTM coordinates and sample descriptions for surface samples can be found in the excel file "Sampling - Surface Sample Locations.xlsx"

If you accessed this thesis from a source other than the University of Waterloo, then you may not have been able to access the high resolution files. Please contact the author at rd2marti@uwaterloo.ca to obtain a copy.

Appendix C

Cross Section Sample Locations

This appendix consists of two N-S cross sections showing the location and name of each sample on each cross section (found below). The CD in the insert in the back of this thesis contains high resolution versions of each cross section and an excel file with the projected northing-depth coordinates of each sample on each cross section.

The cross sections below were generated by projecting drill hole information on 3 adjacent cross sections, looking west, from Northgate's (now AuRico) drill hole database. Drill holes from one section each, at 30m east and west of 22790mE, were projected backwards and forwards, respectively, to the central cross section. Similarly, one section each at 30m east and west of 23240mE were projected backwards and forwards, respectively, to the central cross section. Each of the final cross sections below represents a total slice of 90m through the Young-Davidson syenite.

The file for projected northing-depth drill core sample locations is called "Sampling - Cross Sections Projected Northing-Depth Coordinates.xlsx"

High resolution versions of the cross section presented below have been included on the disc in the back insert of this thesis, named "Maps - 22790mE Sample Locations.pdf" and "Maps - 23240mE Sample Locations.pdf", respectively.

If you accessed this thesis from a source other than the University of Waterloo, then you may not have been able to access these files. Please contact rd2marti@uwaterloo.ca to gain access to the files.

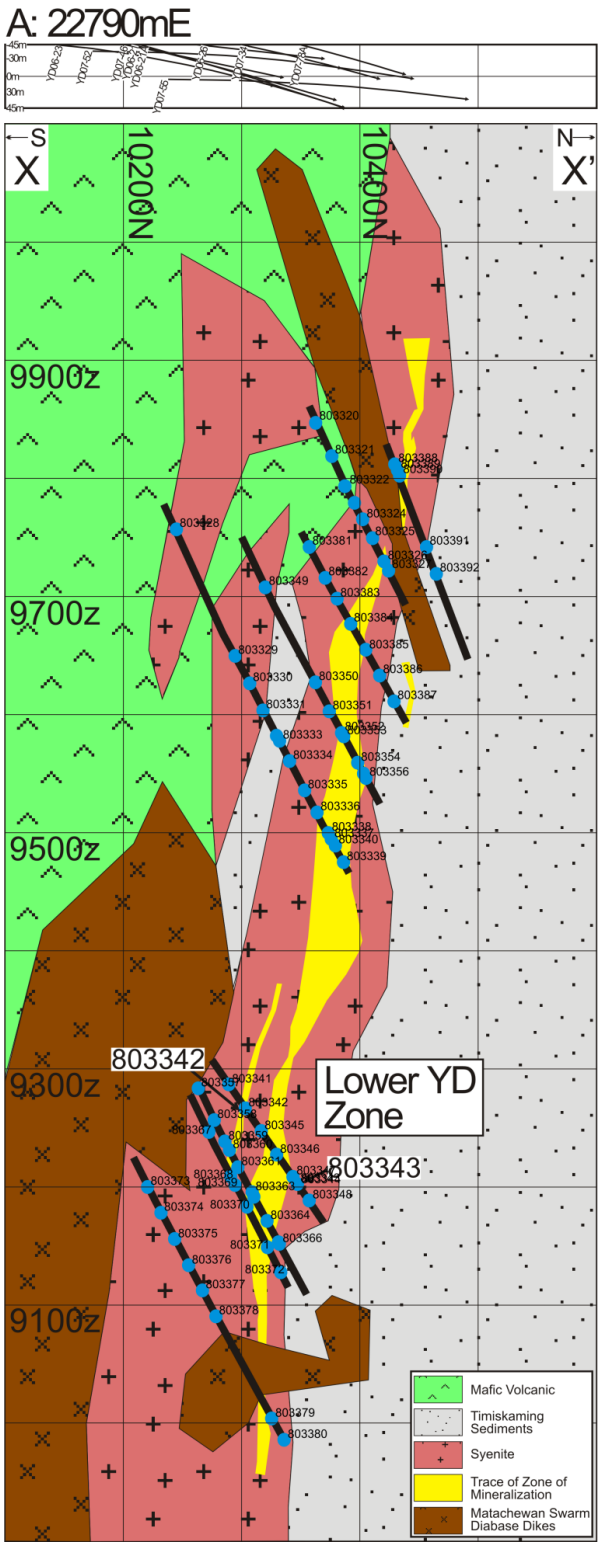
A: 22790mE
45m
30m
0m
30m
45m
YD06-23
YD07-52
YD07-36
YD06-24
YD07-35
YD07-34
YD07-33
YD07-85
S
X
10200N
10400N
N
X'
9900z
9700z
9500z
9300z
9100z
803320
803321
803322
803324
803325
803328
803381
803391
803326
803327
803392
803382
803349
803383
803384
803385
803329
803330
803350
803386
803387
803331
803351
803333
803334
803354
803356
803335
803336
803340
803339
803342
803341
803343
803345
803346
803373
803374
803370
803363
803348
803364
803375
803366
803376
803377
803378
803379
803380
Lower YD Zone
Mafic Volcanic
Timiskaming Sediments
Syenite
Trace of Zone of Mineralization
Matachewan Swarm Diabase Dikes

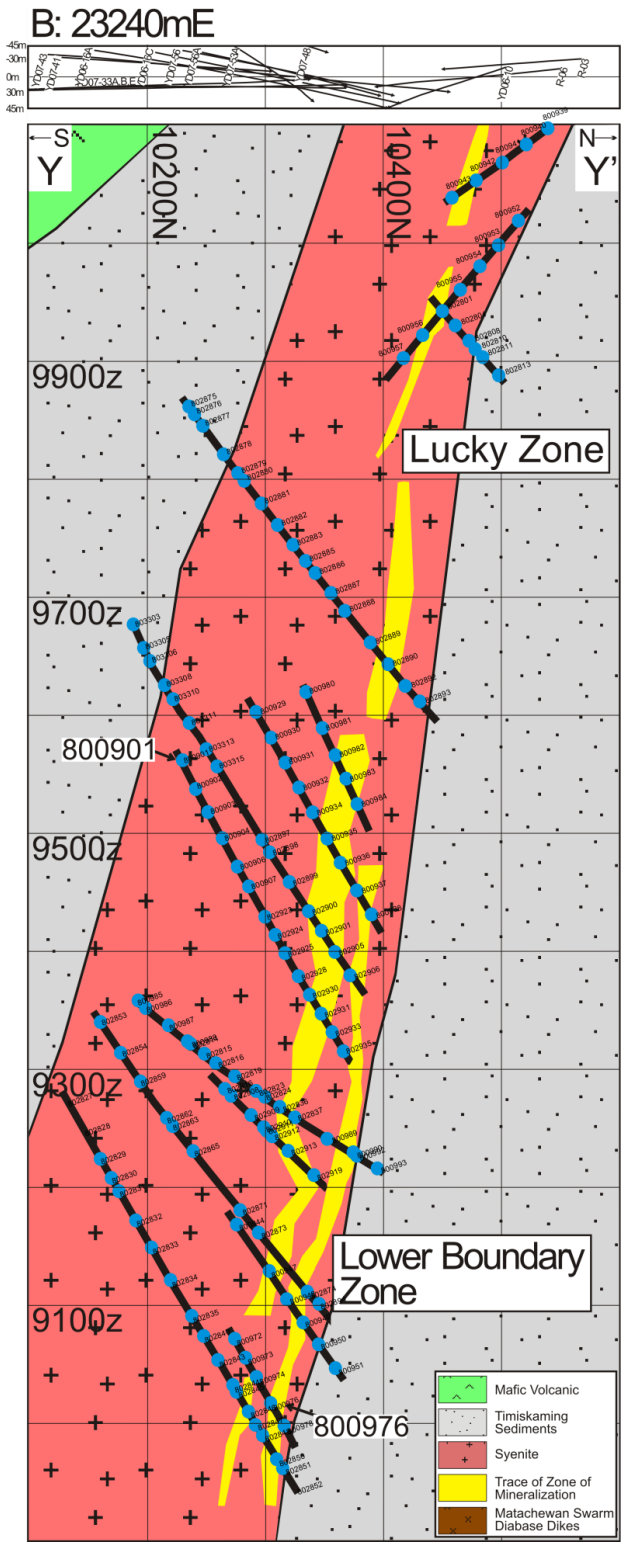
B: 23240mE
-45m
-30m
0m
30m
45m
S
Y
N
Y'
10200N
10400N
9900z
9700z
9500z
9300z
9100z
Lucky Zone
800901
Lower Boundary Zone
800976
Mafic Volcanic
Timiskaming Sediments
Syenite
Trace of Zone of Mineralization
Matachewan Swarm Diabase Dikes

Appendix D

Whole Rock Geochemistry

This appendix consists two excel files found on the CD in the back insert of this thesis. These files include complete raw geochemical analyses for all samples from this study, from GeoLabs and ActLabs, and a comparison example for data from duplicates analyzed at each lab. Data has been screened; any analysis below detection limits has been indicated with 'ldl'.

Complete major and trace element geochemistry tables from both laboratories can be found on separate worksheets in the excel file named "Geochem - Whole Rock Geochemistry.xlsx".

A comparison between duplicate samples analyzed at Geolabs and Actlabs can be found in the excel file named "Geochem - Geolabs Vs Actlabs Duplicates.xlsx".

QAQC calculations for data obtained from each laboratory is contained in the excel file "Geochem - QAQC.xlsx"

If you accessed this thesis from a source other than the University of Waterloo, then you may not have been able to access these files. Please contact rd2marti@uwaterloo.ca to gain access to the files.

Appendix E

Mass Balance Calculations

Excel files containing details for the Isochon and Maclean mass balance calculations are included on the CD in the back insert of this thesis.

The excel file containing the Isochon mass balance calculations is called “Mass Balance - Grant Isochon.xlsx”.

The excel file containing the Maclean mass balance calculations is called “Mass Balance - Maclean.xlsx”.

This appendix also contains Isochon diagrams highlighting typical gains/losses for alteration in volcanic rocks, and gains/losses for alteration of each textural type of syenite (presented below). High resolution copies of each image have been included on the CD in the back insert of this thesis (in .png and .pdf format). The following pages include low resolution examples of each Isochon diagram with the corresponding file name of the high resolution version listed below.

If you accessed this thesis from a source other than the University of Waterloo, then you may not have been able to access these files. Please contact rd2marti@uwaterloo.ca to gain access to the files.

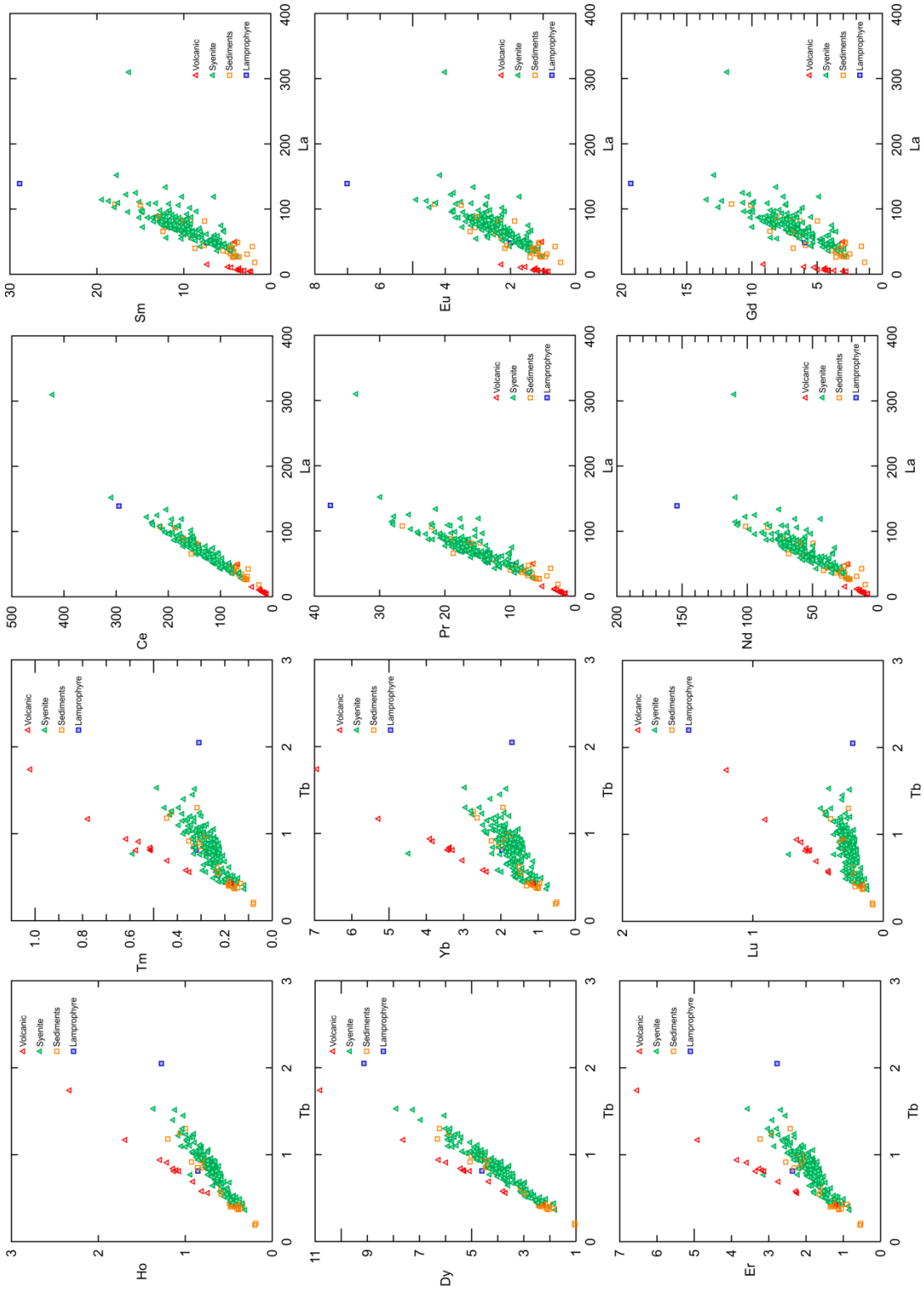

High resolution file: Mass Balance - REE vs REE comparison all rocks.png

Isochon Diagrams - volcanic alteration, YD10-217

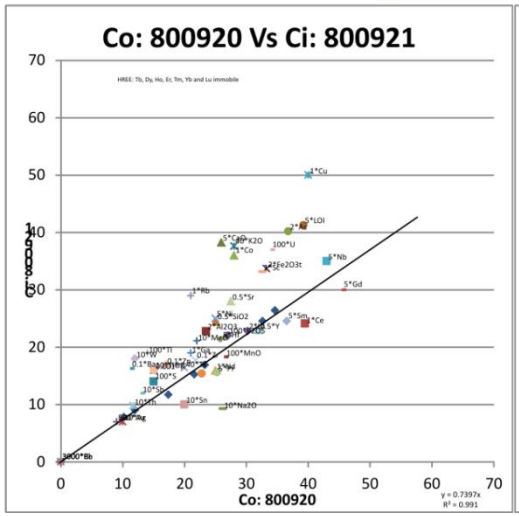

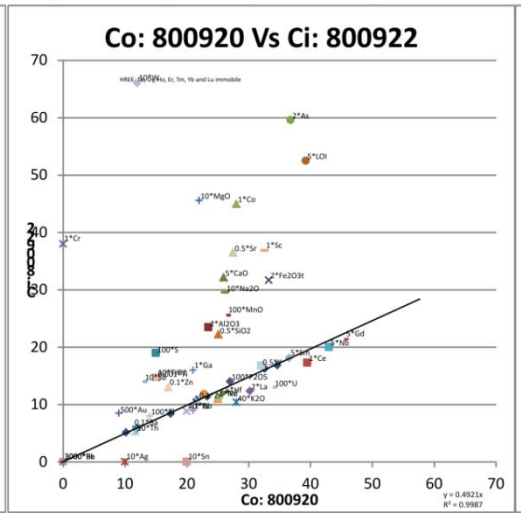

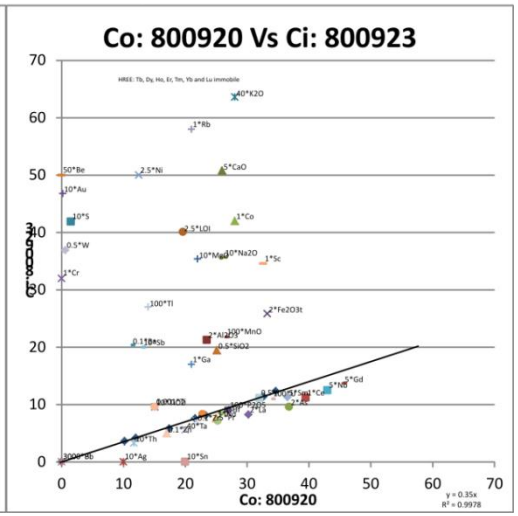

Isochon Diagrams - volcanic alteration, YD10-222

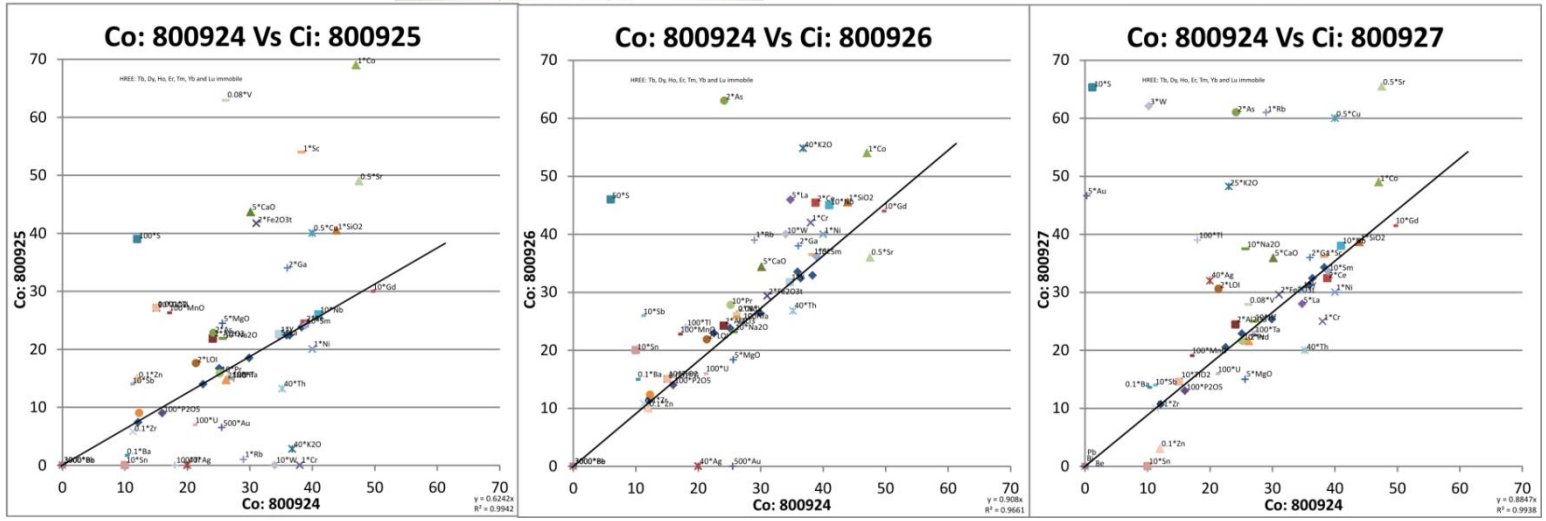

Isochon Diagrams - Massive Syenite

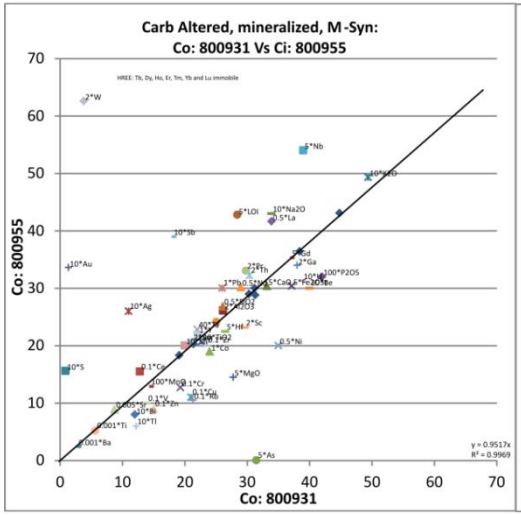

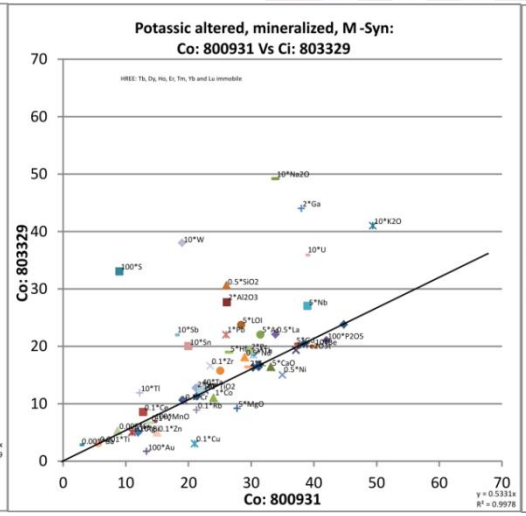

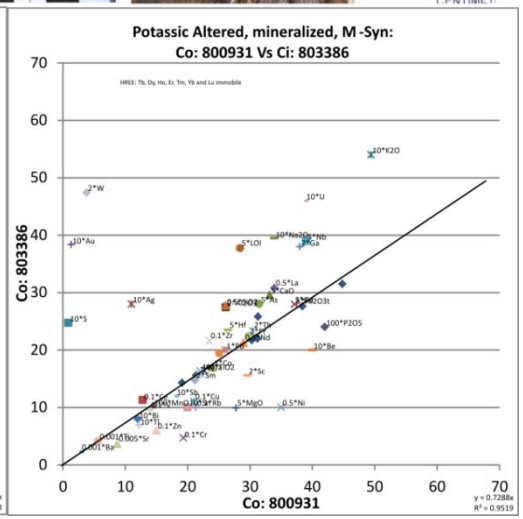

Isochon Diagrams - Porphyritic Syenite

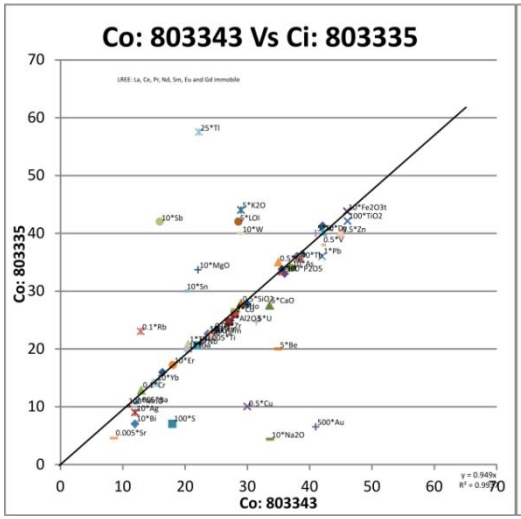

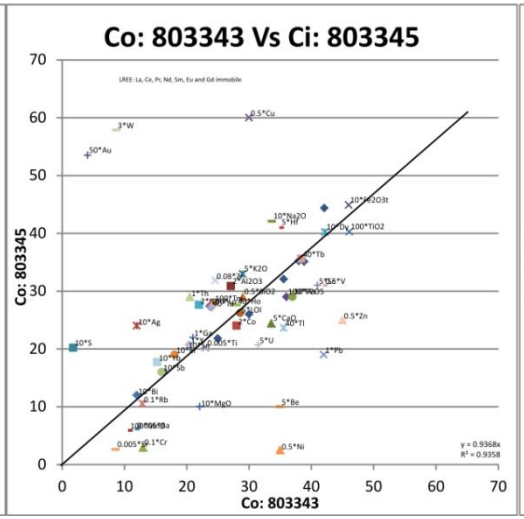

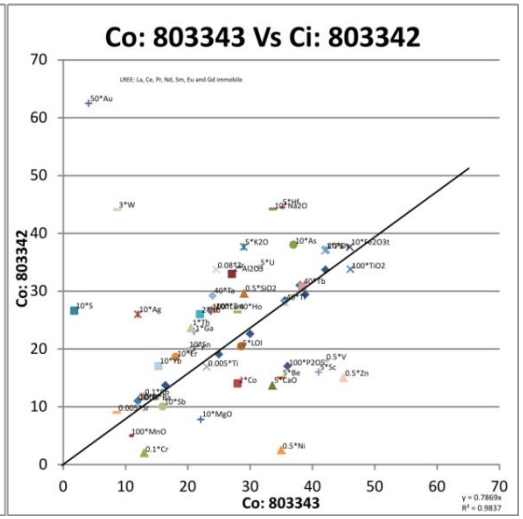

Isochon Diagrams - Trachytic Syenite

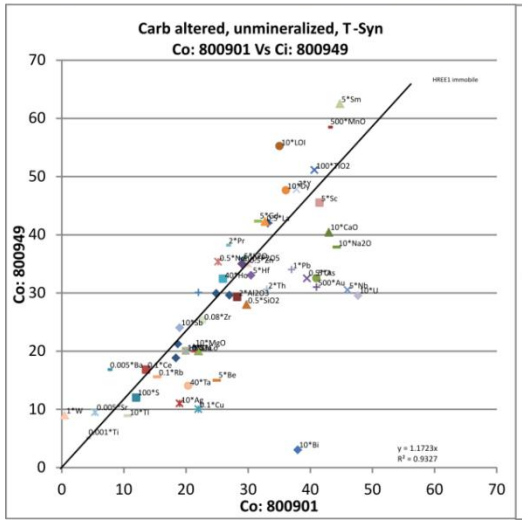

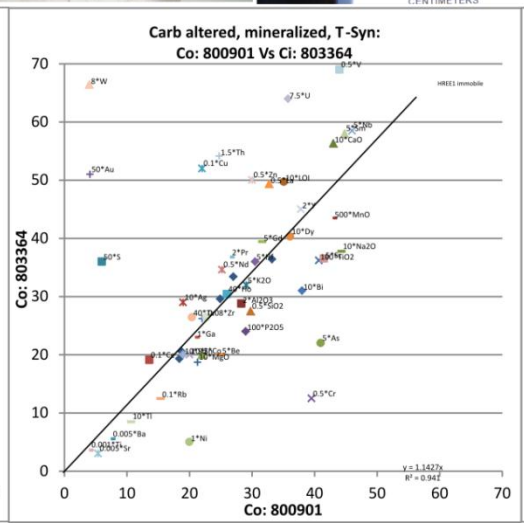

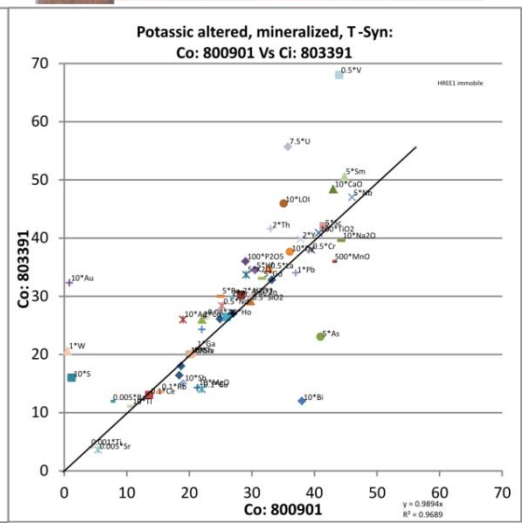

Appendix F

Electron Microprobe Point Analysis Results

This appendix consists three excel files found on the CD in the back insert of this thesis. These files contain complete microprobe analyses for rutile, pyrite and gold. Data has been screened for quality; any analysis with incomplete oxide totals (i.e., <98.5 or >101.5) has been omitted, and any analysis below detection limits has been indicated with 'ldl'.

Complete microprobe analyses of rutile grains are contained in the excel file named "Microprobe - Rutile Analyses.xlsx".

Complete microprobe analyses of pyrite grains are contained in the excel file named "Microprobe - Pyrite Analyses.xlsx".

Complete microprobe analyses of gold grains are contained in the excel file named "Microprobe - Gold Analyses.xlsx".

If you accessed this thesis from a source other than the University of Waterloo, then you may not have been able to access these files. Please contact rd2marti@uwaterloo.ca to gain access to the files.

Appendix G

Electron Microprobe Pyrite TS Photos and Mapping Results

This appendix consists of a .pdf document and photos found on the CD in the back insert of this thesis.

The .pdf document contains thin section photos with the location of point analyses and the outline of maps for each pyrite sample. The corresponding chemical maps for each thin section are contained in the folder labeled “Microprobe Pyrite Maps”.

A complete list of maps is included in the table below.

If you accessed this thesis from a source other than the University of Waterloo, then you may not have been able to access these files. Please contact rd2marti@uwaterloo.ca to gain access to the files.

800918-Py-055_AsKa_5.tif	802825-Py-009color_1_CoKa_2.tif	802940A-Py-003color_3_AsLa_1.tif
800918-Py-055_AsLa_1.tif	802825-Py-009color_1_NiKa_3.tif	802940A-Py-003color_3_CoKa_3.tif
800918-Py-055_CoKa_3.tif	802825-Py-009_AsBg.tif	802940A-Py-003color_3_NiKa_4.tif
800918-Py-055_NiKa_4.tif	802825-Py-009_AsKa_4.tif	802940A-Py-003color_3_SKa_2.tif
800918-Py-055_SKa_2.tif	802825-Py-009_CoBg.tif	802940A-Py-003_AsKa_5.tif
800919A-Py-057_AsKa_5.tif	802825-Py-009_CoKa_2.tif	802940A-Py-003_AsLa_1.tif
800919A-Py-057_AsLa_1.tif	802825-Py-009_NiBg.tif	802940A-Py-003_CoKa_3.tif
800919A-Py-057_CoKa_3.tif	802825-Py-009_NiKa_3.tif	802940A-Py-003_NiKa_4.tif
800919A-Py-057_NiKa_4.tif	802825-Py-009_SBg.tif	802940A-Py-003_SKa_2.tif
800919A-Py-057_SKa_2.tif	802825-Py-009_SKa_1.tif	802940B-Py-004color_4_AsKa_5.tif
800919A-Py-058_AsKa_5.tif	802825-Py-010color_6_AsKa_5.tif	802940B-Py-004color_4_AsLa_1.tif
800919A-Py-058_AsLa_1.tif	802825-Py-010color_6_AsLa_1.tif	802940B-Py-004color_4_CoKa_3.tif
800919A-Py-058_CoKa_3.tif	802825-Py-010color_6_CoKa_3.tif	802940B-Py-004color_4_NiKa_4.tif
800919A-Py-058_NiKa_4.tif	802825-Py-010color_6_NiKa_4.tif	802940B-Py-004color_4_SKa_2.tif
800919A-Py-058_SKa_2.tif	802825-Py-010color_6_SKa_2.tif	802940B-Py-004_AsKa_5.tif
800923B-Py-060_AsKa_5.tif	802825-Py-010_AsKa_5.tif	802940B-Py-004_AsLa_1.tif
800923B-Py-060_AsLa_1.tif	802825-Py-010_AsLa_1.tif	802940B-Py-004_CoKa_3.tif
800923B-Py-060_CoKa_3.tif	802825-Py-010_CoKa_3.tif	802940B-Py-004_NiKa_4.tif
800923B-Py-060_NiKa_4.tif	802825-Py-010_NiKa_4.tif	802940B-Py-004_SKa_2.tif
800923B-Py-060_SKa_2.tif	802825-Py-010_SKa_2.tif	803307A-Py-014color_1_AsKa_5.tif
800991B-Py-091_AsLa_2.tif	802839-Au-024_AsLa_2.tif	803307A-Py-014color_1_AsLa_1.tif
800991B-Py-091_BSEZ_1.tif	802839-Au-024_BSEZ_1.tif	803307A-Py-014color_1_CoKa_3.tif
800991B-Py-091_CoKa_4.tif	802839-Au-024_CoKa_4.tif	803307A-Py-014color_1_NiKa_4.tif
800991B-Py-091_colored_5_AsLa_2.tif	802839-Au-024_colored_3_AsLa_2.tif	803307A-Py-014color_1_SKa_2.tif
800991B-Py-091_colored_5_CoKa_4.tif	802839-Au-024_colored_3_CoKa_4.tif	803307A-Py-014_AsKa_5.tif

800991B-Py-091_colored_5_NiKa_5.tif	802839-Au-024_colored_3_NiKa_5.tif	803307A-Py-014_AsLa_1.tif
800991B-Py-091_FeKa_6.tif	802839-Au-024_FeKa_6.tif	803307A-Py-014_CoKa_3.tif
800991B-Py-091_NiKa_5.tif	802839-Au-024_NiKa_5.tif	803307A-Py-014_NiKa_4.tif
800991B-Py-091_SKa_3.tif	802839-Au-024_SKa_3.tif	803307A-Py-014_SKa_2.tif
802825-P1125-003_AsLa_2.tif	802884-P1125-036_AsLa_2.tif	803323A-Py-159_AsLa_2.tif
802825-P1125-003_BSEZ_1.tif	802884-P1125-036_BSEZ_1.tif	803323A-Py-159_BSEZ_1.tif
802825-P1125-003_CoKa_4.tif	802884-P1125-036_CoKa_4.tif	803323A-Py-159_CoKa_3.tif
802825-P1125-003_colored_1_AsLa_2.tif	802884-P1125-036_colored_2_AsLa_2.tif	803323A-Py-159_colored_AsLa_2.tif
802825-P1125-003_colored_1_CoKa_4.tif	802884-P1125-036_colored_2_CoKa_4.tif	803323A-Py-159_colored_CoKa_3.jpg
802825-P1125-003_colored_1_NiKa_5.tif	802884-P1125-036_colored_2_NiKa_5.tif	803323A-Py-159_colored_CoKa_3.tif
802825-P1125-003_FeKa_6.tif	802884-P1125-036_FeKa_6.tif	803323A-Py-159_colored_NiKa_4.tif
802825-P1125-003_NiKa_5.tif	802884-P1125-036_NiKa_5.tif	803323A-Py-159_NiKa_4.tif
802825-P1125-003_SKa_3.tif	802884-P1125-036_SKa_3.tif	803323B-Au-032_AsLa_2.tif
802825-P1125-004_AsLa_2.tif	802926-P1125-065_AsLa_2.tif	803323B-Au-032_BSEZ_1.tif
802825-P1125-004_BSEZ_1.tif	802926-P1125-065_BSEZ_1.tif	803323B-Au-032_CoKa_3.jpg
802825-P1125-004_CoKa_4.tif	802926-P1125-065_CoKa_4.tif	803323B-Au-032_colored_1_AsLa_2.tif
802825-P1125-004_colored_2_AsLa_2.tif	802926-P1125-065_colored_4_AsLa_2.tif	803323B-Au-032_colored_1_CoKa_3.tif
802825-P1125-004_colored_2_CoKa_4.tif	802926-P1125-065_colored_4_CoKa_4.tif	803323B-Au-032_colored_1_NiKa_4.tif
802825-P1125-004_colored_2_NiKa_5.tif	802926-P1125-065_colored_4_NiKa_5.tif	803323B-Au-032_NiKa_4.tif
802825-P1125-004_FeKa_6.tif	802926-P1125-065_FeKa_6.tif	803323B-Py-165_AsLa_2.tif
802825-P1125-004_NiKa_5.tif	802926-P1125-065_NiKa_5.tif	803323B-Py-165_BSEZ_1.tif
802825-P1125-004_SKa_3.tif	802926-P1125-065_SKa_3.tif	803323B-Py-165_CoKa_3.tif
802825-Py-007color_1_AsKa_5.tif	802934-Py-151_AsLa_2.tif	803323B-Py-165_colored_AsLa_2.tif
802825-Py-007color_1_AsLa_1.tif	802934-Py-151_BSEZ_1.tif	803323B-Py-165_colored_CoKa_3.tif
802825-Py-007color_1_CoKa_3.tif	802934-Py-151_CoKa_4.tif	803323B-Py-165_colored_NiKa_4.tif
802825-Py-007color_1_NiKa_4.tif	802934-Py-151_colored_3_AsLa_2.tif	803323B-Py-165_NiKa_4.tif
802825-Py-007_AsKa_5.tif	802934-Py-151_colored_3_CoKa_4.tif	803364-Py-222_AsLa_2.tif
802825-Py-007_AsLa_1.tif	802934-Py-151_colored_3_NiKa_5.tif	803364-Py-222_BSEZ_1.tif
802825-Py-007_CoKa_3.tif	802934-Py-151_FeKa_6.tif	803364-Py-222_CoKa_3.tif
802825-Py-007_NiKa_4.tif	802934-Py-151_NiKa_5.tif	803364-Py-222_colored_3_AsLa_2.tif
802825-Py-007_SKa_2.tif	802934-Py-151_SKa_3.tif	803364-Py-222_colored_3_CoKa_3.tif
802825-Py-008color_5_AsKa_5.tif	802940A-Py-001color_2_AsKa_5.tif	803364-Py-222_colored_3_NiKa_4.tif
802825-Py-008color_5_AsLa_1.tif	802940A-Py-001color_2_AsLa_1.tif	803364-Py-222_NiKa_4.tif
802825-Py-008color_5_CoKa_3.tif	802940A-Py-001color_2_CoKa_3.tif	803370-Py-227_AsLa_2.tif
802825-Py-008color_5_NiKa_4.tif	802940A-Py-001color_2_NiKa_4.tif	803370-Py-227_BSEZ_1.tif
802825-Py-008color_5_SKa_2.tif	802940A-Py-001color_2_SKa_2.tif	803370-Py-227_CoKa_4.tif
802825-Py-008_AsKa_5.tif	802940A-Py-001_AsKa_5.tif	803370-Py-227_colored_1_AsLa_2.tif
802825-Py-008_AsLa_1.tif	802940A-Py-001_AsLa_1.tif	803370-Py-227_colored_1_CoKa_4.tif

802825-Py-008_CoKa_3.tif	802940A-Py-001_CoKa_3.tif	803370-Py-227_colored_1_NiKa_5.tif
802825-Py-008_NiKa_4.tif	802940A-Py-001_NiKa_4.tif	803370-Py-227_FeKa_6.tif
802825-Py-008_SKa_2.tif	802940A-Py-001_SKa_2.tif	803370-Py-227_NiKa_5.tif
802825-Py-009color_1_AsKa_4.tif	802940A-Py-003color_3_AsKa_5.tif	803370-Py-227_SKa_3.tif

Appendix H

Potassium Feldspar Staining Images

This appendix consists of a collection of pictures of thin section blocks and slabs that have been stained for K-Feldspar. The pictures are contained in the folder "Staining Photos - K-Feldspar". Where available, a photo of the unstained sample is included.

A complete list of K-Feldspar stained samples is included in the table below.

If you accessed this thesis from a source other than the University of Waterloo, then you may not have been able to access these files. Please contact rd2marti@uwaterloo.ca to gain access to the files.

RE19-1.JPG	RE69-2stained.JPG
RE19-1staining.jpg	RE73-3stained.JPG
RE19-2,2staining.jpg	RW25-2staining.jpg
RE19-2.JPG	RW29-2.JPG
RE23-1stained.JPG	RW39-1stained.JPG
RE29-2.JPG	RW41-2staining.jpg
RE29-2staining.jpg	RW45-2,2staining.jpg
RE39-1.JPG	RW45-3.JPG
RE39-1staining.jpg	RW45-3staining.jpg
RE45-1Astaining.jpg	RW49-2.JPG
RE53-1,1staining.jpg	RW49-2staining.jpg
RE53-5.JPG	RW49-3.JPG
RE53-5staining.jpg	RW49-3staining.jpg
RE57-1stained.JPG	RW53-1,1staining.jpg
RE61-2stained.JPG	RW53-1.1.JPG
RE63-1stained.JPG	RW59-2stained.JPG
RE67-1stained.JPG	RW87-1stained.JPG

Appendix I

Iron Carbonate Staining Images

This appendix consists of a collection of pictures of thin section blocks that have been stained for carbonates. The pictures are contained in the folder "Staining Photos - Carbonate". Included in this folder is the unstained and corresponding stained photo for each sample.

A complete list of stained samples is included in the table below.

If you accessed this thesis from a source other than the University of Waterloo, then you may not have been able to access these files. Please contact rd2marti@uwaterloo.ca to gain access to the files.

800924-800927volcanic.JPG	802854.JPG	802908.JPG	RE53-6.2stained.JPG
800924-800927volcanicstained.JPG	802854stained.JPG	802908stained.JPG	RE65-1.JPG
800924.JPG	802855.JPG	802909.JPG	RE65-1stained.JPG
800924stained.JPG	802855stained.JPG	802909stained.JPG	RE69-2.JPG
800925.JPG	802857.JPG	802910.JPG	RE69-2stained.JPG
800925stained.JPG	802857stained.JPG	802910stained.JPG	RE73-1.JPG
800926.JPG	802858.JPG	802911.JPG	RE73-1stained.JPG
800926stained.JPG	802858stained.JPG	802911stained.JPG	RE87-1.JPG
800927A.JPG	802859.JPG	802912.JPG	RE87-1stained.JPG
800927Astained.JPG	802859stained.JPG	802912stained.JPG	RW19-2.JPG
800927B.JPG	802860.JPG	802913.JPG	RW19-2stained.JPG
800927Bstained.JPG	802860stained.JPG	802913stained.JPG	RW29-2.JPG
802801.JPG	802861.JPG	802914.JPG	RW29-2stained.JPG
802801stained.JPG	802861stained.JPG	802914stained.JPG	RW39-1.JPG
802803.JPG	802862.JPG	802915.JPG	RW39-1stained.JPG
802803stained.JPG	802862stained.JPG	802915stained.JPG	RW45-1.JPG
802804.JPG	802863.JPG	802916.JPG	RW45-1stained.JPG
802804stained.JPG	802863stained.JPG	802916stained.JPG	RW45-2.1.JPG
802808.JPG	802864.JPG	802917.JPG	RW45-2.1stained.JPG
802808stained.JPG	802864stained.JPG	802917stained.JPG	RW45-3.JPG
802809.JPG	802865.JPG	802918.JPG	RW45-3stained.JPG
802809stained.JPG	802865stained.JPG	802918stained.JPG	RW47-1.JPG
802810.JPG	802866A.JPG	802919.JPG	RW47-1stained.JPG

802810stained.JPG	802866Astained.JPG	802919stained.JPG	RW49-1.JPG
802811.JPG	802866B.JPG	802920.JPG	RW49-1stained.JPG
802811stained.JPG	802866Bstained.JPG	802920stained.JPG	RW49-2.JPG
802812.JPG	802867.JPG	802921.JPG	RW49-2stained.JPG
802812stained.JPG	802867stained.JPG	802921stained.JPG	RW49-3.JPG
802813.JPG	802868.JPG	802922.JPG	RW49-3stained.JPG
802813stained.JPG	802868stained.JPG	802922stained.JPG	RW49-3stained2.JPG
802814.JPG	802869.JPG	802923.JPG	RW51-1.JPG
802814stained.JPG	802869stained.JPG	802923stained.JPG	RW51-1stained.JPG
802815.JPG	802870.JPG	802924.JPG	RW53-1.1.JPG
802815stained.JPG	802870stained.JPG	802924stained.JPG	RW53-1.1stained.JPG
802816.JPG	802871.JPG	802925.JPG	RW53-1.1stained1.JPG
802816stained.JPG	802871stained.JPG	802925stained.JPG	RW53-1.1stained2.JPG
802817.JPG	802872.JPG	802926.JPG	RW53-1.2.JPG
802817stained.JPG	802872stained.JPG	802926stained.JPG	RW53-1.2stained.JPG
802818.JPG	802873.JPG	802927.JPG	RW55-2.JPG
802818stained.JPG	802873stained.JPG	802927stained.JPG	RW55-2stained.JPG
802819.JPG	802874.JPG	802928.JPG	RW75-1.JPG
802819stained.JPG	802874stained.JPG	802928stained.JPG	RW75-1stained.JPG
802820.JPG	802875.JPG	802929.JPG	RW81-3.JPG
802820stained.JPG	802875stained.JPG	802929stained.JPG	RW81-3stained.JPG
802821A.JPG	802876.JPG	802930.JPG	RW83-1.JPG
802821Astained.JPG	802876stained.JPG	802930stained.JPG	RW83-1stained.JPG
802821B.JPG	802877.JPG	802931.JPG	RW87-1.JPG
802821Bstained.JPG	802877stained.JPG	802931stained.JPG	RW87-1stained.JPG
802822.JPG	802878.JPG	802933.JPG	RW87-2.JPG
802822stained.JPG	802878stained.JPG	802933stained.JPG	RW87-2stained.JPG
802823.JPG	802879.JPG	802934.JPG	YD06-01-3682.JPG
802823stained.JPG	802879stained.JPG	802934stained.JPG	YD06-01-3682stained.JPG
802824.JPG	802880.JPG	802935.JPG	YD06-01-3712.JPG
802824stained.JPG	802880stained.JPG	802935stained.JPG	YD06-01-3712stained.JPG
802825.JPG	802881.JPG	802936.JPG	YD06-01-3732.JPG
802825stained.JPG	802881stained.JPG	802936stained.JPG	YD06-01-3732stained.JPG
802826.JPG	802882.JPG	802937.JPG	YD06-01-3754.JPG
802826stained.JPG	802882stained.JPG	802937stained.JPG	YD06-01-3754stained.JPG

802827.JPG	802883.JPG	802938.JPG	YD06-01-3769.JPG
802827stained.JPG	802883stained.JPG	802938stained.JPG	YD06-01-3769stained.JPG
802828.JPG	802884.JPG	802939.JPG	YD06-01-3791A.JPG
802828stained.JPG	802884stained.JPG	802939stained.JPG	YD06-01-3791Astained.JPG
802830.JPG	802885.JPG	802940A.JPG	YD06-01-3791B.JPG
802830stained.JPG	802885stained.JPG	802940Astained.JPG	YD06-01-3791Bstained.JPG
802831.JPG	802886.JPG	RE19-1.JPG	YD06-01-3796.JPG
802831stained.JPG	802886stained.JPG	RE19-1stained.JPG	YD06-01-3796stained.JPG
802833.JPG	802887.JPG	RE19-2.1.JPG	YD06-01A-3065.JPG
802833stained.JPG	802887stained.JPG	RE19-2.1stained.JPG	YD06-01A-3065stained.JPG
802835.JPG	802888.JPG	RE19-2.JPG	YD06-01A-3378.JPG
802835stained.JPG	802888stained.JPG	RE19-2stained.JPG	YD06-01A-3378stained.JPG
802836.JPG	802889.JPG	RE21-3.1.JPG	YD06-01A-3379.JPG
802836stained.JPG	802889stained.JPG	RE21-3.1stained.JPG	YD06-01A-3379stained.JPG
802837.JPG	802890.JPG	RE21-3.2.JPG	YD06-01A-3397.4.JPG
802837stained.JPG	802890stained.JPG	RE21-3.2stained.JPG	YD06-01A-3397.4stained.JPG
802839.JPG	802892.JPG	RE29-2.JPG	YD06-01A-3493A.JPG
802839stained.JPG	802892stained.JPG	RE29-2stained.JPG	YD06-01A-3493Astained.JPG
802841.JPG	802893.JPG	RE39-1.JPG	YD06-01A-3525.JPG
802841stained.JPG	802893stained.JPG	RE39-1stained.JPG	YD06-01A-3525stained.JPG
802842.JPG	802894.JPG	RE41-1.JPG	YD06-01A-3548.JPG
802842stained.JPG	802894stained.JPG	RE41-1stained.JPG	YD06-01A-3548stained.JPG
802843.JPG	802895.JPG	RE41-2.JPG	YD06-01A-3614.JPG
802843stained.JPG	802895stained.JPG	RE41-2stained.JPG	YD06-01A-3614stained.JPG
802845.JPG	802896.JPG	RE43-2.JPG	YD06-01A-3626.JPG
802845stained.JPG	802896stained.JPG	RE43-2stained.JPG	YD06-01A-3626stained.JPG
802847.JPG	802900.JPG	RE45-1.JPG	YD06-01A-3707.JPG
802847stained.JPG	802900stained.JPG	RE45-1stained.JPG	YD06-01A-3707stained.JPG
802849.JPG	802902.JPG	RE51-2.JPG	YD06-01A-3712.JPG
802849stained.JPG	802902stained.JPG	RE51-2stained.JPG	YD06-01A-3712stained.JPG
802850.JPG	802903.JPG	RE51-3.JPG	YD06-01A-3717.2.JPG
802850stained.JPG	802903stained.JPG	RE51-3stained.JPG	YD06-01A-3717.2stained.JPG
802851.JPG	802904.JPG	RE53-1.1.JPG	YD06-01A-3734.JPG

802851stained.JPG	802904stained.JPG	RE53-1.1stained.JPG	YD06-01A-3734stained.JPG
802852.JPG	802907A.JPG	RE53-3.JPG	YD06-01A-3752.JPG
802852stained.JPG	802907Astained.JPG	RE53-3stained.JPG	YD06-01A-3752stained.JPG
802853.JPG	802907B.JPG	RE53-5.JPG	YD06-01A-3770.JPG
802853stained.JPG	802907Bstained.JPG	RE53-5stained.JPG	YD06-01A-3770stained.JPG